Universidade de Aveiro Departamento de Física
2019

Abel Eduardo Silva Fenta

Estudo local de ad-átomos no grafeno usando espectrocopia de correlação angular perturbada

Locally probing adatoms on graphene using perturbed angular correlation spectroscopy

Universidade de Aveiro Departamento de Física
2019

Abel Eduardo Silva Fenta

Estudo local de ad-átomos no grafeno usando espectrocopia de correlação angular perturbada

Locally probing adatoms on graphene using perturbed angular correlation spectroscopy

Tese apresentada à Universidade de Aveiro para cumprimento dos requisitos necessários à obtenção do grau de Doutor em Engenharia Física, realizada sob a orientação científica do Professor Doutor Vítor Brás de Sequeira Amaral, Professor Catedrático do Departamento de Física da Universidade de Aveiro, do Professor Doutor Lino da Costa Pereira, Professor Assistente do IKS da KULeuven e do Doutor João Guilherme Martins Correia, Investigador Principal do Centro de Ciências e Tecnologias Nucleares do Instituto Superior Técnico.

Tese realizada com apoio financeiro da FCT através da bolsa SFRH/BD/84743/2012

o júri

presidente	Professor Doutor José Rodrigues Ferreira da Rocha Professor Catedrático, Universidade de Aveiro
vogal	Professor Doutor Michel Houssa Professor Assistente, KULeuven
vogal	Professor Doutor João Pedro Esteve de Araújo Professor Associado, Universidade do Porto
vogal	Professor Doutor Tito da Silva Trindade Professor Catedrático, Universidade de Aveiro
vogal	Professor Doutora Florinda Mendes da Costa Professora Associada, Universidade de Aveiro
vogal-orientador	Professor Doutor Lino Miguel da Costa Pereira Professor Assistente, KULeuven
vogal-orientador	Professor Doutor Vítor Brás de Sequeira Amaral Professor Catedrático, Universidade de Aveiro

palavras-chave Grafeno, ad-átomo, ad-molécula, espectroscopia de correlação angular perturbada, teoria do funcional da densidade

keywords Graphene, adatom, admolecule, perturbed angular correlation spectroscopy, density functional theory

Acknowledgements

This manuscript reflects my research work developed during the last five years in close collaboration with the University of Aveiro, KULeuven, and the ISOLDE-CERN. I am sincerely grateful to the countless number of people who were involved and contributed decisively to the accomplishment of this work.

I would like to express my deep gratitude to Professor Vitor Amaral, my first mentor, from the University of Aveiro. Throughout our discussions, Professor Amaral never failed to maintain the enthusiastic way he first introduced me to the preliminary idea and the possibility to do this Ph.D turning our meetings into fascinating lectures. The opportunity to work with him has been a pleasure and a great privilege. My grateful thanks are also extended to Professor Lino Pereira, my supervisor from KULeuven, for his patient guidance, enthusiastic support, and for believing in me and my skills by giving me the opportunity to complete this work. Always constructive and meticulous, Professor Lino Pereira helped me to adopt a scientific attitude in many different phases of my Ph.D. I also wish to acknowledge the help provided by Doctor Guilherme Correira, my supervisor at ISOLDE-CERN. He provided invaluable help with the experimental setup developments achieved during this work. All his advice and discussions were always productive and propelled the research to its completion. I am particularly grateful for his friendship and company at CERN. Professor Vitor Amaral, Professor Lino Pereira, and Doctor Guilherme Correira have been not only great mentors to me, but also good friends who supported me during this period, often troubled and difficult.

My special thanks are extended to Professor Heinz Haas for all his patience, friendship, and a great number of hours dedicated to helping me with the hyperfine methods as well as with the density functional theory.

To Doctor Stefaan Cottenier and Doctor Michel Houssa I am grateful for their help, expertise, and interest in the DFT simulations, as well as for all the advice, crucial to the success of my work.

I am particularly grateful to all the colleagues and friends at CERN, Instituut voor Kern-enStralingsfysica and Departamento de Física da Universidade de Aveiro, especially Professor Joao Pedro Araujo, Professor Ribeiro da Silva, Professor Armandina Lopes, Carlos Amorim, Tania Mendonça, Eric Bosne, Angelo Costa, Narciso Soares, Licinio Ferreira, Joao Pedro Ramos, Lina Pallada, Nuno Fortunato, Maria Joao, Pedro Rodrigues, Ali Baghizadeh, Pegah, Joao Amaral, Marcelo Barbosa, Gonçalo Oliveira, Joao Nuno Gonçalves, Claudia Lopes, Yacine Kadi, Monika Stachura, Alex Gotteberg, Fabio Figueiras, Karl Johnston, Juliana Schell, Maria Borge, Ricardo Teixeira, Gil Fernandes, and many others for their help, friendship, expertise and advice during all these years.

I would like to express appreciation for my friends and co-workers Carlos Amorim, Tania Mendonça, Joao Nuno Gonçalves and Nuno Guerreiro for useful discussions, advice, friendship, dedication, and interest in the developments unfolding during this work.

I am also indebted to Universidade de Aveiro and KULeuven, which have been supporting me not only during this experience but since 2007 when I started my bachelor's in Engineering Physics: Professors Ricardo Dias, Florinda Costa, Armando Lourenco, Luis Pereira, Joaquim Leitao, Joao Veloso, Vitor Torres, Manuel Barroso, Luis Rino, Antonio Luis Ferreira, Maria Celeste, Nikolai Sobolev,José Castanheira, Sushil Mendiratta, Paulo Andre, Luis Cadillon and many others. I would also like to offer sincere thanks to Mr. Francisco Reis, Mr. Ivo, Ms. Cristina Rei, Ms. Fatima Bola and to all former colleagues from Physics and Engineering Physics at the University of Aveiro.

I would like to thank all the members of the ISOLDE collaboration, in particular, the Solid State Physics Group, for always providing an efficient and friendly environment.

I wish to thank my English teacher Ms. Anna Peredelska for the important support and all the fantastic lessons which were fundamental to writing this manuscript.

I would like to thank the members of the jury for taking the time to read this thesis.

Thanks go also to FCT and KULeuven for the financial support.

I cannot thank my friends enough for the tremendous support I receive from them. I consider myself lucky to have you by my side. I am not going to make particular references here because they are too numerous to list and it would be unfair to mention only a few. You guys are really the best!

(In Portuguese) Finalmente, o mais justo dos agradecimentos. À minha família,

aqueles a quem tudo devo, quem me transmitiu os valores da honestidade e respeito pelo outro, quem me ensinou a importância do trabalho e da perseverança, e me fez perceber que a educação é a ferramenta mais leal e a mais bonita para enfrentar a vida: aos meus pais e aos meus avós, à Titi e ao Tá, à Márcia, ao Duarte e ao Afonso, muito obrigado. A vossa história de vida é um exemplo para mim e ensina-me a superar os desafios. À restante família, que por ser tão grande não é possível de mencionar aqui, dizer que me orgulha ser um de vós e agradecer o tanto que me têm dado.

(In Portuguese) Para ti Diana, minha companheira em todas as horas. Foste, de todos, a mais corajosa e mais paciente! Tudo farei para compensar este período de maior ausência. A nossa história continua. Adoro-te! Obrigado ainda à tua família, que considero como minha também, em especial aos teus pais.

Abstract (PT)

A interacção de átomos e moléculas adsorbidos na superfície do grafeno (ad-átomos e ad-moléculas) constitui um tópico de intensa pesquisa no contexto de vários domínios científicos, demonstrando em certos casos a possibilidade do desenvolvimento de novas aplicações tecnológicas. Tendo em conta que as propriedades do sistema grafeno+ad-átomo/ad-molécula são dependentes da configuração de adsorção (ad-átomo isolado, organizado em cluster com diversas geometrias e coordenações) é importante compreender os seus efeitos do ponto de vista teórico mas também desenvolver métodos que permitam o seu estudo a nível experimental. A presente tese centra-se no estudo da interacção de ad-átomos (Hg, Cd, In e Ag) e ad-moléculas (HgO_2) no grafeno, em termos estruturais e das propriedades electrónicas do sistema conjunto.

O estudo teórico, baseado na teoria de funcional de densidade (DFT), focou-se num conjunto de cálculos e simulações para diferentes elementos adsorbidos na superfície do grafeno (Hg, Ag, Cd e In). A energia de ligação e a estrutura electrónica foram obtidas para diferentes posições atómicas (simétricas), desde ad-átomos isolados até arranjos do tipo mono-camada contínua. Um estudo detalhado foi realizado para o grafeno-Hg, como sistema modelo, usando diversos funcionais e testando diferentes concentrações do ád-atomo no grafeno. Para os ad-átomos de Ag, Cd e In, foram realizados estudos mais direccionados, com enfâse em configurações de maior interesse tendo por base o estudo exaustivo realizado para o Hg. Os resultados permitiram perceber que a energia de ligação depende da concentração do ad-átomo no grafeno bem com da posição simétrica de adsorção (H, T, ou B). Todos os elementos estudados são mais estáveis na configuração de ad-átomo isolado, sendo preferêncial relativamente à configuração de mono-camada contínua.

Para cada um dos elementos em estudo, calculou-se o gradiente de campo eléctrico (EFG) (componente V_{zz} e parâmetro de simetria η). Mostrou-se que o EFG é sensível à posição de adsorção bem como à concentração do ad-átomo em relação ao número de átomos de carbono da rede. Além disso, ficou demonstrada

a capacidade de usar o EFG como parâmetro experimental capaz de distinguir o regime de ad-átomos isolados e o regime de mono-camadas contínuas, sendo que em certos casos com variações significativas com a distância ao grafeno e entre diferentes posições simétricas. Com base nos cálculos realizados, é proposto a utilização do gradiente de campo eléctrico (que pode ser obtido experimentalmente recorrendo a técnicas hiperfinas) como parâmetro de estudo da estabilidade e configuração de ad-átomos e ad-moléculas no grafeno. Em particular, demonstrou-se que a sensibilidade do EFG é tanto maior quanto maior a energia de ligação do ad-átomo ao grafeno.

Por último, foi realizado o estudo experimental da adsorção de Hg no grafeno, nas condições normais de temperatura e pressão, recorrendo à técnica de correlações angulares perturbadas (PAC) usando ^{199m}Hg como átomo sonda. A combinação das medidas experimentais e DFT permitiu identificar a coordenação do Hg na superfície de grafeno na forma da molécula linear HgO_2, com elevada energia de ligação (superior a 1 ev) em comparação com ad-átomos de Hg isolados (inferior a 0.2 eV). Os resultados permitem ainda concluir o papel crucial do oxigénio na forte ligação entre a ad-molécula e o grafeno. Este trabalho representa a demonstração da possibilidade do uso de técnicas hiperfinas para estudar à escala atómica a interacção de átomos ou moléculas adsorbidos na superfície do grafeno.

Foi ainda reportada a primeira experiência de PAC realizada no isótopo de ^{68m}Cu para o decaimento ^{68m}Cu ($6^-, 721$ keV, 3.75 min), demonstrando-se a possibilidade de usar este isótopo de cobre como sonda de PAC para aplicações em diversos campos da física do estado sólido em particular no contexto da investigação do grafeno. Tendo em conta que o Cu constitui um dos catalizadores mais amplamente usados na obtenção de monocamadas de grafeno, a caracterização do ^{68m}Cu como nova sonda disponível para PAC permitirá, por exemplo, um estudo à escala atómica da influência do substrato de Cu, ao nível do tamanho de grão e orientação, na qualidade do grafeno obtido.

O presente estudo permitiu encontrar novas direcções de pesquisa com recurso a técnicas hiperfinas para investigação do grafeno e outros materiais 2-D, não apenas para ad-átomos de metais pesados mas para outros elementos. Por exemplo, o estudo de propriedades magnéticas de elementos de transição em grafeno poderá ser estudado por via de uma medida experimental com recurso a técnicas hiperfinas. Diferentes cenários experimentais podem ser idealizados, com diferentes condições de temperatura e pressão, com possiblidade de aplicação de campo eléctrico ou magnético, permitindo a realização de estudos mais detalhados do processo de estabilidade/adsorção de ad-átomos e ad-moléculas no grafeno.

Abstract (EN)

The interest in understanding the interaction between graphene and atoms and molecules that are adsorbed on its surface (adatoms and admolecules) spans a wide range of research fields and applications, for example, to controllably change the properties of graphene in electronic devices or to detect those changes in graphene-based sensors. Since the properties of graphene+adsorbent systems are strongly dependent on the adsorption configuration (e.g. isolated versus clusters, their geometry and coordination), it is important to not only understand these effects from a theoretical point of view, but also to be able to probe them experimentally. This thesis focuses on the interaction between graphene and adatoms (model cases: Hg, Cd, In and Ag) and admolecules (model case: HgO_2), in terms of structural and electronic properties.

The theoretical part of the research was based on density functional theory (DFT) calculations for different heavy elements adsorbed on graphene (Hg, Ag, Cd and In). The binding energy and the electronic structure were calculated for various high-symmetry atomic configurations, from isolated adatoms to a continuous monolayer. Detailed studies were carried out for Hg-graphene, as a model system, i.e. testing various functionals and covering a wide range of nominal concentration. For Ag, Cd, In, we carried out more targeted studies, based on the extensive calculations for Hg. It was demonstrate that the binding energy depends on adatom concentration and as well on adsorption site (H, T, or B). All studied elements are predicted to be more stable as isolated adatoms than as a continuous monolayer.

For each element, we calculated the electric field gradient (EFG) parameters (V_{zz} and asymmetry parameter η). The EFG exhibits some variation when comparing different high-symmetry sites, and also depends on the nominal concentration of the adatom relative to C atoms. Furthermore, the EFG is found to be sensitive to the local atomic structure, distinguishing isolated from monolayer configurations, and for some cases, varying significantly with small variations in adatom position (at the sub-Å scale). Based on these

calculations, we propose that the electric field gradient, which can be measured using hyperfine techniques, can be used as an experimental observable providing insight on the local atomic configuration and bonding stability of adatoms and admolecules on graphene. In particular, our calculations indicate that the level of detail that can be addressed via the EFG parameters (e.g. positional precision) increases with the stability (binding energy). In other words, the more stable the graphene-adatom system (i.e. more relevant in a application scenario), the more it lends itself to be studied using hyperfine techniques.

Finally, adsorption of Hg on graphene in ambient conditions was experimentally studied using perturbed angular correlation (PAC) spectroscopy and ^{199m}Hg as probe nuclei. The combination of PAC measurements and DFT calculations allowed us to conclude that the majority of the Hg probes were adsorbed in the form of linear HgO_2 molecules, which are adsorbed with higher binding energies (exceeding 1 eV) than isolated Hg adatoms (below 0.2 meV), i.e. oxygen plays a crucial role in stabilizing Hg adsorption on graphene. This work constitutes a proof-of-principle for the use of hyperfine techniques to study the interaction between graphene and adsorbed atoms and molecules, at the atomic scale.

We also reported the first PAC experiment based on the decay of ^{68m}Cu ($6^-, 721$ keV, 3.75 min) and demonstrated the feasibility of using this Cu isotope as a probe nuclei for PAC for applications in the fields of solid state physics in particular in the context of graphene research. Since Cu is the most widely employed catalyst for obtaining graphene monolayers with reasonable quality, establishing ^{68m}Cu as a suitable PAC probe enables the use to study the influence of the Cu substrate, e.g. on grain size and orientation, number of layers and quality of the grown graphene.

Our findings open the way for a wide range of applications of hyperfine techniques, including other 2-dimensional materials and other types of adatoms and phenomena. For example, the magnetic properties of transition elements can also be addressed, via the magnetic hyperfine interaction. In addition to the ability to probe multiple adatom properties and phenomena (e.g. structural and magnetic), such an experimental approach based on hyperfine techniques is generally compatible with applied electric or magnetic fields (often used to investigate basic and functional properties), ultra-high vacuum (typically necessary when studying surfaces, to minimize contamination), and low temperature operation (typically necessary when studying isolated adatoms, due to their high surface mobility).

Contents

Chapter 1

Introduction to graphene

Since it was isolated by Andre Geim and Konstantin Novoselov in 2004, who were awarded the Nobel Prize for Physics in 2010, graphene has become a remarkable subject of research that extended to virtually every domain of materials science, exhibiting novel phenomena and with potential for new applications. This chapter consists of an overview of the basic properties of graphene and the related topics. *Section* 1.1 gives a description of carbon and respective allotropic forms and the emergence of graphene as the first two-dimensional crystal in particular. The atomic structure and the main properties of this novel material are presented, respectively, in *section* 1.2 and *section* 1.3. A succinct introduction of the production methods of graphene is given in *section* 1.4. A summary of several promising technological applications of graphene is provided in *section* 1.5 and other different two-dimensional structures that were obtained since graphene was discovered are presented in *section* 1.6. Finally, *section* 1.7 shows the state of the art related to the adsorbed atoms and adsorbed molecules on graphene.

It is this chapter's prime objective to introduce the fascinating world behind the new family of two-dimensional materials where graphene has opened the first window. It intends to provide the fundamental understanding of this atomic crystal comprising the main topic of this thesis and revealing physical concepts that will be crucial in the experimental and theoretical research that will be presented hereafter.

1.1 The history of graphene

Carbon (C) is unquestionably one of the most fascinating elements of the periodic table and the fourth most abundant element in the universe. It is the base component of DNA, thereby being the foundation of life on earth. This chemical element, with 6 electrons, can exist in the most diverse forms and, due to the binding flexibility, carbon-based systems can have an unlimited number of structures with a variety of properties [1–3].

Graphite with a layered planar structure arranged in a hexagonal lattice appears as one of the most common structures and the most stable allotropic form of carbon under standard pressure and temperature conditions. However, under high pressure, carbon can be transformed into a diamond structure which is recognized as a metastable form of carbon [1–3]. Other carbon allotropic forms reveal themselves in a molecular way: for instance, in the structure with 60 atoms (C_{60}) organized as a soccer ball called fullerene [4] or as carbon nanotubes [5] which consists of a kind of a rolled structure.

Graphene was the name first suggested by Hanns-Peter Boehm [6] for a single plane of graphite, a flat monolayer of carbon atoms organized in a two-dimensional (2D) honeycomb lattice that can be viewed as a basic building block of the graphitic materials which have different dimensionalities as is shown in Figure 1.1: it can be wrapped up into fullerenes (nearly a 0D object), rolled into nanotubes (nearly a 1D object) or stacked into graphite [7]. This 2D crystal has been extensively studied, from the theoretical point of view, for more than sixty years and used for describing properties of several carbon allotropes [8–11]. P. R. Wallace [7] presented, in 1947, the theoretical analysis of the electronic structure of this monolayer, reaching the linear dispersion relation. Using Wallace's two-dimensional band structure model, McClure, in 1956, calculated the conduction-electron magnetic susceptibility [8]. However, graphene had not been studied experimentally because it was presumed not to exist in the free state. This idea was widely supported since the early 1930s. In particular, a series of works performed by Peierls [12] in 1935 and Landau [13] in 1937, pointed out that a 2D crystal could not exist because it was thermodynamically unstable, i.e., at any finite temperature the thermal fluctuations in a low-dimensional structure should lead to atoms displacements comparable with interatomic distance. This argument was also later strongly supported by the *Mermin-Wagner theorem* [14] and reinforced by the absence of an experimental observation of any low dimensional material. Such observation came fifty years later, in 2004, when Andre Geim and Konstantin Novoselov surprisingly isolated single-atom-thick crystallites from bulk graphite using micromechanical cleavage (or *scotch-tape method*) [15,16]. They isolated monolayers of carbon, transferred them onto thin silicon dioxide (SiO_2), and performed the characterization using

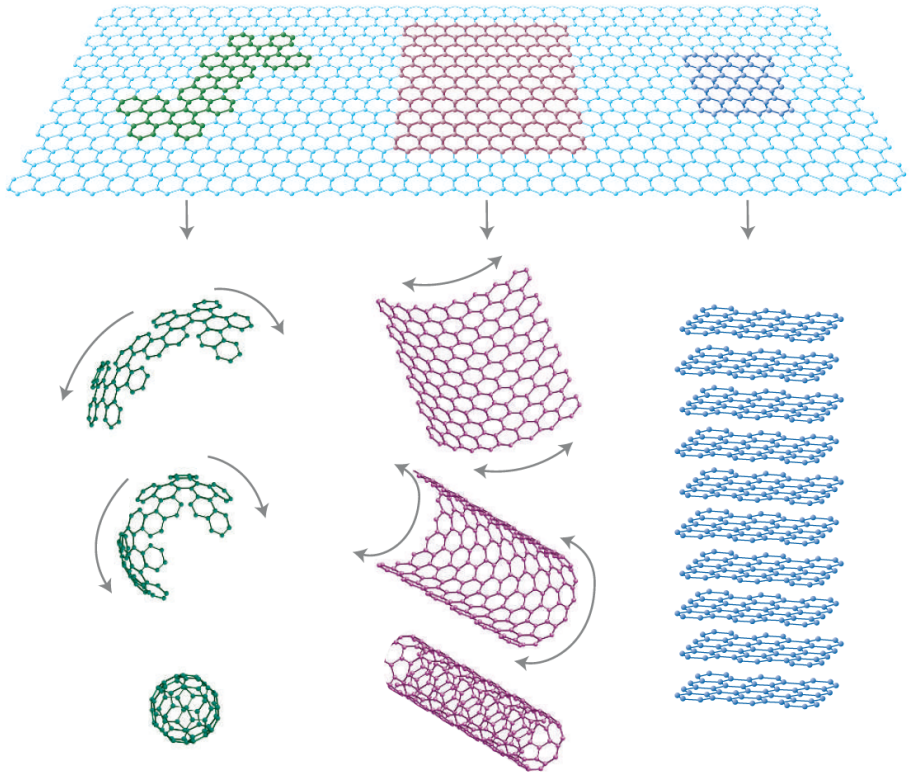

Figure 1.1: Graphene as a 2-dimensional (2D) building block for other forms of carbon with different dimensionalities: it can be wrapped up into fullerenes (nearly 0D), rolled into nanotubes (nearly 1D) or stacked into graphite (3D). Reproduced from [11].

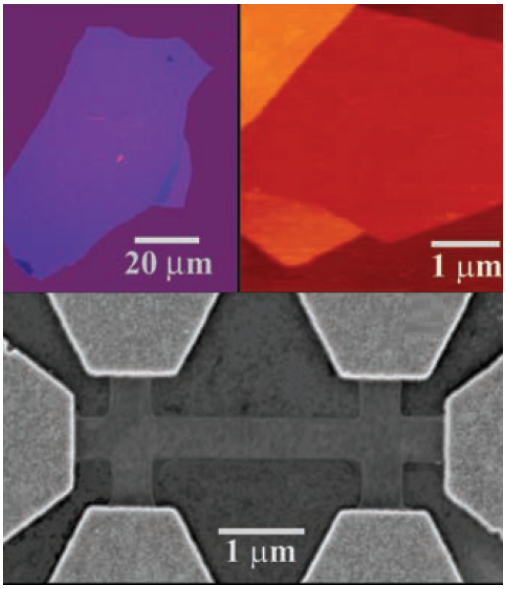

Figure 1.2: Monocrystalline graphitic films, which were described as a few atoms thick stable under ambient conditions. Thin films were recognized as the first two-dimensional crystal found: graphene. At the top-left corner: photograph of graphene flake with thickness about 3 *nm*. At the top-right corner: atomic force microscopy image of single-layer graphene. At the bottom: scanning electron microscopy image of an experimental device prepared with graphene. Reproduced from [15].

optical microscopy, scanning electron microscopy, and atomic-force microscopy (Figure 1.2). However, at the beginning of the process, the yield was extremely low and only a micrometer-sized graphene flake appeared in the large area scanned [17–22]. Despite the attempts to obtain monolayers of graphite made by several groups using mechanical exfoliation [23–26], nothing thinner than 50 to 100 layers had been produced before 2004.

Notwithstanding its short history, graphene has rapidly become one of the most researched on the horizon of materials science and condensed-matter physics, primarily because it was the first example of 2D atomic crystals demonstrating unique physical properties and the potential for a number of applications. More generally, graphene was the first of a new family of materials that offer new phenomena for low-dimensional physics which never ceases to surprise, promising to begin a new technological paradigm [16, 17, 19–22].

1.2 Atomic structure of graphene

Graphene is a 2D atomic crystal which consists of a single graphite layer with strong covalent bonds between carbon arranged in a hexagonal lattice. The variety of structural forms of carbon results from a special electron configuration that provides the ability to organize different types of bonds through atomic orbital hybridisation [2]. The electrons in carbon, in the ground state, occupy the $1s^2$, $2s^2$, $2p_x^1$ and $2p_y^1$ atomic orbitals and, only the four outer electrons participate in the formation of the covalent chemical bonds (tetravalent element). In bonds with other atoms, carbon usually promotes one of the $2s$ electrons into the empty $2p_z$ orbital, resulting in the formation of hybrid orbitals. In graphene only two of the three $2p$ orbitals (p_x and p_y) hybridize to form three new planar orbitals called sp^2, which characterize the σ-bonds. They represent a covalent in-plane bond responsible for the hexagonal lattice structure and the high performance of the mechanical properties of graphene. The p_z orbital with the remaining electron is perpendicular to the plane and can be combined to form the interplane π-bonds, lower in terms of binding energy. Thus, graphene represents a system with one electron per lattice site, i.e., a half-filled system. The p_z orbitals are responsible for the unusual electronic properties observed in graphene [17–19, 22, 27].

The hexagonal lattice of graphene does not represent a Bravais lattice but it can be viewed as two interpenetrating triangular lattices or a basis with two non-equivalent carbon atoms, A and B, as shown in Figure 1.3 (*left*). As the unit cell contains two carbon atoms, the energy spectrum originated from π-orbitals has two energy bands – a valence band and a conduction band. In Cartesian coordinates, the basis vectors $\mathbf{a}_1$ and $\mathbf{a}_2$ of the unit cell in the real space can be written as [27, 28]:

$$a_1 = (\sqrt{3}a/2, a/2) \text{ and } \mathrm{a}_2 = (\sqrt{3}\mathrm{a}/2, -\mathrm{a}/2) \tag{1.1}$$

with $a = \sqrt{3}a_0$, where $a_0 = 1.42$ Å is the nearest neighbor interactomic distance. The reciprocal lattice is described by basis vectors $\mathbf{b}_1$ and $\mathbf{b}_2$:

$$b_1 = (2\pi/\sqrt{3}a, 2\pi/a) \text{ and } \mathrm{b}_2 = (2\pi/\sqrt{3}\mathrm{a}, -2\pi/\mathrm{a}) \tag{1.2}$$

and the reciprocal constant is given by $4\pi/\sqrt{3}a$. Figure 1.3 (*right*) shows the crystal structure of graphene in the first Brillouin zone and the respective high symmetry points Γ, M, K and $K^{'}$.

As previously mentioned, the structural stability of graphene has long been intensively researched and, recently, many studies [29–33] have helped in understanding the phenomenon, showing in-plane and out-of-plane distortions of graphene structure which are crucial for the stability of graphene contradicting

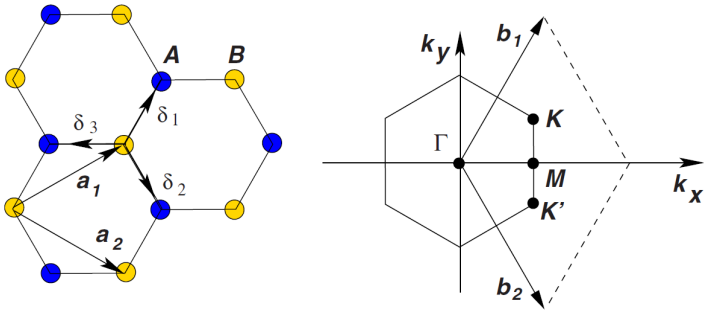

Figure 1.3: Left: The hexagonal lattice of graphene. Graphene can be view as two interpenetrating triangular lattices (is not a Bravais lattice), represented by the lattice unit vectors $\mathbf{a_1}$ and $\mathbf{a_2}$ and the nearest-neighbor vectors $\delta_\mathbf{i}$, $i = 1,\ 2,\ 3$. Right: First Brillouin zone and the high symmetry points: Γ , M, K and $K^{'}$. Reproduced from [28].

the *Mermin-Wagner theorem*, according to which there is no long-range order (crystallographic or magnetic) in two dimensions due to thermal fluctuations. In fact, the stability at room temperature (RT) of graphene, is the consequence of divergences at low $\mathbf{k}$ vectors when the integration of the atomic displacements takes over the whole 2D $\mathbf{k}$-space [33–36]. At any finite temperature, the fluctuations diverge only for infinitely large 2D crystals as the divergences are weak, due to the so-called *logarithmic divergences*, crystals of limited sizes might exhibit infinitely small fluctuations [21, 27, 28].

It is usual to distinguish between single-layer, bilayer and few-layer graphene. As its electronic properties depend strongly on the number of layers, and also their relative orientation, graphene community considers 10 layers as the maximum limit, since for a system with more than 10 layers it is considered to be a thin film of graphite since it essentially behaves as this 3D material [27].

1.3 Properties of graphene

The physical properties of graphene are, in large part, the result of the dimensionality of its structure. This 2D material uniquely combines extreme mechanical strength, exceptionally high electronic and thermal conductivities, impermeability to any gases, as well as many other supreme properties [11,21,22], some of which reach theoretically predicted limits such as Young's modulus

of 1 TPa and intrinsic strength of 130 GPa [37], room-temperature electron mobility of 2.5×10^5 $cm^2V^{-1}s^{-1}$ [38] and an optical absorption in the infrared limit of exactly $\alpha\pi \approx 2.3$ % (where α is the fine structure constant) [39].

1.3.1 Electronic properties

Electronic properties represent the most explored aspect of graphene's physics. Novel electronic properties with unprecedented characteristics are the main reason why graphene has attracted so much scientific and technological interest. A detailed description and extensive theory review were given by Castro Neto et al. and Mikhail I. Katsnelson in references [28] and [40], respectively, as well as in other text books such as references [41, 42].

In graphene, most of the relevant electronic properties can be understood based on the structure of the p_z orbitals of neighboring carbon atoms resulting in delocalized π-bond (occupied or valence) and π^*-bond (unoccupied or conduction). Using tight-binding approach and considering a single electron per atom, the band structure can be adequately described and the energy (E) dispersion relation written as [28]:

$$E^{\pm}(k_x, k_y) = \pm\gamma_0\sqrt{1 + 4cos\frac{\sqrt{3}k_x a}{2}cos\frac{k_y a}{2} + 4cos^2\frac{k_y a}{2}} \tag{1.3}$$

where $a = \sqrt{3}a_0$ keeps the same meaning defined previously in *section* 1.2 and γ_0 is the nearest neighbor overlap which takes a value between 2.5 eV and 3 eV.

Figure 1.4 shows the band structure of graphene calculated using equation 1.3. The physics of graphene is described by the nature of energy spectrum close to the top of the valence band and to the bottom of the conduction band. The momentum values at which the two bands meet are called *Dirac points* (high-symmetry K and $K^{'}$ points). From Figure 1.4 it is clear that graphene is a zero-gap semiconductor and, on the other hand, since the valence and conduction bands only touch at two momentum points, the density of states is zero at the Fermi energy, E_F. This is a consequence of the hexagonal symmetry of graphene (with two atoms per unit cell) which is conceptualized as two interpenetrating triangular lattices. Notice also the conical shape of the valence and conduction bands close to the Dirac points with negative and positive energy values, respectively [18, 28, 42–44].

Equation 1.3 can be expanded close to the Dirac point (K or $K^{'}$), giving the well-known dispersion relation that shows the linear relationship between energy

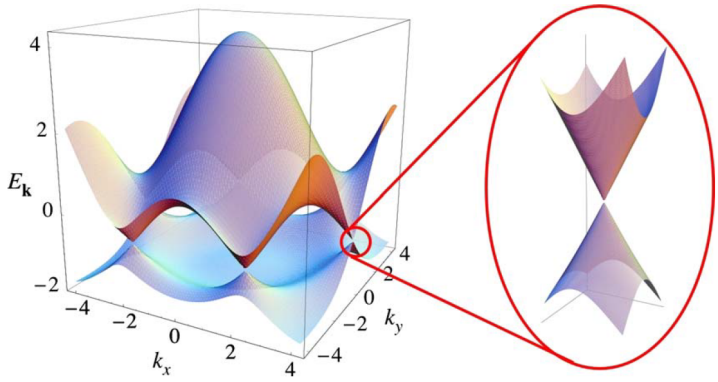

Figure 1.4: Band structure of graphene as a function of the momentum k_x and k_y in the hexagonal lattice, showing that graphene is a zero-gap semiconductor because the valence band (at lower energy) and the conduction band at higher energy are touching each other (at the so-called *Dirac point*). Reproduced from [28].

and momentum, $E(k)$:

$$E^{\pm}(k) = \hbar v_v |k - k^{'}| \tag{1.4}$$

where $k = (k_x, k_y)$ and $v_F = (\sqrt{3}\gamma_0 a/2a\hbar)$. This particular linear-dispersion relation is a direct consequence of the charge carriers behaviour as massless Dirac fermions, which are well described by the relativistic Dirac equation [28], in contrast with the energy-dispersion relation of charge carriers on ordinary metals or semiconductors which is given by $E = p^2/(2m_{eff})$, where m_{eff} is the effective mass of the electrons inside the material usually described by the Schrödinger equation. The relativistic behaviour of the charge carriers (electron or holes traveling with a group velocity of $v_F \simeq 1 \times 10^6$ ms^{-1} which is 300 times lower than the speed of light c) has been known theoretically for many years but the experimental discovery of graphene represents a new opportunity to explore more deeply quantum electrodynamics (QED) phenomena by measuring graphene's electronic properties [18, 28, 43].

Among unusual properties which can manifest themselves in graphene (Figure 1.5) are the experimental observation of the strong ambipolar *electric field effect* [15] and the conductivity, σ, that increases linearly with increasing gate voltage V_g for both polarities and never falls below a minimum value corresponding to the quantum unit of conductance, even for charge carriers concentrations tending to zero. Additionally, the linear dependence of conductivity on the

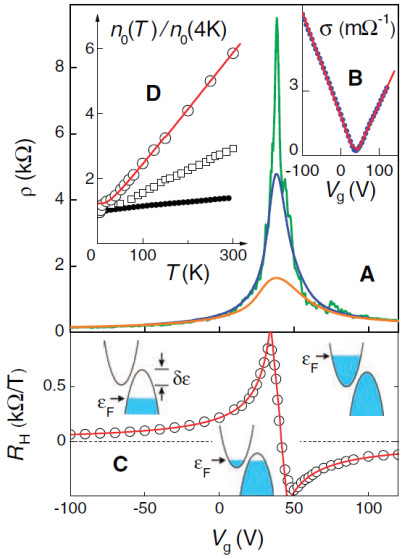

Figure 1.5: First experimental observation of the electric field effect on few layers of graphene by Novoselov et al. (A) Typical dependences of the resistivity (ρ) on gate voltage (for the temperatures $T = 5\ K,\ 70\ K,\ 300\ K$ for top to bottom curves, respectively). (B) Inversion of conductivity (σ). (C) Hall coefficient R_H as a function of the gate voltage, for $T = 5\ K$. (D) Temperature dependence of carrier concentration n_0 for the film in (A) (open circles), a thicker few layers of graphene (squares), and multilayer graphene (circles). Reproduced from [15].

voltage was demonstrated, independent of the temperature, between 10 and 100 K [15, 28].

Another unusual feature of graphene is the so-called *anomalous integer quantum Hall effect* (IQHE) that was already experimentally observed [18, 45]. This new effect which occurs at half-integer filling factors, was suggested by two theory groups [46, 47] and is intimately related to the existence of both electron-like and hole-like Landau states at exactly zero energy. The IQHE was also observed, for example, on Si-GaAlAs heterostructures. However, in graphene, it can be observed at room temperature because of the large cyclotron energies of the Dirac fermions [28].

One of the most interesting phenomena of Dirac fermions theoretically predicted [48] and observed on graphene [49] is the so-called *Klein paradox*. This paradox refers to the ability of Dirac fermions to be transmitted with probability

one through a classically forbidden region, due to the result of suppressed backscattering (massless relativistic particles, such as photons, always move with constant velocity) [28].

1.3.2 Magnetic properties

Although graphene is diamagnetic, local magnetic moments can originate from defects and adsorbed atoms or molecules [27]. Native defects (vacancies) are the result of removing carbon atoms from graphene lattice and can cause quasilocalized states at the Fermi level, which can be responsible for inducing magnetic ordering on graphene [50,51]. Theoretical studies have been undertaken in order to understand the induced magnetic moment for several kinds of defects [27, 52–55] showing that the induced magnetic moment can change between 1.12 μ_B and 1.53 μ_B per vacancy and at same time is highly affected by the defect concentration [52]. However, the local magnetic states caused by defects can be totally destroyed by a simple introduction of hydrogen atoms in the vacancy region [53] or, in the opposite way, give higher macroscopic magnetic interaction when the element is, for example, nitrogen [54]. Magnetic ordering by doping on defects of graphene lattice was also reported for other elements, which can be responsible to promote localization of the π-orbitals of edge regions [56]. It was already confirmed that such doping or adsorption will lead to a magnetic moment around carbon atoms caused by spin-polarized states localized around the external element. For the particular doping with hydrogen atoms on defects regions of graphene, it was shown that when hydrogen atoms are distributed on the same sublattices can induce high ferromagnetic coupling [52, 57]. On the other hand, when the dangling bonds of carbon atoms are saturated, it leads to a non-magnetic system. Other studies for several elements adsorbed or introduced on graphene defects and the ability to induce magnetic phenomena in the graphene-based system can be found in references [58–60].

Besides single-atoms effects, theoretical research predicted that the geometric shape of the defects should play an important role in the magnetic properties of graphene. As the size of sheets is reduced in graphene, edge states can play an important role (Figure 1.6) where unique spin and magnetic states for well-defined graphene nano-geometries were predicted [61–70]. In addition, quantum-dots were reported to switch spin polarization and to unveil the edge states magnetism of graphene. Experimental investigation into the magnetism of intrinsic quantum-dots is of great significance and highly anticipated revealing the vast potential for developing applications such as spintronic devices [71–73].

Despite a great number of publications related to the theoretical studies of spin polarization and magnetism in graphene, experimental research is limited. Many

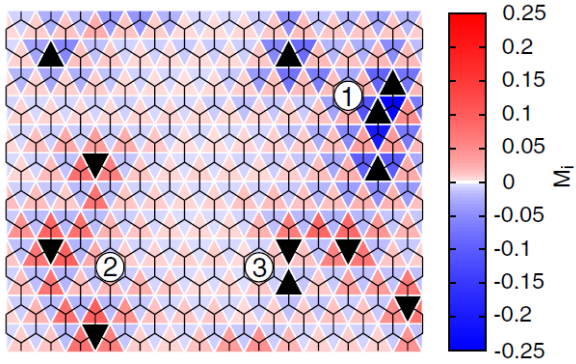

Figure 1.6: Single-atom defects can induce magnetism in graphene: magnetic moments induced by the vacancy disorder in a representative configuration with defects in both sublattices, A and B. In nanometer-size region 1 and 2, the local vacancies with distinctive triangular patterns, determine an orientation of the magnetic moments characterized by an antiferromagnetic coupling between the two lattices. In contrast, in region 3 the proximity of two defects pertaining to opposite sublattices produces no local magnetic moments. Reproduced from [61].

studies are essentially based on superconducting quantum interference device (SQUID) measurements due to its high sensitivity and are focused on the study of the impact of magnetic impurities on the magnetism of graphene [27]. Electron paramagnetic resonance measurements of paramagnetism are also useful but limited because of the large number of spins required for detection. Highlight for Nair et al. [74] that has studied magnetism in graphene by inclusion of point defects and adsorbed atoms on its surface. Adsorption of fluorine results in strong paramagnetism that accrues with increasing concentration of the adsorbed element.

1.3.3 Chemical properties

Graphene has a similar structure of benzene and polycyclic aromatic hydrocarbons and, for this reason, its chemical properties can be inferred from these compounds. The chemical modification of graphene is possible by acting on sp^2 hybridisation by adding new bonds made with exogenic functional groups. However, perfect flat graphene is quite chemically inert because of the high strength of its extremely rigid structure, requiring high temperatures or high energetic species to complete the reactions. Otherwise, the yields of

the reactions are low [75]. In contrast, carbon nanotubes and fullerenes, due to the curved surfaces, can induce a strain in hybridized electronic structure improving the chemical functionalization [75–77]. In this context, it is much easier to manipulate chemically derivative graphene materials than graphene.

The relevant studies on chemical properties and chemical manipulations of graphene and derivative species cover electron transfer chemistry, chemical functionalization, and catalysis, with the special focus on the biomedical applications. Electron transfer is defined as chemical reactions and processes that involve the relocation of an electron between graphene and other chemical species or structures which can work as charge donors or acceptors. In such way, that will be directly responsible for the modification of the properties and capabilities of graphene [78]. The electron transfer is intimately correlated with the chemical functionalization of graphene and how this procedure is activated by breaking up the pristine lattice: covalent or noncovalent $\pi - \pi$ interactions as result of adhesion of atoms or molecules on the graphene surface [79–81]. Note that this procedure can be done with the external help by applying an electrochemical bias or, passively, without it [78]. Figure 1.7 shows the case of incorporation of a functional group on graphene by covalent bonds. This process results in robust linkages to the graphene lattice and electron transfer assumes a prominent role in the nanodesign of the species to obtain the desired functionalization as well as the control of reaction rates, morphologies, and the specific lattice site. Chemical functionalization can be optimized and controlled in a certain way by using different methods with a pertinent interest in the selective etching of graphene to form edges and nanopores which are highly reactive, with unique chemical and physical properties to develop membranes and filtration applications [82–86].

It has been proposed to utilize defects in graphene as catalytic active centers, including oxygenated functional groups, carbon vacancies and holes, edge effects and the presence of dopant elements. The huge potential of graphene as a metal-free catalyst results from the large area available and the collective properties being able to adsorb substrates and reagents and activate them by charge transfer [87–89].

1.3.4 Mechanical properties

The sp^2 hybridisation on graphene, with covalent trigonal bonding, also plays a relevant role in the mechanical properties. According to the principle of maximum overlapping, bonding in graphene should be very strong due to the high level of overlap between atomic orbitals. Taking into account the three-fold

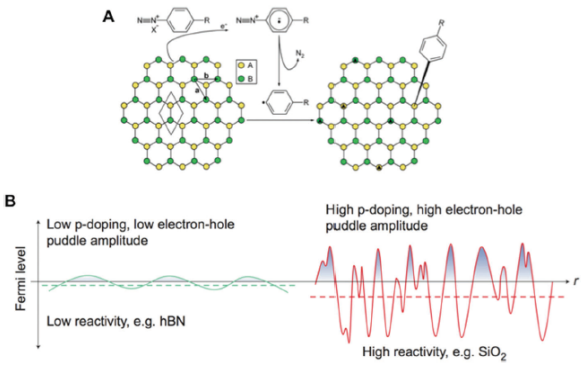

Figure 1.7: Covalent functionalization of graphene via electron transfer: aryl group can be coupled to graphene using aryldiazonium salts and the bond involves electron transfer. (A) Schematic mechanism of electron transfer from graphene generate aryl radical, which forms covalent bond with graphene lattice. (B) The electron transfer is the rate-limiting step: regions of higher electron density are more reactive. Reproduced from [78].

coordinated $C-C$ bond, graphene possesses the strongest chemical bond and exhibits exciting mechanical properties [27, 90].

Atomic force microscopy (AFM) measurements show that a monolayer of graphene is partially elastic with a fracture strain of 25 %, i.e., graphene can expand by approximately 25 % before failing [37, 91, 92]. Having an effective thickness of $\epsilon = 0.335$ nm [93], graphene exhibits a Young's modulus of $E =$ 1.0 TPa, an intrinsic strength of $\sigma_{int} = 130$ GPa, and elastic stiffness ($E \times \epsilon$) of around 335 Nm^{-1} [91, 94]. However, a semiempirical unbinding tensile force model predicts an intrinsic strength 20 % higher than the experimental one of around $\sigma_{int} = 162.7$ GPa [95]. Further, Poisson's ratio obtained by molecular dynamics simulations is in good agreement with the published data [96] of about $\nu_b = 0.21$. Similarly to what happens with other properties, the mechanical properties previously described of graphene sheets are dependent and deeply affected by structural modifications, such as defects, vacancies, grain boundaries, as well as by adsorption of atoms or molecules on the surface [97].

1.3.5 Thermal properties

Graphene shows a very high in-plane and a relatively low out-of-plane thermal conductivity [98]. The unique thermal properties of graphene are largely derived

from the low mass of the carbon atoms and are due to the strong and anisotropic bonding dependent on the covalent sp^2 hybridisation. The thermal properties of graphene at room temperature (RT) are dominated by the acoustic phonons [98] which are strongly dependent on the number of layers of the graphene sample. The specific heat, c, of graphene is considerably higher than that of graphite and diamond below room temperature [98–101].

The thermal conductivity (K) of different forms of carbon varies significantly, from as low as 0.01 W/mK for amorphous carbon to as high as 2000 WmK^{-1} for graphite. Taking into account the intrinsic obstacle for performing thermal measurements with atomically thin materials, the experimental studies on graphene, [27, 102–106] by non-contact Raman optothermal technique, allowed measuring the thermal conductivity above the graphite limit around 3000 WmK^{-1} near RT for sufficiently large areas of graphene flakes.

1.4 Graphene production methods

The evolution of graphene's market is intrinsically connected with the progress and ability to produce large-area, defect-free, single-crystal graphene, reducing the cost and increasing the production capacity. Currently, as shown in Figure 1.8, several methods can be applied to obtain graphene with control on the number of layers and shape but differing in terms of the sample quality as well the corresponding price. The properties and intended applications of a particular grade of graphene depend very much on the quality of the material and, for this reason, it is obvious that an appropriate choice of the production method of the samples must be judicious.

One of the simplest methods to produce graphene is the one applied by Andre Geim and Konstantin Novoselov [15, 16] when they isolated graphene for the first time: the mechanical exfoliation using scotch tape to exfoliate graphite into individual planes. The ease of production and its low cost make this method the most popular way to prepare graphene with flake areas of few micrometers. An alternative but similar way that can be used to obtain individual layers is the liquid-phase exfoliation of graphite by exposing the graphite surface to a non-aqueous solvent and a selected surfactant, applying a surface tension by ultrasonication [107, 108].

High quality graphene samples with micrometers dimensions can also be reached by sublimating Si atoms of a SiC wafer [109–112], molecular beam epitaxy (MBE) [113] as well laser ablation from graphene flakes [114] with micrometer thickness. However, these methods are not cost-effective enough to be applied to produce on a large scale. Other methods of graphene synthesis include

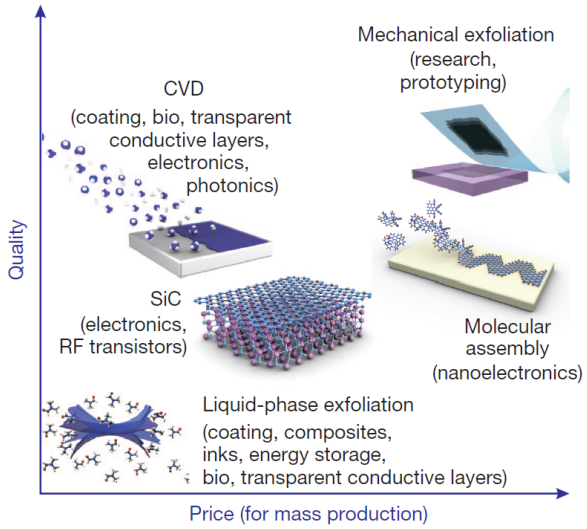

Figure 1.8: Different methods to produce graphene are actually available, which allow a wide choice in terms of size, quality and price, according the intended application. Reproduced from [22].

decomposition of ethanol in a microwave plasma and the spray pyrolysis of sodium ethoxide, as well by the longitudinal cutting of carbon nanotubes, which allow to produce platelets of graphene [115].

However, electronic and other technological applications require the production in large quantities. Chemical vapour deposition (CVD) [116,117] can be used to produce large-area uniform graphene film on a variety of polycrystalline metal substrates using a range of experimental conditions. Copper is one of the most used substrates for graphene growth because of the small solubility of carbon in this metal (even at high temperature), responsible for a self-limited growth mechanism leading to single-layer graphene formation [118]. The process of graphene growth on Cu is essentially guided by surface processes, in particular by diffusion, involving the carbon radicals/atoms released by the catalytic decomposition of the carbon feedstock at high temperature [118]. After CVD graphene growth between 1000 °C and 1100 °C, the metal foil is dissolved by wet chemistry, thus releasing the graphene sample grown on it. The process is typically followed by transfering the graphene layer to the desired substrate, such as Si, Ni, Cu or even other substrates, in particular plastics on which it is difficult to grow graphene directly. This method, which allows to obtain several square meters of graphene, has a number of issues that need to be solved, in

particular, eliminate the presence of defects, essentially due to corrugations, ripples, and wrinkles which result from the transfer method to the substrate. On the other hand, the roughness of the copper substrate is a key parameter for the synthesis of graphene, since it controls defects into graphene films during their growth, not only grain boundaries, but also other kinds of defects. A novel growth technique is being explored in which graphene is synthesized on capped Cu thin films deposited on c-plane sapphire resulting in (111)- oriented films exhibiting millimeter-size grains [119].

In spite of the huge efforts to develop different methods to grow or synthesize graphene, many of which remained unmentioned here, they are intended to become commercially viable to produce graphene in quantity, with areas, and quality enough for both science and industry.

1.5 Emergent applications of graphene

The last decade has witnessed numerous breakthroughs in research of graphene on the horizon of materials science and condensed matter physics and, despite its short history, has already revealed a whole panoply of new applications. Theoretical and experimental studies have been intensively undertaken, regarding the electronic, optical, magnetic, thermal, and mechanical behaviour of this exciting material which has the possibility of being modified in a controllable way. The possibility of engineering a specific chemical and physical property of graphene promises to revolutionize electronics technology and graphene nanodevices are expected to be applied in different fields in our quotidian existence [95, 96, 102, 120–124].

In fact, graphene represents an unusual combination of properties [21] and, for this reason, there is a high level of expectation for the future applications based on this material which is able to replace successfully many materials in a great number of already existing applications. Based on the extreme mechanical strength and high electric conductivity, graphene can be used as the support structure to study biological samples or other kinds of materials in transmission electron microscopy (TEM), moreover, graphene membranes are already available to be bought from several companies [21, 81, 125, 126]. The mechanical strength and high crystallographic quality are also the requirements graphene meets as a perfect gas barrier [127] as well as in strain gauges [128].

Another interesting application which benefits from the high transmittance (of over 90 %) of graphene is the transparent conductive coating applied in optoelectronic devices such as liquid crystal displays, electronic paper, and organic light-emitting diodes, some of which have been already developed

[107, 129]. In addition, high response speed and carrier mobility, outstanding mechanical flexibility, and the chemical durability provide graphene with the capacity to develop flexible electronic devices [117]. The inexistence of a bandgap represents a disadvantage to incorporating graphene into optoelectronic devices due to the short lifetime of exciton separation. However, the interaction of graphene with external elements or molecules and the possibility of tuning up its properties opens new ways to realize optoelectronic devices. Photodetectors have been developed recently from a heterostructure based on graphene on top of a photonic integrated circuit, with large mobility up to 60000 $cm^2V^{-1}s^{-1}$ in response times of 3 ps [130]. Applications of graphene in light emitting diode (LED) are also being developed, where graphene can act as the injector of electrons and holes into the active junction [131, 132].

Ultrafast photodetectors [133] and efficient mode lockers [134] are presently two of the most studied photonic devices, using the behaviour of the massless Dirac fermions with high mobility and high Fermi velocity. Photodetectors with responses of up to 40 GHz [135] and detector operations of 10 GHz [136] have been demonstrated. Nevertheless, some limitations were identified in the maximum responsivity because of the limited absorption due to the small effective detection areas and the thinness of graphene [21, 136].

Field effect transistors based on graphene, with the ability to eliminate the Coulomb and resonant scatters, have allowed to achieve mobilities around 10^6 cm^2/Vs at low temperatures [17] in freestanding devices, indicating the way for developing high-frequency applications. Studies reported a value for the cut-off frequency of around 300 GHz, for a graphene transistor, with the possibility of extending it up to 1 THz, although an order of magnitude lower in comparison with a conventional device [137].

Other applications based on the electronic properties of graphene worth mentioning are sensitive gas detectors [138], which take advantage of the large area available for detecting a single foreign molecule that can be attached.

The research into new efficient renewable energy technologies must include graphene as a pillar of the future studies. Solar cells appear to be the most researched devices in energy storage, where graphene assumes two important roles: it acts as the active medium and as a transparent electrode material [22].

Graphene is extremely sensitive to the environment and it is obvious that its application in the domain of sensory and metrology, for instance, in magnetic field measurements and, to DNA sequencing [22].

The usage of graphene to produce memory devices is also an important sector within the domain of graphene applications. Recently, appeared new memory prototypes using graphene as a floating gate integrated into a heterostructure

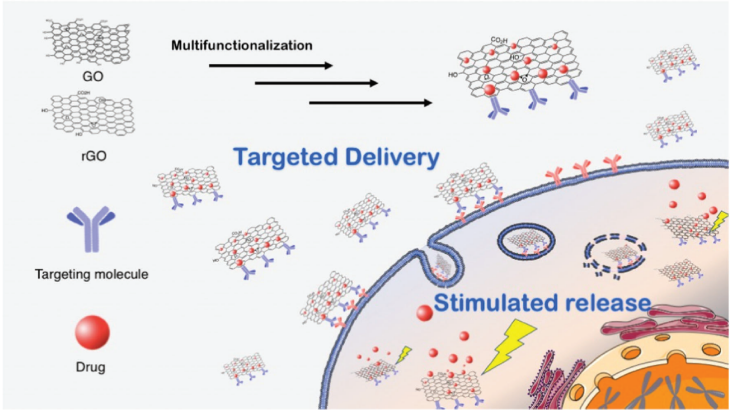

Figure 1.9: Illustration of an application based on graphene oxide as a drug delivery nanodevice. Since graphene oxide exhibits good dispersibility in water allows development of a wide range of biomedical applications. Reproduced from [140].

of MoS_2 and hexagonal Boron Nitride barrier, developed with erase/program ratios as high as 10^9, with retention times over 10^4 s [139]. Several properties including the large area surface, chemical purity, and the possibility of functionalization also make graphene the desired material for bioapplications. Among tissue engineering in regenerative medicine, imaging, and detection of biomolecules including glucose, cholesterol, hemoglobin and DNA, graphene has been proposed as the innovative solution to the whole nanomedicine problem area [132]. The functionalization possibility and the ability of tuning up the electrical properties make graphene the natural choice as a high-sensitivity biosensor. In fact, the biocompatibility of graphene is another issue that must be considered since graphene - a carbon surface- allows strong, non-destructive, interfacial interactions at the cellular level [140–142]. In addition, the precise modification of chemical properties allows to exercise the absolute control over the drug quantity and the release rate in specific parts of the body as drug delivery vehicles (Figure 1.9) [140, 143].

Graphene has also been thought to be a novel material to address the pressing global environmental problems. Graphene-based materials such as sorbent or photocatalytic for environmental decontamination, as membranes for water treatment, desalination, and as electrode materials for contaminant monitoring or removal are some of the solutions proposed in this context [144–148].

1.6 Graphene derivatives and other 2D materials

Despite the similar sp^2 hybridisation and honeycomb structure, when compared with other carbon structures such as fullerenes (0D) and carbon nanotubes (1D), graphene exhibits uncommon physical and chemical properties, also radically different from sp^3 carbon compounds. One of the most studied graphene derivative materials is graphene oxide (GO) which uses graphite oxide as a starting material and is obtained by chemical exfoliation in aqueous media using functional groups to reduce the interplanar forces and with aid of stirring or sonification. Graphene oxide and reduced graphene oxide (rGO) are graphene derivatives materials that appear as alternatives to overcome the expensive and relatively difficult production of graphene. GO is a single-atomic-layer material made by the powerful oxidation of graphite, i.e, is an oxidized form of graphene, decorated with oxygen-containing groups. Note that, due to the disruption of its sp^2 hybridisation, GO is often described as an electrical insulator in contrast with graphene. Despite the rather random functionalisation of each layer and compositional variations depending on the preparation method that is used, it has the advantage of being easily dispersed in water and other organic solvents as well as in different matrices due to the presence of the oxygen functionalities. The chemical reduction of graphene oxide is currently seen as a suitable method of mass production of graphene allowing to separate individual carbon layers and isolate them without modifying their structure [27].

The superlative properties of graphene are the result of the low-dimensional confinement of the charge carriers. Based on this fact, several efforts have been triggered in order to reach other 2D materials with novel and exciting properties, different of their 3D counterparts. As along with graphite, many other crystals are arranged as a layered structure, with strong in-plane bonds and van der Waals inter-plane bonds, which can be exfoliated into a 2D material. The family of layered crystals includes superconductors, metals, semi-metal, semiconductors, and insulators materials, as shown by Figure 1.10 all of them offering a large list of possible new 2D materials. Thus, strategies, similar to those applied to graphene, can be adopted to find other new 2D materials [11, 16, 22].

Other atomic crystals have received attention recently and have been synthesized, including silicene (from Si) [150], antimonene (from Sb) [151] and phosphorene (from P) [152]. All these new atomic crystals possess different physico-chemical properties: silicene is characterized by high instability because it can react with air, antimonene is an indirect gap semiconductor with strong spin-orbit coupling, and phosphorene is a stable allotrope of phosphorus and an semiconductor.

Following graphene's example, using micromechanical or chemical exfoliation applied to layered structures, notable examples were obtained such as $NbSe_2$

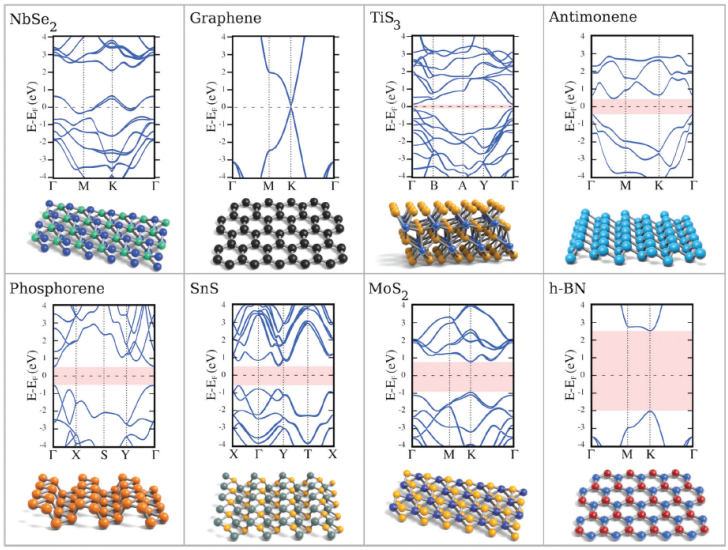

Figure 1.10: Several atomic crystals were already obtained with different electronic behavior: metallic ($NbSe_2$), semi-metallic (graphene), semiconducting (TiS_3, antimonene, phosphorene, SnS, MoS_2) and insulating (h-BN). Band structures an respective crystalline lattice of different 2D materials determined by density functional theory. Reproduced from [149].

[17, 153], MoS_2 [17, 154] and other dichalcogenides, with stoichiometry of MX_2, where M are the metal atoms arranged in hexagonal layer and X is the chalcogen atom [153]. Transition metal dichalcogenides (TMD) represent a large family of crystals, with many different possible structures as well as a wide array of properties. In general, TMD exhibit strong spin–orbit coupling effects, and their electronic band structure is very dependent on the number of layers [155].

Group IV monochalcogenides appear as 2D crystals with 2 elements, with formula MX (M =Ge, Sn and X =S, Se) and orthorhombic structures, capable of having indirect gap in its electronic band structure and evidencing piezoelectric properties with two orders of magnitude higher than TMD [149, 155].

Transition metal trichalcogenides (TMT) with formula MX_3 (M = Ti, Zr, Hf and X = S, Se, Te) represent another family of 2D materials with trigonal prismatic MX_3 chains [149]. TMT, where each transition metal M is coordinated to eight chalcogen atoms, X, show new possibilities in terms of electronic and optical properties [1.125], as was found in the most attractive compound, TiS_3 [155, 156].

Hexagonal boron nitride (h-BN) appears to be one of the first 2D materials researched [16,27,157–159]. With B and N atoms sitting on different sublattices, it is a band insulator and displays a direct band gap of 4.5 eV at K and K' points of the Brilluin zone. h-BN is widely researched also because it can be used as an excellent substrate to support and encapsulate graphene devices.

If 2D materials promise a wide range of new properties, heterostructures made up of different layers of such materials provide even a greater scope. 2D-based heterostructures [20–22] can be tuned up with atomic precision from these 2D building blocks to fit a multitude of possible applications. Several systems have already started to appear, with vertical tunnelling transistors based on this type of new 2D-heterostructures.

Some of the new 2D materials possibilities, isolated or synthesized, were shown here to illustrate the idea of the intense activity in this field of research that promises new exciting phenomena to be discovered and explored.

1.7 Adsorbed atoms and molecules on graphene

The modification of graphene properties in a controllable way is a challenging issue with both fundamental and applied interest. Although the properties of graphene can be modified by the interaction with certain substrates and atomic doping, it is inconvenient because it can promote intrinsic and extrinsic defects (corrugations of the graphene sheet, and short-range structural disorder) degrading the basic electronic structures of graphene that reduce the mobility of charge carriers which are difficult to control [122,160,161]. In this context, the adsorption of atoms (adatoms), molecules (admolecules) or other self-assembled structures on graphene is an attractive approach to tailor the physical properties while minimizing detrimental effects. This work reported in this thesis is framed in this context: studying local atomic configurations of adsorbed species and their stability, as a step towards understanding the modifications induced on the macroscopic properties of graphene.

1.7.1 Stability and structural configurations

Intense experimental and theoretical research is being carried out, addressing the interaction of adsorbed atoms on graphene to form a variety of structures, stable or metastable, which can be manipulated to produce new functional phenomena. So far, theoretical studies have essentially been based on density functional

theory (DFT), focused on the adsorption of different species of adatoms on graphene.

Light elements are probably the most investigated type adatoms. A notable example is the research performed by Simone Casolo et al. [162], with the aim to understanding the adsorption of hydrogen adatoms, individually or in clusters, with different configurations. In the same context, R. Acosta et al. [163] reported electronic structure calculations focused on the influence of an external electric field on the adsorption barrier of hydrogen adatoms. The analysis of the electronic charge density of the graphene-H system allowed to explain the influence of the electric field on hydrogen physisorption-chemisorption, confirming the possibility of manipulating the adsorption of H on graphene by applying an electric field. Extensive DFT calculations [164], which include van der Waals (vdW) interactions, allowed to estimate the activation barriers involved in the desorption and migration processes of a single H adatom on graphene monolayers and bilayers.

Carbon adatoms on graphene were also studied using first-principles calculations to understand the stability, coverage, migration, and cluster formation. The stability of high carbon coverage in a periodic organization was analyzed by C. Ataca et al. [165], focusing on the evaluation of the changes in electronic and magnetic properties. The stability of other adatoms, such as boron and nitrogen, along with organic molecular dopants, is being also studied as a means to modify the electronic structure, optical, and transport properties of graphene [166, 167].

More recently, Ivan Shtepliuk et al. [168] presented an investigation of the interaction between heavy metals (Cd, Hg, and Pb) with graphene quantum dots aiming to understand the behaviour of these metals on graphene surface and the response of graphene to adsorption. This study suggested a route towards the development of a graphene-based sensing platform for the optical detection of toxic heavy metals.

Water molecules are also intensively studied, owing to the fundamental interest as well as its practical impact. Relevant research has been done regarding the behaviour of water on the surface of graphene. DFT calculations have been performed to explore properties of water such as the flow and its structure predicting many phases and configurations. The reported results are however sensitive to the modeling conditions, and appear sometimes conflicting. A particularly relevant DFT work is that of O. Leenaerts et al. [169], dealing with the stability of water admolecules on graphene: equilibrium position, orientation and adsorption energy. Molecular dynamics simulations suggested the appearance of an ice monolayer [170] and a flat hexagonal ice [171] under confinement at ambient conditions, respectively for water inside mica (hydrophilic structure) and graphite (hydrophobic structure). Following those

studies, Algara-Siller et al. [172] observed, using high-resolution electron microscopy, water confined between two graphene sheets, described as an archetypal example of hydrophobic confinement. According to this study, this kind of nanoconfined water at room temperature forms a square ice phase having symmetry qualitatively different from the conventional tetrahedral geometry of hydrogen bonding between water molecules. Other studies based on molecular dynamics simulations indicate that this square ice should be present inside hydrophobic nanochannels independently of their exact atomic nature. This idea based on water contained between two graphene sheets and under ultrahigh pressure was also explored by YinBo Zhu et al. [173]. According to this study, the mechanism of layered structures is mainly attributed to the spatial confinement, where graphene works as an epitaxial template, and the encapsulating pressure is critical for the appearance of in-plane orders. Most of the first-principle studies aiming to unveil the stability of single water molecules or aggregates on graphitic layers use approaches that include empirical van der Waals interaction [174].

Numerous other studies have focused on the stability and effect of adsorbed structures on graphene: acids and oxidants [175] can significantly perturb the electronic sp^2 structure of graphene and functionalize it by forming covalently attached hydroxyl and epoxide groups; benzene and naphthalene bind very weakly on graphene [176]; ring structures of aromatic and non-aromatic molecules, including DNA and proteins [176], interact with graphene through non-covalent bonds, such as van der Waals interactions.

1.7.2 Induced effects

The interest in H adatoms on graphene systems [52,177–180] from the possibility to modify its properties, for example, by inducing an intrinsic magnetic moment around the adsorption site, depending on the spatial configuration of H adatoms. Theoretical studies of the electronic and magnetic properties of graphene functionalized by $3d$ transition-metal (TM) adatoms, predict magnetic properties with potential application in spintronics [73,181]. Sevinçli et al. [182] studied the binding energies, the electronic and magnetic properties of graphene adsorbed with $3d$ TM atoms (Co, Cr, Fe, Mn, and Ti) revealing a wide range of binding energies between 0.10 eV and 1.95 eV, depending on the species and coverage density. The experimental evidence for *Kondo effect* in graphene adsorbed with Co and the great efforts to understand this phenomenon [183, 184], make this element one of the most studied (theoretically and experimentally) among the TM elements [184–189].

Several theoretical and experimental groups have reported that the adsorption of heavy metals on graphene, such as Pd, Au, Ag, and In, can trigger significant

changes in the properties of graphene [190–193]. R. Thapa et al. [190], using first-principles calculations, studied the electronic and magnetic properties of Pd adatoms and dimers adsorbed on graphene. A shift of π and π^* bands and a magnetic moment for Pd dimer adsorption and its direct relationship with the spatial configuration was reported.

The influence of water clusters on the electronic properties of graphene was studied by O. Leenaerts based on DFT [194]. In this study, water was found in a cluster configuration which tends to orient their dipole moments in opposite directions, canceling them on average. Alternatively, for an ice structure on freestanding graphene sheets, an appreciable total dipole moment was found. It is also accepted that the hydrophilic property of graphene can be affected by the underlying substrate. Other DFT studies have predicted that water physisorption may induce impurity states close to the Fermi level of graphene [174] and that the presence of small adsorbed aggregates has a small influence on the electron mobility. Water adsorption has been proposed as a means to open an energy gap in the band structure of graphene. Yavari et al. [195] have achieved a tunable bandgap of up to $\sim 0.21\ eV$ using a technique based on water adsorption to the graphene surface, without chemically changes on graphene.

Studies addressing many other molecules adsorbed on graphene have been reported, including small gas molecules (H_2, O_2, CO, NO_2, NO, and NH_3), aromatic, and non-aromatic molecules (F4-TCNQ, PTCDA, TPA, Na-NH_2, An-CH_3, An-Br, Poly (ethylene imine) (PEI), and diazonium salts), and various biomolecules such as peptides, DNA fragments, and other derivatives [27, 122]. First principle calculations of adsorption of small gas molecules on graphene, such as NH_3, CO, NO_2, N_2O and NO show that the molecules can act as electronic acceptor or as donor [169]; NO_2 can introduce a relatively strong p-type doping but NO causes a n-type doping. According to X. Wang [66], who focused on the analysis of NH_3 admolecules on graphene, the process of charge depends on the orientation of the molecule, and there is almost no charge transfer when the H atoms are pointing towards the graphene surface. It seems evident that modifications in the electronic structure of graphene strongly depend on the balance between adsorbate–adsorbate interactions and adsorbate–graphene interactions. For example, adsorption of molecules of NH_3, CO and HF which stabilize on graphene with different binding energies [196] can induce a band gap, up to 1.5 eV – 2.0 eV [197].

1.7.3 Experimental techniques

Experimentally investigating the interaction between graphene and individual adatoms or admolecules, and how these adsorbed impurities are organized the on graphene lattice, is a challenging task. Recent developments in microscopy techniques enable direct imaging of individual adatoms and admolecules on graphene as well as revealing the local electronic structure [198].

Transmission electron microscopy (TEM) has been a useful tool used for studying individual adatoms and admolecules on graphene since it enables one to image with atomic resolution, and also allows to conduct various other characterizations simultaneously. The resolution limits of TEM systems are being pushed by the inclusion of aberration correctors and other techniques such as monochomators. Aberration-corrected transmission electron microscopy (AC-TEM) can provide information about atomic arrangements, elemental nature and site of individual of adsorbent within graphene at low accelerating voltages, reducing specimen damage, although images are often noisy and difficult to interpret. High-angle annular dark field imaging performed in scanning transmission electron microscopy (STEM) produces higher definition images, which allows one to more readily distinguish between lighter and heavier adatoms in an image, but may degrade graphene monolayers due to the high electron flux of the highly focused electron beam [198]. A fast Fourier transformation (FFT) of the diffraction pattern obtained by TEM is also used to obtain the images of the species adsorbed on the graphene. One such study was performed by Schaeffel et al. [199], dedicated to the investigation of the dynamics of N-Methyl-2-pyrrolidone (NMP) hydrocarbon molecules and other adatoms on few-layer graphene. The non-destructive images obtained by TEM [200] were fundamental to demostrate that Pb and Te adatoms deposited on graphene are attached to a surface layer of amorphous carbon that resides upon the graphene, as well as in the edge regions. By combination of AC-TEM and data from a focal series of low beam density images, Reza J. Kashtiban et al. [201] showed a stable C_2F chair on graphene by direct imaging of individual C atoms and alternating C–F atom pairs at atomic resolution. Besides that, the obtained images also indicate a pristine long-range order in this structure. T. P. Hardcastle et al. [202], explored the stability of Al and Au adatoms on graphene using STEM images. The mentioned adatoms were observed exclusively at edge sites, and also on hydrocarbon-contaminated regions. On the other hand, the pristine regions of the graphene lattice are completely devoid of adatoms. Based on a combination of STEM and EELS, Quentin M. Ramasse et al. [203], revealed striking differences in electronic structure between two distinct geometries of single substitutional Si in graphene. Individual Au atoms and Au clusters were observed on few-layer graphene using STEM with high-angle annular dark-field image [204]. This study identified the individual atom positions using the

corresponding STEM bright-field image and also demonstrated that the clusters nucleate exclusively in the hydrocarbon surface contamination.

Scanning tunneling microscopy (STM) and spectroscopy (STS) are also widely used for the characterization of adatoms and admolecules on graphene, as well as to study the influence of adsorbent species on the morphology and electronic structure of graphene. The work performed by M. Gyamfi at al. [205] using STM to study the stability of iron adatoms on graphene is a particularly representative example. It revealed, on the one hand, the capabilities of this technique for studying single adatoms and, on the other hand, demonstrated that graphene-Fe system exhibit different electronic properties depending on the Fe adsorption site. The measurements performed by V. W. Brar et al. [206] using STM showed that Co adatoms on graphene can be controllably ionized by application of a bias voltage. This study also demonstrated that Co adatoms can be reversibly ionized. STM has also been used to study the *Kondo effect* of a single magnetic adatom on the surface of graphene [207], demonstrating the influence of the direct tunneling channel between the STM tip and graphene and also that the lineshape of the Kondo resonance is unaffected.

Various other methods are used in the context of adatoms and admolecules on graphene, such as surface enhanced Raman scattering (SERS) [208, 209] and X-ray photoelectron spectroscopy (XPS) [210, 211], often providing complementary information on the local atomic configuration, the electronic structure, and the effect on the properties of graphene induced by the adsorption.

Chapter 2

Objectives and outline

The goal of the work described in this thesis is to advance the understanding of adsorption of heavy metals on graphene. In particular, we explored the capabilities of a novel experimental approach based on hyperfine techniques, combined with density functional theory (DFT) calculations. To accomplish this goal, we followed three main paths:

(1) Investigating the interaction of heavy metal adatoms with pristine graphene, without interference from other species, in terms of the stability of different local atomic configurations and the associated electronic structure. For different heavy metal elements (Ag, Cd, In and Hg), local configurations and nominal concentrations, we studied the electronic structure, binding energy and migration energy using DFT. Detailed studies were carried out for Hg-graphene, as a model system, i.e. testing various functionals and covering a wide range of nominal concentrations. For Ag, Cd, In, we carried out more targeted studies, based on the extensive calculations for Hg.

(2) Exploring the capabilities of hyperfine techniques to experimentally probe graphene-adatom interactions. The DFT study mentioned above included the calculation of the hyperfine parameters for each configuration. Based on these calculations, we investigated to what extent the electric field gradient (EFG) can be used as a signature of the local atomic configuration and bonding stability. In an experimental scenario, avoiding interference from other species in the adsorption mechanism corresponds to performing the deposition and characterization *in-situ*, under ultra-high vacuum conditions. The DFT study presented in this thesis forms the basis for a new experimental approach that is currently being developed at the ISOLDE facility at CERN, using

the ASPIC setup (Apparatus for Surface Physics and Interfaces at CERN), where a multitude of radioactive isotopes can be deposited and measured using perturbed angular correlation (PAC) spectroscopy.

(3) Investigating the role of extrinsic species on the adsorption and stability of Hg. In parallel to the DFT studies mentioned above, dealing with the adatom-graphene interaction without interference from other species (1 and 2), we studied the effect of extrinsic molecules (e.g. water and oxygen, in solution or in the atmosphere). For that purpose, we carried out PAC measurements and interpreted the experimental results using DFT calculations. In addition to providing new insights on heavy-metal adsorption on graphene, this work was aimed as a proof-of-principle for the use of hyperfine techniques to study the interaction between graphene and adsorbed atoms or molecules, at the atomic scale.

The first chapter of this thesis introduces graphene, in terms of its historical context, atomic structure and main properties. Particular emphasis is given to adsorbents (adatoms and admolecules) on its surface and the induced effects. The specific problems addressed in this thesis are positioned within the available literature, defining the directions which motivated our studies. A brief overview of the production methods, technological applications, and other 2D materials is also given in *Chapter* 1. *Chapter* 3 consists of a synthetic description of density functional theory (DFT), from the initial idea to the crucial theorems of Hohenberg and Kohn and to the development of the theory. The exchange-correlation functionals used in this thesis as well the principal software (WIEN2K and VASP) are also introduced. *Chapter* 4 contains a general overview of the main experimental technique used here: perturbed angular correlation (PAC) spectroscopy. The theory behind PAC as well the technical aspects of the experimental setup are presented. In this context, the ISOLDE-CERN radioactive on-line facility, where the radioactive samples were prepared and measured, is also introduced. The results are presented in *Chapter* 5 and *Chapter* 6, based on the manuscripts which have been published, submitted or are in preparation for submission. At the end of the thesis, a general conclusion summarizes the results and discusses their implications for the future of the field.

Chapter 3

Density functional theory for materials modelling

A complete overview of ab-initio density functional theory is beyond the scope of this chapter. For such, several references are available [212–214]. To understand the basic concepts of this theory and the relevance in the context of materials science, an introduction is presented in the *section* 3.1: in the subsequent subsections, the formulation of the many-particle system and the history of the original very naive Thomas-Fermi theory and later Hohenberg, Kohn, and Sham theories are displayed as the starting point of the success of density functional theory. All the theoretical aspects of exchange-correlation interaction and respective functionals are shown in the *section* 3.2. A brief review of the linearized augmented plane wave method is presented in *section* 3.3. The electric field gradient tensor parameter in LAPW is shortly explained in the *section* 3.4. Finally, the current chapter finishes in *section* 3.5 where the two main packages used in this work, WIEN2K and VASP, are presented.

3.1 Density Functional Theory

Theoretical physics, using mathematical tools, searches for complete models able to predict and explain the behaviour of any macro or microsystem, which can or cannot be measured experimentally. The research of new models which can advance the description of a certain system even before the experimental verification is called theoretical modelization.

In many fields within physical sciences and engineering, the objective of theoretical modelization is to develop understanding and even to engineer a certain property at the atomic or molecular level. Often, it is not possible to obtain an exact solution to the quantum many-body problem and approximations have to be used to find solutions to the Schrödinger equation. Density functional theory (DFT) [212, 213, 215–217] appears to be one of the most common approaches in solid state and condensed matter physics to solve many-particle problems. It has been employed with success in a large number of fields, not just in physics but also in areas such as materials science, chemical engineering, geology, and other disciplines. DFT represents an important ab-initio method alongside other significant ones such as molecular dynamics (MD), Monte Carlo (MC) and Hartree-Fock (HF).

The primitive idea behind DFT consists of solving an intractable many-particle Schrödinger equation by replacing the complete electron-wave function by the ground-state electron density, the latter assuming the role of the fundamental variable [218]. DFT guarantees that all observables can be obtained from the charge density functional of the ground state.

The primordial work which suggests the electron density instead of the eigenstates to describe any system was performed by H. Thomas [219] and E. Fermi [220], independently. However, it was only in 1964, almost half a century later, that the exact proof was obtained by Hohenberg, Kohn, and Sham [221]. They established a rigorous density functional theory of the ground state on the basis of quantum mechanics and started the introduction of an approximative explicit theory called the local density approximation [221]. From that time on, although some points were left somewhat obscure in the basic theory, DFT has grown vastly in popularity and became a computational tool of huge utility. It must be clarified that only in the early eighties the basic theory in the final form was formulated, mathematically consistent and rigorous, essentially by Levy and Lieb [213, 221].

3.1.1 Many-body system

For any quantum many-particle system governed by the Hamiltonian $\hat{H}$, if $|\Psi\rangle$ is the eigenstate of the system in a Hilbert space, its time-evolution is given by the Schrödinger equation [214, 222, 223]:

$$\hat{H}\,|\Psi\rangle = i\hbar\frac{\partial}{\partial t}\,|\Psi\rangle \tag{3.1}$$

The time-independent Schrodinger equation allows to determine the stationary states with definite energies, in particular, the ground state of the system:

$$\hat{H}\,|\Psi\rangle = E\,|\Psi\rangle\,,\ \langle\Psi|\Psi\rangle = 1 \tag{3.2}$$

In a solid composed by N atoms and, as such, N nuclei and ZN electrons, where Z is the atomic number, the real problem focuses on a set of $N + ZN$ electromagnetically interacting particles. The exact many-particle Hamiltonian for this system is given by [214]:

$$\begin{aligned}\hat{H} = -\frac{\hbar^2}{2}\sum_i \frac{\nabla^2_{\vec{R}_i}}{M_i} - \frac{\hbar^2}{2}\sum_i \frac{\nabla^2_{\vec{r}_i}}{m_e} - \frac{1}{4\pi\epsilon_0}\sum_{i,j}\frac{e^2 Z_i}{|\vec{R}_i - \vec{r_j}|} \\ + \frac{1}{8\pi\epsilon_0}\sum_{i\neq j}\frac{e^2}{|\vec{r_i} - \vec{r_j}|} + \frac{1}{8\pi\epsilon_0}\sum_{i\neq j}\frac{e^2 Z_i Z_j}{|\vec{R}_i - \vec{R}_j|}\end{aligned} \tag{3.3}$$

where M_i is the mass of the nucleus at the position $\vec{R}_i$ and m_e is the mass of the electron at $\vec{r_i}$. The first two terms of Equation 3.3 represent the kinetic energy operator for the nucleus and electrons, repectivelly. The Coulomb interaction is described for the last three terms: the first of them is the interaction between electrons and the nucleus, the second between electrons and other electrons, and, finally, the last term represents the interaction between the nuclei.

In order to find an acceptable solution to this Hamiltonian, it is necessary to make approximations at three different levels [213, 214]. The first of them that allows to simplify the complexity of the problem is the *Born-Oppenheimer approximation*. According to this approximation, as the nucleus is much heavier and therefore much slower than the electrons, it is possible to consider that the nuclei keep their position invariant and the electrons are in instantaneous equilibrium with them. In this way, it is possible to treat the motions of the nuclei and electrons uncoupled and, therefore, the wave function can be written as a product of two independent wave functions, one for the nuclei and other for electrons. Consequently, as the nucleus does not move any more, its kinetic energy is zero and the first term disappears and, on the other hand, the last term reduces to a constant [213, 214]. The second approximation introduced is supported by considering the nucleus as classic particle treated by Newtonian Physics disregarding relativistic effects. The last two approximations allow to re-write the Hamiltonian as [213, 214, 224]:

$$\hat{H} = \hat{T} + \hat{V_{ne}} + \hat{V_{ee}} = \sum_{i=1}^{N}(-\frac{1}{2}\nabla_i^2) + \sum_{i=1}^{N} v(\mathbf{r_i}) + \sum_{\mathbf{i<j}}^{\mathbf{N}}(\frac{\mathbf{1}}{\mathbf{r_{ij}}}) \tag{3.4}$$

$\hat{T}$, $\hat{V_{ne}}$ and $\hat{V_{ee}}$ are the kinetic energy of electrons, the potential on the electrons due to the fixed nuclei and the electron-electron interaction, respectively. It was

defined $v(\mathbf{r_i}) = \sum_\alpha \mathbf{Z}_\alpha / \mathbf{r_{i\alpha}}$, as the external potential acting in the electron i due to the nucleus of charge Z_α. For a certain state of the Hamiltonian described by the eigenstates $|\Psi\rangle$, and the corresponding energy, E, the following condition must be respected [213, 214, 224]:

$$E[\Psi] \geq E_0 \tag{3.5}$$

i.e. the computed energy of the state $|\Psi\rangle$ is an upper bound to the true ground state energy, $E_0 = E[\Psi_0]$. Thus, to find the energy of the ground state, it is required to minimize the functional of the energy, i.e, $E_0 = minE[\Psi]$ and the Schrödinger equation corresponds to the variational principle:

$$\delta E[\Psi] = 0 \tag{3.6}$$

To obtain a solution to the many-body electron problem, different methods can be applied based on the expansion of the wave function in Slater determinants, such as the Hartree-Fock method. However, it is a very complex method which requires much computational time even for small systems because each of N-electrons has 3 degrees of freedom. Using density functional theory, the calculation scheme uses the electronic density with only 3 degrees of freedom that depends only on the three position coordinates of the density, instead of three position coordinates for each of N electron. Despite this change, in principle, DFT calls for only one approximation, related with the correlation potential used to define the respective functional [213, 214, 224].

3.1.2 The Thomas-Fermi model

The work developed by Thomas [219] and Fermi [220] can be considered as an important initial step responsible for the development of DFT, although, conceptually, in the initial form despite being similar. According to this model, kinetic energy is a functional of the density of charge, combined with the electron-electron and electron-nucleus interaction which are treated classically. The model neglects the exchange-correlation interaction and, for this reason, only works for simple systems. Some developments were introduced later by Dirac [225] to include an exchange energy functional but are still incomplete.

3.1.3 Hohenberg and Khon theorems

Hohenberg and Kohn's contribution was fundamental to the development of the theory behind DFT because it legitimized the use of the electronic density to characterize absolutely any system [226]. The hypothesis for using the charge

density as the fundamental variable is supported by two different theorems. The first theorem argues that an external potential $v(\mathbf{r})$ is determined by the electron density, $\rho(\mathbf{r})$, within a trivial additive constant. Therefore, the ground-state wave function and all the other electronic properties of the system can be achieved by using the density of charge. Thus, it is possible to write the total energy of the ground state as a functional of the charge density, i.e [213,214,224]:

$$E_v[\rho] = T[\rho] + V_{ne}[\rho] + V_{ee}[\rho] = \int \rho(\mathbf{r})v(\mathbf{r})d\mathbf{r} + F_{HK}[\rho] \tag{3.7}$$

$F_{HK}[\rho]$ is the *Hohenberg-Kohn functional* defined by the expression $F_{HK}[\rho] = T[\rho] + V_{ee}[\rho]$, where $T[\rho]$ is defined as the electronic kinetic energy and the interaction electron-electron appears as $V_{ee}[\rho] = J[\rho]+\zeta[\rho]$, where $J[\rho]$ represents the classical repulsion:

$$J[\rho] = \frac{1}{2}\int\int \frac{1}{r_{12}}\rho(r_1)\rho(r_2)dr_1dr_2 \tag{3.8}$$

$\zeta[\rho]$ is the non-classical term of the exchange-correlation energy. The exchange-correlation energy is described as the interacting part of the electronic kinetic energy plus the non-classical electron-electron interaction expressed by:

$$E_{ec}[\rho] = T[\rho] - T_S[\rho] + V_{ee}[\rho] - J[\rho] \tag{3.9}$$

where $T_S[\rho]$ represents the non-interacting part of the electronic kinetic energy.

The second theorem of Hohenberg and Kohn is based on the fact that the total energy of the ground-state can be obtained by Equation 3.7 by determination of the respective local minimum [213,214,224]. The charge density that corresponds to the minimum of the functional expressed by Equation 3.7 is the ground-state charge density, $\rho_0(\mathbf{r})$. In summary, the previous Hohenberg-Kohn theorems can be revealed by the variational principle which argues that the ground-state of any system is the state of the minimum of energy, E_0, that is, $E_0 \leq E_v[\check{\rho}]$, with $\check{\rho}(\mathbf{r}) \geq 0$ and $\int \check{\rho}(\mathbf{r})d\mathbf{r} = N$. Both Hohenberg-Kohn theorems establish further that the ground-state density of charge univocally defines this state, i.e., there is a one-to-one correspondence between the charge density and the external potential [214].

3.1.4 The Kohn-Sham equations

The equations of Kohn and Sham (KS), published in 1965, start from the Hohenberg-Kohn theory and allow to solve interacting many-particles systems, for the ground-state, and in an exact way [227]. The approach uses an auxiliary problem that simplifies the original system with the same charge density as

the initial system, but with independent particles. The corresponding non-interacting system is described by the Hamiltonian [213, 214, 224]:

$$\hat{H}_S = \sum_i (-\frac{1}{2}\nabla_i^2) + \sum_i^N v_S(\mathbf{r_i}) \tag{3.10}$$

in which there are no electron-electron repulsion terms and $v_S(\mathbf{r_i})$ is the effective potential of a single-particle problem. For this system, the ground-state density is exactly determined, ρ, as well as the wave function of each electron, Ψ_i, and therefore the total wave function of the system in the ground-state, $\Psi_S = \frac{1}{\sqrt{N}} det[\Psi_1 \Psi_2 ... \Psi_N]$. The individual wave functions of each electron of the non-interacting particles system can be determined solving the equation [214, 224]:

$$\hat{h}_S \Psi_i = [-\frac{1}{2}\nabla^2 + v_S(\mathbf{r})]\Psi_\mathrm{i} = \epsilon_\mathrm{i}\Psi_\mathrm{i} \tag{3.11}$$

The kinetic energy, $T[\rho]$, for this system can be now obtained from the previous wave functions:

$$T[\rho] \propto \sum_i^N \langle \Psi_i | - \frac{\hbar^2}{2m}\nabla^2 | \Psi_i \rangle \tag{3.12}$$

Using the Hohenberg-Kohn variational problem and the orbital functions Ψ_i, a set of equations can be derived, the Kohn-Sham Equations [214, 224]:

$$[-\frac{1}{2}\nabla^2 + v_{eff}]\Psi_i = \epsilon_i \Psi_i \tag{3.13}$$

with:

$$v_{eff} = v(\mathbf{r}) + \int \frac{\rho(\mathbf{r'})}{|\mathbf{r} - \mathbf{r'}|} d\mathbf{r'} + v_{xc}(\mathbf{r}) \tag{3.14}$$

where the exchange-correlation term is given by $v_{xc}(\mathbf{r}) = \delta E_{xc}/\delta\rho(\mathbf{r})$, in which E_{xc} is exchange-correlation energy.

These equations are computed using an iterative self-consistent method, starting with a guess for the initial charge that allows to determine, v_{eff}, solve the KS Equation and determine Ψ_i. With Ψ_i it is possible to achieve the new density of charge and again, the new effective potential, repeating this cycle until convergence is reached [213, 214, 224]. This procedure is illustrated in Figure 3.1.

3.2 The exchange-correlation functional

In a many-body system, finding the ground-state energy of the Schrödinger equation represents an exhausting task. The theory developed by Hohenberg,

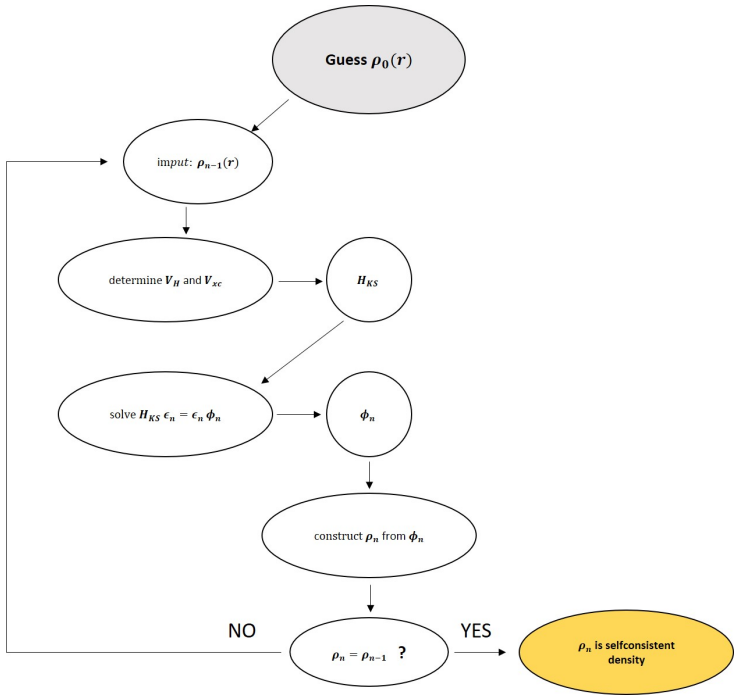

Figure 3.1: Flow chart for the n^{th} iteration in the selfconsistent procedure to solve the Kohn-Sham equations.

Kohn, and Sham demonstrated that the ground-state can be obtained by minimizing the energy of an energy functional computed by a self-consistent solution to a set of single-particle equations [213, 214, 224].

Beyond the *Born-Oppenheimer* approximation, no other approximation was introduced in the Kohn-Sham equations. However, this is the critical point that was not completely clarified: in order to solve the KS Equation, the exchange-correlation function must be specified. It is here that approximations enter in DFT. The functionals for exchange and correlation are not defined in a closed form; however, there are two main types of exchange/correlation functionals used in DFT: the local density approximation (LDA) and the generalized gradient approximation (GGA).

3.2.1 Local density approximation

The simplest and most extensively known approximation, called local density approximation (LDA), assumes that the exchange-correlation dependes only on density and can be expressed by [213, 214, 224]:

$$E_{xc}^{LDA} = \int \rho(\mathbf{r})\epsilon_{xc}(\rho(\mathbf{r}))d\mathbf{r} \tag{3.15}$$

$\epsilon_{xc}(\rho)$ is a function (not functional) for homogeneous electron gas whose definition can be found in reference [214]. The assumption of LDA is that the exchange-correlation energy can be found by dividing the material in infinitesimal volumes. Each such volume has a constant density and, as such, makes the same contribution to the total exchange-correlation, in a way similar to a volume filled with homogeneous electron gas. However, as it cannot be guaranteed that E_{xc} has this form, the above-mentioned remains an assumption. For systems with slowly varying density, LDA is expected to work conveniently but, surprisingly, it described many other cases reasonably well [214].

For magnetic systems, LDA functional must include spin interaction and the functional is called local spin density approximation (LSDA) [213, 214, 224, 228]. By construction, the spin density $\rho_\sigma(r)$ is the key quantity and the exchange-correlation energy has the following form:

$$E_{xc}^{LDA} = \int \mu_{xc}(\rho_\uparrow, \rho_\downarrow)[\rho_\uparrow + \rho_\downarrow]dr \tag{3.16}$$

where $\mu_{xc}(\rho_\uparrow, \rho_\downarrow)$ is a local exchange-correlation energy (that can exhibit different forms according to the literature) and $[\rho_\uparrow + \rho_\downarrow]$ the total electron density.

3.2.2 Generalized gradient approximation

New approximations beyond the LSDA have been explored: however, in order to improve LDA, it is considered that the exchange-correlation does not depend only on the local density but also on the density of the neighbouring volumes. This contribution is reached by adding the gradient of the electron density or its corresponding potential. This approximation, called the generalized gradient approximation (GGA), is still local, although it takes into account the gradient of the density [213, 214, 224, 228–231]. GGA can be represented by the general expression:

$$E_{xc}^{GGA}[\rho^\alpha(\mathbf{r}), \rho^\beta(\mathbf{r})] = \int d\mathbf{r} f[\rho^\alpha(\mathbf{r}), \rho^\beta(\mathbf{r}), \nabla\rho^\alpha(\mathbf{r}), \nabla\rho^\beta(\mathbf{r})] \tag{3.17}$$

where α and β are the indexes for different spins when spin polarized calculation is used. One of the most common GGA functionals was developed by Perdew, Burke, and Ernzerhof (PBE) [229, 230] and is widely used.

Despite the great versatility of GGA, there are a few weaknesses. The first to mention is that there is some freedom to add the density gradient, thus several versions of GGA. Second, GGA calculations are referenced as no ab-initio calculation because some experimental information is used. Nevertheless, GGA functionals parameters are freely available [214].

3.2.3 The van der Waals interaction and its calculation

Unlike ionic or covalent bonds, Van der Waals forces (vdW) refer to the interactions that do not result of any chemical electronic bond. vdW are comparatively weak and quickly vanish at long distances and they are more susceptible to being perturbed [232]. These interactions contain the Pauli exclusion repulsion, dipole-dipole, dipole-induced dipole, and instantaneous dipole-induced dipole terms. The last one, usually referred to as the London dispersion, often includes the binding of the low dimension systems, such as small clusters, narrow fibers, and layered materials [233]. As the dispersion energy is present, it is obvious it will affect the structure in terms of the geometry, bond lengths, energies as well as other properties.

DFT has not provided a complete description of the systems in which dispersion forces are relevant, as for example, in a wide variety of weakly bonded molecular complexes, because the approximations for the exchange-correlation energy previously described happens to be poor and limited. As LDA and GGA functionals are given by the integrals of the local functions of the density of charge, alone and with its gradient, respectively, the vdW interactions are characterized by a non-local correlation effect that is neglected by the first functionals [233]. Many relevant works have been written to achieve some corrections to DFT or develop new functionals which can be more appropriate to describe the dispersive interactions that play a major role in some systems in the gas phase and in the solid state.

Several functionals have recently been reported and the Grimme approach [234–236], known as DFT-D, with three different versions, with semi-empirical corrections for vdW interactions seems to generally give a reasonable prediction of the adsorption properties. The vdW energy is obtained by a sum of pairwise interatomic interaction terms over all atom pairs in the system [233]. The

expression of that function (version function on r^{-6}) is given by:

$$E_6^{(2)} = s_6 \sum_{i<j} \frac{C_6^{ij}}{|r_i - r_j|^6} f_{d,6}|r_i - r_j| \tag{3.18}$$

The superscript (2) mentions atom pairs, s_6 is an overall scaling factor, set to 1 in the most recent DFT-D3 version [236] and $f_{d,6}$ is the damping function, essential to damp the singularity in r^{-6} (it approaches 1 at large $|r_i - r_j|$ and 0 at small $|r_i - r_j|$). C_6^{ij} are the coefficients determined empirically in different ways depending on the version which uses different methods. In DFT-D1 [234], this coefficient is determined by the average of the empirical coefficient values over the hybridization states of each atom. For DFT-D2 [235], C_6^{ij} are given as a function of the atomic ionization energies and polarizabilities, which is obtained with PBE hybrid functional [237]. In the last version, DFT-D3 [236], the coefficient is obtained using time-dependent DFT (TDDFT) for different sample geometries, posteriorly interpolated, making this the only version where vdW interactions of an atom are sensitive to its local environment.

A family of such methods has been developed with the same sum over pairwise interactions as in Equation 3.18 and successfully applied to a variety of systems, including small molecules, water clusters, graphite and graphene, water layers interacting with graphite, interfacial water on semiconducting substrates, hydrogenated carbon nanotubes, molecular solids, and the interaction of rare gases and small molecules with metal surfaces [238–243]. In particular, the Tkatchenko-Scheffler (TS) method [244] is a different method to calculate C_6^{ij}, relating the atomic polarizability to the atomic effective volume which is found from Hirshfield partitioning [245]. Many-body-vdW interactions [246] and the screening for binding on inorganic surfaces [247] were added to this method.

From a theoretical point of view, all these approaches offer a possible solution to the problem associated with dispersion forces which can reveal interesting phenomena in low dimensional materials, such as graphene.

3.3 The linearized augmented plane wave

To compute Equation 3.1 using DFT, a basis set is required in which the eigenstates, Ψ_i, of the Hamiltonian can be expanded. A plane wave ($f(\mathbf{r}) = e^{(ik.\mathbf{r})}$) is a mathematically simple way (unbiased and efficient) to describe a basis set and therefore any eigenfuntion $\Psi_{\mathbf{k}}^n$ of a periodic Hamiltonian can be expressed exactly in this basis set using an infinite set of coefficients $c_{\mathbf{K}}^{n,\mathbf{k}}$ [214, 228]:

$$\Psi_k^n = \sum_{\mathbf{K}} c_{\mathbf{K}}^{n,\mathbf{k}} e^{i(\mathbf{k}+\mathbf{K})\mathbf{r}} \tag{3.19}$$

k is any vector of the first Brillouin zone and **K** any vector of the reciprocal lattice. The basis sets are:

$$|\phi_{\mathbf{K}}\rangle = e^{i(\mathbf{k}+\mathbf{K})\mathbf{r}} \tag{3.20}$$

Different **k** represents different basis sets and the maximum value of **K** gives the dimension of the basis set. This value, which limits the set, corresponds to the radius K_{max} of a sphere at the origin of the reciprocal space and to corresponding energy $E = \hbar^2 K_{max}/2m_e$, usually called *cutoff-energy* [214, 224]. All reciprocal lattice vectors inside this sphere belong to the basis set. In the region close to the nucleus (small radius) where electrostatic potential is high and the wave function needed to describe the electronic state is very steep or extremely oscillating, it is necessary to use a large number of plane waves. For this case, the increase in the number of plane waves is so big that it means that the consumed computer time is not manageable. To overcome this adversity, sometimes, a pseudopotential is used [228,248]. By the inclusion of the pseudopotential, the wave function close to the nucleus becomes smooth and a minor number of plane waves is needed to describe it. The main disadvantage of this method is that it is not the most aproppriate for calculations of the electric field and magnetic hyperfine fields gradients because the region of interest for calculation of hyperfine fields is the one closer to the nucleus. Thus, alternatives to this method can be made more efficient.

Another option that represents a viable alternative to the pseudopotentials is the so-called augmented plane waves (APW). This method considers the space divided as *core states*, which include electrons bound to the nucleus as if they were in a free atom, and *valence states* that participate in the chemical reactions with the neighboring atoms [214, 224, 228]. Therefore, space is divided in two different regions as is shown in Figure 4.2: spheres region around each atom, S_α, called *muffin-tin spheres* and the remaining space outside, which is called the *interstitial region*, I. Core states and the valence states inside spheres, as they are shielded from the interactions with exterior atoms, can be described by an atomic-like wave functions, considering spherical harmonics, $Y_l^{m\ell}$. In the interstitial region, plane waves are used because it is possible to assume the electrostatic potential to be zero. One APW used in the expansion of $\Psi_{\mathbf{k}}^n$ can be expressed as:

$$\phi_{\mathbf{K}}^{\mathbf{k}} = \begin{cases} \dfrac{1}{\sqrt{V}} e^{i(\mathbf{k}+\mathbf{K})\mathbf{r}}, & \mathbf{r} \in I \\ \displaystyle\sum_{\ell,m} A_{\ell m}^{(\alpha \mathbf{k}+\mathbf{K})} u_\ell^\alpha(\mathbf{r}', E) Y_m^\ell(\mathbf{r}'), & \mathbf{r} \in S_\alpha \end{cases} \tag{3.21}$$

Plane waves in the interstitial region are augmented by atomic-like functions

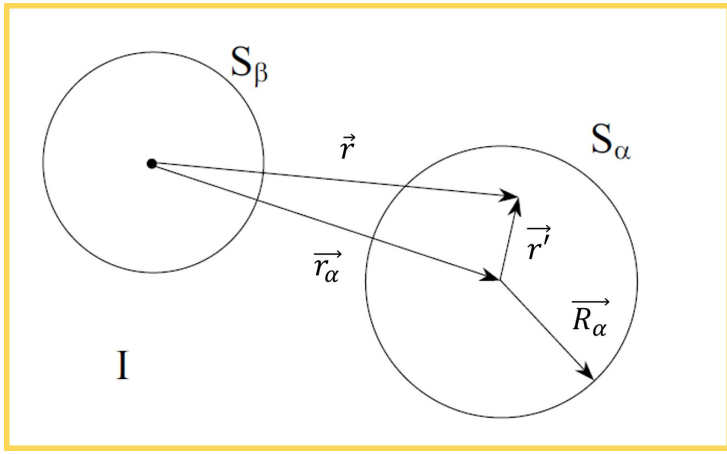

Figure 3.2: Division of a unit cell in *muffin tin* regions and the interstitial region, for a case with two atoms. The black dot is the origin of the axis system (which may but need not to coincide with the nucleus of an atom).

in the spheres region. $\mathbf{k}$,$\mathbf{K}$ and $\mathbf{r}$ keep the same meaning described previously, V is the volume of the unit cell, α is the index of the muffin-tin spheres and $\mathbf{r}' = \mathbf{r} - \mathbf{r}_\alpha$ gives the center position of each spheres. The length of $\mathbf{r}'$ is r', and the angles θ' and ϕ' specifying the direction of $\mathbf{r}'$ in spherical coordinates. Y_m^ℓ are spherical harmonics and u_ℓ^α are the solution to the radial part of Schrödinger equation for a free atom α at an energy E. The $A_{\ell m}^{(\alpha,\mathbf{k}+\mathbf{K})}$ are yet undetermined parameters defined by the boundary conditions: these two sets of functions must match at the sphere boundaries:

$$\frac{1}{\sqrt{V}} e^{i(\mathbf{k}+\mathbf{K})\mathbf{r}} = \frac{4\pi}{\sqrt{V}} e^{i(\mathbf{k}+\mathbf{K})\mathbf{r}_\alpha} \sum_{\ell,m} i^\ell j_\ell(|\mathbf{k}+\mathbf{K}||\mathbf{r}|) Y_m^{\ell *}(\mathbf{k}+\mathbf{K}) Y_m^\ell \qquad (3.22)$$

where j_ℓ is a Bessel function of ℓ order.

The condition expressed by Equation 3.22 gives an infinite number for $A_{\ell m}^{(\alpha,\mathbf{k}+\mathbf{K})}$. In practice, the expression is truncated and is only considered as the sum of these values until the maximum value, ℓ_{max}. However, the need of an eigenvalue for energy, E, to determine with accuracy the eigenstate based on the set APW is inconvenient because E is also unknown and one is forced to decide on an estimated value to start the calculation [214]. For this reason, the computer time is much longer in comparison with the pseudopotential method, because in the latter one diagonalization of the secular matrix gives all the eigenvalues as opposed to APW that needs one diagonalization for each eigenvalue. Because

of this, APW is not used anymore but it represents an important introduction for the next method [214, 224]. The linearized augmented plane wave (LAPW) method solves this obstacle and appears to be a convenient alternative [214]. LAPW works based in a Taylor expansion around energy, E_0, to determine the radial solution $u_\ell^\alpha(\mathbf{r}', E)$ [214]:

$$u_\ell^\alpha(\mathbf{r}', \epsilon_{\mathbf{k}}^n) = u_\ell^\alpha(\mathbf{r}', E) + (E_0 - \epsilon_{\mathbf{k}}^n)\frac{\partial u_\ell^\alpha(\mathbf{r}', E)}{\partial E}_{|E=E_0} + O(E_0 - \epsilon_{\mathbf{k}}^n)^2 \quad (3.23)$$

Instead of starting with a guessed value for the energy of the eigenstate, $E = \epsilon_{\mathbf{k}}^n$, to achieve $u_l^\alpha(\mathbf{r}', E_0)$, the LAPW method overcomes this difficulty by calculating $u_\ell^\alpha(\mathbf{r}', E_0)$ based on known quantitites. The substitution of the first two terms of the expansion on the APW equation gives the LAPW:

$$\phi_{\mathbf{K}}^{\mathbf{k}} = \begin{cases} \frac{1}{\sqrt{V}} e^{i(\mathbf{k}+\mathbf{K})\mathbf{r}}, & \mathbf{r} \in I \\ \sum_{\ell,m} (A_{\ell m}^{(\alpha \mathbf{k}+\mathbf{K})} u_\ell^\alpha(\mathbf{r}', E_0) + B_{\ell m}^{(\alpha \mathbf{k}+\mathbf{K})} u_\ell^\alpha(\mathbf{r}', E_0)) Y_m^\ell(\mathbf{r}'), & \mathbf{r} \in S_\alpha \end{cases} \quad (3.24)$$

The coefficients $A_{\ell m}^{(\alpha,\mathbf{k}+\mathbf{K})}$ and $B_{\ell m}^{(\alpha,\mathbf{k}+\mathbf{K})}$ are determined by the requirement of matching wave functions at the sphere boundary. The second coefficient, $B_{\ell m}^{(\alpha,\mathbf{k}+\mathbf{K})}$, is necessary to determine the difference $E_0 - \epsilon_{\mathbf{k}}^n$. Equation 3.24 does not represent the final definition of an LAPW set. For example, finding a description for the eigenstate $\Psi_{\mathbf{k}}^n$, of an atom α, that is predominantly p-character ($\ell = 1$): with $A_{(\ell=1)m}^{(\alpha,\mathbf{k}+\mathbf{K})}$ large, it will be obvious to choose E_0 near the center of the p-band and, in this way, the term $O(E_0 - \epsilon_{\mathbf{k}}^n)$ will remain small. This argument can be repeated for every physically important ℓ, ($s-, d-, f-$ states) and for every atom. In this way, it is better for accurate results not to choose only one E_0, but instead a set of well-chosen $E_(1, \ell)^\alpha$ up to $\ell = 3$ [214, 224, 228]. Thus, it is possible to re-write a LAPW basis set:

$$\phi_K^k = \begin{cases} \frac{1}{\sqrt{V}} e^{i(\mathbf{k}+\mathbf{K})\mathbf{r}}, & \mathbf{r} \in I \\ \sum_{\ell,m} (A_{\ell m}^{(\alpha \mathbf{k}+\mathbf{K})} u_\ell^\alpha(\mathbf{r}', E_{1,\ell}^\alpha) + B_{\ell m}^{(\alpha \mathbf{k}+\mathbf{K})} u_\ell^\alpha(\mathbf{r}', E_{1,\ell}^\alpha)) Y_m^\ell(\mathbf{r}'), & \mathbf{r} \in S_\alpha \end{cases} \quad (3.25)$$

K_{max} will define the accuracy of a plane wave basis set and the efficiency of the calculation. However, the product $R_\alpha^{min} K_{max}$, between the smallest muffin thin radius and K_{max}, represent a better parameter to evaluate the accuracy of the LAPW method. The increase of R_α^{min} of the sphere allows to reduce K_{max}, keeping the same accuracy. Reducing K_{max} means reducing the size of the matrices and, of course, cut the computation time. On the other hand, R_α^{min}

cannot be large because spherical harmonics are not appropriate to describe the region far away from the nuclei. To find the suitable $R_{\alpha}^{min}K_{max}$, is the initial step of any calculation because this parameter should be large enough to allow the required accuracy but balanced with the computational time needed to establish it [214, 224, 228].

The LAPW basis set can be much smaller than a plane wave basis set. K_{max} required is around $K_{max} = (7.5 \longleftrightarrow 9.0)/(R_{\alpha}^{min}) \simeq 4au^{(-1)}$ depending on the accuracy that is needed and this yields $P \simeq 195$ as the basis set size ($P \simeq 270$ for plane waves). The computation time is a function of the third power of the basis set size and, as the dimention of a LAPW basis set is smaller, it can make the calculation about 2 or 3 times faster that for the plane waves [214].

The LAPW basis set can be inefficient sometimes, when the eigenstate is a mix between different valence states, for exemple, states with same value of l but differing in therms of the principal quantum number n. In these particular cases, a better solution is found by adding complementary information to the LAPW set, i.e., another type of basis function called *local orbital* (LO) [214]:

$$\phi_{\alpha,LO}^{\ell m}(\mathbf{r}) = \begin{cases} 0, & \mathbf{r} \notin I \\ \sum_{\ell,m}(A_{\ell m}^{(\alpha,LO)} u_{\ell}^{\alpha}(\mathbf{r}', E_{1,\ell}^{\alpha}) + \\ +B_{\ell m}^{(\alpha,LO)} u_{\ell}^{\alpha}(\mathbf{r}', E_{1,\ell}^{\alpha}) + \\ +C_{\ell m}^{(\alpha,LO)} u_{\ell}^{\alpha}(\mathbf{r}', E_{2,\ell}^{\alpha}))Y_{m}^{\ell}(\mathbf{r}'), & \mathbf{r} \in S_{\alpha} \end{cases} \tag{3.26}$$

LO is defined for a particular sphere, for a particular ℓ and n, and it is zero in the interstitial region as well as for the spheres that belong to other atoms. The values of $A_{\ell m}^{(\alpha,LO)}$, $B_{\ell m}^{(\alpha,LO)}$ and $C_{\ell m}^{(\alpha,LO)}$ are determined again by the imposition of the boundary conditions. The use of LO leads to a better result in terms of accuracy but with a consequent slight increase in the computational time.

3.4 The electric field gradient calculation

The electric field gradient (EFG) tensor will be used in the present study as a relevant parameter to understand the interactions and effects between the adsorbed atoms and the surface of graphene, at the atomic local scale. The EFG allows to research the electron density, atom position, stability and dynamics. The EFG is just introduced here to understand how it can be obtained using DFT calculations. However, it will be presented hereafter in more detail: its

definition and properties and how it can be determined experimentally with spectroscopic methods.

EFG can be obtained by ab-initio calculation from the Kohn-Sham Equations, using LAPW methods and LSDA or GGA approximations [214, 224]. The component V_{zz} of the tensor EFG is determined by the density of charge $\rho(\mathbf{r})$, using the expression [224]:

$$V_{zz} = \int \rho(r) \frac{2P_2 cos(\theta)}{r^3} dr \tag{3.27}$$

where P_2 represents a Legendre polynomial of order 2 defined by:

$$P_2(x) = \frac{1}{2}(3x^2 - 1) \tag{3.28}$$

3.5 wien2k and VASP software

The success of DFT calculations is intrinsically connected with the appropriate choice of the software because each code implements the formalism in a different way. Over the years, many alternative codes have been developed in different academic groups and several of them used in numerous scientific communities resulting in a huge number of papers published in the DFT domain [217], predicting the structure and properties of solids at the molecular or atomic scale. As it was previously mentioned, the exchange-correlation functional represents the unknown part of the interaction energy and, for this reason, has been intensively researched leading to a panoply of available functionals in solid-state physics [249–253] and quantum chemistry [254–256].

In this work, the electronic structure calculations were performed using WIEN2K© [257] and VASP© [258] computer DFT programs. Both were developed in Vienna University of Technology, respectively, at the Institute of Materials Chemistry and Faculty of Physics - Computational Materials Physics and they are written in the FORTRAN programming language. Each code solves the Kohn-Sham Equations and determines the eigenstates and eigenvalues in its own way by using different approaches in the computational procedure.

WIEN2K employs LAPW and LAPW+LO basis sets to solve KS-Equations and uses an all-electron scheme which builds the density from single-particle wave functions [257]. In spite of the fact that the wave functions are described as a linear combination of a pre-defined basis function, the KS-Equations appear in a simplified way as a matrix equation, where the exact solution can be found [218]. In the current work, most calculations were performed using WIEN2K, which can be executed by using the graphic interface or the command line. The program is

started defining the structure file (cif-file import, spacegroup support, symmetry detection) and, in the initialization task, the nearest neighbors are calculated, the overlapping of the spheres checked, the point and spacegroups calculated and atomic densities generated and, finally, it is determined how the orbitals are treated in the band structure calculations, i.e., as core or band states, with or without local orbitals. The corresponding KS-Equations must be solved iteratively untill self-consistency is reached. The basic quantity achieved is the electron density which is obtained by summing over the occupied KS orbitals.

VASP uses the projector augmented wave (PAW) approach, which consists of an explicit transformation between all-electron and pseudopotential wave functions by means of additional partialwave basis functions [218, 258]. It makes PAW codes practical when small numbers of plane waves are needed or for large grid spacings giving very precise results. However, the suitable choice of partial-wave projectors is not trivial. PAW methods, as well as pseudo-potential methods, are generally designated pseudization approaches. Although, in pseudization, not so good precision is achieved when compared with all-electron codes, the computation time decreases significantly [218]. Hybrid functionals that mix the Hartree-Fock approach with DFT are implemented in VASP as well as Green's functions methods and many-body perturbation theory [258].

In present work, DFT calculations intend to study the adsorption process of atoms of several elements on the surface of graphene, determining physical parameters such as adsorption energy, the electric field gradient, density of states, band structure, and charge distribution in the unit cell of the system graphene-adatom. Some of these calculations were done to interpret experimental results obtained by the perturbed angular correlation spectroscopy measurements performed at ISOLDE, in order to give an explanation for the nanoscopic properties and atomic/molecular configurations observed.

Chapter 4

Perturbed Angular Correlation spectroscopy

An experimental study was carried out using perturbed angular correlation spectroscopy. This chapter consists of a brief description of this hyperfine method starting with an overview of the interaction between the nucleus and an external electric/ magnetic field, which is called hyperfine interaction (*section* 4.1). An explanation of the general theory of perturbed angular correlations (*section* 4.2) and the radioactive ion beam production facilities at ISOLDE (*section* 4.3), as well as the experimental setup and procedures (*section* 4.4) are contextualized taking into account the importance to achieve the main goals of this thesis.

4.1 Hyperfine interaction

A nucleus in matter interacts with the local environment and is subject to extranuclear electric and magnetic fields. Hyperfine interaction is the interaction between the nuclear moments and the external fields, i.e., the interaction between the nuclear quadrupole moment with the electric field gradient (EFG) and/or the nuclear dipole magnetic moment with the magnetic hyperfine field (HMF). The measurement of this interaction that rises up the splitting of the nuclear sublevels can represent a sensitive and an accurate method to obtain the direct information about the local charge distribution and the magnetic hyperfine fields, providing a description of the atomic local environment. Therefore, nuclear hyperfine methods such as nuclear magnetic resonance (NMR), nuclear

quadrupole interactions (NQI), Mössbauer effect (ME), or perturbed angular correlation (PAC) appear to be reliable tools to investigate the structural, magnetic and electronic properties at atomic scale in the condensed matter in a large variety of materials, in several fields of physics, chemistry, and biophysics [259, 260].

4.1.1 Magnetic interaction

According to quantum mechanics, the magnetic moment, μ, is defined as the component of this operator, $\hat{\mu}$, along *z-axis* of a general state $|I, m\rangle$ with $m = I$, where I and m are respectively the quantum numbers for the total angular momentum and the projection along z. In this way, one can write [260–262]:

$$\mu = \langle I, I| \hat{\mu}_z |I, I\rangle = \gamma \langle I, I| \hat{I}_z |I, I\rangle = \gamma \langle I, I| m\hbar |I, I\rangle \tag{4.1}$$

So, the dipole moment of a nuclear charge distribution, which is proportional to its angular momentum $\hbar I$, is described in the following way:

$$\mu = \gamma \hbar I \tag{4.2}$$

where γ is the nuclear gyromagnetic ratio and is defined as:

$$\gamma = g\frac{\mu_N}{\hbar} \tag{4.3}$$

knowing that g is the dimensionless *g-factor* (defined for the angular momentum L and for the spin S of the nucleus) and μ_N is the nuclear magneton, defined from the proton mass, m_p, and electron charge, e:

$$\mu_N = e\frac{\hbar}{2m_p} = 5.05082(2) \times 10^{-27}\ J.T^{-1} \tag{4.4}$$

For a magnetic interaction, the Hamiltonian is diagonal in the $|I, m\rangle$ basis if the magnetic field is applied parallel to the z *axis*, B_z. The eigenvalues are given by:

$$E_m = \langle I, m| - \hat{\mu}_z \hat{B}_z |I, m\rangle = -g\frac{\mu_N}{\hbar} B_z \langle I, m| \hat{I}_z |I, m\rangle = -g\mu_N B_z m \tag{4.5}$$

This means that the degeneracy of the $2I + 1$ is completely lifted by the interaction. Thereby, the energy splitting between any two adajacent m sublevels can be obtained by:

$$\Delta E_m = g\mu_N B_z = \gamma \hbar B_z = \hbar \omega_L \tag{4.6}$$

Looking at Equation 4.6 one can realize that the splitting is the same between all neighbouring m sublevels. The Larmor frequency, ω_L, can be now obtained by the expression:

$$\omega_L = \gamma B_z = g\frac{\mu_N}{\hbar} B_z \tag{4.7}$$

4.1.2 Electric interaction

From the classical description, the electrostactic energy of a nuclear charge distribution $\rho(r)$ in an external electrical potential $\Phi(\mathbf{r})$ is given by [259–261]:

$$E = \int \rho(\mathbf{r})\Phi(\mathbf{r})d^3r \tag{4.8}$$

where the total nuclear charge can be described as:

$$q = \int \rho(\mathbf{r})d^3r = Ze \tag{4.9}$$

where Z is the atomic number and e is the electron charge. Taking into account that the electrostatic potential is slowly varying over the nucleus region where $\rho(\mathbf{r})$ is nonnegligible then it is convenient to expand it in a Taylor series around the origin ($\mathbf{r} = 0$):

$$\Phi(\mathbf{r}) = \Phi(0) + \mathbf{r}.\nabla\Phi(0) + \frac{1}{2}\sum_{i,j} x_i x_j \Big(\frac{\partial^2\Phi}{\partial x_i \partial x_j}\Big)_0 + ... \tag{4.10}$$

Based on this Taylor expansion, the electrostatic energy can be rewritten as:

$$E = q\Phi(0) + \mathbf{p}.\nabla\Phi(0) + \frac{q}{6} < r^2 > \nabla^2\Phi(0) + \frac{e}{6}\sum_{i,j}\Phi_{ij}Q_{ij} \tag{4.11}$$

where $\mathbf{p}$ is the electric dipole moment, Q_{ij} is the electric quadrupole moment tensor which is defined as $Q_{ij} = \frac{1}{e}\int \rho(\mathbf{r})(3x_i x_j - r^2\delta_{ij})d^3r$ and, for simplicity, $\Phi_{ij} = \Big(\frac{\partial^2\Phi}{\partial x_i \partial x_j}\Big)_0$ was defined.

Examining the meaning of each term individually [259,260] it is noticed that the zero-order term (E^0) corresponds to the electrostatic energy, which is constant and does not contribute to the energy splitting. The first order term (E^1) represents the electric dipole interaction between the electric field at the origin and the electric dipole moment of the nuclear charge distribution. This term is zero because the quantum mechanical expectation value of the nuclear electric dipole is zero, since the nuclear states have definite parity. The third and fourth terms in Equation 4.11 represent the second-order term (E^2) of the multipolar expansion: the first of these two represents the monopole term and is directly related to the mean square nuclear radius and to the electron charge density at the nucleus. The contribution of this term for perturbed angular correlations is zero because it does not change the energy splitting of the measuring nuclear state. It just only shifts the nuclear levels being responsible for the so called *isomer-shift* in Mössbauer spectroscopy. The last term in Equation 4.11 is the electric quadrupole interaction and is of particular interest because it represents

the most relevant electric interaction being responsible for the nuclear level splitting in nuclei with nonnegligible quadrupole moment. Taking into account that Q_{ij} is a traceless tensor, it is helpfull to introduce the electric field gradient (EFG) tensor $V_{ij}=\Phi_{ij}-\frac{1}{3}Tr(\Phi)$ as a traceless part of the second derivatives tensor of the potential at the nucleus. The quadrupole energy can be written since it is invariant under the substitution of Φ_{ij} by V_{ij} [260]:

$$E_Q = \frac{q}{6}\sum_{i,j} V_{ij}Q_{i,j} \tag{4.12}$$

Since the electric field gradient is a symmetric tensor, it is possible to find an eigenvector basis where V_{ij} is diagonal [260]. The EFG is a traceless symmetric rank 2 tensor so that the system of axis can be defined in a way that the EFG tensor representation has only three non-vanishing diagonal components defined as $|V_{zz}| \geq |V_{yy}| \geq |V_{xx}|$. For simplicity, it is common to characterize the EFG tensor by its main component V_{zz} and the axial asymmetry parameter, η, that means the local charge distribution from axial symmetry:

$$\eta = \frac{V_{yy} - V_{xx}}{V_{zz}} \tag{4.13}$$

taking into account that the three remaining degrees of freedom are characterized by the Euler angles that correlate the principal axis system (where the EFG is diagonal) with the axis system where the laboratory is defined. The expression of the quadrupole energy can be written based on the EFG components in the explicit way:

$$E_Q = \frac{eV_{zz}}{12}\Big[3Q_{zz} + \eta(Q_{xx} - Q_{yy})\Big] \tag{4.14}$$

Based on the quantum mechanics formalism, one can write the Hamiltonian, $\hat{H}_Q$, in a more convenient form and determine the effect of quadrupole interaction at a nuclear level characterized by its angular momentum, $\hbar I$. The equation above remains valid for the interaction Hamiltonian, $\hat{H}_Q$, with the quadrupole tensor components, Q_{ii} substituted by the correspondent quantum operators, $\hat{Q}_{ii}$. Since the quadrupole operators are homogenous functions of the coordinates (x, y, z) their matrix elements in the $2I + 1$ manyfold, $\langle I, m|\, \hat{Q}_{ii}\, |I, m\rangle$, are proportional to those of an operator where each coordinate is substituted by the correspondent angular momentum operators $(\hat{I}_x, \hat{I}_y, \hat{I}_z)$ [259], taking into account the *Wigner-Eckart theorem* [263]. Therefore it is possible to write:

$$\langle I, m|\, \hat{Q}_{ii}\, |I, m'\rangle = \alpha(I)\, \langle I, m|\, 3\hat{I}_i^2 - I(I+1)\, |I, m'\rangle \tag{4.15}$$

The proportionality constant $\alpha(I)$ can be obtained based on the definition of the quadrupole moment Q which is the expectation value of the quadrupole

operator Q_{zz} in the nuclear state $|I, I\rangle$ [260], then:

$$Q = \langle I, I| \hat{Q}_{zz} |I, I\rangle = I(2I-1)\alpha(I) \Rightarrow \alpha(I) = \frac{Q}{I(2I-1)} \tag{4.16}$$

and the quadrupole interaction Hamiltonian is expressed as:

$$\hat{H}_Q = \frac{eQV_{zz}}{4I(2I-1)}\left[3\hat{I}_z^2 - I(I+1) + \eta(\hat{I}_x^2 - \hat{I}_y^2)\right] \tag{4.17}$$

From the previous equation one can define the quadrupole frequency as:

$$\omega_Q = \frac{eQV_{zz}}{4I(2I-1)\hbar} \tag{4.18}$$

For a non-axial symmetric quadrupole interaction ($\eta \neq 0$) this Hamiltonian cannot be diagonalized exactly, but for an axial interaction ($\eta = 0$) the eigenvalues of $\hat{H}_Q$ are determined by:

$$E_Q = \hbar\omega_Q[3m^2 - I(I+1)] \tag{4.19}$$

The energy splitting of the transition between two sublevels, m and m', is calculated by:

$$\Delta E_Q = 3\hbar\omega_Q|m^2 - m'^2| \tag{4.20}$$

where $|m^2 - m'^2|$ is always an integer and, consequently, all transition frequencies are multiple of ω_Q. The lowest observable frequency is ω_0. $\omega_0 = 6\omega_Q$ for I half-integer and $\omega_0 = 3\omega_Q$ for I integer. Then it is usual to use another quantity, the so called fundamental frequency:

$$\nu_Q = \frac{eQV_{zz}}{h} = \omega_0\frac{4I(2I-1)}{2\pi k} \tag{4.21}$$

where $k = 6$ (for I half-integer) and $k = 3$ (for I integer).

4.2 General theory of perturbed angular correlation

Perturbed angular correlation (PAC) spectroscopy is a particularly suited nuclear hyperfine method extensively employed to investigate the structural, magnetic, and electronic properties at the atomic scale in condensed matter physics. It works based in radioactive isotope probes to extract both HMF and the EFG, with high sensitivity and accuracy. Often, the abbreviation TDPAC is used to emphasize that this technique is time differential PAC as opposed to the time integrated PAC [259]. Specifically, the PAC acronym used in this thesis is synonymous with TDPAC.

Historically, the first report on perturbed $\gamma - \gamma$ angular correlation measurment was performed by H. P. Lehmann and J. Miller et al. [264] in the fifties. In this early period, the experiments intended only to collect data on the electric field gradients in noncubic metal and magnetic hyperfine fields in ferromagnetic materials. Many PAC studies have been reported since then and, nowadays, it is a recognized as well as valuable tool used in the context of numerous fields, not only in condensed matter physics, but also in chemistry, biology and medicine [259, 260]. The research of the interaction between the EFG and the nuclear quadrupole moment is more recent than the studies on the interaction between HMF and nuclear magnetic moment because the first one is more complicated for a number of reasons [259, 260]: i) the EFG of sufficient magnitude cannot be produced externally and, consequently cannot be varied at will; ii) it is difficult to calculate with high accuracy electric field gradients; iii) the sign of the EFG tensor is not obtained by a simple PAC experiment and, iv) due to the possible occurrence of many frequency patterns, the effect observed can be of difficult interpretation.

Still, PAC spectroscopy has been successfully applied to a multitude of physics problems and it can provide the specific microscopic information about macroscopic properties of solids, whether physical or thermodynamic because they are linked to the underlying atomic local behavior. Among recent hyperfine studies, J. N. Gonçalves [265] predicted a relation between the electric field gradients in ferroelectric perovskite oxides and the macroscopic electric polarization. Sill, the research into the coupling of the nuclear spin system with magnetic and/or electric hyperfine fields may prove fundamental in studies such as point defects in metals, atomic diffusion in solids, phase transitions in solids, and surface or interface physics [259, 260]. This method shows several advantages over other nuclear techniques such as temperature independency of the sensitivity and a small number of radioactive nuclei required (10^{10} - 10^{11} probe atoms) to perform an experiment. However, meticulous methods are needed to introduce the radioactive isotopes inside the sample's material which will act as a PAC probe-nuclei.

In this section, the most relevant aspects of the theory and mathematic formalism behind this technique are presented which have been extensively reported in several textbooks and review articles [266–270].

4.2.1 Unperturbed angular correlation

PAC represents a nuclear hyperfine method that works based on the emission of two consecutive γ-rays (or $e - \gamma$) from internal decay of a radioactive isotope acting as a probe nucleus [259]. In the process of emission of two consecutive

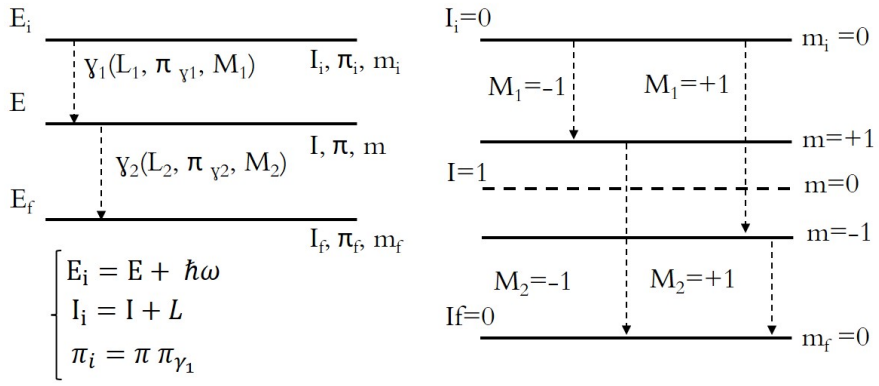

Figure 4.1: (Left) Emission of two γ photons from a radioactive decay through a cascade between the nuclear states $E_i \to E \to E_f$. The states are characterized by the angular moment, I, and parity, π. The conservation relations are also shown. (Right) An example of the alignment of the intermediate state of the cascade $I_i = 0 \to I = 1 \to I_f = 0$, i.e., the sublevel $m = 0$ is not populated.

γ-photons (or $e - \gamma$) from internal decay of a nucleus, there is a correlation between the emission directions of these two photons, $\boldsymbol{k}_1$ and $\boldsymbol{k}_2$, because the angular momentum, I, must be conserved. Figure 4.1 shows the angular correlations measured between γ_1 and γ_2, concerning the decays from the initial state $|I_i, m_i\rangle$ into the intermediate state $|I, m\rangle$ and then into the final state $|I_f, m_f\rangle$ [259].

The probability of emission of two consecutive γ-photons from a radioactive nucleus depends on the angle between the directions of emissions and of the nuclear spins of the cascade transitions. In general, in a set of nuclei the spins are randomly oriented and the emitted radiation is isotropic. An anisotropic emission of γ-rays is obtained when the nuclear state from which the radiation is emitted is well-oriented, "aligned", or "polarized", i.e. the $2I + 1$ degenerated m sublevels are differentially populated. The nuclei are "aligned" if the density of states $\rho(m)$ depends only on the absolute value of m, $\rho(m) = \rho(-m) \neq \rho(m')$, and are considered to be "polarized" if the density of states dependes on m, $\rho(m) \neq \rho(-m)$ [259, 271]. Several methods can be used to orient a set of nuclei, as, for example, an oriented state can be accomplished by applying low temperatures and a strong magnetic field giving rise to a dependence of the density of states $\rho(m)$ according to the Boltzman distribution [259]. In the case of PAC spectroscopy, the oriented set of nuclei is obtained by choosing only the nuclei whose spins happen to lie in a preferred direction [259, 271]. Considering

a nucleus in an initial state $|I_i, m_i\rangle$, that decays through a cascade emitting two successive gamma photons, γ_1 and γ_2, and assuming a random orientation for this initial state, i.e. $\rho(m_i) \neq \rho(m_i')$. As a consequence of the angular momentum conservation and the angular distribution of the electromagnetic radiation, the observation of γ_1 in a fixed direction $\boldsymbol{k}_1$ selects an ensemble of nuclei in the intermediate state $|I, m\rangle$ whose m sublevels are differently populated, since only transitions with $\Delta m = \pm 1$ are possible. Due the alignment of the intermediate state, the emission pattern of γ_2, becomes anisotropic and the transition amplitudes for the γ-emission from the initial to the intermediate state and for the intermediate to the final state depend on the matrix elements [259]:

$$\langle I, m| \hat{H}_1 |I_i, m_i\rangle \ \ and \ \ \langle I_f, m_f| \hat{H}_2 |I, m\rangle \tag{4.22}$$

That can be rewritten using the shorthand notation:

$$\langle m| \hat{H}_1 |m_i\rangle \ \ and \ \ \langle m_f| \hat{H}_2 |m\rangle \tag{4.23}$$

where $\boldsymbol{k}_i$ is the wave vector of the photon γ_i and $\hat{H}_i$ represent the Hamiltonian of the emission interaction of γ_i. Now, the unperturbed angular correlation can be expressed for a specific transition, between m_i and m_f, by [259, 271]:

$$W(m_i \rightarrow m_f) = \Big| \sum_m \langle m_f| \hat{H}_2 |m\rangle \langle m| \hat{H}_1 |m_i\rangle \Big|^2 \tag{4.24}$$

It is important to mention that only the initial and final states are observable so it corresponds to the summation of its transition amplitudes and not to its transition probabilities. According to Frauenfelder and Steffen [271], using the density matrix formalism, after calculating the matrix elements and summing, one obtains the general expression:

$$W(\boldsymbol{k}_1, \boldsymbol{k}_2) = W(\theta) = \sum_{k=0}^{k=k_{max}} A_k(\gamma_1) A_k(\gamma_2) P_k cos(\theta) \tag{4.25}$$

i.e, the probability $W(\theta)$ of finding γ_2 in a certain direction $\boldsymbol{k}_2$ with an angle θ relatively to the first photon γ_1 with the direction defined by $\boldsymbol{k}_1$, and in coincidence. The sum runs over the values k as a result of parity conservation of the electromagnetic interaction which is responsible for γ-emission and has the values:

$$0 \leq k \leq \ minimum \ of \ (2I, l_1 + l_1', l_2 + l_2') \tag{4.26}$$

where I is the spin of the intermediate nuclear state and $l_{1,2}$ and $l_{1,2}'$ are the multipolarities of the transitions. The cascade anisotropy terms, $A_k(\gamma_1)$ and $A_k(\gamma_2)$ represent the deviation of the coincidence probability from the isotropic case where $W(\theta) = 1$ [260]. The coefficient $A_k(\gamma_1)$ depends only on the first

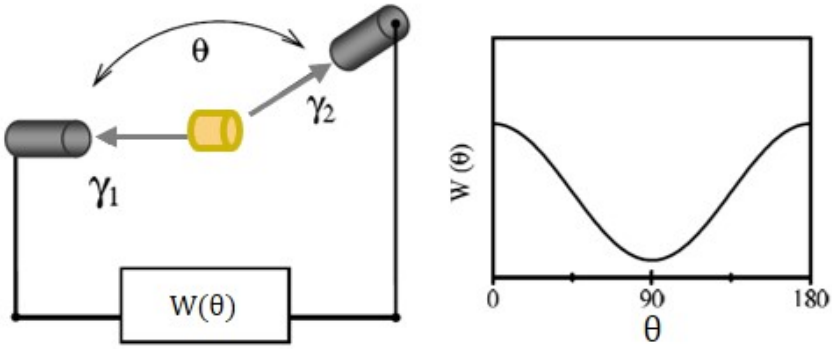

Figure 4.2: Experimental setup to measure the $\gamma - \gamma$ angular correlation, $W(\theta)$.

transition and $A_k(\gamma_2)$ depends only on the second, i.e., both only depend on the correspondent angular momentum of the involved levels and on the type and multipolarity of the emitted radiation (its values have been tabulated in [272]). P_k are the Legendre polynomials, which describe the spatial angular distributions of the emitted particles. With a system of two detectors mounted on a plane, one of them fixed and one movable, as shown in Figure 4.2, it is possible to measure experimentally the angular correlations of one emission pattern, for γ-photons or other type of emitted particles [260].

Admitting that the involved interactions are only genuinely of the dipolar or quadrupolar type, knowing that in an electromagnetic transition the parity is conserved, only even terms in k are obtained and for this reason Equation 4.25 can be written as:

$$W(\theta) = 1 + A_{22}P_2cos(\theta) + A_{44}P_4cos(\theta) \tag{4.27}$$

4.2.2 Perturbed angular correlation

The description presented in the previous section was made for the free nuclei in the absence of extra-nuclear fields. However, when the radioactive nuclei are in the material, the nuclear moment of the intermediate state of the cascade interact with those fields, disturbing the angular distribution of the second γ-ray, because the interaction could cause a substantial repopulation or phase change of the correspondent m sublevel. In the time interval t elapsed between the emissions of the first photon, γ_1, and the second photon, γ_2, corresponding with the time the nucleus remains at the intermediate state, it occurs that, transitions on different

sublevels ($m - m'$ transitions) and, consequently, the emission probability of γ_2, in a certain direction, becomes time dependent [259]. The intermediate state has a characteristic mean lifetime, τ, and for the nuclei under the influence of hyperfine interactions the repopulations or state transitions occur before the emission of the second photon. Mathematically, that is considered by the perturbation factor which introduces the changes in the occupancy of the m sublevels of the intermediate state during the time interval t, when their repopulation occurs.

At this point, it should be introduced the density operator $\hat{\rho}(\boldsymbol{k}_1)$ which represents the system immediately after the emission of γ_1 (when $t = 0$), based on the *Liouville-von Neumann* equation [259, 260]:

$$\frac{d\hat{\rho}(\boldsymbol{k}_1, t)}{dt} = -\frac{i}{\hbar}\Big[\hat{H}, \hat{\rho}(\boldsymbol{k}_1, t)\Big] \tag{4.28}$$

where $\hat{H}$ is the Hamiltonian of the system which describes the interaction of the extranuclear fields with nuclear moments. For a static Hamiltonian, the density operator is then given by:

$$\hat{\rho}(\boldsymbol{k}_1, t) = \hat{\Lambda}(t)\hat{\rho}(k_1)\hat{\Lambda}^{\dagger}(t) \tag{4.29}$$

Taking into account the time-evolution operator $\hat{\Lambda}(t)$:

$$\hat{\Lambda}(t) = e^{-\frac{i}{\hbar}\hat{H}t} \tag{4.30}$$

the angular correlation function considering the influence of the perturbation in the intermediate state is given by:

$$W(\boldsymbol{k}_1, \boldsymbol{k}_2, t) = Tr\{\hat{\rho}(\boldsymbol{k}_1, t), \hat{\rho}(\boldsymbol{k}_2)\} = Tr\{\hat{\Lambda}(t)\hat{\rho}(\boldsymbol{k}_1)\hat{\Lambda}^{\dagger}(t), \hat{\rho}(\boldsymbol{k}_2)\} \tag{4.31}$$

After elaborate and lengthy calculation, one obtains the following rigorous form for the time dependent $\gamma - \gamma$ angular correlation [271]:

$$W(\boldsymbol{k}_1, \boldsymbol{k}_2, t) = \sum_{k_1, k_2, N_1, N_2} A_{k_1}(\gamma_1) A_{k_2}(\gamma_2) \frac{Y_{k_1}^{N_1}(\theta_1, \phi_1) Y_{k_2}^{N_2}(\theta_2, \phi_2)}{\sqrt{(2k_1 + 1)(2k_2 + 1)}} G_{k_1 k_2}^{N_1 N_2} \tag{4.32}$$

where $A_{k_i}(\gamma_i)$ are the anisotropy terms described above and $Y_{k_i}^{N_i}(\theta, \phi)$ are the spherical harmonics with directions defined by the angles θ and ϕ. The term $G_{k_1 k_2}^{N_1 N_2}$ is the perturbation factor and has the information about the hyperfine fields and depends only on the interaction of the intermediate nuclear state with its environment, having no relation with nuclear transitions. The perturbation

factor can be expressed in terms of $3j$ *symbols*, by [259, 260, 267]:

$$G_{k_1k_2}^{N_1N_2(t)} = \sum_{M_a,M_b} (-)^{2I+m_a+mb}\sqrt{(2k_1+1)(2k_2+1)} \begin{bmatrix} I & I & k_1 \\ m'_a & -m_a & N_1 \end{bmatrix} \begin{bmatrix} I & I & k_2 \\ m'_b & -m_b & N_2 \end{bmatrix} \langle m_b|\,\hat{\Lambda}(t)\,|m_a\rangle \langle m'_b|\,\hat{\Lambda}(t)\,|m'_a\rangle^* \tag{4.33}$$

The k_i are restricted to $k_i = 0, 2, \ldots, \text{Min}(2I, l_i + l'_i)$ with $i = 1, 2$. The N_i are restricted to $|N_i| \leq k_i$. $m_{a,b}$ and $m'_{a,b}$ refers the m quantum numbers of the intermediate state defined by the rule $|m_{a,b}| \leq I$ and $|m'_{a,b}| \leq m_{a,b} - N_i$. Note that Equation 4.33 reduces to Equation 4.25 in the limit of vanishing perturbation [259, 260, 267].

The perturbed angular correlation function depends on the crystalline nature of the radioactive ion source and can be obtained in a very simplified form when the sample in study is a polycrystal. In this situation, the $W(\boldsymbol{k}_1, \boldsymbol{k}_2, t)$ is calculated by averaging the angular correlation over all possible orientations of the EFG and/or MHF because only the relative angles θ between the two consecutive γ_1 and γ_2, are of importance. On the other hand, if the Hamiltonian is static and diagonal, as for the magnetic interactions with the magnetic field along the quantization axis or axially symmetric quadrupole interactions, the matrix elements of the time evolution operator can be expressed by [267]:

$$\langle m_b|\,\hat{\Lambda}(t)\,|m_a\rangle = \langle m_b|\,e^{-\frac{i}{\hbar}\hat{H}t}\,|m_a\rangle = e^{-\frac{i}{\hbar}E_m(t)}\delta_{m,m_a}\delta_{m,m_b} \tag{4.34}$$

and Equation 4.32 becomes:

$$W(\theta, t) = \sum_{k}^{k=k_{max}} A_{k_1}(\gamma_1)A_{k_2}(\gamma_2)G_{kk}(t)P_k cos(\theta) \tag{4.35}$$

and using the relation 4.34 the perturbation function writes:

$$G_{kk}(t) = \sum_{M,M'} \begin{bmatrix} I & I & k \\ m' & -m & m-m' \end{bmatrix}^2 e^{-\frac{i}{\hbar}(E_m - E_{m'})t} \tag{4.36}$$

The $G_{kk}(t)$ retains information on the energy splitting $(E_m - E_{m'})$ of the involved m sublevels of the intermediate state due to the magnetic dipolar and electric quadrupole interactions. Therefore, it is possible to measure the hyperfine fields from a perturbed angular correlation experiment.

4.2.3 Data Analysis

All information concerning hyperfine interactions is contained in the perturbation function $G_{kk}(t)$ described by Equation 4.36. The perturbation function is

experimentally obtained from the coincidence count rates, $N(\theta, t)$, as a function of the time delay between the emission of γ_1 and γ_2, at a fixed detector angle, θ. A PAC experimental setup consists of a group of detectors geometrically arranged in such a way that each pair of detectors has the angle 90° or 180° between them. If a certain γ-ray, with energy E_{γ_1}, is detected by the detector i a clock starts counting. Then, after a certain time a second γ-ray, will reach one of the other detectors, j. If this second γ-ray has the expected energy, E_{γ_2}, the clock will stop and this event is counted and stored in the coincidence counter of the (i, j) pair of detectors. Based on that, and taking into account the exponencial decay of the nucleus the coincidence count rate of any pair of detectors (i, j) is given by [259]:

$$N_{ij}(\theta, t) = N_0 e^{-t/\tau} W(\theta, t) + B \tag{4.37}$$

where θ is the angle between the pair of detectors (i, j) and $t = t_{\gamma_2} - t_{\gamma_1}$ refers to the time delay between detection of the two γ-rays. N_0 is proportional to the number of radioactive nuclei in the sample. $W(\theta, t)$, given by Equation 4.35, is the perturbed angular correlation. τ is the mean lifetime of the probing state and B is proportional to the chance coincidence rate of γ-rays emmited from different nuclei, which is time independent. Once the coincidence histograms is obtained between different combinations of detectors, an appropriate experimental perturbation function, $R_{exp}(t)$, should be constructed reproducing all the relevant information. Depending on the type of the setup, several spectra, usually taken for $\theta = 90°$ and $\theta = 180°$, are combined in order to eliminate the exponential decay. From the experimental results, the $R_{exp}(t)$ function is obtained from [259]:

$$R_{exp}(t) = 2\frac{N(180°, t) - N(90°, t)}{N(180°, t) + 2N(90°, t)} \tag{4.38}$$

where $N(\theta, t)$ is calculated by appropriate averaging $N(\theta, t) = \sqrt[N_\theta]{\Pi_{ij} N_{ij}(\theta, t)}$ [273] for correction of different detector's efficiencies, after the random coincidence background (B) subtraction. Here N_θ is the total number of spectra at a certain angle, e.g., for a 6-detector spectrometer there are 6 combination at 180 ∘ and 24 at 90 ∘.

The $R_{exp}(t)$ function is the best way to get the information about the hyperfine interaction since it gives relevance to the perturbation function $G_{kk}(t)$, which contains all information. Note that Equation 4.38 eliminates the exponential component due the half-life contribution of the intermediate state of the cascade [273].

To extract the quantitative information from the $R(t)$ experimental function a theoretical fit, $R_{fit}(t)$, is performed. The theorectical function $R_{fit}(t)$ is

calculated numerically using the support of the full Hamiltonian for the nuclear electric quadrupole and/or magnetic dipole hyperfine interactions. The needed calculation of the eigenvalues and eigenstates of this full Hamiltonian is carried out using a computer software [274]. Considering the finite time, the resolution of the PAC setup the perturbation factor G_{kk} is corrected by multiplying each frequency term in the sum by $P(F^*_{whm},w_n)=e^{-\frac{w_n^2 F^{*2}_{whm}}{16ln2}}$, where F^*_{whm} is the full-width half-maximum associated with the time resolution distribution function of the spectrometer. Additionally, possible EFG distributions are taken into account by multiplying the G_{kk} terms by the distribution's Fourier transform $D(F^*_{whm},t)$:

$$G'_{kk}(t) = \sum_n s_{kn} cos(w_n t) D(F^*_{whm},t) P(F^*_{whm},w_n) \tag{4.39}$$

The corresponding perturbed angular correlation function $W'(\theta,t)$ is then obtained for $\theta = 90°$ and $\theta = 180°$ and the function whose parameters are changed during the fit, is constructed as:

$$R_{fit}(t) = 2\frac{W'(180°,t) - W'(90°,t)}{W'(180°,t) + 2W'(90°,t)} \tag{4.40}$$

Commonly different fractions of probes can interact with distinct EFG and/or MHF and the effective fit function should be written as:

$$\bar{W}'(\theta,t) = \sum_i f_i W'_i(\theta,t) \tag{4.41}$$

where f_i (with $\sum f_i = 1$) are the relative intensies of each $W'_i(\theta,t)$ angular correlation function characterizing the *ith* fraction of probe atoms interacting with a particular EFG/MHF. Particularly, for an electric interaction data analysis PAC allows to characterize the electric field gradient tensor principal component, V_{zz}, and the asymmetry paramter, η, which were already previously described. The EFG can be understood as an observable that depends on the charge density and its local symmetry in the vicinity of the probing nuclei, characterized as a highly sensitive method to the electric bonds, lattice site and position, defects and electronic phase transitions.

4.3 ISOLDE: isotope production facilities

To perform local probe measurements by using PAC technique, with the necessary radioactive isotopes with short lifetimes (< day), an on-line production facility is needed. The ISOLDE facility [275], located at the Meyrin site of

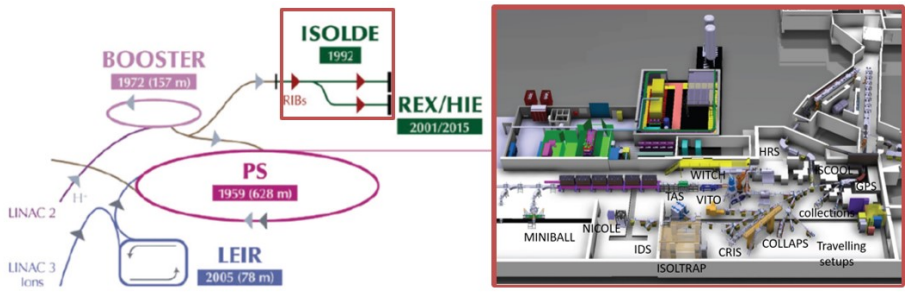

Figure 4.3: Overview of CERN accelerators and ISOLDE hall layout with GPS and HRS separators.

CERN and supported by the ISOLDE collaboration, is identified as the world reference of Isotope Separator On-Line (ISOL) facility [276].

ISOLDE has been part of CERN (European Organization for Nuclear Research) accelerator complex opperating from 1964. Since 1992, protons are delivered from CERN's Synchrotron Booster (PSB) to the ISOLDE targets for isotope production, in the beginning with 1 GeV, and from 1999, upgraded to 1.4 GeV with 2 μA of intensity [275, 277]. Currently, ISOLDE uses around 50% of all CERN protons, and accommodates more than 450 scientific users in almost 100 experiments. The facility runs 24 hours per day, around 8 months each year, only with technical stops during the winter period for upgrades and maintenance [278].

ISOLDE is dedicated to the production of a large number of radioactive ion beams for many different experiments in the fields of nuclear, atomic, condensed matter physics, and biophysics. At ISOLDE, isotopes are produced by spallation, fission, or fragmentation reactions via irradiation of an appropriate target by the 1.4 GeV - 2.4 μs proton beam pulses [277]. The structure of the targets, which supplies the radioactive beam, is essentially a tantalum tube filled with material that consists of the physical target with a length from 10 cm to 20 cm and 10 mm to 20 mm in diameter, allowing the passage of the primary proton beam along the axis. The target is heated up to 2200 °C due to the Joule effect by the passage of a current of few hundred Amperes at the tantalum container. The nuclear reaction products are released from the interior zone of the target to the surface and effuse to the transfer line tube [279]. The cilindrical tube that works as a transfer line has a hole in the center that allows to connect the transfer line to the ion source. There are different kinds of ion sources available (surface, plasma, lasers). The resonant ionization laser ion source (RILIS) [280] has high capacity of selectivity providing very pure elemental beams. The target

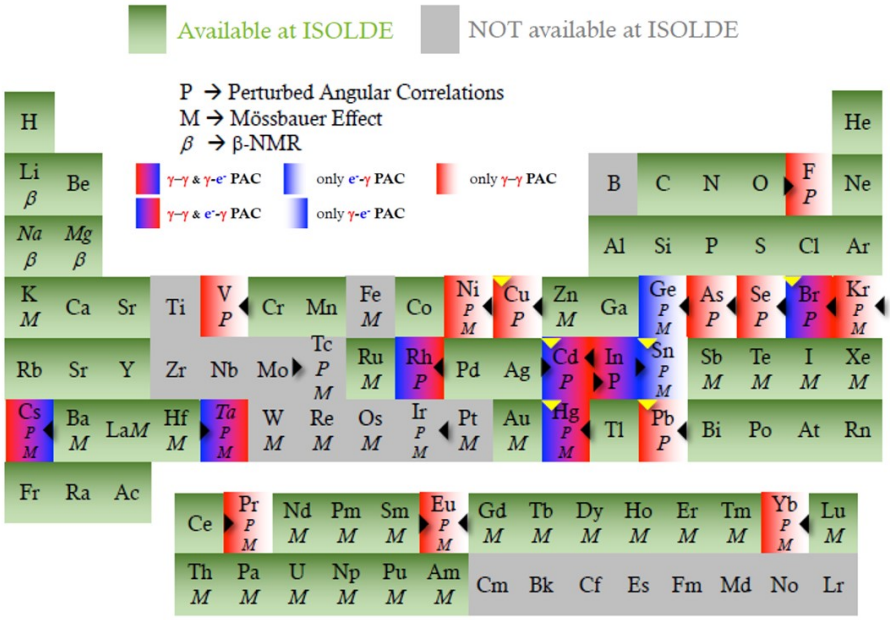

Figure 4.4: Periodic table showing the elements produced at ISOLDE (light green). In the figure are represented also the elements for which suitable isotopes exist for solid-state experiments in particular possible PAC probe-elements.

chambers are handled and changed by mobile robots due to the high level of radiation in the zone.

After ionization and acceleration in the target front-ends, the radioactive ion beam is magnetically mass-separated via the two isotope separators on-line: the General Purpose Separator (GPS) and the High Resolution Separator (HRS). The GPS has a bending magnet and an electrostatic switchyard letting the simultaneous delivery of three different mass-separated beams, while the HRS has two bending magnets delivering one single ion beam with better mass resolution [277]. Two GPS beam lines, GLM and GHM (low mass and high mass beam line respectivelly), are used for solid state physics group. Figure 4.3 shows the layout of the ISOLDE facilities evidencing the main areas in the hall.

Presently, ISOLDE can deliver more than 70 elements and 1000 isotopes, where some of those are suitable to use as probes for PAC spectroscopy as shown in Figure 4.4.

4.4 Experimental setup and procedure

Solid state physics experiments at ISOLDE are usually performed at the GPS separator using one available implantation chamber, which is mounted at the end of GLM or GHM beam line. The control of the separator and beam line equipment is accomplished from the control room where computers and PC-consoles are installed, equipped with specific software that allows to access the hardware for control and management of the isotope collections.

4.4.1 Ion implantation

The first step to perform a PAC experiment requires collecting the desired isotope and bring it at contact or inside de material under study. However, before that, the optimization of the ion beam that will arrive in the implantation chamber is required. After pre-selection of the radioactive isotope in the mass control setup, this optimization is made by setting the parameters of the focusing. The vaccum conditions, in the beam line and in the implantation chambers, can be also monitored in the control-room as well as the valves of the beam line, accessed by the special controller. The implantation chambers are made of stainless steel to easily achieve relatively very low pressures ($< 10^{-6}$ mbar) and are equipped with collimators and appropriate sample holders. The collimator's aperture and sample holder position are controlled by a step-motor that is also operated remotely. During the process of the implantation, the ion beam can be swept in order to produce a homogeneous implanted area at the sample. The effective doses implanted (measured and monitorized on-line) are, in general, in between $10^{11} - 10^{12}$ at.cm^{-2} per sample. The profiles of the implantations can be calculated using the software TRIM [281] code (beam energy $20 - 60$ keV).

For bulk material, the samples are directly implanted, i.e. the sample mounted in the sample holder is bombarded with the radioactive beam ions. However, since graphene samples are two-dimensional crystals, the usual procedure of implantation is not appropriate. New kind of low energy implantation methods are being researched and developed, nevertheless, in this work, an alternative solution to place the isotopes on the surface of 2D material was found, without damaging to the sample and avoiding the introduction of isotopes in the substrate. This method analogous to the used for biophysics studies uses ultra pure water (UPW) as support material where the isotopes are firstly implemented and transfered to the graphene's samples. The samples consist of 0.2 ml frozen UPW sustained inside a teflon cup that is mounted on a cold-finger cooled by an external liquid nitrogen bath (biophysics chamber). Once the collection is finished the frozen UPW is transferred inside a glove box for the

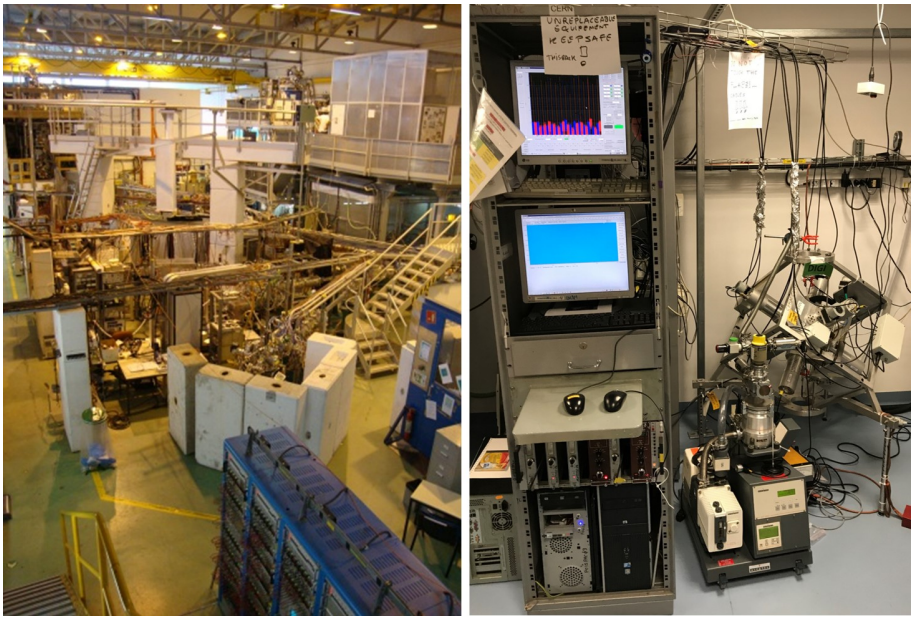

Figure 4.5: (Left) ISOLDE Hall. (Right) The PAC experimental setup equipped with 6 highly efficient detectors.

remaining manipulations. Inside the glove box, the radioactive ice is melted and transferred to wet the graphene sample, previously mounted on a hot plate to promote water evaporation.

Although several isotopes were used in the atomic local study of graphene using PAC spectroscopy (^{111}In, ^{111}Cd, ^{111}Ag), this thesis only concentrated the efforts on the analysis of the experimental results with ^{199m}Hg.

4.4.2 PAC measurement

After the ion implantation of the frozen UPW and then the transfer of the radioactive isotopes to graphene performed inside a cleaned glove-box, the graphene sample is then sealed inside an eppendorf and transferred to the measuring PAC setup. The activity of the radioactive isotopes that remains on the graphene sample are monitored with the contamination radiation detector. PAC measurements can be performed from 10 K up to 1300 K, in different atmospheres such as O_2, N_2 and Ar. All measurements here were performed

at a low temperature (from 10 K to room temperature), in which samples are mounted on a closed-cycle helium refrigerator equipped with resistive heater and PID temperature controller.

The PAC experimental setup consists of a six detectors spectrometer (38 mm diameter $\times$ 38 mm height La(Ce)Br_3 scintillators with 650 ps time resolution mounted on $XP2020URQ$ photomultipliers) arranged in a cube. Data acquisition is performed with the digital and FPGA (Field-programmable gate array) signal processing DIGIPAC setup [282–284]. This digital PAC machine maximize the information gain without loosing frequency resolution due to poor true to chance coincidence ratios. It suffices to set the energy windows, to specify the time range for coincidences, and to set the t0 offset. Therefore, FPGAs are used to create the time stamps, to produce detector tags, and to select the γ-energies. With these FPGAs it is, e.g., possible to implement digital filters, mathematical functions or data forwarding circuits [282].

Chapter 5

Establishing the first Cu isotope suitable for PAC experiments

This thesis is embedded in a wider effort to develop a new experimental approach at the ISOLDE facility at CERN, using the ASPIC setup (Apparatus for Surface Physics and Interfaces at CERN) to probe adatoms on 2-dimensional materials under ultra-high vacuum (UHV) conditions, using hyperfine techniques [285]. In ASPIC, a multitude of radioactive isotopes can be deposited and measured *in-situ* using perturbed angular correlation (PAC) spectroscopy [285]. In the particular context of this thesis, the need for *in-situ* operation under UHV is imposed by the goal of investigating the interaction between the adatoms and the 2-dimensional material without interference from other species such as oxygen or water present in atmosphere (objective (1) and (2)). On the other hand, *in-situ* operation also has the advantage of allowing to use isotopes with shorter half-lives compared to the more commonly used PAC probes (since the time between implantation or deposition and measurement is greatly decreased). In particular, this would allow to expand the range of adatom elements that can be probed at ASPIC. As a crucial step towards that goal, we successfully tested and established the first Cu isotope suitable for PAC experiments: ^{68m}Cu with an half-life of 3.75 minutes. These experiments are presented in this section (manuscript 1).

In the context of graphene research, Cu is the most widely employed catalyst due to its low cost and ease-of-use for obtaining graphene monolayers with reasonable

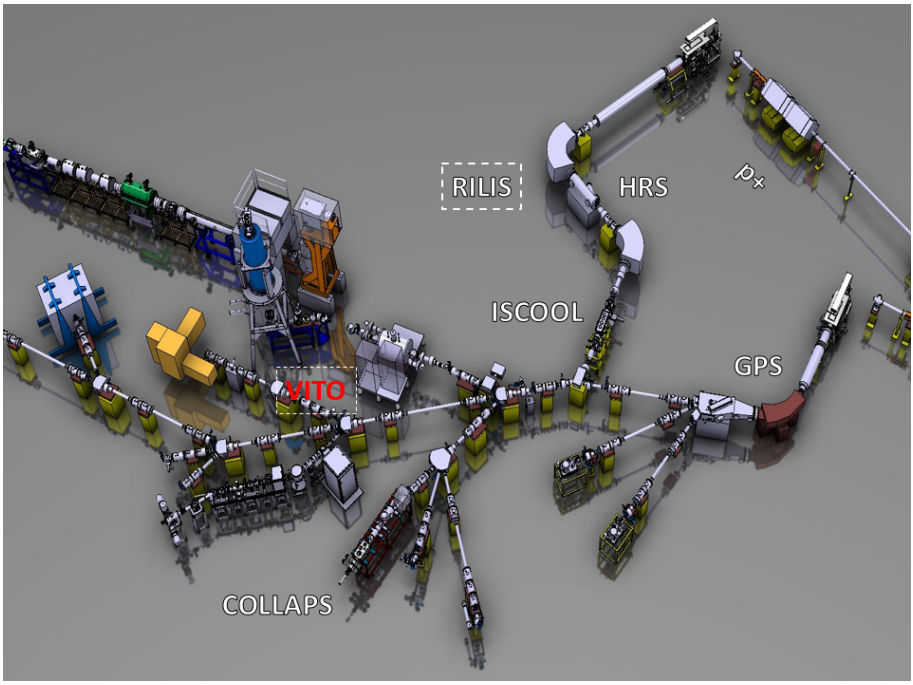

Figure 5.1: ISOLDE-CERN Facility Layout, including VITO beam line.

.

quality, with single crystalline graphene domains of several millimeters in size [286, 287]. Therefore, ^{68m}Cu PAC spectroscopy at ASPIC could potentially be used in the future to study the growth of graphene from the perspective of Cu atoms at the surface of the Cu foils or thin films (e.g. C nucleation at specific sites) and to investigate the influence of specific features of the Cu surface (structure, local defects etc.) on the graphene growth. In the broader context, this work establishes a suitable Cu probe for PAC for applications in a wide rage of fields, from solid state physics to chemistry, and biophysics.

Twenty nine copper isotopes are known, among which two are stable, ^{63}Cu and ^{65}Cu. From the remaining, ^{67}Cu with half-life of 61.83 hours and ^{54}Cu with half-life of approximately 75 ns are the most stable and fastest decaying isotopes, respectively. The other radioactive isotopes have half-lives from several tens of miliseconds to minutes. Seven isotopes have relatively long lived metastable sates, ^{62}Cu, ^{68}Cu, ^{69}Cu,^{70}Cu, ^{71}Cu, ^{72}Cu and ^{76}Cu [288]. The most stable of these is ^{68m}Cu with an half-life of 3.75 minutes, which today's availability is a practical result of the progressive development of on-line radioactive ion beam

facilities. The particular selection of $^{68m}Cu/^{68}Cu$ as the suitable Cu isotope for PAC was made taking into account the properties of the decay scheme, which include two gamma cascade ($\gamma - \gamma$), the parents and intermediate state life times, the intermediate state spin, the $\gamma - \gamma$ angular anisotropies and the yields that are available at ISOLDE facility. Perturbed angular correlation of γ-rays experiments were performed in 2015 for the first time in the decay ^{68m}Cu ($6^-, 721$ keV, 3.75 min). This work (manuscript 1), where we characterize the nuclear moments for this state, was published in 2016 in Europhysics Letters (EPL) and featured as an EPL highlight of 2016.

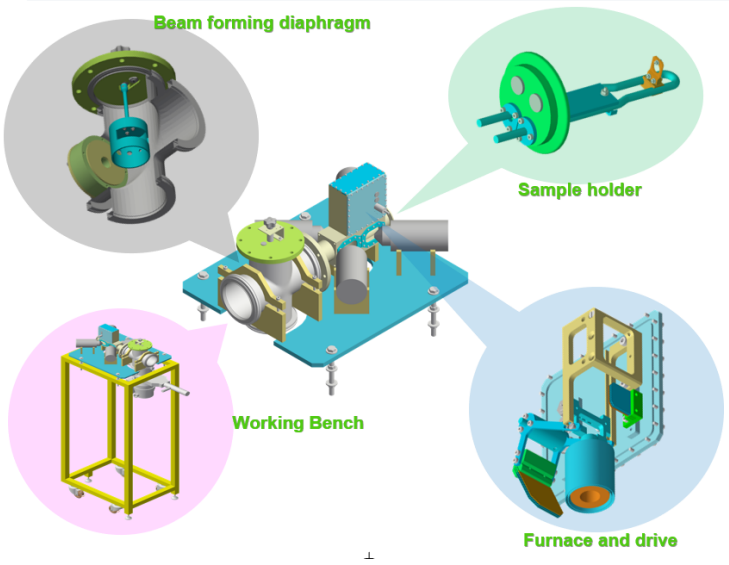

Figure 5.2: New *PAC Short Lived Isotope set-up* (PAC-SLI) designed by Prof. Manuel Ribeiro da Silva. The present design constitutes a compact and mobile setup, allowing it to be easily relocated within ISOLDE.

The experiments were performed at the VITO beam line at ISOLDE. VITO (Versatile Ion-polarized Techniques Online) consists of a modification of the previous UHV line and was installed permanently in the low-energy part of the ISOLDE hall as shown in figure 5.1. This new beam line opened up numerous possibilities for carrying out multidisciplinary studies in the areas of biophysics, nuclear and solid state physics, and fundamental interaction physics. Part of the work of construction and commissioning of VITO beam line, in which I actively participated in the context of this thesis (since the beam line hosts the ASPIC setup), is reported in reference [289].

Due to the short half-life of the ^{68m}Cu isotope, the implantation and PAC measurements were performed online in an experimental setup consisting of four $LaBr_3$ scintillator detectors in a perpendicular plane with respect to the ion beam. Motivated by the success of these experiments, we began the development of a more complex setup (*PAC Short Lived Isotope set-up*, PAC-SLI), which allows to cycle through different steps of ion implantation, data acquisition and thermal annealing (Figure 5.2), which in addition allows for easy and fast sample change, as well as continuous control of beam current and temperature.

5.1 Manuscript 1

A Letters Journal Exploring the Frontiers of Physics

September 2016

EPL, **115** (2016) 62002 www.epljournal.org
doi: 10.1209/0295-5075/115/62002

The ^{68m}Cu/^{68}Cu isotope as a new probe for hyperfine studies: The nuclear moments

A. S. Fenta[1,2,3], S. Pallada[3,4,5], J. G. Correia[3,6], M. Stachura[3,7], K. Johnston[3], A. Gottberg[3,7], A. Mokhles Gerami[8], J. Röder[3,9], H. Grawe[10], B. A. Brown[11], U. Köster[12], T. M. Mendonça[3], J. P. Ramos[3,13], B. A. Marsh[3], T. Day Goodacre[3,14], V. S. Amaral[1], L. M. C. Pereira[2], M. J. G. Borge[3] and H. Haas[1,3]

[1] *Department of Physics and CICECO, University of Aveiro - 3810-193 Aveiro, Portugal*
[2] *KU Leuven, Instituut voor Kern- en Stralingsfysica - Celestijnenlaan 200 D, 3001 Leuven, Belgium*
[3] *CERN, 1211 Geneva 23, Switzerland*
[4] *Department of Chemistry, Faculty of Science, University of Copenhagen - Universitetsparken 5, 2100 Copenhagen, Denmark*
[5] *Department of Medicine, Democritus University of Thrace, Alexandroupoli Campus 6 km Alexandroupolis-Makris, 68100 Alexandroupoli, Greece*
[6] *Centro de Ciências e Tecnologias Nucleares (C2TN), Instituto Superior Técnico, Universidade de Lisboa 2686-953 Sacavém, Portugal*
[7] *TRIUMF - 4004 Wesbrook Mall Vancouver, BC V6T 2A3, Canada*
[8] *Department of Physics, K.N.Toosi University of Technology - P.O.Box 15875-4416, Tehran, Iran*
[9] *Institute of Physical Chemistry, RWTH-Aachen - Aachen, Germany*
[10] *GSI Helmholtzzentrum für Schwerionenforschung GmbH - D-64291 Darmstadt, Germany*
[11] *National Superconducting Cyclotron Laboratory and Department of Physics and Astronomy, Michigan State University - East Lansing, MI 48824-1321, USA*
[12] *Institut Laue-Langevin - 71 avenue des Martyrs, F-38042 Grenoble, France*
[13] *Laboratory of Powder Technology, École Polytechnique Fédérale de Lausanne (EPFL) - CH-1015, Switzerland*
[14] *School of Physics and Astronomy, The University of Manchester - Manchester, M13 9PL, UK*

received 24 June 2016; accepted in final form 6 October 2016
published online 7 November 2016

PACS 21.10.Ky – Electromagnetic moments
PACS 23.20.En – Angular distribution and correlation measurements
PACS 21.60.Cs – Shell model

Abstract – Time Differential Perturbed Angular Correlation of γ-rays (TDPAC) experiments were performed for the first time in the decay of ^{68m}Cu ($6^-, 721\,\text{keV}, 3.75\,\text{min}$) produced at the ISOLDE facility at CERN. Due to the short half-life of the source isotope, the measurements were carried out online. The intermediate state ($2^+, 84.1\,\text{keV}, 7.84\,\text{ns}$) offers the unique opportunity to study the electromagnetic fields acting at a copper probe in condensed matter via hyperfine interactions. The present work allowed determination of the nuclear moments for this state. The electric quadrupole moment $|Q(2^+, 84.1\,\text{keV})| = 0.110(3)$ b was obtained from an experiment performed in Cu_2O and the magnetic dipole moment $|\mu| = 2.857(6)\,\mu_N$ from measurements in cobalt and nickel foils. The results are discussed in the framework of shell model calculations and the additivity rule for nuclear moments with respect to the robustness of the $N = 40$ sub-shell.

editor's choice Copyright © EPLA, 2016

Introduction. – Copper (Cu) in its native form is, reportedly, the first metal to be used by mankind, with mechanical, chemical and electronic properties that makes it, still today, a reference in human activities and welfare. Furthermore, Cu plays a key role in every life form [1] acting as a cofactor in metabolic enzymes, which are involved in cellular reparation, respiration or photosynthesis [2,3]. In living systems Cu is present in two oxidation states, Cu(I) and Cu(II), ruling electron transfer in vital redox mechanisms. Due to its unpaired electron

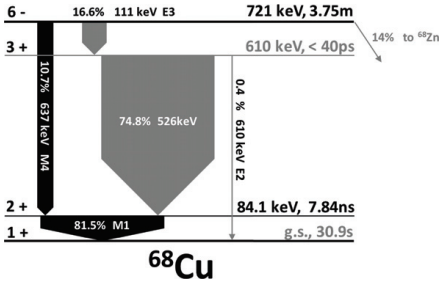

Fig. 1: Decay scheme of ^{68m}Cu/^{68}Cu. In black are the relevant gamma lines for the TDPAC experiment. Width and length of the arrows are proportional to intensity and energy, respectively.

and characteristic *d-d* transition absorption, Cu(II) is well studied with different spectroscopic methods [4], while Cu(I) is difficult to observe because of its closed shell (d^{10}) electronic structure leading to basically featureless spectroscopic properties. On the other hand, as a diamagnetic ion, Cu(I) can potentially be investigated by Nuclear Magnetic Resonance (NMR)/Nuclear Quadrupole Resonance (NQR) spectroscopy.

^{63}Cu and ^{65}Cu are stable isotopes which have been used very successfully in studies of bulk matter, notably recently the high-T_c superconductors. Such experiments, however, require a large amount of sample material and are often restricted to low temperatures. In biological systems, the use of the solution-phase NMR is often the method of choice for studying structure and dynamics at the metal binding sites. This technique has a very limited application to Cu(I) containing complexes, due to the large nuclear quadrupole moments of ^{63}Cu and ^{65}Cu NMR nuclei and their low gyromagnetic ratios. These cause low sensitivity and broad resonance lines [5–7]. Therefore, there is considerable interest in searching for other techniques, which have potential for characterizing the Cu(I) binding structure and electronic states in diluted concentrations of the probing isotope in biological and solid-state materials. A practical solution can be given by radioactive hyperfine techniques, such as Mössbauer spectroscopy (MS) or Time-Differential Perturbed Angular Correlation (TDPAC) [8–10]. These are sensitive to the interaction of the nuclear electric quadrupole and/or magnetic dipole moments with the electric field gradients (EFG) or the magnetic hyperfine fields (B_{hf}) generated by the external charge distribution and polarization of the host material [11]. Unfortunately, no copper isotope is available for MS experiments. By looking at the decay schemes of Cu isotopes, one finds that ^{68m}Cu with a half-life of 3.75 minutes and its decay cascade (shown in fig. 1) appears as the best TDPAC candidate to be used as a copper probe for future applications in the fields of materials physics, chemistry and biophysics. The selection of the ^{68m}Cu/^{68}Cu isomeric decay was made considering several favorable properties: a) a cascade with suitable gamma-ray energies 637 keV and 84 keV; b) an intermediate 2^+ state with 7.84 ns half-life c) a high expected angular anisotropy factor of 15%. The latter is easily measurable and defines the maximum observable amplitude of the TDPAC perturbation function. Moreover, a TDPAC cascade with a starting isomeric parent state is particularly useful, since perturbations due the electronic rearrangement following a chemical valence change after electron capture or beta decay are avoided.

The half-life of 3.75 minutes is short, but it can still allow post-implantation sample conditioning and data taking. The hyperfine interactions are measured consequently at the intermediate state (2^+, 84.1 keV, 7.84 ns). Last but not least, the current ^{68m}Cu yields available at the ISOLDE facility [12,13], when combined with an efficient detection system with good energy and time resolution, made these experiments possible.

Herein, we report the first TDPAC experiment performed on a Cu isotope, which simultaneously provided the first measurement of the nuclear electric quadrupole and magnetic dipole moments of the (2^+, 84.1 keV, 7.84 ns) state of ^{68}Cu, obtained in the isomeric decay of ^{68m}Cu. From the nuclear physics point of view these data are of particular interest, because in the empirical shell model the 1^+ ground state (*g.s.*) and the 2^+ isomer in ^{68}Cu are assumed to form a $\pi p_{3/2} \times \nu p_{1/2}^{-1}$ doublet relative to $Z = 28$, $N = 40$ ^{68}Ni. Nuclear moments are known for the g.s. and the ^{68m}Cu, 6^- isomer [14]. The present values for the 2^+ isomer doublet partner complete this information on the robustness of the $N = 40$ sub-shell closure.

Experiment. – The ^{68m}Cu$^+$ ion beam was produced online at ISOLDE by the bombardment of a UC$_x$ target with the 1.4 GeV proton beam from the CERN Proton Synchrotron Booster and selective Cu ionization using the RILIS (Resonance Ionization Laser Ion Source) [15,16]. The target/ion source parameters were optimized to enhance ^{68m}Cu/^{68}Cu and suppress surface ionized ^{68}Ga such that [Cu]/[Ga] $\approx$ 80. The pure ^{68}Cu beam with 30 keV energy was then redirected to the VITO (Versatile Ion-polarized Techniques Online) [17] beam line where a sample holder was mounted inside a quartz finger collection chamber with 2 mm wall thickness. This minimized the gamma absorption and allowed direct view to the sample. The TDPAC set-up mounted online consisted of four $LaBr_3$ gamma detectors with good energy resolution (11.6% at 84.1 keV and 3.0% at 637 keV) and time resolution of 800 ps for the selected cascade. Data acquisition was performed with the digital and FPGA signal processing DIGIPAC setup [18–20]. The detectors were positioned in a plane perpendicular to the direction of the radioactive beam, each detector placed at $\pm 90°$ and $180°$ with respect to the others, as shown in fig. 2. The samples were placed in the geometrical center of the setup. Implantation and measurement were performed simultaneously

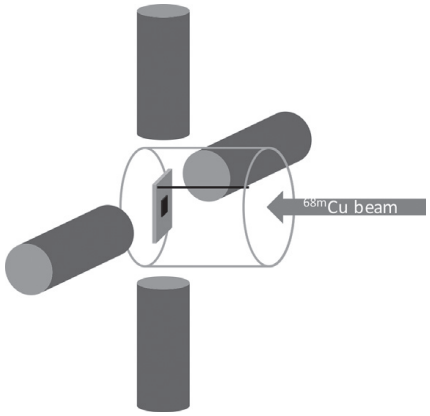

Fig. 2: Scheme of the experimental PAC set-up online at ISOLDE. The quartz finger (transparent cylinder in the center) and the four cylindrical $LaBr_3$ detectors (38 mm diameter, 38 mm length) surrounding it are shown.

at room temperature. The maximum beam intensity delivered at the sample position for ^{68}Cu in isomeric and ground state was 5×10^7 atoms/s. However, an effective lower beam intensity of about 1×10^7 atoms/s was maintained to avoid gamma pile-up saturation of the detectors, keeping a reasonable 50 kHz count rate per detector. Depending on the sample and beam conditions the data were acquired from two to four hours per sample, achieving a maximum of $2{\times}10^{11}$ implanted atoms, with an estimated dose not greater than 10^{12} at/cm^2 per sample.

Analysis. – For nuclei implanted into a polycrystalline host material, the angular probability distribution, $W(\theta)$, of finding γ_1-γ_2 emitted with a certain angle θ can be expanded into a Legendre polynomial series $P_k(\cos\theta)$ as [9,10]

$$W(\theta) = \sum_k A_{kk}\,(\gamma_1,\gamma_2)\,G_{kk}\,(t)\,P_k\,(\cos\,(\theta)); \qquad (1)$$

A_{kk} are the anisotropy coefficients of the γ-γ cascade. $G_{kk}(t)$ is the perturbation factor that contains all the information about the magnetic dipole and/or the electric quadrupole interactions. The TDPAC setup measures the number of γ_1-γ_2 coincidences, $N_{ij}(\theta,t)$, as a function of time t between detection of γ_1 and γ_2 for every pair of detectors (i,j). Then, the random coincidences are subtracted and the multiple spectra are combined correcting for efficiencies and sample misalignment in two single spectra $N(180°,t)$ and $N(90°,t)$. These are used to build the experimental perturbation function, $R(t)$, eliminating the exponential part of $N(\theta,t)$ and revealing the perturbation function to be analyzed [9,10]:

$$R\,(t) = 2\frac{N\,(180°,t) - N\,(90°,t)}{N\,(180°,t) + 2N\,(90°,t)}. \qquad (2)$$

For the geometry chosen here $R(t)$ is simply a sum of cosine functions of the quadrupole or magnetic interaction frequencies. Our analysis used the previously known electric field gradients and magnetic fields for copper in the selected materials, in order to extract the nuclear electric quadrupole moment, Q, as well as the nuclear magnetic dipole moment, μ, of the 2^+ state in ^{68}Cu.

In the case of integer spin I and axial symmetry of the EFG, $\eta = 0$, the quadrupole coupling constant, ν_Q, is directly related to the quadrupole moment, Q, and to the observable frequency, ω_0, by the expression

$$\nu_Q = \frac{eQV_{zz}}{h} = \omega_0\frac{2I\,(2I-1)}{3\pi}, \qquad (3)$$

where V_{zz} is the principal component of the EFG tensor at the nuclear site [9,10].

In a similar way, the magnetic dipole moment can be obtained from the precession frequency, ω_L, of the magnetic moment in the magnetic hyperfine field, B_{hf}, as given by the Larmor equation:

$$\omega_L = \mu B_{hf}/I\hbar = g\mu_N B_{hf}/\hbar, \qquad (4)$$

where μ is the magnetic dipole moment of the intermediate state of the probe nuclei and g the dimensionless g-factor.

The analysis of the observable perturbation function, $R(t)$, depends on several factors such as the time resolution of the experimental apparatus and the probing state lifetime that determines the observable frequencies, the latter being proportional to the product of the hyperfine fields and nuclear moments.

Results. – Figure 3 illustrates the $R(t)$ experimental perturbation functions obtained for 3a) ^{68}Cu in Cu_2O, 3b) ^{68}Cu in Co and 3c) ^{68}Cu in Ni. All the fits to the experimental data were performed assuming a solid angle corrected, effective anisotropy coefficient $A_{22}^{eff} = -0.13(1)$ for the angular correlation of the γ_1(637 keV)-γ_2(84 keV) cascade with theoretical values expected for this cascade $A_{22} = -0.1545$ and $A_{44} = 0$ [21,22]. For the data fitting procedure, we refer the readers to [23,24] and references therein. When there is evidence for multiple sets of nuclei interacting with different local environments the fit function considers a summation of $G_i(t)$, describing each perturbation factor, weighted by the respective fraction of nuclei, f_i, where $\sum f_i = 1$.

Copper oxide, Cu_2O, known as cuprite, was chosen to measure the nuclear quadrupole interaction and determine the quadrupole moment, Q, of the ^{68}Cu, 2^+ excited state. Cuprite has a simple cubic structure, in which oxygen is tetrahedrally coordinated by copper atoms, while copper is linearly coordinated by two oxygen atoms. Due to this low coordination of Cu, this site has a non-cubic point symmetry and a strong EFG with zero asymmetry parameter, $\eta = 0$. The fitting of the experimental perturbation function $R(t)$ (fig. 3(a)) shows a predominant fraction of 89(3)% of ^{68}Cu with a characteristic quadrupole frequency $\omega_0 = 21.3(3)$ Mrad/s and $\eta = 0$. For spin 2, the respective

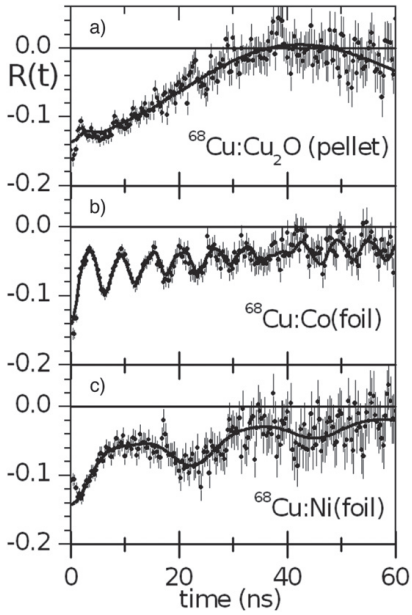

Fig. 3: The $R(t)$ function obtained from the decay of ^{68m}Cu implanted in different host materials: a) Cu_2O (pellet), b) Co (foil), c) Ni (foil).

quadrupole coupling constant is $\nu_Q = 27.14(44)$ MHz. Knowing ν_Q and using the quadrupole coupling constant $\nu_Q(^{65}\mathrm{Cu}, \mathrm{g.s.}, 3/2) = 48.138(12)$ MHz for ^{65}Cu nuclei in Cu_2O obtained by nuclear quadrupole resonance (NQR) measurements [25] the ratio of the quadrupole coupling constants is obtained. With the quadrupole moment $Q(^{65}\mathrm{Cu}, 3/2^+) = -0.195(4)$ b [14] the absolute value for the quadrupole moment of the ^{68}Cu, 2^+ state is calculated to be $|Q(^{68}\mathrm{Cu}, 2^+, 84.1\,\mathrm{keV})| = 0.110(3)$ b.

To measure the magnetic hyperfine interaction, cobalt and nickel sample hosts were implanted with ^{68m}Cu. Figure 3(b) shows the experimental $R(t)$ function obtained for ^{68m}Cu in a cobalt foil. Three different fractions (f) of Cu nuclei interacting with different local environments have been identified ($f_1 = 22(1)\%$, $f_2 = 32(1)\%$ and $f_3 = 46(2)\%$). Even though the present measurements were performed without an external applied field, the $R(t)$ function is not typical for a random distribution of fields in the foil, as expected for a polycrystalline-like sample. Instead, the $R(t)$ function revealed a preferred orientation of the magnetization along the foil surface, within the detector plane, around 45 degrees in-between detectors. This is presumably due to the rolling process during manufacture and shape anisotropy of the foil.

The analysis of the $f_3 = 46(2)\%$ fraction, resulting in the slowly decaying component of the spectrum, is not compatible with the hyperfine fields expected for Cu in the cobalt host. Apparently, a fraction of the nuclei was implanted into the aluminium sample holder, due to a non-optimal beam focusing. The $f_2 = 32(1)\%$ fraction is assigned to ^{68}Cu interacting with non-identified point defects created during room temperature implantation in the Co foil. The remaining $f_1 = 22(1)\%$ fraction of atoms on unperturbed lattice sites of the Co hcp lattice interact with a strong magnetic field, producing a very clear spectrum from which one obtains the magnetic precession frequency $\omega_L = 1079.1(34)$ Mrad/s.

Table 1: Experimental parameters obtained from fitting the $R(t)$ function. Only relevant parameters for the calculation of the nuclear moments are shown.

	A_{22}^{eff}	f_1 (%)	ω_0 (Mrad/s)	ω_L (Mrad/s)
Cu_2O	−0.13(1)	89	21.3(4)	–
Co	−0.13(1)	22	–	1079.1(34)
Ni	−0.13(1)	44	–	273.7(48)

Table 2: Nuclear moments of the ^{68}Cu(2^+, 84.1 keV) state calculated with the experimental data obtained in this work. Previously measured and extrapolated hyperfine fields as explained in the text have been used.

	$\lvert Q\rvert$ (b)	$\lvert g\rvert$	$\lvert\mu\ (\mu_N)\rvert$
Cu_2O	0.110(3)	–	–
Co	–	1.429(6)	2.859(13)
Ni	–	1.402(43)	2.804(85)
	0.110(3)	1.429(6)	2.857(6)

As reference, one has the precise magnetic frequencies values from previous nuclear magnetic resonance (NMR) measurements for ^{63}Cu in Co, $\omega_L = 1117.8(3)$ Mrad/s, and for ^{65}Cu in Co, $\omega_L = 1198.2(3)$ Mrad/s [26]. Since the magnetic hyperfine field is independent of the Cu isotope embedded in Co, by using the g factor for ^{63}Cu and ^{65}Cu ($g = 1.480(0)$, $g = 1.580(5)$) [27], and eq. (4), one computes $g = g_i\omega_L/\omega_{Li}$, where ω_L is the value obtained in this work for the 2^+, 84.1 keV of ^{68}Cu, and the index i refers to each ^{63}Cu or ^{65}Cu parameters. Two slightly different values for the g factor of the ^{68}Cu, 2^+ state are obtained, which were averaged leading to $|g(2^+, 84.1\,\mathrm{keV})| = 1.429(6)$. Note that the magnetic frequencies ω_L mentioned above from ref. [26] were obtained by nuclear magnetic resonance (NMR) measurements at a temperature of 282 K. The small difference in temperature between the NMR (282 K) and the current TDPAC measurements (295 K) is irrelevant, since the expected hyperfine field changes in Co are smaller than 0.2%. Finally, the absolute value for the magnetic dipole moment of the ^{68}Cu, 2^+ state is determined to be $|\mu(2^+, 84.1\,\mathrm{keV})| = 2.859(13)\,\mu_\mathrm{N}$.

Figure 3(c) shows complementary TDPAC measurements obtained for ^{68m}Cu implanted in a nickel foil. A similar spectrum analysis to the Co case was made,

Table 3: Experimental, additivity extrapolated and shell model g factors and quadrupole moments.

	Experiment[a]			Additivity		Shell model[b]	
	I	g	Q (b)	g	Q (b)	g	Q (b)
^{69}Cu	$3/2^-$	1.8922(7)	−0.147(16)			1.854	−0.1547
^{67}Cu	$3/2^-$	1.6761(4)	−0.174(8)			1.784	−0.1875
^{68}Cu	1^+	2.3933(6)	−0.082(13)	1.930	−0.080(3)	2.367	−0.0945
						2.057[c]	−0.084[c]
	2^+	**(+)1.429(6)**	**(−)0.110(3)**	1.639	−0.160(6)	1.173	−0.190
						1.581[c]	−0.168[c]
	6^-	0.1925(1)	−0.44(2)	0.380		0.254	−0.358
						0.241[c]	−0.474[c]
^{67}Ni	$1/2^-$	1.202(5)				0.874	
	$9/2^+$	−0.125(6)				−0.283	−0.250

[a] Present work (bold) and refs. [14,28].

[b] $\pi\nu pf_{5/2}g_{9/2}$ model space with jj44b interaction; $e^\pi = 1.5\ e$, $e^\nu = 1.1\ e$ and $g_s^\nu = 0.7\ g_s^{free}$ [29].

[c] Inferred from ^{67,69}Cu , ^{67}Ni shell model by additivity.

reveiling that the $R(t)$ function can be described by only two fractions of Cu nuclei in different environments. Again, a slow frequency component is present, $f_2 = 56(3)\%$ of Cu atoms which have landed in the aluminium sample holder. Nonetheless, $f_1 = 44(2)\%$ of the Cu nuclei interact with a well-defined magnetic field, characterized by a magnetic precession frequency $\omega_L = 273.7(48)$ Mrad/s.

As reference, one has the magnetic hyperfine field obtained in [30] $B_{hf} = -4.7(1)$ T at 4 K. This value was then rescaled to 105 K using the magnetization saturation curve of [31], obtaining $B_{hf} = -4.6(1)$ T. A final extrapolation of the hyperfine magnetic field was performed to 304 K using the time differential perturbed angular distribution (TDPAD) measurements for ^{62}Cu in Ni [32]. From that work the magnetic frequencies, at 105 K and 304 K, were graphically extracted, $\omega_L = 153.8(17)$ Mrad/s and $\omega_L = 135.5(10)$ Mrad/s, respectively. One calculates the final extrapolated field $B_{hf} = -4.08(10)$ T. With the present experimental frequency, $\omega_L = 273.7(48)$ Mrad/s one obtains $|g(2^+, 84.1\,\mathrm{keV})| = 1.402(43)$. The magnetic dipole moment is determined as $|\mu(2^+, 84.1\,\mathrm{keV})| = 2.804(85)\,\mu_\mathrm{N}$.

From the two independent crosscheck experiments using cobalt ($\mu = 2.859(13)\,\mu_\mathrm{N}$) and nickel ($\mu = 2.804(85)\,\mu_\mathrm{N}$) hosts, the average (error weighted) value of $\mu = 2.857(6)\,\mu_\mathrm{N}$ has been adopted. Tables 1 and 2 summarize the relevant experimental parameters obtained in the present work and the calculated nuclear quadrupole and magnetic moments.

Discussion. – When preparing the present experiment, we had to estimate the nuclear properties of the ^{68}Cu, 2^+ state. Since the structure of the low-lying 1^+, 2^+ doublet is expected to be essentially $(^{68}\mathrm{Cu}; 1^+, 2^+) = (^{69}\mathrm{Cu}; 3/2^-) \times (^{67}\mathrm{Ni}; 1/2^-)$, largely independent of the assumption of a specific configuration, predictions of the nuclear moments may be calculated from experimental values in neighboring nuclei. This empirical approach is expected to include the major part of correlations of the true wave function, even if $Z = 28$, $N = 40$ is not a robust shell closure. The additivity rule for nuclear moments, see, *e.g.*, [33], yields for the quadrupole moments in the stretched $I^\pi = 2^+$ state $Q(^{68}\mathrm{Cu}; 2^+) = Q(^{67,69}\mathrm{Cu}; 3/2^-)$ as $Q(^{67}\mathrm{Ni}; 1/2^-) \equiv 0$, whereas angular momentum re-coupling yields $Q(^{68}\mathrm{Cu}; 1^+) = 1/2 \times Q(^{67,69}\mathrm{Cu}; 3/2^-)$. Similarly, one gets $\mu(^{68}\mathrm{Cu}; 2^+) = \mu(^{67,69}\mathrm{Cu}; 3/2^-) + \mu(^{67}\mathrm{Ni}; 1/2^-)$ and $\mu(^{68}\mathrm{Cu}; 1^+) = 5/6 \times \mu(^{67,69}\mathrm{Cu}; 3/2^-) - 1/2 \times \mu(^{67}\mathrm{Ni}; 1/2^-)$. The validity of additivity of nuclear moments in the vicinity of ^{68}Ni has been discussed by Vingerhoets *et al.* in the framework of shell model calculations [14]. In table 3 experimental data are compared to results inferred from additivity. The data for ^{67}Ni neighbours are listed for comparison. For empirical interpolation the mean value of ^{67,69}Cu values was always used. For g factor and Q of ^{68}Cu, 2^+ positive, respectively negative signs were adopted following the shell model expectation.

When it was noted that the nuclear moments measured in this work were only qualitatively reproduced by the additivity treatment, shell model calculations in the $\pi\nu(f_{5/2}, p, g_{9/2})$ model space above an inert ^{56}Ni core were performed with the jj44b [34] interaction. The results for the copper isotopes and ^{67}Ni are shown in table 3. Even though the moments of the ^{68}Cu, 1^+ ground state are quite well reproduced, the theoretical results for the 2^+ and 6^- state, as well as for ^{67}Ni, are quite far from the experimental ones. For the magnetic moments this is mainly due to the ^{67}Ni, $1/2^-$ value, which is underestimated in the shell model with the effective operator used as specified in the footnotes to table 3.

The deviation in the empirical value, however, points to a more complicated structure beyond the simple $\pi p_{3/2} \times \nu p_{1/2}^{-1}$ configuration of the wave function, which is also observed for the ^{68}Cu, 6^- state. This is even more apparent

in the 2^+ state. Note that shell model interactions fail to predict the correct 1^+-2^+ sequence [14]. Inspection of the shell model wave function indicates a substantial difference in the two wave functions yielding a $\geq 20\% \pi p_{3/2} \times \nu f_{5/2}^{-1}$ component in the 2^+, while it is $< 1\%$ in the 1^+ state, in agreement with ^{67}Ni, $1/2^-$.

This also manifests itself in the observation, that the actual shell model value for the g factor of the 1^+ state is smaller than the one calculated assuming additivity of the shell model values of the ^{67,69}Cu and ^{67}Ni neighbors (also included for comparison in table 3), while for the 2^+ state the opposite is found. It is interesting to note, that the additivity values for the g factors of the 1^+ and 2^+ states, when corrected for this wave function effect, come much closer to the experimental results. Thus it may be concluded, that a successful theoretical shell model description would have to include also particle-hole excitations across the $Z = 28$ shell, in agreement with the observation in [33] for the heavy odd-A copper isotopes. Unfortunately, such calculations are not available for the odd-odd isotopes, and are beyond the scope of the present work. The fact that the ratio of the experimental quadrupole moments of the 2^+ to the one of the 1^+ state is far from the value of about 2, expected both in additivity and the straight shell model, could be a particularly critical check of such calculations, since they would also include the changes of collective properties from one isotope to the next [35].

Conclusions. – The TDPAC technique was used to measure for the first time the electric quadrupole and the magnetic dipole moments of the first excited state in ^{68}Cu$(2^+, 84.1\,\text{keV})$. Values of $Q = -0.110(3)\,\text{b}$ and $\mu = 2.857(6)\,\mu_\text{N}$ were obtained.

The differences between measured and shell model predicted values for the nuclear moments can be explained by limitations of the model space, which excluded proton particle-hole excitations across the $Z = 28$ closed shell. The additivity rules for magnetic and quadrupole moments yield only qualitative estimates for configurations composed of single particle/hole states. This may be traced back to the weak $N = 40$ subshell closure at $Z = 28$.

The present work clearly demonstrates the feasibility of using the ^{68m}Cu/^{68}Cu isomeric decay as a unique copper probe for hyperfine interactions studies in areas such as condensed and soft matter physics, biophysics and chemistry.

* * *

The authors would like to thank the ISOLDE operation and technical teams. We kindly acknowledge Prof. Daniel Galaviz for the valuable suggestions improving the readability of the paper. This project has received funding through the European Union's Seventh Framework Programme for Research and Technological Development under Grant Agreements 262010 (ENSAR) and 289191 (LA3NET), by the Found for Scientific Research-Flanders (*G*.0983.15) and the KU Leuven BOF (CREA/14/013 and STRT/14/002) from Belgium, by project from the Foundation for Science and Technology (FCT) of Portugal (CERN-FIS-NUC-0004-2015) and by project CICECO-Aveiro Institute of Materials, (POCI-01-0145-FEDER-007679) - FCT Ref. (UID/CTM/50011/2013), financed by national funds through the FCT/MEC and when appropriate co-financed by FEDER under the PT2020 Partnership Agreement. ASF acknowledges the PhD grants support by FCT (SFRH/BD/84743/2012) and KU Leuven. BAB acknowledges NSF grant (PHY-1404442). SP acknowledges the Greek State Scholarships Foundation (I.K.Y.), Project scholarships I.K.Y. from resources of "Education and Lifelong Learning", the European Social Fund (ESF) NSRF, 2007–2013.

REFERENCES

[1] da Silva J. F. and Williams R., *The Biological Chemistry of the Elements*, 2nd edition (Oxford University Press, Oxford) 2002.
[2] Tapiero H., Townsend D. and Tew K., *Biomed. Pharmacother.*, **57** (2003) 386.
[3] Linder M., *Biochemistry of Copper*, 2nd edition (Plenum Press, New York) 1991.
[4] Ambundo E. A., Yu Q., Ochrymowycz L. A. and Rorabacher D. B., *Inorg. Chem.*, **42** (2003) 5267.
[5] Imai S., Fujisawa K., Kobayashi T., Shirasawa N., Fujii H., Yoshimura T., Kitajima N. and Moro-oka Y., *Inorg. Chem.*, **37** (1998) 3066.
[6] Lipton A. S., Heck R. W., de Jong W. A., Gao A. R., Wu X., Roehrich A., Harbison G. S. and Ellis P. D., *J. Am. Chem. Soc.*, **131** (2009) 13992.
[7] Irangu J. K. and Jordan R. B., *Inorg. Chem.*, **42** (2003) 3934.
[8] Butz T., Saibene S., Fraenzke T. and Weber M., *Nucl. Instrum. Methods Phys. Res. A*, **284** (1989) 417.
[9] Butz T., *Hyperfine Interact.*, **52** (1989) 189.
[10] Haas H. and Shirley D. A., *J. Chem. Phys.*, **58** (1973) 3339.
[11] Schatz G. and Weidinger A., *Nuclear Condensed Matter Physics: Nuclear Methods and Applications* (Wiley) 1995.
[12] `http://test-isolde-yields.web.cern.ch`.
[13] Stora T., *Nucl. Instrum. Methods Phys. Res. B*, **317** (2013) 402.
[14] Vingerhoets P., Flanagan K. T., Avgoulea M., Billowes J., Bissell M. L., Blaum K., Brown B. A., Cheal B., de Rydt M., Forest D. H., Geppert C., Honma M., Kowalska M., Krämer J., Krieger A., Mané E., Neugart R., Neyens G., Nörtershäuser W., Otsuka T., Schug M., Stroke H. H., Tungate G. and Yordanov D. T., *Phys. Rev. C*, **82** (2010) 064311.
[15] Mishin V., Fedoseyev V., Kluge H.-J., Letokhov V., Ravn H., Scheerer F., Shirakabe Y., Sundell S. and Tengblad O., *Nucl. Instrum. Methods Phys. Res. B*, **73** (1993) 550.

[16] Köster U., Catherall R., Fedoseyev V. N., Franchoo S., Georg U., Huyse M., Kruglov K., Lettry J., Mishin V. I., Oinonen M., Ravn H., Seliverstov M. D., Simon H., van Duppen P., van Roosbroeck J. and Weissman L., *Hyperfine Interact.*, **127** (2000) 417.
[17] Stachura M., Gottberg A., Johnston K., Bissell M., Garcia Ruiz R., Martins Correia J., Granadeiro Costa A. R., Dehn M., Deicher M., Fenta A. S., Hemmingsen L., Molholt T. E., Munch M., Neyens G., Pallada S., Silva M. R. and Zakoucky D., *Nucl. Instrum. Methods Phys. Res. B*, **376** (2016) 369.
[18] Jäger M., Iwig K. and Butz T., *Hyperfine Interact.*, **198** (2010) 167.
[19] Jäger M., Iwig K. and Butz T., *Rev. Sci. Instrum.*, **82** (2011) 065105.
[20] Jäger M. and Butz T., *Nucl. Instrum. Methods Phys. Res. A*, **674** (2012) 24.
[21] Nagl M. A., Barbosa M. B., Vetter U., Correia J. G. and Hofsass H. C., *Nucl. Instrum. Methods Phys. Res. A*, **726** (2013) 17.
[22] Krane K. S. and Steffen R. M., *Phys. Rev. C*, **2** (1970) 724.
[23] Barradas N. P., Rots M., Melo A. A. and Soares J. C., *Phys. Rev. B*, **47** (1993) 8763.
[24] Lopes A., *Local Probe Studies on Lattice Distortions and Electronic Correlations in CMR Manganites* (Aveiro University) 2006.
[25] de Wijn H. W. and de Wildt J. L., *Phys. Rev.*, **150** (1966) 200.
[26] Kushida T., Silver A. H., Koi Y. and Tsujimura A., *J. Appl. Phys.*, **33** (1962) 1079.
[27] Lutz O., Oehler H. and Kroneck P., *Z. Phys. A*, **288** (1978) 17.
[28] `http://www.nndc.bnl.gov/endsdf/`.
[29] Lisetskiy A. F., Brown B. A., Horoi M. and Grawe H., *Phys. Rev. C*, **70** (2004) 044314.
[30] Kontani M., Asayama K. and Itoh J., *J. Phys. Soc. Jpn.*, **20** (1965) 1737.
[31] Kittel C., *Introduction to Solid State Physics*, 6th edition (John Wiley & Sons, Inc., New York) 1986.
[32] Bleck J., Butt R., Lindenberger K. H., Ribbe W. and Zeitz W., *Z. Phys.*, **263** (1973) 169.
[33] Neyens G., *Rep. Prog. Phys.*, **66** (2003) 633.
[34] Verney D., Ibrahim F., Bourgeois C., Essabaa S., Galès S., Gaudefroy L., Guillemaud-Mueller D., Hammache F., Lau C., Blanc F., Mueller A. C., Perru O., Pougheon F., Roussière B., Sauvage J. and Sorlin O., *Phys. Rev. C*, **76** (2007) 054312.
[35] Sieja K. and Nowacki F., *Phys. Rev. C*, **81** (2010) 061303.

Chapter 6

Adsorption of heavy metals on graphene

Graphene holds the promise to revolutionize electronics technology, owing to our ability to engineer its physical and chemical properties. Adsorbed atoms (adatoms) and molecules (admolecules) on graphene are a particularly promising route towards controllable modification of graphene's properties. A wide range of studies, some experimental, but more often theoretical studies, have been carried out to understand the stability and coordination of several adsorbed species on graphene and also to investigate and exploit the induced properties (c.f. *section* 1.7). This chapter presents the main results of the research carried out within the framework of this thesis, dealing with the fundamental understanding of the interaction between graphene and adatoms (model cases: Hg, Cd, In and Ag) and admolecules (model case: HgO_2), in terms of structural and electronic properties. The research approach is based on density functional theory (DFT) calculations, complemented whenever possible by perturbed angular correlation (PAC) experiments. The chapter is structured according to manuscripts 2 to 4, which have been submitted or prepared for submission.

Section 6.1: *Hg adatoms on graphene*

This section (manuscript 2) deals with objectives (1) and (2) (c.f. *Chapter* 2), i.e. to investigate the interaction of heavy metal adatoms with pristine graphene, without interference from other species). In this section, we focus on Hg as model heavy metal adatom. Atomic positions and their stability, binding energies, diffusion and agglomeration processes, electronic structure,

and associated hyperfine parameters, are studied using DFT. The calculations presented in this section for Hg are particularly detailed, i.e. various functionals are tested and a wide range of nominal Hg concentration is covered. The outcome of these detailed studies on Hg allowed us to narrow down the relevant range of parameters to what is used in *section* 6.2, extending these calculations to other heavy metal elements (Ag, Cd and In).

Section 6.2: *Ag, Cd and In adatoms on graphene*

This section (manuscript 3) also deals with objectives (1) and (2), extending from Hg (*section* 6.1) to other heavy metal elements (Ag, Cd and In). These DFT studies not only provide new fundamental insight on graphene-adatom interactions, but also form the basis for a new experimental approach which is currently being developed at the ISOLDE facility at CERN, using ASPIC (Apparatus for Surface Physics and Interfaces at CERN). The principle of this approach is described in Ref. [285], which includes a (preliminary) subset of the DFT calculations presented here in full. ASPIC will allow to avoid the interference from other species in the adsorption mechanism since deposition and characterization are carried out *in-situ*, under ultra-high vacuum conditions.

Section 6.3: *HgO_2 admolecules on graphene*

While the DFT studies mentioned above considered the interaction of one adatom element with pristine graphene, this section (manuscript 4) deals objective (3), i.e. how the adsorption of Hg is affected by other species (e.g. water and oxygen, in a solution or in the atmosphere). Adsorbed molecules directly affect many of graphene's physical and chemical properties, such as "wetting" [290], adhesion [291], electrical doping [292], carrier mobility [293]. The importance of understanding this interaction between graphene and admolecules spans a wide range of applications, from graphene transfer processes to bio-sensing applications and water filtration.

PAC experiments were performed using graphene on different substrates (Cu, SiO_2, PET, Quartz) and ^{199m}Hg as a probe, at different temperatures (from room temperature down to 77 K). ^{199m}Hg was implanted into ice, which upon melting was deposited onto the graphene surface. There is a clear trend across all these experiments (different substrates, different temperatures, repetitions under the same conditions). Two distinct fractions (describing two distinct EFG) are typically observed experimentally. DFT calculations modeling several kinds of coordination on graphene were performed in order to achieve a consistent interpretation of the PAC experimental results. The

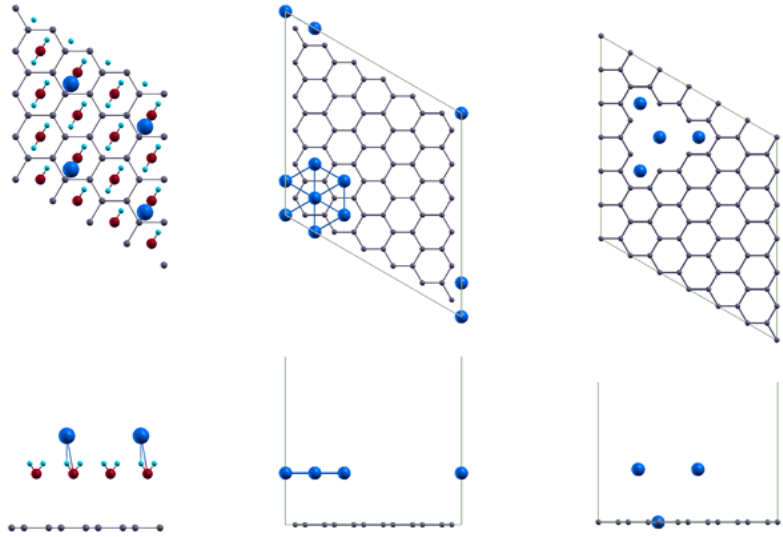

Figure 6.1: View from the top and from the side of different configurations investigated by DFT: water and Hg on top of graphene, Hg-cluster with 7 Hg atoms on pristine graphene and Hg-cluster with 4 Hg atoms on graphene with vacancies

.

configurations which were considered fall within the following groups: water admolecules with Hg incorporated in different spatial configurations; Hg-clusters with different configurations up to 7 atoms on pristine graphene and also on graphene with defects; Hg coordinated by oxygen and hydrogen assuming different configurations. Some of the mentioned configurations are depicted in Figure 6.1. For simplicity, only a subset of these experiments and of the configurations considered in the DFT calculations are presented in manuscript 4. *Appendix A* gives a complete overview of the DFT calculations. The DFT analysis strongly suggest that the high V_{zz} experimentally identified can only originate from linear HgO_2 admolecules on the surface of graphene, which to the best of our knowledge had not been observed before. In addition to the insight they provide on adsorption of heavy metals on graphene, these results show that the EFG tensor is very sensitive with respect to the coordination (spatial configuration and adsorption site on graphene).

6.1 Hg adatoms on graphene: manuscript 2

Hg adatoms on graphene: A first-principles study

A. S. Fenta[1,2,3], C. O. Amorim[2], J. N. Gonçalves[2], N. Fortunato[2], M. B. Barbosa[4], J. P. Araujo[4], M. Houssa[5], S. Cottenier[6,7], S. Cottenier[6,7], M. J. Van Bael[1], V. S. Amaral[2], and L. M. C. Pereira[1]

[1] *KU Leuven, Instituut voor Kern- en Stralingsfysica, Celestijnenlaan 200 D, 3001 Leuven, Belgium*

[2] *Physics Department and CICECO, University of Aveiro, 3810-193 Aveiro, Portugal*

[3] *CERN, 1211 Geneva 23, Switzerland*

[4] *IFIMUP and IN-Institute of Nanoscience and Nanotechnology, Departamento de Física e Astronomia da Faculdade de Ciências da Universidade do Porto, Rua do Campo Alegre 687, 4169-007 Porto, Portugal*

[5] *KU Leuven, Department of Physics and Astronomy, Celestijnenlaan 200 D, 3001 Leuven, Belgium*

[6] *Center for Molecular Modeling, Ghent University, 9052 Zwijnaarde, Belgium*

[7] *Department of Electrical Energy, Metals, Mechanical Constructions and Systems, Ghent University, 9052 Zwijnaarde, Belgium and*

[8] *C2TN, Instituto Superior Técnico, Campus Tecnológico e Nuclear, EN10, 2695-066 Bobadela LRS*

The interest in understanding the interaction between graphene and atoms that are adsorbed on its surface (adatoms) spans a wide range of research fields and applications, for example, to controllably change the properties of graphene in electronic devices or to detect those changes in graphene-based sensors. We present a density functional theory study of the interaction between graphene and adatoms of Hg, as a model heavy metal element. Binding energy, electronic structure and electric field gradient were calculated for various high-symmetry atomic configurations, from isolated adatoms to a continuous Hg monolayer. Hg as isolated adatom was found to be the most stable configuration, with a binding energy of 188 meV. Whereas isolated adatoms have a minor effect on the electronic structure of graphene (only a small acceptor-like effect), Hg monolayer configurations induce a metallic state, with the Fermi level moving well above the Dirac point (donor-like behavior). Based on the electric field gradient calculated for the various configurations, we discuss how hyperfine techniques (perturbed angular correlation spectroscopy, in particular) can be used to experimentally study Hg adsorption on graphene.

I. INTRODUCTION

Since it was isolated as a 2-dimensional material [1], graphene has become a remarkable subject of research across various fields [1–11]. In particular, thanks to the ability to controllably change its physical and chemical properties, for example, in field-effect transistors [1, 12], transparent electrodes [13, 14], energy-storage materials [15, 16], and chemical and biosensors [17, 18], graphene shows tremendous potential to revolutionize various technologies. A key area of research, which is common across many of these fields and applications, is the interaction between graphene and atoms that are adsorbed on its surface (adatoms), either as a means to actively change its properties (e.g. adatom doping to tune the Fermi level in a transistor-type device) or simply to detect those changes when an adatom is adsorbed (e.g. in sensing applications). In this context, substantial research has been carried out to understand how adatoms of different elements bind to graphene, which stable atomic configurations they form, how they migrate and agglomerate, and how they affect the electronic properties of graphene in the various possible configurations (e.g. different sites and local concentrations, isolated versus clustered, etc.). The majority of these studies have relied on density functional theory (DFT) calculations for various adatom elements, dealing with the adsorption stability and effect on the properties of graphene (structural, electric, magnetic, etc.). Among the earlier DFT studies, S. Casolo et al. [19] studied hydrogen adsorption on graphene, as isolated atoms or in cluster configurations, revealing a relationship between the stability of the adatom, the substrate and the induced electronic properties. Mao et al. [20] predicted the emergence of high magnetic moments when transition metal (TM) atoms (Fe, Co, and Mn) are adsorbed on graphene. Sevinçli et al. [21] studied the binding energies and the electronic and magnetic properties of graphene adsorbed with TM atoms (Co, Cr, Fe, Mn, and Ti), revealing a wide range of binding energies, from 0.10 to 1.95 eV, depending on the species and coverage density. In the same work, Sevinçli et al. also predicted the occurrence of ferromagnetic and antiferromagnetic ordering when 3d TM are adsorbed on graphene. Adsorption of heavy metals (HM) and its influence on the properties of graphene have also been investigated, not only in terms of the basic physics of adsorption, stability, electric and magnetic properties, but also considering its potential application, for example, in spintronics (e.g. Os, Ir [22], and Pb [23] inducing a topological insulator state thanks to the high-spin orbit coupling in heavy elements), catalysis (e.g. Au [24] and Pd [25]), detection of toxic heavy metals (e.g. Cf, Hg and Pb [26]), and their removal from water (e.g. Pb [27]). Since adatoms tend to have low migration energies on the surface of graphene, they typically diffuse well below room temperature [28]. Adatom elements for which a

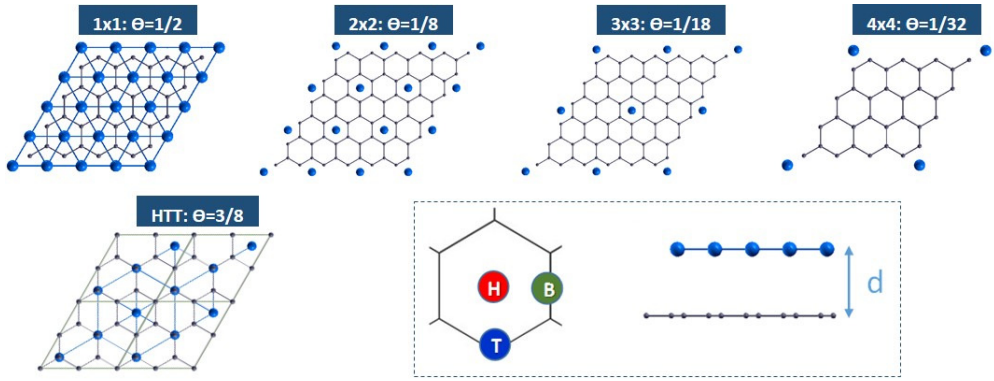

Figure 1. **Top: 1×1, 2×2, 3×3 and 4×4 supercells for a Hg atom in the hollow site (H) on graphene lattice, corresponding to nominal Hg concentrations (θ) of $1/2$, $1/8$, $1/18$, and $1/32$, with respect to the number of carbon atoms. The calculations were performed for all three high-symmetry positions for adatoms on graphene (depicted in the bottom right figure), as a function of graphene-Hg distance d: the hollow (H) site above the center of the hexagon, the top (T) site directly above the C atoms, and the bridge (B) site above the middle of the C-C bond. Bottom left: configuration consisting of a Hg monolayer here referred to as HTT configuration since Hg atoms are placed in a sequence of one H and two T sites ($\theta = 3/8$).**

cluster configuration is energetically favorable will therefore agglomerate (e.g. Au [24]). Since the properties of the graphene+adatoms system are strongly dependent on the adsorption configuration (e.g. isolated adatoms versus clusters), it is important to not only understand these effects (configuration-dependent properties and migration) from a theoretical point of view, but also to be able to probe them experimentally.

Here we present a DFT study of Hg adatoms on graphene, as a representative case of heavy metal adsorption. We investigate the stability of various adsorption configurations as well as their effect on the electronic structure of graphene. Moreover, based on the calculation of the hyperfine parameters associated with the different configurations, we discuss how hyperfine techniques can be used to experimentally study Hg adsorption on graphene, in particular, to distinguish isolated from cluster configurations. These calculations not only provide new insights on graphene-adatom interactions, they also form the basis for a new experimental approach which is currently being developed at the ISOLDE facility at CERN, using ASPIC (Apparatus for Surface Physics and Interfaces at CERN) [29].

II. COMPUTATIONAL METHOD

The DFT calculations were performed using WIEN2k code [30], which implements the linearized augmented plane waves (LAPW) method. This method divides the space into non-overlapping spheres, described with spherical harmonics and the interstitial region, described with plane waves. It is an all-electron code (i.e. it employs the full charge distribution of all electrons) and is for this reason more suitable to calculate hyperfine parameters. The muffin-tin radii were set to 1.29 and 1.70 atomic units, for the carbon atoms and for mercury adatoms, respectively. The number of plane waves is set by the parameter $RMT \times K_{max} = 5.5$, where $RMT = 1.29$ au (the radius of the smallest sphere). Different concentrations of adatoms were studied by constructing differently sized supercells, each including one Hg adatom and multiple graphene C-hexagons. Figure 1 shows projections along the *c-axis* of the 1×1, 2×2, 3×3 and 4×4 ($C - hexagon$) supercells (with the corresponding number of *k-points* considered being $18 \times 18 \times 1$, $10 \times 10 \times 1$, $8 \times 8 \times 1$, and $6 \times 6 \times 1$, respectively). These configurations correspond to nominal Hg concentrations (θ) of $1/2$, $1/8$, $1/18$, and $1/32$, with respect to the number of carbon atoms. For each concentration, three sets of calculations were performed, for Hg atoms on each of the three high-symmetry positions: hollow (H), top (T) and bridge (B) (Figure 1). An additional configuration was also considered in the calculations: an hexagonal Hg monolayer with the Hg atoms in a sequence of H-T-T sites (therefore designated here as HTT configuration), with a concentration of $\theta = 3/8$ with respect to C atoms, which is equivalent to a (111) plane of a cubic Hg lattice. A vac-

uum spacing of at least 15 Å is placed between adjacent graphene layers to minimize layer-layer interactions. The calculations did not consider spin polarization. Three different exchange correlation functionals were used: local spin density approximation (LSDA) [31], generalized gradient approximation (GGA-PBE) [32] and GGA-PBE with van der Waals correction (DFT-D3) [33]. The vdW corrections of DFT-D3 method are restricted to shorter correlation length scales. We have used the experimental lattice parameter $a = b = 2.46$ Å, which is close to our optimized parameters with LDA (2.45 Å) and GGA (2.47 Å) for undoped graphene. The results presented in the following correspond to calculations performed without including spin-orbit coupling. Calculations for representative cases, namely for the lowest-energy configurations with θ of 1/18 (isolated adatoms) and 3/8 (HTT monolayer), including spin-orbit (SO) coupling, revealed no significant differences.

For each configuration and nominal concentration, we studied the stability of the adatoms with respect to displacements in-plane (between the high-symmetry sites) and out-of-plane (varying distance d to the graphene layer) directions, as well as the associated electronic structure. In-plane displacements provide insight into adatom migration and diffusion mechanisms, whereas out-of-plane displacement is related to the adsorption stability. Additionally, the electric field gradient (EFG) tensor calculated for every configuration can be compared to experimentally determined values, as a sensitive local probe for the structural configuration of Hg adatoms on graphene.

III. RESULTS

A. Choice of functionals

Figure 2 shows the adsorption energy of graphene-Hg system as a function of graphene-adatom distance, d, for the supercell 2×2 ($\theta = 1/8$) when Hg is at the H site (as an example; B and T sites show equivalent behavior), obtained using each of the three used functionals (LSDA, PBE and PBE+DFT-D3). Since adatoms on surfaces are subject to dispersion forces, commonly referred to as van der Waals interactions, which are not accounted for with PBE nor LSDA, we included the DFT-D3 correction to the PBE functional. As it can be seen in the Figure 2, the DFT-D3 correction results in a strengthening of the binding: lower energy minimum and corresponding distance d. LSDA calculations also show a much stronger binding of the Hg atom to the graphene layer compared to PBE (and smaller equilibrium distance). This is however expected, since LSDA does not provide an adequate description for weakly bound adatoms, and is known to overestimate binding energies.

It is important to note that while the choice of functionals determines the energy balance of the system, it leaves the EFG generaly unaffected. The EFG is a traceless symmetric rank 2 tensor so that the axis system can be defined in a way that the EFG tensor representation has only three non-vanishing diagonal components defined as $|V_{zz}| \geq |V_{yy}| \geq |V_{xx}|$. For simplicity, it is common to characterize the EFG tensor by its main component V_{zz} and the axial asymmetry parameter, η, defined as $\eta = \frac{V_{xx} - V_{yy}}{V_{zz}}$, taking into account that the three remaining degrees off freedom are characterized by the Euler angles that relate the principal axis system (where the EFG is diagonal) to the laboratory axis system. The EFG tensor is extremely sensitive to the charge distribution (and its symmetry, in particular) in the region of the nucleus, which does not appear to vary significantly when using the different functionals considered here. This is illustrated in Figure 3, where the EFG parameters, V_{zz} and η, for Hg in the H site, are plotted as a function of the

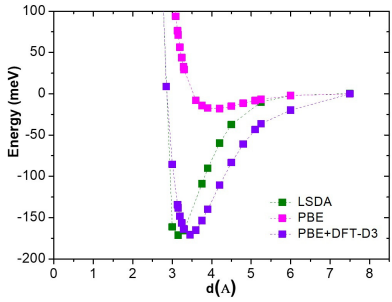

Figure 2. **Energy landscape of graphene-Hg system as a function of graphene-adatom distance, d, using LSDA, PBE and PBE+DFT-D3 functionals. Supercell 2×2 ($\theta = 1/8$) and Hg at the H site.**

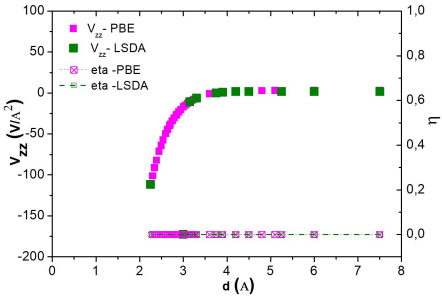

Figure 3. **EFG components (V_{zz} and the axial asymmetry parameter, η) of Hg as a function of graphene-Hg distance, d, using LSDA and PBE functionals. Supercell 2×2 ($\theta = 1/8$) and Hg at the hollow symmetric site. DFT-D3 is not shown since it is only a correction to the energies and forces, i.e. does not affect the EFG.**

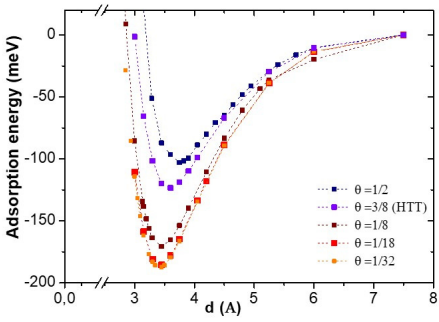

Figure 4. **Adsorption energy of graphene-Hg system as a function of graphene-Hg distance, d, for different nominal concentrations (θ). Except for the HTT case ($\theta = 3/8$), which is a mix of H and T sites, data are shown for Hg located at the H site. Adsorption energies are normalized to a cell that contains 1 Hg atom per supercell.**

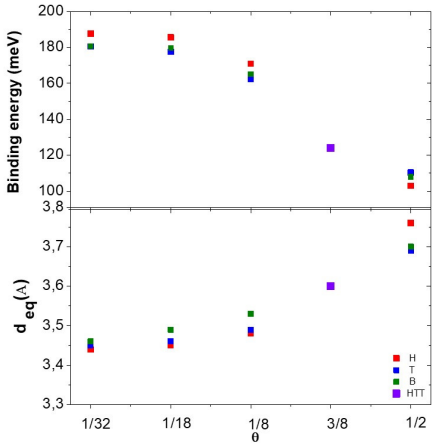

Figure 5. **a) (top) Binding energy of Hg defined as the absolute value of the minimum of the adsorption energy and b) (bottom) corresponding distance, d_{eq}, for different nominal concentration (θ), for each site H, T and B, as well as for the HTT configuration.**

distance d: LSDA and PBE calculations yield virtually the same values. For a distance $d = 3.48$ Å, i.e. at the equilibrium position determined by the minimum of the energy with PBE+DFT-D3 functional, the EFG values at the Hg site are $V_{zz} = -3.0$ V/Å^2 and $\eta = 0$ (the axial asymmetry parameter η is always zero for Hg at H site).

B. Stability versus adatom position and concentration

In the following we focus on the results obtained using the PBE+DFT-D3 functional. To understand the stability of Hg adatoms on graphene, for different nominal concentrations, the adsorption energy was studied as a function of the distance d, for each one of the three high symmetry sites. Figure 4 shows the calculated adsorption energy as a function of d, for different θ, when Hg is at the H symmetric site (except for $\theta = 3/8$, for which the Hg atoms are in mix of H and T sites). The adsorption energy is calculated as: $E_{ads} = E_{G+adatom} - E_G - E_{adatom}$, where $E_{G+adatom}$ is the energy of the system *graphene + adatom*, and E_G and E_{adatom} are the energy of graphene and the energy of adatom, respectively. Although with a qualitatively similar shape, the adsorption energy curves for the different Hg concentrations (θ) have different minima (i.e. different binding energies) at different distance values. For $\theta = 1/18$ and $\theta = 1/32$, however, the curves virtually coincide, indicating that a supercell 3×3 ($\theta = 1/18$) is already large enough to adequately describe non-interfering, isolated Hg adatoms (i.e. further increasing the dilution would have a negligible effect).

Figure 5 compiles the binding energy (defined as the absolute value of the minimum of the adsorption energy) and the corresponding equilibrium distance (d_{eq}) obtained for Hg at H, T and B sites, for each of the θ values considered here. For each nominal concentration, both binding energy and corresponding distance depend on the position (H, T or B) occupied by the Hg adatom. The main conclusion to be extracted from these calculations is that the most stable configuration for Hg on graphene is as isolated adatoms (e.g. 188 meV for $\theta = 1/32$) which is, in particular, more stable than the HTT monolayer (123 meV and $\theta = 3/8$).

C. Diffusion and agglomeration

Above, we considered the relative stability of the Hg adatoms in various high-symmetry configurations. In this section we examine the energy barriers governing the migration of Hg adatoms in the dilute regime (i.e. the migration paths between H, B and T sites). In a practical scenario, adatoms are randomly deposited on a graphene surface, evolving from dilute to more concentrated configurations. Therefore, these migration barriers can also be regarded as governing the agglomeration of dilute Hg adatoms into other configurations (e.g. HTT configuration). Figure 6 shows how the adsorption energy varies along straight H$\longleftrightarrow$T and H$\longleftrightarrow$B paths (with d optimized at each intermediate position). From these calculations, we derive H$\longleftrightarrow$T and H$\longleftrightarrow$B migration barriers of ~ 8.0 meV and ~ 5.6 meV, respectively, i.e. the overall migration barrier for isoltated Hg adatoms on graphene is therefore ~ 5.6 meV. These can be considered low mi-

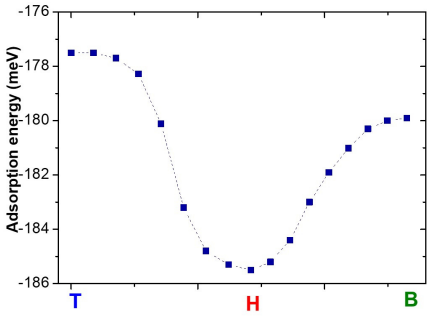

Figure 6. **Adsorption energy along H $\longleftrightarrow$ T and H $\longleftrightarrow$ B paths, in the dilute regime ($\theta = 1/18$, 3×3 configuration), i.e. governing the migration of isolated Hg adatmos on the surface of graphene. The adsorption energy is plotted for each path divided in segments of equal lengths.**

gration barriers, when compared to other metal adatoms such as Au (7 meV), Ag (10 meV), Cr (22 meV), Pd (80 meV) and Al (166 meV) [28, 34]. From these migration barriers, one can estimate a characteristic temperature above which the adatoms become mobile (i.e. start to diffuse and eventually agglomerate). Within an Arrhenius model, the rate Λ of thermally activated jumps between H sites is given by $\Lambda = \nu_0 e^{-\frac{E_a}{k_B T}}$, where ν is the attempt frequency (which we take as $\nu_0 = 10^{12}$ s^{-1}, of the order of the lattice vibrations), and k_B and T the Boltzmann constant and the temperature. The average period between jumps is therefore given by Λ^{-1}, from which we can estimate the threshold temperatures for surface diffusion of Hg adatoms, for a given length and time scales. For example, the temperature corresponding to one jump between adjacent H sites is given by $T = -\frac{E_a}{k_B ln(t\nu_0)}$, where t is the time interval in question. For one minute ($t = 60$ s) and $E_a = 5.6$ meV (corresponding to H$\longrightarrow$B$\longrightarrow$H), we obtain $T = 2.2$ K. In other words, isolated (dilute) Hg adatoms on an ideal (defect-free) graphene surface can only be observed if the deposition and subsequent characterization are performed at very low temperature, of the order of few K. Increasing temperature will activate surface diffusion, resulting in other kind of agglomeration of Hg adatoms on graphene. During diffusion, Hg adatoms may also become trapped in defective regions (e.g. graphene edges, Stone Wales defects, vacancies, grain boundaries) [28, 35, 36].

D. Electronic properties

Figure 7 shows the band structure (BS) and density of states (DOS) for graphene and for graphene+Hg for the cases of the HTT configuration and for $\theta = 1/8$ and $\theta = 1/32$. The system remains gapless even when we consider SO-coupling in the calculations. Aside from the emergence of Hg-related bands, the main observation is the shift of the Fermi level with respect to the Dirac point of graphene, which depends on Hg concentration (summarized in Figure 8). In the more dilute regime ($\theta = 1/32$ and $\theta = 1/18$), there is a small shift of the Fermi level to below the Dirac point, indicating a slight acceptor behavior of the isolated Hg adatoms. For an adatom concentration of $\theta = 1/18$, this shift becomes even more pronounced. However, when the concentration further increases to $\theta = 3/18$, in the HTT configuration, the effect reverses, with a shift of the Fermi level to above the Dirac point, i.e. suggesting a donor behavior. This reversal can be understood as due to the change from isolated adatoms to the formation of a Hg monolayer. The observed donor behavior of the Hg monolayer is consistent with the simple analytical model proposed in reference [37] for the heavy elements Ag, Au, and Pt, characterizing the graphene-metal interface solely in terms of the work function: the work function of Hg (~ 4.5 eV [38]) is below the ~ 5.4 eV threshold where n-type behaviour is observed [37]. The formation of the Hg monolayer also renders the entire system (graphene plus Hg monolayer) metallic: the Hg monolayer introduces energy bands that cross the Fermi level (i.e. the Hg monolayer is metallic), which in addition is shifted upwards in energy, i.e. to a region of higher DOS in the Dirac cone of graphene (i.e. the graphene layer itself becomes more metallic).

E. EFG as a structural local probe

In this section, we discuss how the calculated EFG parameters, which strongly depends on the local charge distribution, can be used in an experimental setting to identify the spatial configurations of Hg adatoms on graphene. This involves comparing the EFG values calculated for multiple possible configurations to those measured experimentally using hyperfine techniques. Figure 9 shows the EFG parameters, V_{zz} and η, calculated at the Hg nucleus, for the different nominal concentrations and different high-symmetry sites, at the equilibrium distance, d_{eq}, between Hg and graphene. Table 1 compiles all the relevant parameters obtained in these calculations: binding energy and the corresponding distance d_{eq}, and the EFG parameters, V_{zz} and η. The calculated EFG values show some variation when comparing different high-symmetry sites, and are in particular strongly dependent on concentration θ, i.e. the V_{zz} strongly increases in the monolayer-type configurations ($\theta = 3/8$ and $\theta = 1/2$) due to the Hg coordination, making EFG a clear indicator of the concentration and position of Hg on graphene. We evaluated the role of the different orbitals in the obtained EFG values. Significant contributions are observed for p-p, d-d and s-d orbitals. Although total V_{zz} changes significantly from the highest nominal concentration ($\theta = 1/2$) to the dilute regime ($\theta = 1/32$), contributions from the

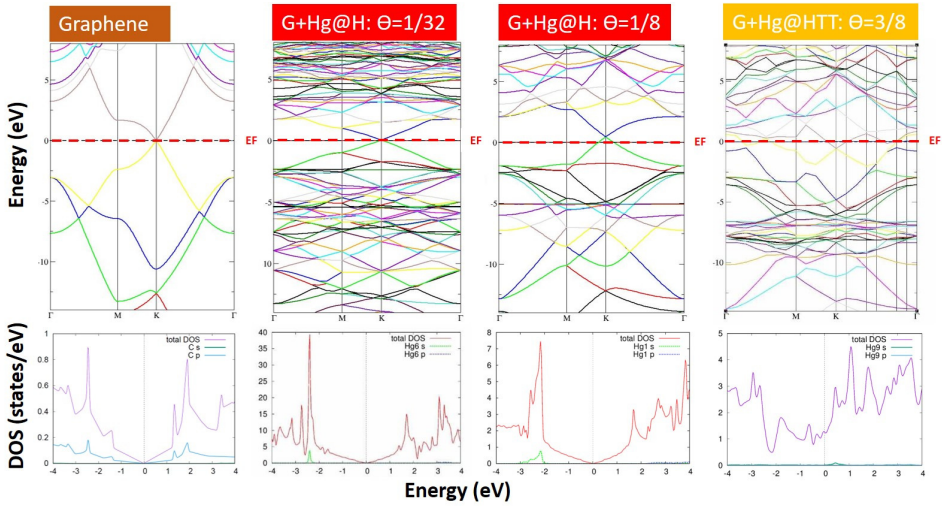

Figure 7. **a) (top) Band structure and b) (bottom) density of states for pristine graphene and for graphene + Hg for $\theta = 1/32$, $\theta = 1/8$ (at H high symmetric site) and $\theta = 3/8$ (HTT configuration).**

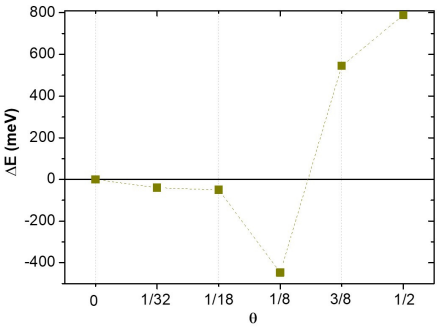

Figure 8. **Shift of the Fermi level relative to the Dirac point (ΔE), as a function of the nominal concentration (θ). Positive ΔE corresponds to a Fermi level above the Dirac point. Except for the HTT configuration ($\theta = 3/8$) data are shown for Hg at the H site.**

p-p orbitals always dominate (73% and 87% for the two extremes, respectively). Figure 10 shows the charge distribution and the charge isolines when Hg adatoms are at equilibrium d_{eq} for the metallic configuration HTT and isolated adatoms with $\theta = 1/18$. There are noticeable differences between the charge distribution of these two regimes (isolated versus monolayer) which help understand the drastically different V_{zz}. On the one hand, the small V_{zz} for $\theta = 1/18$ agrees with the nearly perfectly circular isolines of the charge distribution representing the outer electronic shells of the Hg adatoms. On the other hand, the high V_{zz} for the HTT monolayer is a consequence of the non-spherical charge distribution around Hg, mostly due to the interaction with the Hg nearest neighbors.

Perturbed angular correlation (PAC) spectroscopy is a particularly suited technique to measure the EFG parameters which can be compared to the calculated values presented here. For PAC experiments on Hg, the ^{199m}Hg/^{199}Hg isomeric decay, with an intermediate $5/2^-$ state with 2.45 ns half-life, is well established [39, 40]. PAC is a time differential statistical measurement where the observable is the decay histogram of two consecutive γ-rays in coincidence. Taking into account the short half-life of the probing state ^{199m}Hg of 2.45 ns, no more than 20 ns (approximately 8 half-lives) can be resolved with enough statistics. Therefore, we estimate a limit such that half a period of the characteristic PAC perturbation function can still be interpreted, i.e. 20/2 ns, leading to a minimum value of V_{zz} to be experimentally determined of 100 V/Å^2. The time experimental resolution is below 0.8 ns being the precision of the V_{zz} mainly dependent of the error of the quadrupole moment of about 9 % [39]. This implies that based on PAC measurements of V_{zz}, it would be possible to distinguish the two regimes of Hg adatom concentration discussed above, i.e. between isolated Hg adatoms and the onset of aggregation into a metallic Hg monolayer. Such experiments can be performed, for example, using the ASPIC setup at the

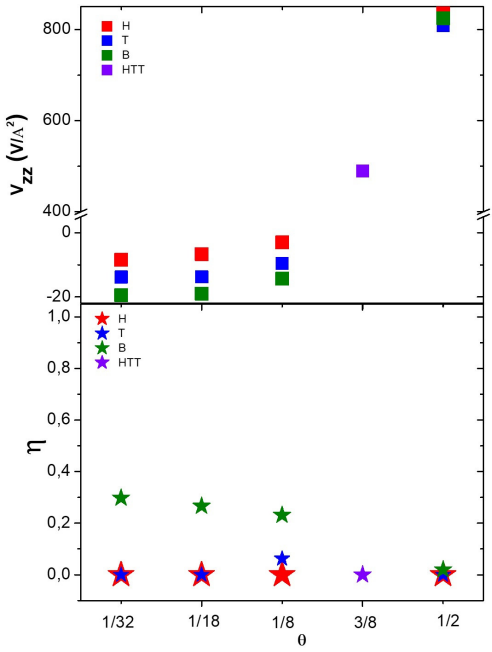

Figure 9. V_{zz} **and** η **EFG parameters at Hg site at the equilibrium energy, for all nominal concentration** (θ)**, for each site H, T and B.**

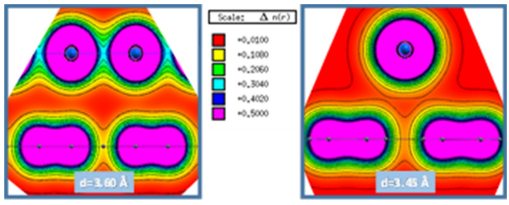

Figure 10. **Charge distribution** (e/Å^3) **of graphene-Hg system for HTT metallic configuration (left) and for the nominal concentration of** $\theta = 1/18$ **for Hg at H position distribution (right).**

ISOLDE facility at CERN [29], where adatoms can be deposited at low temperature, down to liquid He, and PAC measurements can be performed *in-situ* as a function of temperature. Based on the calculations presented here, one can expect that, upon deposition at low temperature, one would first observe the low V_{zz} associated with isolated Hg adatoms on H sites. Increasing temperature would eventually activate diffusion and segregation, and the much larger V_{zz} values associated with metallic Hg layers could then be observed. This type of experiments has been previously performed at ASPIC to investigate structural and magnetic properties of metal surfaces (e.g. Ni and Pd) [29]. The calculations presented here show the potential of hyperfine techniques in the context of adatoms on 2-dimensional materials. One of the advantages of this approach is that it allows to locally probe the adatom without affecting it, i.e. avoiding the influence of external probes, such as the tip of a scanning probe microscope or the intense electron beam of a transmission electron microscope. Additionally, a PAC spectrum can be measured with as little as 10^{10} probe atoms, corresponding to a coverage of 0.01 % for a typical 5×5 mm^2 sample, i.e. the approach can be applied down to extreme levels of adatom dilution. Moreover, measurements are compatible with applied electric or magnetic fields [29].

IV. CONCLUSIONS

We carried out a density functional theory study of Hg adatoms on graphene. Hg as isolated adatom (with concentration $\theta = 1/32$) at H-symmetric site was found to be the most stable configuration, with a binding energy of 188 meV. For isolated adatoms, the binding energy increases with decreasing adatom concentration and depends on adsorption site (H, T, or B). A migration barrier of ~ 5.6 meV along H$\longleftrightarrow$B$\longleftrightarrow$H paths was estimated, corresponding to a threshold temperature for adatom surface mobility of a few Kelvin.

The effect of Hg adsorption on the electronic structure of graphene is strongly dependent on adatom coverage. Whereas isolated adatoms have only a small acceptor-like effect, leaving the electronic structure of graphene virtually unaffected, Hg monolayer configurations induce a metallic state, with the Fermi level moving well above the Dirac point (donor-like behavior).

Based on the electric field gradient calculated for the various configurations, we propose that hyperfine techniques can be used to experimentally study Hg adsorption on graphene, in particular by measuring the EFG using PAC spectroscopy (^{199m}Hg/^{199}Hg isomeric decay, with an intermediate $5/2^-$ state with 2.45 ns half-life). For example, upon deposition of dilute, isolated Hg adatoms below the mobility threshold temperature (few Kelvin), it would be possible to detect the onset of migration and agglomeration (with increasing temperature) into the HTT monolayer configuration. Although the calculations presented here suggest that the dilute configuration is more stable than monolayer configurations, it is plausible that under different conditions, segregation may occur. For example, shifts of the Fermi level due to defects or specific substrates may affect the electrostatic interaction between the Hg adatoms and thereby stabilize cluster or monolayer configurations. Such hyperfine studies could be correlated with transport measurements, which, based on our calculations, would show a change from p-type to n-type conduction. Such PAC

Table I. Binding energy and the corresponding distance (d_{eq}) and EFG parameters (V_{zz} and η), for all different nominal concentration (θ), for each high symmetric positions H, T and B and for HTT configuration.

Nominal Concentration θ	**Site**	**Binding energy meV**	d_{eq} **Å**	V_{zz} **V/Å^2**	η
	H	103	3.76	837.3	0.00
1/2	T	110	3.69	808.6	0.00
	B	108	3.70	824.6	0.02
3/8	*HTT*	123	3.60	489.7	0.00
	H	171	3.48	−3.0	0.00
1/8	T	162	3.49	−9.6	0.00
	B	165	3.53	−14.3	0.23
	H	186	3.45	−6.6	0.00
1/18	T	178	3.46	−13.8	0.00
	B	180	3.49	−19.0	0.27
	H	188	3.44	−8.4	0.00
1/32	T	180	3.45	−13.8	0.00
	B	181	3.46	−19.5	0.30

experiments would allow to locally probe adatoms in the low-coverage extreme (down to ~ 0.01 %), while being compatible with applied electric and magnetic fields, and avoiding the influence of external probes and particle beams.

V. ACKNOWLEDGEMENTS

This work was funded by the Portuguese Foundation for Science and Technology (FCT) ($CERN-FIS-NUC-0004-2015$, $CERN-FIS-PAR-0005-2017$, $SFRH/BPD/82059/2011$, $SFRH/BD/93336/2013$ and $SFRH/BD/84743/2012$), by CICECO-Aveiro Institute of Materials ($POCI-01-0145-FEDER-007679$) - FCT Ref. ($UID/CTM/50011/2013$), by the Scientific Research Flanders ($G.0983.15$) and the KU Leuven BOF ($CREA/14/013$ and $STRT/14/002$).

[1] K. S. Novoselov, A. K. Geim, S. V. Morozov, D. Jiang, Y. Zhang, S. V. Dubonos, I. V. Grigorieva, and A. A. Firsov *Science*, vol. 306, no. 5696, pp. 666–669, 2004.

[2] A. K. Geim and K. S. Novoselov *Nature Materials*, vol. 6, pp. 183–191, 2007.

[3] N. M. R. Peres *Europhysics News*, vol. 40, no. 3, pp. 17–20, 2009.

[4] C. Lee, X. Wei, J. W. Kysar, and J. Hone *Science*, vol. 321, p. 385, 2008.

[5] A. S. Mayorov, R. V. Gorbachev, S. V. Morozov, L. Britnell, R. Jalil, L. A. Ponomarenko, P. Blake, K. S. Novoselov, K. Watanabe, T. Taniguchi, and A. K. Geim *Nano Letters*, vol. 11, no. 6, pp. 2396–2399, 2011.

[6] R. R. Nair, P. Blake, A. N. Grigorenko, K. S. Novoselov, T. J. Booth, T. Stauber, N. M. R. Peres, and A. K. Geim *Science*, vol. 320, no. 5881, pp. 1308–1308, 2008.

[7] A. H. Castro Neto, F. Guinea, N. M. R. Peres, K. S. Novoselov, and A. K. Geim *Reviews of Modern Physics*, vol. 81, pp. 109–162, 2009.

[8] K. S. Novoselov, D. Jiang, F. Schedin, T. J. Booth, V. V. Khotkevich, S. V. Morozov, and A. K. Geim *Proceedings of the National Academy of Science*, vol. 102, pp. 10451–10453, 2005.

[9] D. A. Areshkin, D. Gunlycke, and C. T. White *Nano Letters*, vol. 7, no. 1, pp. 204–210, 2007.

[10] K. S. Novoselov, Z. Jiang, Y. Zhang, S. V. Morozov, H. L. Stormer, U. Zeitler, J. C. Maan, G. S. Boebinger, P. Kim, and A. K. Geim *Science*, vol. 315, p. 1379, 2007.

[11] Y. Zhang, Y.-W. Tan, H. L. Stormer, and P. Kim *Nature*, vol. 438, pp. 201–204, Nov. 2005.

[12] B. Li, X. Cao, H. G. Ong, J. W. Cheah, X. Zhou, Z. Yin, H. Li, J. Wang, F. Boey, W. Huang, and H. Zhang *Advanced Materials*, vol. 22, no. 28, pp. 3058–3061, 2010.

[13] J. Zhao, S. Pei, W. Ren, L. Gao, and H.-M. Cheng *ACS Nano*, vol. 4, no. 9, pp. 5245–5252, 2010.

[14] A. Kasry, M. A. Kuroda, G. J. Martyna, G. S. Tulevski, and A. A. Bol *ACS Nano*, vol. 4, no. 7, pp. 3839–3844, 2010.

[15] N. Yang, J. Zhai, D. Wang, Y. Chen, and L. Jiang *ACS Nano*, vol. 4, no. 2, pp. 887–894, 2010.

[16] L. Gomez De Arco, Y. Zhang, C. W. Schlenker, K. Ryu, M. E. Thompson, and C. Zhou *ACS Nano*, vol. 4, no. 5,

pp. 2865–2873, 2010.
[17] P. K. Ang, W. Chen, A. T. S. Wee, and K. P. Loh *Journal of the American Chemical Society*, vol. 130, no. 44, pp. 14392–14393, 2008.
[18] X. Dong, Y. Shi, W. Huang, P. Chen, and L.-J. Li *Advanced Materials*, vol. 22, no. 14, pp. 1649–1653, 2010.
[19] S. Casolo, O. M. Lovvik, R. Martinazzo, and G. F. Tantardini *The Journal of Chemical Physics*, vol. 130, no. 5, pp. 054704–054704, 2009.
[20] Y. Mao, J. Yuan, and J. Zhong *Journal of Physics: Condensed Matter*, vol. 20, no. 11, p. 115209, 2008.
[21] H. Sevinçli, M. Topsakal, E. Durgun, and S. Ciraci *Physical Review B*, vol. 77, p. 195434, 2008.
[22] J. Hu, J. Alicea, R. Wu, and M. Franz *Physical Review Letters*, vol. 109, p. 266801, 2012.
[23] I. I. Klimovskikh, M. M. Otrokov, V. Y. Voroshnin, D. Sostina, L. Petaccia, G. Di Santo, S. Thakur, E. V. Chulkov, and A. M. Shikin *ACS Nano*, vol. 11, no. 1, pp. 368–374, 2017.
[24] L. Liu, Z. Zhou, Q. Guo, Z. Yan, Y. Yao, and D. W. Goodman *Surface Science*, vol. 605, no. 17, pp. L47 – L50, 2011.
[25] R. Thapa, D. Sen, M. K. Mitra, and K. K. Chattopadhyay *Physica B Condensed Matter*, vol. 406, pp. 368–373, 2011.
[26] I. Shtepliuk, N. M. Caffrey, T. Iakimov, V. Khranovskyy, I. A. Abrikosov, and R. Yakimova *Scientific Reports*, vol. 7, p. 3934, 2017.
[27] D. Vilela, J. Parmar, Y. Zeng, Y. Zhao, and S. SÃąnchez *Nano Letters*, vol. 16, no. 4, pp. 2860–2866, 2016.
[28] T. P. Hardcastle, C. R. Seabourne, R. Zan, R. M. D. Brydson, U. Bangert, Q. M. Ramasse, K. S. Novoselov, and A. J. Scott *Physical Review B*, vol. 87, p. 195430, 2013.
[29] K. Potzger, T. E. Molholt, A. S. Fenta, and L. M. C. Pereira *Journal of Physics G: Nuclear and Particle Physics*, vol. 44, no. 6, p. 064001, 2017.
[30] "WIEN2k web page: http://susi.theochem.tuwien.ac.a." Accessed: 2018-02-17.
[31] R. O. Jones *Reviews of Modern Physics*, vol. 87, pp. 897–923, 2015.
[32] J. P. Perdew, K. Burke, and M. Ernzerhof *Physical Review Letters*, vol. 77, pp. 3865–3868, 1996.
[33] S. Grimme *Journal of Computational Chemistry*, vol. 25, no. 12, pp. 1463–1473, 2004.
[34] A. Ishii, M. Yamamoto, H. Asano, and K. Fujiwara *Journal of Physics: Conference Series*, vol. 100, no. 5, p. 052087, 2008.
[35] Q. Zhou, Y. Tang, C. Wang, Z. Fu, and H. Zhang *Computational Materials Science*, vol. 81, pp. 348 – 352, 2014.
[36] Q. Zhou, Z. Fu, Y. Tang, H. Zhang, and C. Wang *Physica E: Low-dimensional Systems and Nanostructures*, vol. 60, pp. 133 – 138, 2014.
[37] G. Giovannetti, P. A. Khomyakov, G. Brocks, V. M. Karpan, J. van den Brink, and P. J. Kelly *Physical Review Letters*, vol. 101, p. 026803, 2008.
[38] R. C. Weast, . Lide, David R., and U. of Rhode Island. Coastal Resources Center, "Crc handbook of chemistry and physics," 1978.
[39] W. Tröger, T. Butz, P. Blaha, and K. Schwarz *Hyperfine Interactions*, vol. 80, pp. 1109–1116, 1993.
[40] J. G. Correia, J. P. Araújo, S. M. Loureiro, P. Toulemonde, S. Le Floch, P. Bordet, J. J. Capponi, R. Gatt, W. Tröger, B. Ctortecka, T. Butz, H. Haas, J. G. Marques, and J. C. Soares *Physical Review B*, vol. 61, pp. 11769–11775, 2000.

6.2 Ag, Cd and In adatoms on graphene: manuscript 3

The electric field gradient as a signature of the binding and the local structure of adatoms on graphene

A. S. Fenta[1,2,3], C. O. Amorim[2], J. N. Gonçalves[2], N. Fortunato[2], M. B. Barbosa[4], S. Cottenier[5,6], M. J. Van Bael[1], J. G. Correia[3,7], L. M. C. Pereira[1], and V. S. Amaral[2]

[1] *KU Leuven, Instituut voor Kern-en Stralingsfysica, Celestijnenlaan 200 D, 3001 Leuven, Belgium*

[2] *Physics Department and CICECO, University of Aveiro, 3810-193 Aveiro, Portugal*

[3] *CERN, 1211 Geneva 23, Switzerland*

[4] *IFIMUP and IN-Institute of Nanoscience and Nanotechnology, Departamento de Física e Astronomia da Faculdade de Ciências da Universidade do Porto, Rua do Campo Alegre 687, 4169-007 Porto, Portugal*

[5] *Center for Molecular Modeling, Ghent University, 9052 Zwijnaarde, Belgium*

[6] *Department of Electrical Energy, Metals, Mechanical Constructions and Systems, Ghent University, 9052 Zwijnaarde, Belgium and*

[7] *C2TN, Instituto Superior Técnico, Campus Tecnológico e Nuclear, EN10, 2695-066 Bobadela LRS*

The adsorption stability of heavy metals (Ag, Cd, In and Hg) on graphene was studied based on density functional theory calculations. Binding energy and electric field gradient were calculated for each adatom, for various high-symmetry atomic configurations. Two coverage regimes were considered: a ratio of metal to carbon atoms of 1:18, corresponding to nearly isolated adatoms, and a ratio of 3:8 corresponding to a continuous metal monolayer. All of the studied elements are more stable as an isolated adatom. This study also establishes a relation between the binding energy and the hyperfine electric field gradient (EFG) tensor for each adatom, suggesting that the EFG can be used to probe the binding stability of adatoms on graphene. Furthermore, the EFG is found to be sensitive to the local atomic structure, distinguishing isolated from monolayer configurations, and for some cases, varying significantly with small variations in adatom position (at the sub-Å scale). Based on these calculations, we propose that hyperfine techniques that can measure the EFG and for which suitable isotopes exist, such as perturbed angular correlation spectroscopy, can be used to experimentally unravel details of atomic adsorption on graphene, and by extension on 2-dimensional materials in general.

I. INTRODUCTION

Graphene properties are intimately dependent on the two-dimensionality (2D) of its structure [1–4]. Being a single atomic layer, the adsorption of guest atoms (adatoms) or molecules (admolecules) has a strong effect on the properties graphene. Adatoms and admolecules are therefore a promising way to modify the properties of graphene and engineer a specific functionality that can be used in technological applications. Several studies have reported that structural, electronic and magnetic properties of graphene can be manipulated using adsorption of atoms, individually or organized in clusters [5–14]. Understanding the adsorption process of certain species on graphene requires studying their position stability relative to the underlying carbon honeycomb lattice [15]. Techniques such as scanning tunneling microscopy (STM) [16] and transmission electron microscopy (TEM) [17] have been extensively used to characterize the topographic and local electronic structure of graphene-adsorbent systems. Here we investigate to what extent the electric field gradient (EFG) can be used to probe the adatom-graphene interaction, adsorption stability, and local atomic configuration, owing to the high sensitivity of the EFG to changes in the local charge distribution. The EFG can be measured experimentally via its interaction with the nuclear electric quadrupole moment of a suitable probe atom, using techniques such as nuclear quadrupole resonance (NQR), Mössbauer spectroscopy (MS) or perturbed angular correlation (PAC) technique. Such measurements are particularly sensitive to changes induced by lattice distortions, such as host impurities or defects [18, 19] because they modify the local electrostatic potential, thus creating its own characteristic EFG. Therefore, the process of adsorption, spatial configuration and the stability of a certain adatom on graphene can be directly related to the experimentally determined EFG. The EFG is a traceless symmetric rank 2 tensor, defined as:

$$V_{ij} = \Phi_{ij} - \frac{1}{3} Tr(\Phi) \tag{1}$$

where $\Phi(\vec{r})$ is the electric potential due to the electron cloud at the nucleus position ($\vec{r} = 0$) and Φ_{ij} is defined as $\Phi_{ij} = \frac{\partial^2 \Phi(\vec{r})}{\partial x_i \partial x_j}$ [18, 20]. The tensor is symmetric due to the commutation of the second partial derivatives of the electrostatic potential $\Phi(\vec{r})$ and it is also a traceless at the probe site by definition, since the nucleus is approximated to a point charge from the point of view of the external electronic charge. The axis system can be defined in a way that the EFG tensor representation has only three non-vanishing diagonal components defined as

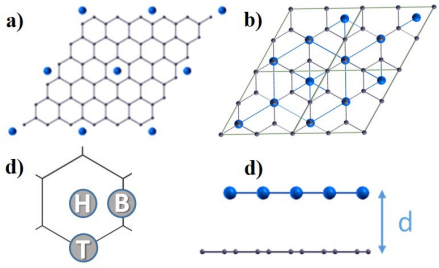

Figure 1. **Atomic configurations considered in the calculations: (a) 3×3 supercell for adatoms at the hollow site (H) on graphene, corresponding to a nominal concentration of $\theta = 1/18$ with respect to the number of carbon atoms; (b) the monolayer in a HTT configuration, with nominal concentration of $\theta = 3/8$; (c) the three high-symmetry positions on graphene, i.e. the hollow (H) site above the center of the hexagon, the top (T) site on top of the C atoms, and the bridge (B) site above the middle of the C-C bonds; d) graphene-adatom distance d.**

$|V_{zz}| \geq |V_{yy}| \geq |V_{xx}|$. For simplicity, it is common to characterize the EFG tensor by its main component V_{zz} and the axial asymmetry parameter, η, defined by:

$$\eta = \frac{V_{yy} - V_{xx}}{V_{zz}} \tag{2}$$

taking into account that the three remaining degrees of freedom are characterized by the Euler angles that correlate the principal axis system where the EFG is diagonal with the axis system where the laboratory is defined.

A precise calculation of the entire electronic configuration of graphene and the adatoms can be performed using density functional theory (DFT). DFT calculations have assumed an important role in experimental data interpretation of the EFGs measured with hyperfine techniques [21, 22]. This paper presents a set of DFT studies of electronic structure and EFG tensor for selected adatom elements on graphene: Ag, Cd, In and Hg, which are widely studied using PAC spectroscopy due to the availability of suitable isotopes (with favorable and well-established decay schemes and nuclear moments). These calculations provide insight on the stability of various adsorption configurations and its relation with the EFG tensor. In particular, it sets the basis for a new experimental approach that is currently being developed at the ISOLDE facility at CERN [23], using the ASPIC setup (Apparatus for Surface Physics and Interfaces at CERN) [24], where a multitude of radioactive isotopes can be deposited and measured *in-situ* with PAC spectroscopy.

II. COMPUTATIONAL METHOD

The DFT calculations were performed using WIEN2K [25], which implements the linearized augmented plane wave (LAPW) method. This method divides space into non-overlapping spheres described by spherical harmonics and the interstitial region, described by plane waves. It is an all-electron code (employing the full charge distribution of all electrons) and for this reason particularly stuited to calculate hyperfine parameters. The muffin-tin radii were set to 1.29 and 1.70 atomic units, for the carbon atoms and for the adatoms, respectively. The number of plane waves is set by the parameter $R_{mt} \times K_{max} = 5.5$, where $R_{mt} = 1.29$ au (the radius of the smallest sphere). The nominal concentrations of the adatoms with respect to the number of carbon atoms was $\theta = 1/18$, corresponding to a 3×3 (C-hexagon) supercell, with a grid of $10 \times 10 \times 1$ k-points. Three sets of calculations for each adatom were performed for the different adsorption sites allowed by symmetry (Figure 1): the hollow (H) site, the top (T) site, and the bridge (B) site. An additional configuration was also considered in the calculations: an hexagonal monolayer with the atoms in a sequence of H-T-T sites (therefore designated here as HTT configuration), with a concentration of $\theta = 3/8$ with respect to C atoms, with an inplane interatomic distance (2.84 Å) which is comparable to solid Ag, Cd, In and Hg, in bulk. The HTT configuration is equivalent to a (111) plane of a cubic lattice, which is a typical interfacial structure between graphene on various $< 111 >$ oriented metal substrates (e.g. Al, Au, Pd, and Pt) [26]. A vacuum spacing of at least 16 Å between adjacent layers is used, to minimize interlayer interactions. The calculations did not consider spin polarization. The generalized gradient approximation (GGA-PBE) [27] with van der Waals correction (DFT-D3) [28] for the exchange correlation functional was used. The experimental lattice parameter $a = b = 2.46$ Å which is close to the optimized parameters with GGA (2.47 Å) for undoped graphene was adopted.

III. RESULTS

We start by analyzing the isolated adatom regime ($\theta = 1/18$), for the different high-symmetry positions (H, T, B). Figure 2 shows the adsorption energy curves of the graphene-adatom system, as a function of graphene-adatom distance d for Ag, Cd, In and Hg. The adatom stability on graphene is related to the adsorption energy (E_{ads}) which can be defined as:

$$E_{ads} = E_{G+adatom} - E_G - E_{adatom} \tag{3}$$

where $E_{G+adatom}$ is the energy of the system graphene plus adatom, and E_G and E_{adatom} are the energy of

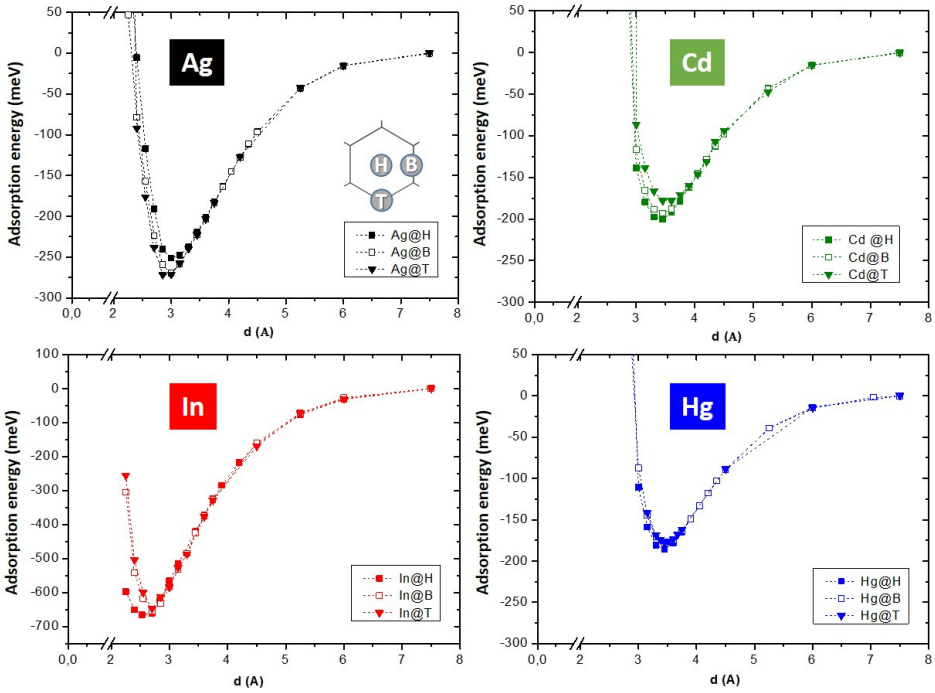

Figure 2. **Adsorption energy of the graphene-adatom system as a function of the distance (d) between graphene and the adatom for the three high-symmetry positions (H, B and T), for Ag, Cd, In and Hg, for a nominal concentration of $\theta = 1/18$.**

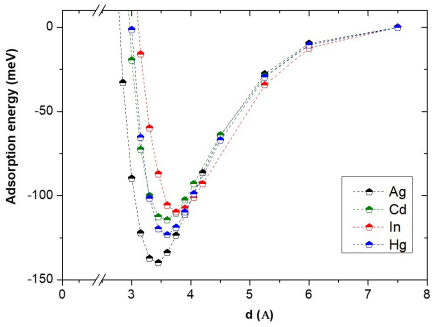

Figure 3. **Adsorption energy of the HTT configuration ($\theta = 3/8$) as a function of distance, d, for Ag, Cd, In and Hg.**

graphene and the energy of the adatom, respectively. Larger absolute values of the adsorption energy correspond to stronger binding of the adatom to the surface of graphene. The binding energy (E_b) is defined as the absolute value of the minimum of the adsorption energy at a corresponding equilibrium distance (d_{eq}). Each adatom element (Ag, Cd, In and Hg) presents qualitatively similar shapes of the adsorption energy curve for the various high-symmetry sites (H, T, and B). However, both E_b and d_{eq} depend on the adatom element and adsorption site (Table 1). Apart from the Ag case, for which the binding energy reaches its highest value for the T-site (274 mev), all the other adatoms have their highest binding energy at the H-site. Among the elements studied here, in the dilute regime ($\theta = 1/18$), we can conclude that In has the highest binding energy (666 meV), and Hg the lowest (186 meV). Also, with increasing binding energy, the corresponding graphene-adatom distance tends to decrease and therefore In stabilizes closer to the surface of graphene ($d_{eq} = 2.63$ Å) compared to Hg ($d_{eq} = 3.45$ Å).

Next we compare the stability of the isolated adatoms

Table I. **High-symmetry positions, binding energy (E_b) and corresponding distance (d_{eq}), EFG parameters (V_{zz} and η), stable isolated site (i.e. site with highest binding energy in the isolated configuration) meta-stable position (i.e. site with the second highest binding energy in the isolated configuration) and respective energy barrier for hopping between stable sites (ΔE_{hop}, i.e. energy difference between stable and meta-stable sites), for isolated adatoms (θ = 1/18) and the HTT configuration (θ = 3/18), for adsorbed Ag, Cd, In and Hg on graphene.**

	Concentration	**Position**	E_b	d_{eq}	V_{zz}	η	**Stable isolated site**	**Meta-stable isolated site**	ΔE_{hop}
θ			**(meV)**	**(Å)**	**(V/Å^2)**				**(meV)**
Ag	1/18	H	252	3.10	−0.7	0.00			
	1/18	T	**274**	**2.90**	**-12.5**	**0.00**	**T**	**B**	5
	1/18	B	269	3.00	1.0	0.24			
	3/8	HTT	140	3.45	65.10	0.00			
Cd	1/18	H	**201**	**3.43**	**-2.4**	**0.00**			
	1/18	T	181	3.60	−0.30	0.00	**H**	**B**	7
	1/18	B	194	3.44	−0.49	0.36			
	3/8	HTT	115	3.60	227.10	0.00			
In	1/18	H	**666**	**2.63**	**25.0**	**0.00**			
	1/18	T	645	2.73	−1.6	0.00	**H**	**B**	14
	1/18	B	652	2.71	8.4	0.90			
	3/8	HTT	110	3.75	149.04	0.00			
Hg	1/18	H	**186**	**3.45**	**-6.6**	**0.00**			
	1/18	T	178	3.46	−13.8	0.00	**H**	**B**	6
	1/18	B	180	3.49	−19.0	0.27			
	3/8	HTT	124	3.60	489.70	0.00			

(θ = 1/18) to the HTT monolayer configuration (θ = 3/8). Figure 3 displays the adsorption energy as a function of graphene-adatom distance, for Ag, Cd, In and Hg in a HTT configuration. The respective binding energies are also compiled in Table 1. When the adatoms assume the HTT configuration on graphene, Ag has the largest binding energy (420 meV) in contrast to In, with the lowest binding energy (330 meV). For all the studied elements the isolated adatom regime is predicted to be the most stable configuration when compared to the HTT monolayer configuration. The equilibrium site for Cd, In and Hg is found to be the H site and for Ag the T site.

In addition to the adsorption energies discussed above, for each configuration, we calculated the respective EFG parameters (V_{zz} and η). Since, only the isolated configuration on B sites, which is never the most stable position, exhibits a non-vanishing η value, we will not further discuss the η parameter.[1] The first key observation is that different configurations are associated with different values of V_{zz} (Table 1). In particular, the V_{zz} value is always significantly larger for the HTT configuration, compared to the stable isolated site. Before discussing (in the next paragraph) what kind of information can be experimentally assessed based on measurements of the EFG parameters, we first comment on the observed dependence of the V_{zz} on the distance d between the adatom and the graphene layer in the dilute regime (θ = 1/18). In Figure 4 the absorption energy and the V_{zz} (for each adatom element in the respective stable site, i.e. H or T) is plotted as a function of distance d (in $\sim$ 10 pm steps) in the vicinity of the equilibrium position d_{eq}. The figure shows that the sensitivity of V_{zz} to changes in d ($\Delta V_{zz}/\Delta d$) varies significantly among the different elements. Indium, which among the considered elements exhibits the highest binding energy and V_{zz} (25.0 VÅ^{-2}), also shows the largest $\Delta V_{zz}/\Delta d$ value (2.50 VÅ^{-2}/pm). To further analyze the trend across the different elements, let us define a relative variation, i.e. dividing $\Delta V_{zz}/\Delta d$ by the absolute value of the V_{zz} at the equilibrium distance ($\mid V_{zz}^{eq} \mid$), and expressing it as a percentage ($(\Delta V_{zz}/(\mid V_{zz}^{eq} \mid \Delta d)) \times 100\%$). These values (1.9 %, 2.1 %, 2.8 % and 10 % per pm, for Hg, Cd, Ag and In respectively) are plotted in Figure 5 as a function of the calculated binding energy (E_b). The monotonous increase with increasing E_b suggests that there is a close relation between the strength of the graphene-adatom binding and the EFG in the isolated adatom regime (θ = 1/18). This relation can be understood based on the fact that the binding and the EFG have a common origin: orbital overlap (charge sharing) between the adatom and the graphene layer. In order to gain further insight into how the binding (i.e. the

[1] For H and T sites η must necessarily be zero, since the z-axis is a 3-fold rotation axis.

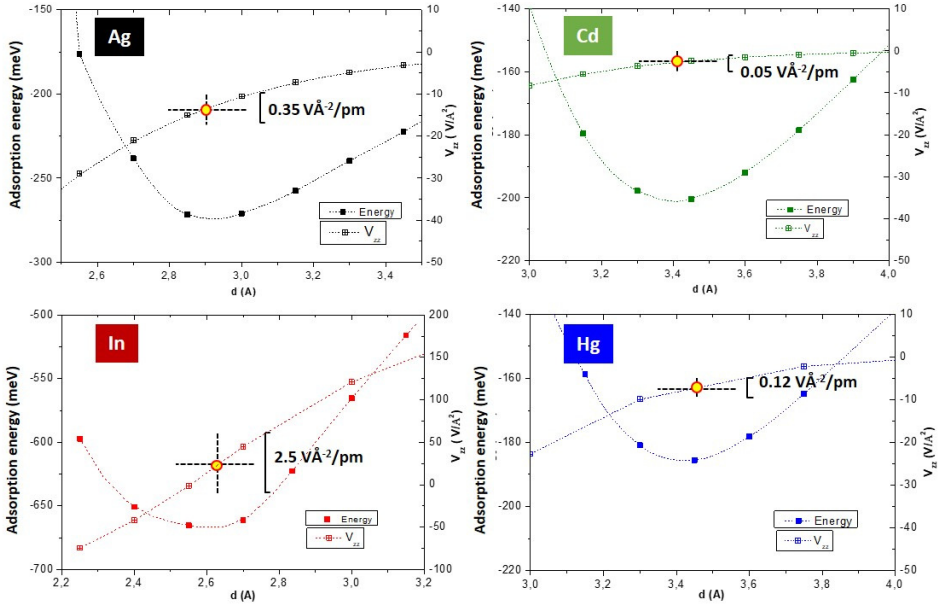

Figure 4. V_{zz} **at the adatom site and adsorption energy as a function of distance** d **for the most stable site: Ag (in a T site), Cd (in a H site), In (H) and Hg (H). The sensitivity of** V_{zz} **to the distance** d**, in the vicinity of the equilibrium position, is represented by a cross: the horizontal line has a length of** $\Delta d = 20$ **pm, i.e. of the order of the** d **steps used in the calculations; the vertical line has a length** ΔV_{zz} **corresponding to a** $\Delta d = 20$ **pm around the equilibrium position; the value of** $\Delta V_{zz}/\Delta d$ **is also given in units of V Å**$^{-2}$**/pm.**

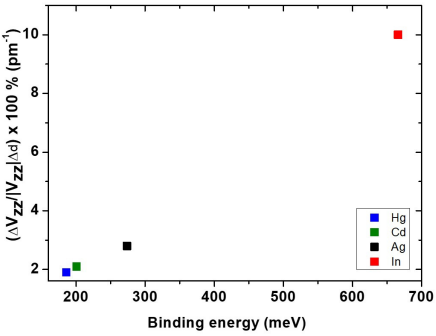

Figure 5. **Relative variation of** V_{zz} $((\Delta V_{zz}/(\mid V_{zz}^{eq} \mid \Delta d)) \times 100\ \%)$ **in the vicinity of the equilibrium position, as a function of binding energy, for Ag, Cd, In and Hg adatoms, in the isolated regime** ($\theta = 1/18$)**.**

electronic density distribution) is related to the EFG, we analyzed the contributions to EFG from the obitals involved in the binding (for each adatom element in its equilibrium position). The EFG inside the spheres can be analyzed by separating the atomic-like functions into contributions corresponding to *Gaunt* numbers with different pairs of angular orbital momentum numbers [18]: *p-p*, *d-d* (*s-d*and *p-f*), which may be interpreted as electrons from the corresponding orbitals contributing to the EFG. For all the cases, the most significant contribution to the V_{zz} arises from *p-p* orbitals. The large difference between the most (In) and least (Cd) sensitive element in terms of V_{zz} results from the contrasting degrees of *p-orbital* superposition. To further illustrate this relation between the binding and the EFG, Figure 6 shows the charge distribution and the charge isolines in the adatom-graphene system, from which the degree of charge sharing can be inferred. The highly symmetric charge distribution, with circular isolines of the outer electronic shells of the adatoms for the case of Cd and Hg (*d orbitals* fully-filled), leads to low V_{zz} values (-2.4 V/Å^2 and -6.6 V/Å^2, respectively). On the other hand, the

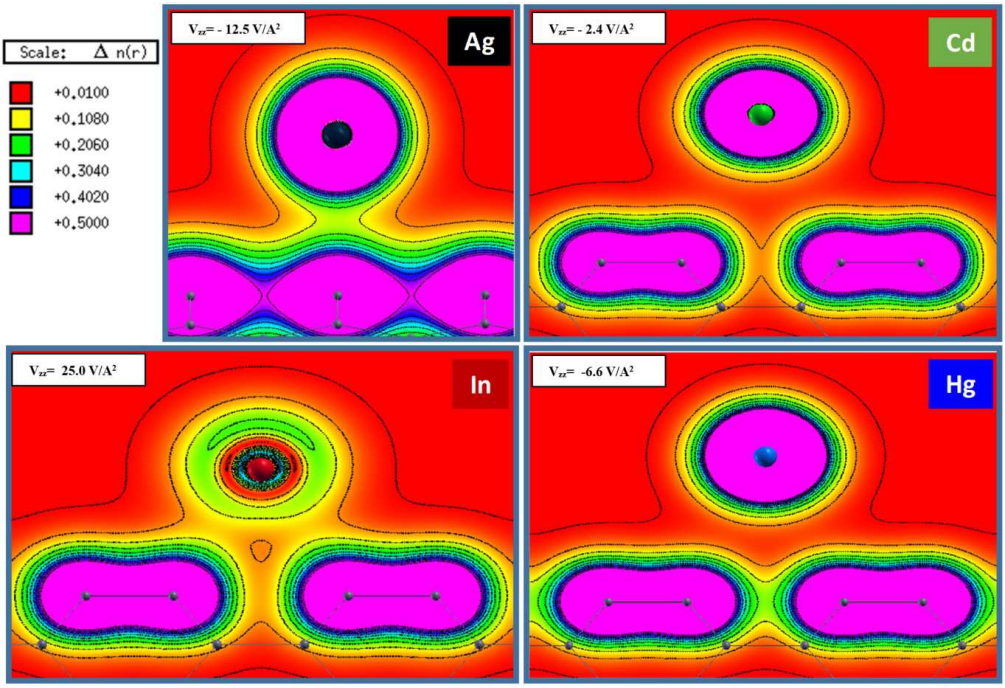

Figure 6. **Charge density (in units of $e/\text{Å}^3$) of the graphene-adatom system for the stable site and equilibrium distance of each adatom element: Ag (in a T site), Cd (in a H site), In (H) and Hg (H). The respective calculated V_{zz} is given in the inset. The orbital overlap decreases from In to Ag and then to Hg and Cd. As discussed in the text, the orbital overlap (charge sharing) is closely related with the binding strength and the EFG parameters.**

higher V_{zz} values observed for In and Ag (25.0 V/Å^2 and -12.5 V/Å^2, respectively), are a consequence of the non-spherical charge distribution around the adatom (with s and p incomplete orbitals for In and Ag, respectively), caused by the strong interaction with the graphene lattice. In other words, stronger charge sharing implies a stronger binding and more pronounced asymmetry of the outer electron shells along the binding direction, which in turn tends to produce a larger V_{zz} and a stronger sensitivity of V_{zz} to variations in d (since an increasing d is associated with a decrease in charge sharing). This notion is further supported by the fact that the same trend is not observed for the monolayer (HTT) regime, since there the EFG is dominated by contributions from the neighboring metal atoms (in the isolated adatom regime, this contribution is negligible), masking the effects of the interaction with the graphene lattice.

Finally, we discuss how the calculated EFG parameters, which strongly depend on the local charge distribution, can be used in an experimental setting to study the binding and spatial configurations of adatoms on graphene. This involves comparing the EFG values calculated for possible configurations to those measured experimentally using hyperfine techniques. Perturbed angular correlation (PAC) spectroscopy is a particularly suited technique to measure the EFG parameters. In order to illustrate what kind of information can be obtained from PAC experiments on atomic adsorption on graphene, we take the case of In, for which the EFG shows the highest sensitivity among the elements considered here. As an isolated adatom, In exhibits a migration barrier (ΔE_{hop} along H$\longleftrightarrow$B paths) of $\sim$ 14 meV which corresponds to a threshold temperature for diffusion of the order of 5 K.[2] In an experimental scenario, this implies that if In atoms are randomly deposited on

[2] Assuming an Arrhenius model for thermally activated diffusion, we have $\Lambda = \nu_0 e^{-\frac{E_a}{k_B T}}$, where Λ is the the rate of thermally activated jumps, ν is the attempt frequency (which we take as

graphene at liquid He temperatures, the mobility will be sufficiently low to allow to study In adatoms in their most stable high-symmetry site in an ideal (defect-free) graphene surface (H sites, based on the calculations presented here). At higher temperatures, with increasing mobility on the graphene surface, the adatoms would likely diffuse and become trapped in defective regions (e.g. graphene edges, Stone Wales defects, vacancies, grain boundaries) [29–31]. For PAC experiments on In, the decay of ^{117}Cd to the 315 keV excited state of ^{117}In through the 660 keV intermediate state (where the PAC measurement takes place) with spin of $3/2^-$ and 53.6 ns half-life is well established [32]. PAC is a time differential statistical measurement where the observable is the decay histogram of two consecutive γ-rays in coincidence. Taking into account the half-life of the mentioned probing state, no more than 400 ns (approximately 8 half-lives) can be resolved with enough statistics. Therefore, we estimate a limit such that half a period of the characteristic PAC perturbation function can still be resolved, i.e. 400/2 ns, leading to a minimum value of V_{zz} to be experimentally determined of 1.8 V/Å^2, with an uncertainty of about 2 % estimated from the uncertainty associated with the quadrupole moment. This implies that based on PAC measurements of V_{zz}, it would be possible to distinguish the two main regimes of In adatom concentration on graphene, i.e. between isolated In adatoms ($\theta = 1/18$) with $V_{zz} = 25$ V/Å^2 and the HTT monolayer ($\theta = 3/8$) $V_{zz} = 149$ V/Å^2 . Furthermore, in the isolated adatom regime, an experimental measurement would allow to identify which high-symmetry sites are occupied by In adatoms on graphene, and determine the adatom-graphene distance with high (sub-Å) precision (Table 1). Although according to the calculations presented here, for In adatoms on free standing graphene, the equilibrium configuration is that of isolated In adatoms on H sites, other configurations may be populated under the effect of additional parameters, such as an underlying substrate or applied fields. Similar considerations could be done for example for Ag, although in that case, the H site was predicted to be the equilibrium site. Upon random deposition of sub-monolayer amounts of Ag at a sufficiently low temperature, the isolated state would in principle be observed. With increasing temperature, and therefore increasing mobility of the Ag adatoms, the monolayer configuration and its associated higher V_{zz} could eventually be observed. Although the calculations presented here suggest that the dilute configuration is more stable than monolayer configurations, it is plausible that under different conditions, segregation may occur. For example, shifts of the Fermi level due to defects or specific substrates may affect the electrostatic interaction between the adatoms and thereby stabilize monolayer configurations. Such experiments can be performed, for example, using the ASPIC setup at the ISOLDE facility at CERN [24], where adatoms can be deposited at low temperature, down to liquid He, and PAC measurements can be performed *in-situ* as a function of temperature. While ASPIC has been previously used to investigate structural and magnetic properties of metal surfaces (e.g. Ni and Pd) [24], the calculations presented here show the potential of hyperfine techniques in the context of adatoms on graphene and on 2-dimensional materials in general, by extension. One of the advantages of this approach is that it allows to locally probe the adatom without affecting it, i.e. avoiding the influence of external probes, such as the tip of a scanning probe microscope or the intense electron beam of a transmission electron microscope. Additionally, a PAC spectrum can be measured with as little as 5^{10} probe atoms, corresponding to a coverage of 0.01 % for a typical 5×5 mm^2 sample, i.e. the approach can be applied down to extreme levels of adatom dilution. Moreover, measurements are compatible with applied electric or magnetic fields [24]. Also very importantly, our calculations strongly indicate that the amount of information that can be addressed via the EFG parameters (sensitivity of the V_{zz} to changes in the atomic configuration) increases with the stability (binding energy), i.e. that the more robust the graphene-adatom system, the more prone it is to be studied using this approach. In future studies, it would be interesting to extend these calculations to, for example, transition elements such as 3d transition metals or 4f rare earths. Not only can these elements be expected to exhibit even higher binding energies than In (e.g. in excess of 1 eV for Fe, Co and Ti [7]), and therefore even higher sensitivity of the EFG to structural observables, magnetic properties (e.g. local moment, magnetic order etc.) could also be addressed via the magnetic hyperfine interaction.

IV. CONCLUSIONS

For In, Ag, Cd, and Hg, the isolated adatom regime is predicted to be the equilibrium configuration, which is more stable than the continuous monolayer configuration. The equilibrium site for Cd, In and Hg is found to be the H site; for Ag the T site. The binding energy associated with the equilibrium configuration varies significantly among the elements considered here, from 110 meV for a continuous In monolayer, to 666 meV for isolated In adatoms. In the isolated adatom regime, a close relation is found between the binding stability (binding energy) and the sensitivity of the V_{zz} parameter to the local atomic configuration. We interpret this relation as due to the shared origin of the graphene-adatom binding and the associated EFG at the adatom site: the orbital overlap (charge sharing) between the single adatom

---

$\nu_0 = 10^{12}$ s^{-1}, of the order of the lattice vibrations), k_B the Boltzmann constant and and T the temperature. We can then estimate the temperature regime associated with jumps between neighboring sites within a certain time scale. For $\Delta E_{hop} = 14$ meV, the temperature associated with 1 jump between neighboring H sites within 1 minute (60 s) window is 5 K.

and the graphene layer and the associated asymmetry of the outer electron shells along the binding direction. Based on this relation, we propose that the V_{zz} parameter, which can be measured using hyperfine techniques, can be used in an experimental setting to probe the stability of atomic adsorption. Furthermore, the EFG is found to be sensitive to the local atomic structure, distinguishing isolated from monolayer configurations, and for some cases, allowing to identify the high-symmetry site occupied by the adatoms and even monitor small variations in graphene-adatom distance with sub-Å precision. In particular, our calculations indicate that the level of detail that can be addressed via the EFG parameters (e.g. positional precision) increases with the stability (binding energy). In other words, the more stable graphene-adatom system (i.e. more relevant in a application scenario), the more it lends itself to be studied using hyperfine techniques. Future studies could extend these calculations to other 2-dimensional materials and other types of adatoms. For example, transition elements typically have high binding energies, and therefore can be expected to exhibit a high sensitivity of the EFG to structural observables. Moreover, their magnetic properties could also be addressed via the magnetic hyperfine interaction. In addition to the ability to probe multiple adatom properties and phenomena (e.g. structural and magnetic), such an experimental approach based on hyperfine techniques is generally compatible with ultra-high vacuum (typically necessary when studying surfaces, to minimize contamination), low temperature (typically necessary when studying isolated adatoms, due to their high surface mobility), and applied electric or magnetic fields (often used to investigate both basic and functional properties).

V. ACKNOWLEDGEMENTS

This work was funded by the Portuguese Foundation for Science and Technology (FCT) ($CERN-FIS-NUC-0004-2015$, $CERN-FIS-PAR-0005-2017$, $SFRH/BPD/82059/2011$, $SFRH/BD/93336/2013$ and $SFRH/BD/84743/2012$), by CICECO-Aveiro Institute of Materials ($POCI-01-0145-FEDER-007679$) - FCT Ref. ($UID/CTM/50011/2013$), by the Scientific Research Flanders ($G.0983.15$) and the KU Leuven BOF ($CREA/14/013$ and $STRT/14/002$).

[1] K. S. Novoselov, A. K. Geim, S. V. Morozov, D. Jiang, Y. Zhang, S. V. Dubonos, I. V. Grigorieva, and A. A. Firsov *Science*, vol. 306, no. 5696, pp. 666–669, 2004.

[2] A. K. Geim and K. S. Novoselov *Nature Materials*, vol. 6, pp. 183–191, 2007.

[3] N. M. R. Peres *Europhysics News*, vol. 40, no. 3, pp. 17–20, 2009.

[4] C. Lee, X. Wei, J. W. Kysar, and J. Hone *Science*, vol. 321, p. 385, 2008.

[5] K. T. Chan, J. B. Neaton, and M. L. Cohen *Physical Review B*, vol. 77, p. 235430, 2008.

[6] Y. Mao, J. Yuan, and J. Zhong *Journal of Physics Condensed Matter*, vol. 20, no. 11, p. 115209, 2008.

[7] H. Sevinçli, M. Topsakal, E. Durgun, and S. Ciraci *Physical Review B*, vol. 77, p. 195434, 2008.

[8] A. V. Krasheninnikov, P. O. Lehtinen, A. S. Foster, P. Pyykkö, and R. M. Nieminen *Physical Review Letters*, vol. 102, p. 126807, 2009.

[9] R. C. Longo, J. Carrete, J. Ferrer, and L. J. Gallego *Physical Review B*, vol. 81, p. 115418, 2010.

[10] C. Cao, M. Wu, J. Jiang, and H.-P. Cheng *Physical Review B*, vol. 81, p. 205424, 2010.

[11] H. Johll, J. Wu, S. W. Ong, H. C. Kang, and E. S. Tok *Physical Review B*, vol. 83, p. 205408, 2011.

[12] T. O. Wehling, A. I. Lichtenstein, and M. I. Katsnelson *Physical Review B*, vol. 84, p. 235110, 2011.

[13] M. K. Srivastava, Y. Wang, A. F. Kemper, and H.-P. Cheng, "Density functional study of gold and iron clusters on perfect and defected graphene," *Physical Review B*, vol. 85, p. 165444, 2012.

[14] R. Zan, U. Bangert, Q. Ramasse, and K. S. Novoselov *Nano Letters*, vol. 11, no. 3, pp. 1087–1092, 2011.

[15] M. Vojta, L. Fritz, and R. Bulla *Europhysics Letters*, vol. 90, no. 2, p. 27006, 2010.

[16] V. W. Brar, R. Decker, H.-M. Solowan, Y. Wang, L. Maserati, K. T. Chan, H. Lee, Ç. O. Girit, A. Zettl, S. G. Louie, M. L. Cohen, and M. F. Crommie *Nature Physics*, vol. 7, pp. 43–47, 2011.

[17] C. Gong, A. W. Robertson, K. He, C. Ford, A. A. R. Watt, and J. H. Warner *Dalton Transactions*, vol. 43, pp. 7442–7448, 2014.

[18] S. C. Katrin Koch, *Analysis of an Electric-Field Gradient (EFG): the EFG-switch in LAPW2*. 2006.

[19] A. Lopes, *Local probe studies on lattice distortions and electronic correlations in CMR Manganites*. Aveiro University, 2006.

[20] K. Koch, *Crystal structure, electron density and chemical bonding in inorganic compounds studied by the Electric Field Gradient*. University of Dresden, 2009.

[21] S. Dey, C. Dey, S. Saha, and J. Belošević-Čavor *Intermetallics*, vol. 84, pp. 112 – 120, 2017.

[22] L. Errico, K. Lejaeghere, J. Runco, S. N. Mishra, M. Rentería, and S. Cottenier *The Journal of Physical Chemistry C*, vol. 120, no. 40, pp. 23111–23120, 2016.

[23] http://isolde.web.cern.ch/.

[24] K. Potzger, T. E. Mølholt, A. S. Fenta, and L. M. C. Pereira *Journal of Physics G: Nuclear and Particle Physics*, vol. 44, no. 6, p. 064001, 2017.

[25] http://susi.theochem.tu.ac.at.

[26] G. Giovannetti, P. A. Khomyakov, G. Brocks, V. M. Karpan, J. van den Brink, and P. J. Kelly *Physical Review Letters*, vol. 101, p. 026803, 2008.

[27] J. P. Perdew, K. Burke, and M. Ernzerhof *Physical Review Letters*, vol. 77, pp. 3865–3868, 1996.

[28] S. Grimme, J. Antony, S. Ehrlich, and H. Krieg *Journal of Chemical Physics*, vol. 132, no. 15, pp. 154104–154104, 2010.

[29] T. P. Hardcastle, C. R. Seabourne, R. Zan, R. M. D. Brydson, U. Bangert, Q. M. Ramasse, K. S. Novoselov, and A. J. Scott *Physical Review B*, vol. 87, p. 195430, 2013.

[30] Q. Zhou, Y. Tang, C. Wang, Z. Fu, and H. Zhang *Computational Materials Science*, vol. 81, pp. 348 – 352, 2014.

[31] Q. Zhou, Z. Fu, Y. Tang, H. Zhang, and C. Wang *Physica E: Low-dimensional Systems and Nanostructures*, vol. 60, pp. 133 – 138, 2014.

[32] A. Burchard, M. Deicher, V. N. Fedoseyev, D. Forkel-Wirth, R. Magerle, V. I. Mishin, D. Steiner, A. Stötzler, R. Weissenborn, T. Wichert, and ISOLDE Collaboration *Hyperfine Interactions*, vol. 120, pp. 389–395, Sept. 1999.

6.3 HgO_2 admolecules on graphene: manuscript 4

Adsorption of Hg on graphene stabilized by the formation of HgO_2 molecules

A. S. Fenta[1,2,3], C. O. Amorim[2], J. N. Gonçalves[2], N. Fortunato[2], T. M. Mendonça[3], M. B. Barbosa[4], G. Lippertz[1], J. McNulty[1], E. Moyen[5], Youngwoo Kim[6], D. Pribat[5], Y. Kadi[3], V. S. Amaral[2], L. M. C. Pereira[1], and J. G. Correia[3,7]

[1] *KU Leuven, Instituut voor Kern-en Stralingsfysica, Celestijnenlaan 200 D, 3001 Leuven, Belgium*

[2] *Physics Department and CICECO, University of Aveiro, 3810-193 Aveiro, Portugal*

[3] *CERN, 1211 Geneva 23, Switzerland*

[4] *IFIMUP and IN-Institute of Nanoscience and Nanotechnology, Departamento de Física e Astronomia da Faculdade de Ciências da Universidade do Porto, Rua do Campo Alegre 687, 4169-007 Porto, Portugal*

[5] *Department of Energy Science, Sungkyunkwan University, Suwon 16419, Republic of Korea*

[6] *Advanced Display Research Center (ADRC), Department of Information Display, Kyung Hee University, Seoul 02447, Republic of Korea and*

[7] *C2TN, Instituto Superior Técnico, Campus Tecnológico e Nuclear, EN10, 2695-066 Bobadela LRS*

Adsorption of Hg on graphene, in the form of linear HgO_2 molecules, was experimentally observed using perturbed angular correlation (PAC) spectroscopy and ^{199m}Hg as probe nuclei, combined with density functional theory (DFT) calculations. The formation of stable HgO_2 molecules is crucial for the efficient adsorption, since the O atoms strengthen the binding to graphene (binding energy above 1 eV). This work also constitutes a proof-of-principle for the use of hyperfine techniques to study the interaction between graphene and adsorbed atoms and molecules, at the atomic scale. The electric field gradient (EFG), which can be measured using hyperfine techniques such as PAC, and can be calculated for various possible configurations using DFT, is characteristic of the charge distribution around the probe nucleus, therefore providing a specific signature of the binding of the adsorbed species with graphene.

I. INTRODUCTION

The physical properties of graphene are directly affected by adsorption of atoms (adatoms) or molecules (admolecules). In analogy with the effects observed in ordinary metals that exhibit exotic properties such as magnetism or superconductivity when doped with transition metals, adatoms and admolecules have the potential to enable the use of graphene in a novel generation of nanodevices, provided that the adsorption is functionally stable [1, 2]. In graphene, all the atoms in the two-dimensional (2D) carbon lattice are available to participate in the binding to foreign elements or organized structures. The search for new forms of nucleation and doping, aiming to tune a specific property, constitutes today an active branch of research on graphene and 2D materials in general [3, 4].

The adsorption of heavy metals (HM) and its influence on the properties of graphene has been widely investigated, not only in terms of the basic physics of adsorption, stability, electric and magnetic properties [5], but also considering its potential application, for example, in catalysis reactions (e.g. Au [6] and Pd [7]), detection of toxic heavy metals (e.g. Cf, Hg and Pb [8]), and their removal from water (e.g. Pb [9]). Various molecular species, on the other hand, have also been investigated, in particular water, owing to the fundamental interest as well as its practical implications [10–18]. Other molecular adsorbates being investigated include small gas molecules (for example, H_2, O_2 and CO) [2, 19], aromatic and non-aromatic molecules [2, 19, 20]. Understanding the the adsorption mechanisms requires detailed insight into the local atomic structure and local electronic properties, which in turn typically involves both theoretical and experimental research. Density functional theory (DFT) has been extensively used to explore the stability of different adatoms and admolecules predicting many distinct phases, structural configurations and binding energies [21–24]. Experimental studies dealing with adatoms or adamolecules on graphene are often based on techniques such as scanning tunnelling microscopy (STM) or transmission electron microscopy (TEM) which allow to characterize the topographic and local electronic structure of the graphene-adsorbent system [25, 26]. Here we report on a novel approach to locally probe adsorption on graphene, consisting of the combination of DFT calculations with experimental techniques based on hyperfine interactions. Taking Hg as model case, we identify its adsorption on graphene in the form of linear HgO_2 molecules and characterize it in terms of the local atomic configuration and binding stability.

II. EXPERIMENTAL METHOD

Since there are no stable Hg nuclei with appropriate nuclear moments and spin properties for standard hyperfine techniques such as nuclear magnetic/quadrupole resonance, we used perturbed angular correlation (PAC) spectroscopy and the ^{199m}Hg/^{199}Hg isomeric decay. The experiments were performed at the ISOLDE laboratory where ^{199m}Hg is produced by bombardment of a hot liq-

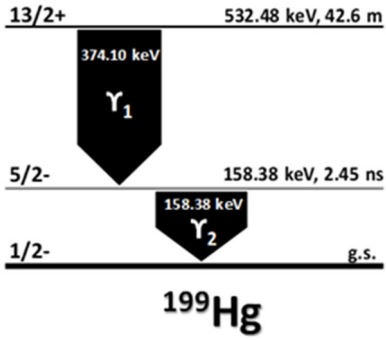

Figure 1. **Decay scheme of ^{199m}Hg/^{199}Hg. In black are the relevant gamma lines for the PAC experiment.**

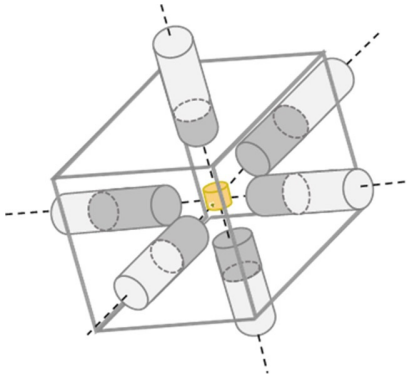

Figure 2. **Schematic representation of the 6-detector PAC spectromter. The sample is mounted in the center of the detectors.**

uid lead target with the 1.4 GeV proton beam from the CERN Proton Synchrotron Booster. The radioactive Hg vapor is then selectively ionized using the RILIS (Resonance Ionization Laser Ion Source) [27] and extracted with 30 keV energy. The ^{199m}Hg beam is then mass separated and directed to the low mass (GLM) beam line where a sample holder was mounted inside a vacuum chamber. The implanted samples consist of 0.2 ml frozen ultra pure water (UPW) sustained inside a teflon cup that is mounted on a cold-finger cooled by an external liquid nitrogen bath. Once the implantation is finished (2×10^{11} Hg atoms per sample) the frozen UPW is transferred inside a glove box for the remaining manipulations. The graphene samples consist of single-layer graphene grown on Cu by chemical vapor deposition (CVD) and transferred to thermally oxidized Si (standard SiO_2/Si substrates) [28, 29]. Inside the glove box, the ^{199m}Hg implanted ice is melted and droplets of the radioactive solution are pipetted onto the graphene surface. This occurs with the graphene samples mounted on a hot plate to promote water evaporation. The dry graphene sample is then transferred to the PAC setup where it is measured under ambient atmosphere.

The PAC setup consists of six $LaBr_3$ γ-detectors with energy resolution of 11.6% at 374.10 keV and 3.0% at 158.38 keV and time resolution of 800 ps for the ^{199m}Hg/^{199}Hg isomeric decay, with an intermediate $5/2^-$ state with 2.45 ns half-life (Figure 1). The detectors were positioned in a cubic arrangement, each detector placed at $\pm90°$ and $\pm180°$ with respect to the others, as shown in Figure 2. Data acquisition was performed with the digital and FPGA signal processing DIGIPAC setup [30–32].

PAC spectroscopy is based on the observation of the anisotropic emission of two consecutive γ-photons by a radioactive nucleus placed in the host material. The time dependent variation of the anisotropy due to the interaction of the nuclear momenta with the extranuclear fields, leads to an observable "perturbation function" that contains the information regarding the local environment, originating the hyperfine fields: electric field gradient (EFG) and the hyperfine magnetic field (HMF). In this work, the EFG is the experimental observable that characterizes the atomic local environment and its coordination. The EFG is a traceless symmetric tensor of rank 2 here characterized by its main component, V_{zz}, and the axial asymmetry parameter $0 \leq \eta \leq 1$ defined as $\eta = (V_{yy} - V_{xx})/V_{zz}$, where the three non-vanishing diagonal components are defined as $|V_{zz}| \geq |V_{yy}| \geq |V_{xx}|$. For a radioactive nucleus in a host material the angular probability distribution, $W(\theta)$, of finding γ_1-γ_2 emitted with a certain angle (θ) can be expanded into a Legendre polynomial series $P_k \cos(\theta)$ as [33, 34]:

$$W(\theta) = \sum_k A_{kk}\left(\gamma_1,\gamma_2\right) G_{kk}\left(t\right) P_k\left(cos\left(\theta\right)\right) \qquad (1)$$

A_{kk} are the anisotropy coefficients of the first and second γ-trasitions. $G_{kk}\left(t\right)$ is the perturbation factor that contains all the information about the magnetic dipole and/or the electric quadrupole interactions. The PAC setup measures the number of $\gamma_1-\gamma_2$ coincidence counts, $N_{ij}(\theta,t)$, as a function of time t between detection of γ_1 and γ_2 for every pair of detectors (i,j). The experimental perturbation function, $R(t)$, is extracted by eliminating the exponential part of $N(\theta,t)$ [33, 34]:

$$R\left(t\right) = 2\frac{N\left(180°,t\right) - N\left(90°,t\right)}{N\left(180°,t\right) + 2N\left(90°,t\right)} \qquad (2)$$

The experimental $R(t)$ is then fitted with a computer generated function consisting of a sum of *cos* functions with amplitudes and frequencies resulting from solving the appropriate Hamiltonian of the quadrupole / magnetic interactions [35, 36]. Our analysis used the nuclear

Table I. Experimental PAC results.

	f_1				f_2			
	%	ω_0	V_{zz}	η	%	ω_0	V_{zz}	η
		$Mrad/s$	(V/Å^2)			$Mrad/s$	(V/Å^2)	
UPW	82(4)	1.5(10)	1(7)	0.05(2)	18(4)	384(40)	250(27)	0.80(2)
SiO_2	28(4)	1.5(10)	1(7)	0.05(2)	72(4)	467(40)	304(26)	0.40(2)
Sample 1	41(4)	787(25)	512(16)	0.20(2)	59((4)	1265(20)	822(13)	0.00(2)
Sample 2	40(4)	1615(21)	1050(12)	0.00(2)	60(4)	1364(32)	887(20)	0.00(2)

electric quadrupole moment, $Q = 0.674 \pm 077$ barn of the ^{199m}Hg, 2.45 ns, excited 158.38 keV state [37]. For the case of half-integer spin ($I = 5/2$) and axial symmetry of the EFG the quadrupole precession frequency, ν_Q, is directly related to the spectroscopic quadrupole moment, Q and to the observable frequency, ω_0, by the expression:

$$\nu_Q = \frac{eQV_{zz}}{h} = \omega_0 \frac{I\,(2I-1)}{3\pi} \qquad (3)$$

where V_{zz} is the principal component of the EFG tensor at the nuclear site [33, 34].

PAC measurements were done at room temperature (20 °C) for graphene samples (1 and 2) subject to different cleaning conditions: sample 1 was used as-obtained, after transfer to the SiO_2/Si substrate; sample 2 was annealed under ultra-high vacuum at 350 °C for 60 min to remove surface contaminants, before being wet with the radioactive UPW solution. The UPW solution was measured individually for comparison, as well as an SiO_2/Si substrate subject to the same wetting and drying procedure as the graphene/SiO_2/Si samples.

III. EXPERIMENTAL RESULTS

Figure 3 shows the $R(t)$ experimental PAC perturbation functions obtained for the UPW (Figure 3a), the SiO_2/Si substrate (b), sample 1 (c) and sample 2 (d). When the data indicates the presence of multiple components (sets of ^{199m}Hg nuclei interacting with different local environments) the fit function considers a summation of $G_i(t)$, describing each perturbation factor, weighted by the respective fraction of nuclei, f_i, where $\sum f_i = 1$.

The $R(t)$ functions of UPW and SiO_2 show damped spectra, which are characteristic of random distributions of EFGs due to Hg probe atoms interacting with a variety of different local environments and weak electrical quadrupole interactions. On the other hand, the graphene samples (1 and 2) show clear spectra typical of strong quadrupole electric interactions between the nuclear quadrupole moment of the ^{199m}Hg nuclei and the EFG produced by external charge distributions. Each of these $R(t)$ functions are described by two components (with fractions f_1 and f_2) of ^{199m}Hg probes, i.e. Hg in four different local environments in total. Table I summarizes the PAC parameters obtained from the fit for each sample and each component. Fraction 1 of sample 1 (not cleaned) differs from the other three by its lower V_{zz} (512(16) V/Å^2) and non-vanishing $\eta = 0.20(2)$. The

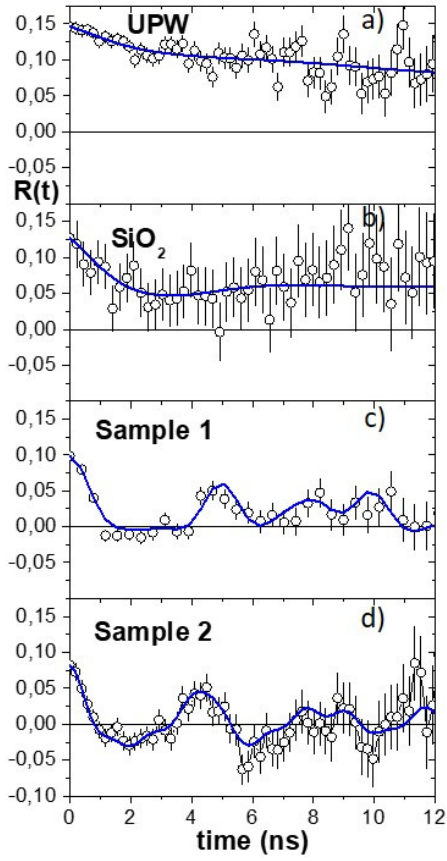

Figure 3. **R(t) function obtained from the decay of ^{199m}Hg/^{199}Hg implanted into ultra pure water (a) and after wetting and drying on: b) SiO_2/Si substrate, c) Sample 1, as-obtained graphene/SiO_2/Si and d) Sample 2, graphene/SiO_2/Si thermally annealed in ultra-high vacuum.**

lack of axial symmetry in the Hg coordination ($\eta \neq 0$) and the fact that this component is not observed in sample 2 (annealed in UHV) indicate that it corresponds to Hg atoms adsorbed in regions of the graphene surface which are disordered or contaminated (most likely polymer residues from the transfer process). The higher V_{zz} and vanishing η values of the other three components suggest well-defined atomic configurations (with axial symmetry). In particular, the similar V_{zz} for fraction 2 of samples 1 and 2 ($V_{zz} = 822(13)$ V/Å^2 and $V_{zz} = 887(20)$ V/Å^2) suggest a common origin, possibly disturbed in sample 1 by surface contaminants. Further insight into

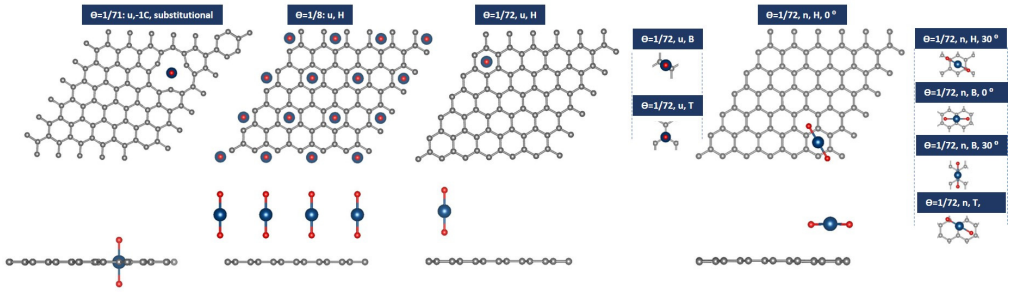

Figure 4. **Top- and side-view of the various configurations of HgO_2 on top of graphene that were simulated. From left to righ (nominal concentration of Hg, orientation, symmetric site, rotation):** $(\theta = 1/71, u, -1C, 0°)$**,** $(\theta = 1/8, u, H, 0°)$**,** $(\theta = 1/72, u, H, 0°)$**,** $(\theta = 1/72, u, B, 0°)$**,** $(\theta = 1/72, u, T, 0°)$**,** $(\theta = 1/72, n, H, 0°)$**,** $(\theta = 1/72, n, H, 30°)$**,** $(\theta = 1/72, n, B, 0°)$**,** $(\theta = 1/72, n, B, 30°)$ **and** $(\theta = 1/72, n, T, 0°)$

the origin of these hyperfine parameters, i.e. of the associated atomic configurations, is provided by the DFT calculations described next.

IV. DFT ANALYSIS

DFT calculations were performed using the VASP code [38], which implements the projector augmented wave (PAW) method. A vacuum spacing of at least 20 Å is placed between adjacent layers of carbon to hinder the layer-layer interactions. The calculations did not consider spin polarization. We used the generalized gradient approximation (GGA-PBE) with van der Waals correction (DFT-D3) [39, 40] for exchange correlation functionals. A *cut-off energy* of 850 eV and a *k-point* mesh of $3 \times 3 \times 2$ are used for large supercell geometries. We have used the experimental lattice parameter $a = b = 2.46$ Å for graphene, which is close to our optimized parameters with LDA (2.45 Å) and GGA (2.47 Å) for undoped graphene. The electronic self-consistent cycles are considered converged when the energy differences between two iterations are less than 10^{-5} eV. All calculations were made allowing full ionic relaxation of all fractional coordinates, minimizing the Hellmann-Feynman forces below a tolerance value of 0.02 eV/Å.

A wide range of atomic configurations were simulated, considering various plausible scenarios for the experimental observations. These can be divided in three groups: 1) single and clustered Hg atoms in different adsorption configurations (on top and within the graphene layer, for pristine graphene as well as in the presence of C vacancies), but no atomic or molecular species other than Hg and graphene; 2) complexes of Hg atoms and water molecules, which are abundantly available in the atmosphere and during the deposition of the radioactive solution; 3) complexes of Hg atoms and Oxygen, which is also abundantly available in the atmosphere and in possibly (partially) oxidized regions of the graphene surface. One clear match was found: fraction 2 of sample 2 (60%), with $V_{zz} = 887(20)$ V/Å^2, $\eta = 0.00(2)$ matches the calculated parameters for linear HgO_2 molecules (O-Hg-O) adsorbed on graphene. This is also consistent with the V_{zz} value of 893 ± 100 V/Å^2 (with $\eta = 0$) previously observed for the Hg site in PAC measurements on $HgBa_2CuO_{4+\delta}$ high-T_c superconductor [42, 43]. In that work, DFT calculations indeed confirmed that Hg is tightly bound to the two apical oxygen atoms, whose contributions dominate the EFG at the Hg site. Since the other two sets of calculations (Hg only and Hg+water in a wide rage of configurations) do not reproduce the observed experimental parameters, in the following we focus on the Hg+O case.

Several configurations of freestanding HgO_2 molecules on the graphene surface were simulated: with the linear axis of the HgO_2 molecule pointing up (u) along the graphene surface normal; parallel to the graphene surface (n), with the central atom (Hg) located on top of different high-symmetry positions of the graphene lattice. These high-symmetry positions are: hollow (H), top (T) and bridge (B). For the n configuration, when Hg is on H or B high symmetric sites, there are two orientations allowed by symmetry, defined by rotation of 0° and 30° around the surface normal axis. Two different nominal concentration (θ) of HgO_2 were studied by constructing differently sized super-cells, each including one HgO_2 admolecule and multiple graphene C-hexagons: the 2×2 supercell corresponds to a nominal HgO_2 concentration of $\theta = 1/8$ and the 6×6 supercell to $\theta = 1/72$. For each studied configuration, the EFG tensor on the Hg site, as well as the binding energy of the HgO_2 molecule, were examined after ionic relaxation of the structure. Table II summarizes the obtained DFT results. The HgO_2 molecule stabilizes with high binding energies ($\sim$ 1100

Table II. Calculated parameters for the various configurations of the graphene+HgO_2 system: EFG parameters (at Hg atom), binding energy and correspondent distance between graphene and HgO_2 (d). The values for isolated Hg adatoms at the H site are also shown (from [41]).

Nominal concentration θ	O-Hg-O orientation	Symmetric site	Rotation (°)	$\lvert V_{zz} \rvert$ @Hg (V/Å^2)	Direction [x,y,z]	η @Hg	Binding energy (meV)	Distance Hg-G (Å)	Distance Hg-O (Å)
-	Isolated HgO_2	-	-	934.9	[0 0 1]	0	0	-	-
1/71	u	substitutional	-	62.0	[0 0 1]	0	-	-	-
1/8	u	H	0	917.5	[0 0 1]	0	601.4	4.38	1.91
1/72	u	H	0	899.9	[0 0 1]	0	962.0	4.55	1.92
1/72	u	T	0	905.3	[0 0 1]	0	926.3	4.58	1.92
1/72	u	B	0	904.9	[0 0 1]	0	930.0	4.57	1.92
1/72	n	H	0	887.6	[0.5 0.866 0]	0	1112.5	3.09	1.92
1/72	n	H	30	892.2	[0.866 0.5 0]	0	1004.9	3.16	1.92
1/72	n	B	0	889.7	[-1 0 0]	0	1112.3	3.07	1.92
1/72	n	B	30	892.3	[0 1 0]	0	1095.5	3.13	1.92
1/72	n	T	0	892.9	[-0.866 -0.5 -0.023]	0	1102.2	3.14	1.92
1/32	Hg adatom on graphene [41]	H	-	8.4	[0 0 1]	0	188.8	-	3.44

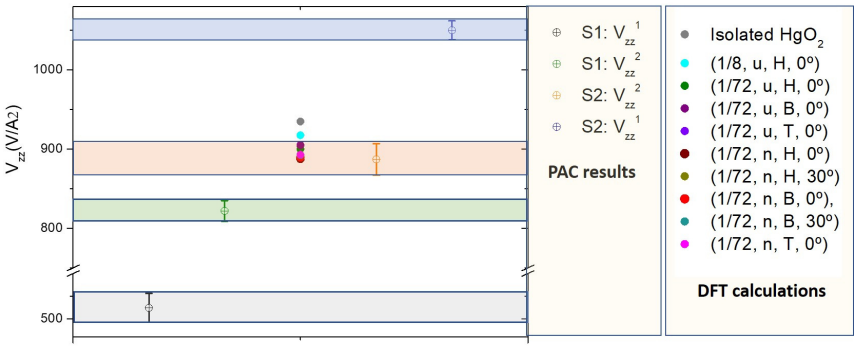

Figure 5. **Comparison between the experimental V_{zz} values obtained from the PAC measurements and the calculated V_{zz} for various configurations of the HgO_2 molecules on graphene. The shaded areas indicate the V_{zz} range spanned by the experimental error bars, on the as obtained sample 1 and UHV cleaned sample 2.**

meV) when compared with isolated adatoms of Hg (186 meV [41]). The formation of stable HgO_2 molecules is therefore crucial for the efficient adsorption of Hg on graphene. The equilibrium distance between HgO_2 and graphene and the structural properties of this molecule such as the O−Hg bonds (e.g. angle and length) are dependent on the configuration and on the rearrangement of this molecule on the graphene lattice. The calculated adsorption energies suggest that the most stable configuration for HgO_2 on graphene is that (labeled as $(n, H, 0°)$) of a linear HgO_2 molecule laying parallel to the graphene plane, with the Hg atom at the H site, with the O-Hg-O bonds pointing along the direction of the C-C bonds. This $(n, H, 0°)$ configuration has a binding energy of 1112.5 meV and distance to the graphene of 3.09 Å. The calculations also show that the EFG of Hg is very sensitive with respect to the stability and spatial configuration of the HgO_2 adamolecule on graphene: each configuration of the admolecule has a characteristic EFG, a consequence of the high sensitivity of the EFG with respect to changes in the local charge distribution and symmetry. In the following section we discuss and compare the EFG parameters obtained experimentally with those calculated for the various configurations of the HgO_2 molecules.

V. COMPARISON BETWEEN CALCULATED AND EXPERIMENTAL EFG PARAMETERS

Figure 5 compares the experimental V_{zz} and respective error bars obtained from the PAC measurements with the V_{zz} determined using DFT for various configurations of the HgO_2. As mentioned above, the V_{zz} calculated for the HgO_2 configurations agrees well with the experimental $V_{zz} = 887(20)$ V/Å^2 of fraction 2 of sample 2 (cleaned in UHV). This is, in fact, only the case for the more dilute case ($\theta = 1/72$); the calculated value for the higher concentration ($\theta = 1/8$) fall outside the error bar of the experimental value (same for the isolated HgO_2,

i.e. without graphene). This is consistent with the fact that the Hg concentration in our experiments is very low, in fact even lower than $\theta = 1/72$, since each sample was deposited with at most 2×10^{11} Hg atoms over an area of several mm^2 (likely much less due to losses in the transfer and drying process). However, it is not possible to identify the exact configuration of the HgO_2 molecule with respect to graphene, since for $\theta = 1/72$, all calculated values fall within the experimental error bar. Nevertheless, considering the calculated binding energy, the $(n, H, 0°)$ configuration is the most stable (with $E = 1112.5$ meV), and furthemore the one with the V_{zz} value (887.6 V/Å^2) that is closest to the experimental one (887(20) V/Å^2).

Although one cannot unambiguously identify the other three components, some scenarios can be proposed. As mentioned above, the lower V_{zz} and non-vanishing η of fraction 1 of sample 1 (not cleaned) suggests that this component corresponds to Hg atoms adsorbed in contaminated regions of the graphene (most likely polymer residues from the transfer process); since the fraction of the graphene surface in such conditions is minimized upon thermal annealing in UHV, that component decreases and is not detected in sample 2. Regarding the V_{zz} of fraction 2 of sample 1 (822(13) V/Å^2), although lower than that of fraction 2 of sample 2 and than the calculated values discussed above, it is likely still associated with HgO_2 molecules on graphene. The slight decrease in V_{zz} maybe be due to interaction of such HgO_2 molecules with surface contaminants; again, since the fraction of contaminated graphene surface decreases upon thermal annealing in UHV, sample 2 exhibits the parameters calculated for unperturbed HgO_2 molecules on graphene. Finally, the higher V_{zz} of fraction 1 of sample 2 (1050(12) V/Å^2) may be associated with atomic Hg forming complexes with defects (e.g. C vacancies) introduced during annealing; however at this stage we are unable to unambiguously identify this configuration. This proposed identification of the three fractions is further supported by the similarity between the weights (%) of the components: in both samples, about 60% of the Hg atoms are stabilized in the form of HgO_2 molecules in well-ordered and clean areas of graphene; in the as obtained sample 1, the reminder (about 40%) is adsorbed in contaminated areas of graphene; in the UHV cleaned sample 2 these contaminated regions are strongly minimized, so that Hg is instead trapped in defects with a well defined local structure (e.g. C vacancies, which may in fact be formed, or their concentration increased, during the thermal annealing).

VI. CONCLUSIONS

Combining perturbed angular correlation spectroscopy (using radioactive ^{199m}Hg) with density functional theory calculations, we show that the majority of the Hg atoms were adsorbed in the form of linear HgO_2 molecules. Our data indicates that these highly stable HgO_2 molecules are oriented parallel to the graphene plane, with the Hg atom at the H site, and with the O-Hg-O bonds pointing parallel to the C-C bonds. The HgO_2 molecules are adsorbed with higher binding energies (exceeding 1 eV) than isolated Hg adatoms (below 0.2 meV), i.e. oxygen plays a crucial role on the stabilization of Hg adsorption. Graphene acts as an epitaxial template, possibly also responsible for the specific coordination of the formed Hg-oxygen complex, with oxygen possibly delivered by partially oxidized graphene. This work also constitutes a proof-of-principle for the use of hyperfine techniques to study the interaction between 2D materials and adsorbed atoms and molecules, at the atomic scale.

VII. ACKNOWLEDGMENTS

This work was funded by the Portuguese Foundation for Science and Technology (FCT) ($CERN - FIS - NUC - 0004 - 2015$, $CERN - FIS - PAR - 0005 - 2017$, $SFRH/BPD/82059/2011$, $SFRH/BD/93336/2013$ and $SFRH/BD/84743/2012$), by CICECO-Aveiro Institute of Materials ($POCI - 01 - 0145 - FEDER - 007679$) - FCT Ref. ($UID/CTM/50011/2013$), by the Scientific Research Flanders ($G.0983.15$) and the KU Leuven BOF ($CREA/14/013$ and $STRT/14/002$).

[1] F. Schedin, A. K. Geim, S. V. Morozov, E. W. Hill, P. Blake, M. I. Katsnelson, and K. S. Novoselov *Nature Materials*, vol. 6, pp. 652–655, 2007.

[2] L. Kong, A. Enders, T. S. Rahman, and P. A. Dowben *Journal of Physics Condensed Matter*, vol. 26, p. 443001, 2014.

[3] J. Warner, F. Schaffel, M. Rummeli, and A. Bachmatiuk, *Graphene: Fundamentals and Emergent Applications*. Elsevier, 2013.

[4] P. Solis-Fernandez, M. Bissett, and H. Ago *Chemical Society Reviews*, vol. 46, pp. 4572–4613, 2017.

[5] J. Hu, J. Alicea, R. Wu, and M. Franz *Physical Review Letters*, vol. 109, p. 266801, 2012.

[6] L. Liu, Z. Zhou, Q. Guo, Z. Yan, Y. Yao, and D. W. Goodman *Surface Science*, vol. 605, no. 17, pp. L47 – L50, 2011.

[7] R. Thapa, D. Sen, M. K. Mitra, and K. K. Chattopadhyay *Physica B Condensed Matter*, vol. 406, pp. 368–373, 2011.

[8] I. Shtepliuk, N. M. Caffrey, T. Iakimov, V. Khranovskyy, I. A. Abrikosov, and R. Yakimova *Scientific Reports*, vol. 7, p. 3934, 2017.

[9] D. Vilela, J. Parmar, Y. Zeng, Y. Zhao, and S. Sánchez *Nano Letters*, vol. 16, no. 4, pp. 2860–2866, 2016.

[10] M. D. Fayer *Accounts of Chemical Research*, vol. 45, no. 1, pp. 3–14, 2012.

[11] X. Qin, Q. Yuan, Y. Zhao, S. Xie, and Z. Liu *Nano Letters*, vol. 11, no. 5, pp. 2173–2177, 2011.

[12] N. Severin, P. Lange, I. M. Sokolov, and J. P. Rabe *Nano Letters*, vol. 12, no. 2, pp. 774–779, 2012.

[13] R. R. Nair, H. A. Wu, P. N. Jayaram, I. V. Grigorieva, and A. K. Geim *Science*, vol. 335, no. 6067, pp. 442–444, 2012.

[14] T. Daio, T. Bayer, T. Ikuta, T. Nishiyama, K. Takahashi, Y. Takata, K. Sasaki, and S. Matthew Lyth *Scientific Reports*, vol. 5, p. 11807, 2015.

[15] Y. Zhu, F. Wang, J. Bai, X. C. Zeng, and H. Wu *Physical Chemistry Chemical Physics*, vol. 18, pp. 22039–22046, 2016.

[16] B. Bera, N. Shahidzadeh, H. Mishra, and D. Bonn *ArXiv e-prints*, 2016.

[17] G. Hong, Y. Han, T. M. Schutzius, Y. Wang, Y. Pan, M. Hu, J. Jie, C. S. Sharma, U. Muller, and D. Poulikakos *Nano Letters*, vol. 16, no. 7, pp. 4447–4453, 2016.

[18] Y. Jiang, P. Biswas, and J. D. Fortner *Environmental Science: Water Research and Technology*, vol. 2, pp. 915–922, 2016.

[19] E. Bekyarova, M. E. Itkis, P. Ramesh, C. Berger, M. Sprinkle, W. A. de Heer, and R. C. Haddon *Journal of the American Chemical Society*, vol. 131, no. 4, pp. 1336–1337, 2009.

[20] J. Antony and S. Grimme *Physical Chemistry Chemical Physics.*, vol. 10, pp. 2722–2729, 2008.

[21] M. Sargolzaei and F. Gudarzi *Journal of Applied Physics*, vol. 110, no. 6, p. 064303, 2011.

[22] M. K. Srivastava, Y. Wang, A. F. Kemper, and H.-P. Cheng *Physical Review B*, vol. 85, p. 165444, 2012.

[23] A. AlZahrani *Applied Surface Science*, vol. 257, no. 3, pp. 807 – 810, 2010.

[24] A. Ambrosetti and P. L. Silvestrelli *The Journal of Physical Chemistry C*, vol. 115, no. 9, pp. 3695–3702, 2011.

[25] M. Gyamfi, T. Eelbo, M. Waśniowska, and R. Wiesendanger *Physical Review B*, vol. 84, no. 11, p. 113403, 2011.

[26] C. Gong, A. W. Robertson, K. He, C. Ford, A. A. R. Watt, and J. H. Warner *Dalton Transactions*, vol. 43, pp. 7442–7448, 2014.

[27] V. Mishin, V. Fedoseyev, H.-J. Kluge, V. Letokhov, H. Ravn, F. Scheerer, Y. Shirakabe, S. Sundell, and O. Tengblad vol. 73, no. 4, pp. 550–560, 1993.

[28] D. Lee, G. D. Kwon, J. H. Kim, E. Moyen, Y. H. Lee, S. Baik, and D. Pribat *Nanoscale*, vol. 6, pp. 12943–12951, 2014.

[29] G. D. Kwon, E. Moyen, Y. J. Lee, Y. W. Kim, S. H. Baik, and D. Pribat *Materials Research Express*, vol. 4, no. 1, p. 015604, 2017.

[30] M. Jäger, K. Iwig, and T. Butz *Hyperfine Interactions*, vol. 198, pp. 167–172, 2010.

[31] M. Jäger, K. Iwig, and T. Butz *Review of Scientific Instruments*, vol. 82, no. 6, p. 065105, 2011.

[32] M. Jäger and T. Butz vol. 674, pp. 24–27, 2012.

[33] T. Butz *Hyperfine Interactions*, vol. 52, pp. 189–228, 1989.

[34] H. Haas and D. A. Shirley *Journal of Chemical Physics*, vol. 58, p. 3339, 1973.

[35] N. P. Barradas, M. Rots, A. A. Melo, and J. C. Soares *Physical Review B*, vol. 47, pp. 8763–8768, 1993.

[36] A. Lopes, *Local probe studies on lattice distortions and electronic correlations in CMR Manganites*. Aveiro University, 2006.

[37] W. Tröger, T. Butz, P. Blaha, and K. Schwarz *Hyperfine Interactions*, vol. 80, pp. 1109–1116, 1993.

[38] "VASP web page." https://www.vasp.at. Accessed: 2018-02-17.

[39] S. Grimme, J. Antony, S. Ehrlich, and H. Krieg *The Journal of Chemical Physics*, vol. 132, no. 15, pp. 154104–154104, 2010.

[40] S. Grimme *Journal of Computational Chemistry*, vol. 25, pp. 1463–1473, 2004.

[41] A. S. Fenta, C. O. Amorim, J. N. Gonçalves, N. Fortunato, M. B. Barbosa, J. P. M. Araujo, M. Houssa, S. Cottenier, J. G. Correia, V. S. Amaral, and L. M. C. Pereira *To be published*, 2018.

[42] J. G. Correia, J. P. Araújo, S. M. Loureiro, P. Toulemonde, S. Le Floch, P. Bordet, J. J. Capponi, R. Gatt, W. Tröger, B. Ctortecka, T. Butz, H. Haas, J. G. Marques, and J. C. Soares *Phys. Rev. B*, vol. 61, pp. 11769–11775, 2000.

[43] T. M. Mendonça, J. G. Correia, H. Haas, P. Odier, P. B. Tavares, M. R. da Silva, A. M. L. Lopes, A. M. Pereira, J. N. Gonçalves, J. S. Amaral, C. Darie, and J. P. Araujo *Physical Review B*, vol. 84, p. 094524, 2011.

Chapter 7

Conclusion and outlook

This chapter gives an overview of the main achievements of this work, which were described in more detail in the previous two chapters. We finalize with a summary review of some suggestions for further research on this topic.

Adatoms or admolecules on graphene are considered as a promising way to manipulate the electronic structure and engineer a specific property in order to use graphene as building block for a novel generation of nanodevices. Since the properties of graphene+adsorbent system are strongly dependent on the adsorption configuration (e.g. isolated versus clusters their geometry and coordinations), it is important to not only understand these effects (configuration-dependent properties and migration) from a theoretical point of view, but also to be able to probe them experimentally. Substantial research has been carried out to understand how adatoms of different elements and admolecules bind to graphene, which stable configurations they form, how they migrate and agglomerate, and how they affect the electronic structure of graphene in the various possible configurations (e.g. different sites and local concentrations, isolated versus clustered, etc.). In this Ph.D. thesis, we addressed the following aspects of adsorbed species on graphene: *i)* the stability and migration mechanisms of the heavy element Ag, Cd, Hg and In on graphene based on density functional theory (DFT); *ii)* the possibility to use the hyperfine electric field gradient (EFG) tensor as an observable to probe the bonding and stability of adatoms of heavy elements on graphene and *iii)* the new forms of coordination on graphene and the study of its stability by using perturbed angular correlation (PAC) spectroscopy as a local probe technique.

The theoretical part of the research was based on DFT calculations for different heavy elements adsorbed on graphene (Hg, Ag, Cd and In). We carried a

detailed study of the interaction between graphene and Hg, as a model heavy metal element, and building on that understanding of the Hg+graphene system, we extended it to Ag, Cd and In adatoms.

For Hg, we investigated the stability of various adsorption configurations, with different nominal Hg concentrations with respect to the number of carbon atoms. For each nominal concentration, it was demonstrated that both binding energy and corresponding graphene-adatom distance depend on the configuration/high-symmetric position of Hg adatoms. The main conclusion to be extracted is that Hg is more stable as isolated adatom than, in particular, in a HTT monolayer. For isolated adatoms, the binding energy increases with decreasing adatom concentration and depends on adsorption site (H, T, or B), reaching 188 meV for a concentration 1 : 32 of Hg adatoms on H sites. It was shown that the adsorption energy of isolated Hg adatoms varies along straight H$\longleftrightarrow$T and H$\longleftrightarrow$B paths with migration barriers of $\sim$ 8.0 meV and $\sim$ 5.6 meV, respectively, which is low when compared to other metal adatoms (such as Au (7 meV), Ag (10 meV), Cr (22 meV), Pd (80 meV) and Al (166 meV)).

The adsorption stability on graphene was also studied for other heavy metals (Ag, Cd, In). As in the case of Hg, for Ag, Cd and In the isolated adatom configuration is predicted to be the most stable, with binding energies of 274 meV, 201 meV and 666 meV respectively. The binding energy for isolated adatoms varies significantly among the elements considered here and the equilibrium site for Cd and In is found to be the H site and for Ag is the T site.

The effect on the electronic structure of graphene was also investigated for different nominal concentrations of Hg adatoms based on the calculation of the band structure (BS) and density of states (DOS). Although a gapless BS observed for all cases studied, the effect of Hg adsorption on the electronic structure of graphene is strongly dependent on adatom coverage (concentration). Whereas isolated adatoms have a minor effect on the electronic structure of graphene (only a small acceptor-like effect) Hg monolayer configurations induce a metallic state, with the Fermi level moving well above the Dirac point (donor-like behavior). Additionally, we showed that the formation of the Hg monolayer also renders the entire system metallic since the Hg monolayer introduces energy bands that cross the Fermi level.

The electric field gradient (EFG) was studied for each adatom on graphene, for different configuration/high-symmetric positions. For each adatom element, the calculations showed that EFG exhibits some variation when comparing different high-symmetry sites (with different correspondent binding energies) and are dependent on the nominal concentration of the adatom relative to C atoms. It was found that the EFG is extremely sensitive to the local atomic structure, distinguishing isolated from monolayer configurations, and for some

cases, allowing to identify the high-symmetry site occupied by the adatoms.

For each element, we calculated the respective EFG parameters (larger value V_{zz} and assymmetry parameter η), and we studied the observed dependence of the V_{zz} on the graphene-adatom distance d in the dilute regime, for a ratio metal to carbon atoms of 1 : 18. In fact, the sensitivity of V_{zz} to changes in d varies significantly among the different elements. Indium, which exhibits the highest binding energy also has the highest V_{zz} (25.0 VÅ^{-2}), as well the largest $\Delta V_{zz}/\Delta d$ value (2.50 VÅ^{-2}/pm). We established a relation between the binding energy and the EFG tensor for each adatom, suggesting that the EFG can be used to probe the binding stability of adatoms on graphene. A close relation between the strength of the graphene-adatom binding and the EFG in the isolated adatom regime was demonstrated, a clear indication that the binding and the EFG have a common origin: orbital overlap (charge sharing) between the adatom and the graphene layer. In other words, stronger charge sharing implies a stronger binding and more pronounced asymmetry of the outer electron shells along the binding direction, which in turn tends to produce a larger V_{zz} and a stronger sensitivity of V_{zz} to variations in d (since an increasing d is associated with a decrease in charge sharing). This notion is further supported by the fact that the same trend is not observed for the monolayer (HTT) regime, since there the EFG is dominated by contributions from the neighboring metal atoms (in the isolated adatom regime, this contribution is negligible), masking the effects of the interaction with the graphene lattice.

Our findings show that the EFG can be used to study the stability of adatom-graphene systems and to measure small variations in graphene-adatom distance with sub-Å precision due to its high sensitivity with respect to changes in the local charge distribution at the adatom. In particular, the calculations indicate the level of detail that can be addressed via the EFG parameters (e.g. positional precision) which increases with the stability (binding energy). In other words, the more stable graphene-adatom system (i.e. more relevant in a application scenario), the more it lends itself to be studied using hyperfine techniques. In this context, we discussed how perturbed angular correlation (PAC) spectroscopy can be used to measure the EFG parameters and thereby provide detailed information of the atomic local environment. As an example, we discussed the In case, for which the EFG shows the highest sensitivity among the elements considered here. Based on PAC measurements of V_{zz} on the decay of ^{117}Cd to ^{117}In through the 660 keV intermediate state $3/2^-$ state with 53.6 ns half-life (where the PAC measurement takes place), it would be possible to distinguish the two main regimes of In adatom concentration on graphene, i.e. between isolated In adatoms (1 : 18) and the HTT monolayer (3 : 8). Furthermore, in the isolated adatom regime, a measurement of the EFG would allow to identify which high-symmetry sites are occupied by In

adatoms on graphene, and determine the adatom-graphene distance with high (sub-Å) precision. Upon random deposition of sub-monolayer amounts of this atoms at a sufficiently low temperature, the isolated state would in principle be observed. With increasing temperature, and therefore increasing mobility of the adatoms, the monolayer configuration and its associated higher V_{zz} could eventually be observed. Although for perfect and free-standing graphene we predict that the dilute configuration is more stable than monolayer or cluster configurations, it is plausible that under different conditions, clustering may occur. For example, shifts of the Fermi level due to defects or specific substrates may affect the electrostatic interaction between the adatoms and thereby stabilize monolayer/cluster configurations. Similar considerations could be done for example for Cd, Ag, and Hg, for which suitable isotopes exist for PAC spectroscopy, to experimentally unravel details of atomic adsorption on graphene. Such experiments can be performed, for example, using the ASPIC setup at the ISOLDE facility at CERN, where adatoms can be deposited at low temperature, down to liquid He, and PAC measurements can be performed *in-situ* as a function of temperature. While ASPIC has been previously used to investigate structural and magnetic properties of metal surfaces (e.g. Ni and Pd), the calculations presented here show the potential of hyperfine techniques in the context of adatoms on graphene and on 2-dimensional materials in general, by extension. The principle of this approach is described in Ref. [285], which includes a (preliminary) subset of the DFT calculations presented in full in the present thesis. One of the advantages of this approach is that it allows to locally probe the adatom without affecting it, i.e. avoiding the influence of external probes, such as the tip of a scanning probe microscope or the intense electron beam of a transmission electron microscope. Additionally, a PAC spectrum can be measured with as little as 10^{10} probe atoms, corresponding to a coverage of 100 ppm for a typical 5×5 mm^2 sample, i.e. the approach can be applied down to extreme levels of adatom dilution. Moreover, measurements are compatible with applied electric or magnetic fields. Also very importantly, our calculations strongly indicate that the amount of information that can be addressed via the EFG parameters (sensitivity of the V_{zz} to changes in the atomic configuration) increases with the stability (binding energy), i.e. that the more robust the graphene-adatom system, the more prone it is to be studied using this approach.

The DFT studies mentioned above considered the interaction of one adatom element with pristine graphene, without interference from other species (e.g. gaseous species in the atmosphere). In an experimental scenario, this corresponds to deposition and characterization under ultra-high vacuum conditions. In this thesis, we investigated as well the role of extrinsic species on the adsorption and stability of Hg, by implanting radioactive ^{199m}Hg into ice, depositing the radioactive solution on graphene, and evaporating the water before carrying out PAC measurements. Combining the PAC results with density functional theory

(DFT) calculations, we concluded that a significant part of the Hg probes were adsorbed in the form of linear HgO_2 molecules. Our data indicates that these highly stable O-Hg-O molecules are oriented in a configuration, where O-Hg-O is parallel to the graphene plane, with the Hg atom at the H site, with O-Hg-O bonds pointing in the direction of the C-C bonds. The formation of stable HgO_2 molecules is crucial for the efficient adsorption, since the O atoms strengthen the binding to graphene (binding energy above 1 eV). Graphene acts as an epitaxial template, possibly also responsible for the specific coordination of the formed Hg-oxygen complex, with oxygen delivered by partially oxidized graphene. This work also constitutes a proof-of-principle for the use of hyperfine techniques to study the interaction between graphene and adsorbed atoms and molecules, at the atomic scale.

Outlook

It would be interesting to extend our study in heavy metals (Ag, Cd, In and Hg) to other elements, particularly to transition elements (e.g. 3d transition metals and 4f rare earths). In fact, transition metals typically have high binding energies, and therefore , based on our findings for Ag, Cd, In and Hg, they can be expected to exhibit a high sensitivity of the EFG to structural observables. Moreover, their magnetic properties could also be addressed via the magnetic hyperfine interaction. In addition to the ability to probe multiple adatom properties and phenomena (e.g. structural and magnetic), such an experimental approach based on hyperfine techniques is generally compatible with ultra-high vacuum (typically necessary when studying surfaces, to minimize contamination), low temperature (typically necessary when studying isolated adatoms, due to their high surface mobility), and applied electric or magnetic fields (often used to investigate both basic and functional properties).

Moreover, in this thesis we also reported the first PAC experiment based on the decay of ^{68m}Cu ($6^-, 721$ keV, 3.75 min). By characterizing the nuclear moments for this state we demonstrated the feasibility of using a copper isotope (^{68m}Cu) as a probe nuclei for PAC for applications in the fields of solid state physics, chemistry, and biophysics. In the context of graphene research, since Cu is the most widely employed catalyst for obtaining graphene monolayers with reasonable quality, establishing ^{68m}Cu as a suitable PAC probe enables the use of PAC spectroscopy to study the influence of the Cu substrate, e.g. on grain size and orientation, number of layers and quality of the grown graphene.

The effects on the intrinsic properties, particularly in the electronic band structure of graphene, should be assessed in more detail using other theoretical methods such as hybrid functionals and Green's functions to obtain with more accuracy the intrinsic changes of graphene induced by the adatoms.

I believe that there is great potential in continuing this study and extend it to other 2-dimensional materials and their heterostructures. If on the one hand, the adsorbed atoms or molecules on graphene promote modifications of its functionality, allowing to obtain systems with tunable properties, the combination of different 2D materials would increase that versatility even more.

Future experimental studies can be carried out at the ISOLDE facility at CERN, using ASPIC (Apparatus for Surface Physics and Interfaces at CERN) for graphene and other 2D materials, using different probe-isotopes and hyperfine techniques such as PAC and MS spectroscopy. In ASPIC it is possible to gently deposit the adatoms and carry out the measurements in an ultra-high vacuum, in contrast to the experiments presented here where water was used as ion carrier. The results of such experiments could then be interpreted using the DFT studies reported in *sections* 6.1 and 6.2 of this thesis.

Appendix A

Other DFT calculations

Density functional theory (DFT) calculations were performed to model different kinds of coordination on graphene to support the interpretation of the experimental data obtained with perturbed angular correlation (PAC) spectroscopy. The electric field gradient (EFG) tensor was examined after ionic relaxation of the structure using VASP code. The following configurations were considered:

i) Water and Hg orderd on graphene (Figure A.1 (a)). We examined the adsorption of H_2O on graphene at the center of a carbon hexagon by employing 1×1 graphene periodic supercell (one H_2O molecule per two C atoms) representing a full monolayer of ordered "ice". Different orientations of the freestanding H_2O molecule with respect to the graphene surface were studied: starting from the O atom the H-O bonds pointing up (u), down (d) or parallel to the graphene surface (n). Hg can be located relative to the H_2O molecule above H atoms (site i) or above O atoms (site ii). The constructed supercell reproduces a nominal concentration (θ) of 1 Hg per 8 C atoms.

ii) Hg-cluster up to 7 atoms in a pristine graphene lattice (Figure A.1 (b)): supercell 6×6 (72 C atoms) for each Hg-cluster with a specific dimension ($dim_{max} = 7$) in terms of the number of Hg atoms. Two main configurations were assumed for the clusters: linear alignment (l) and a t-shaped cluster (t).

iii) Hg-cluster up to 7 atoms on damaged graphene with different kinds of defects on its lattice (Figure A.1 (c)): Graphene removed of 1, 2 or 4 C atoms in a 6×6 periodic supercell works, underneath different Hg-clusters in terms of dimensions and shape.

iv) ordered structures based on Hg adatoms coordinated with oxygen or hydrogen (Figure A.1 (*d*)). Several configurations in terms of the kind of defect, coordination and spatial orientation were considered.

Table A.1 summarizes the DFT results obtained for the mentioned configurations that are shown in Figure A.1. In particular the table shows for each configuration the V_{zz} and η EFG parameter of the Hg atoms and the Hg-graphene equilibrium distance (d).

The results show that V_{zz} and η are very sensitive with respect to the coordination of the system (e.g. for G+W+Hg, or G+Hg-cluster), shape, dimension of the cluster and spatial configuration. A wide range of values of V_{zz} EFG component are obtained for the different configurations. It shows that the EFG parameters are a powerful observable to probe the configuration and position of a certain structure adsorbed on graphene.

Configuration	**NºHg/NºC**	**Defects**	V_{zz} **(V/Å^2)**	η	d_{Hg-G} **(Å)**
u,i	1/8	-	30.4	0.2	7.2
u, ii	1/8	-	30.8	0.3	7.1
d, i	1/8	-	2.2	0.0	-3.3
d, ii	1/8	-	−2.3	0.1	3.2
n, i	1/8	-	1.8	0.0	7.8
n, ii	1/8	-	0.4	0.1	7.4
2, l	2/72	-	24.1	0.1	
			−24.1	0.1	
3, l	3/72	-	−25.3	0.1	
			−48.2	0.0	
			−26.4	0.1	
3, t	3/72	-	27.4	0.9	
			27.0	0.9	
			27.0	0.9	
4,l	4/72	-	−42.2	0.0	
			−45.4	0.0	
			−46.4	0.0	
			−43.2	0.0	
4, t	4/72	-	−28.2	0.8	
			37.5	0.2	
			37.5	0.2	
			−26.8	0.8	
5, t	5/72	-	31.9	0.9	
			69.0	0.8	

			−32.6	0.9	
			−32.5	0.9	
			−32.5	0.9	
7, t	7/72	**-**	35.8		
			65.3	0.2	
			35.8	0.0	
			36.0	0.2	
			36.4	0.2	
			36.4	0.2	
			35.8	0.2	
-1C, 1Hg	1/71	−1C	1064.6	0.0	
-2C, 1Hg	1/70	−2C	1411.0	0.0	
-4C, 1Hg	1/68	−4C	491.9	0.0	
-4C, 4Hg	4/68	−4C	487.8	0.0	
			23.7	0.9	
			23.5	0.9	
			23.5	0.9	
-4C, 6Hg	4/66	−4C	−1503.5	0.7	
			1219.0	0.3	
			1219.0	0.3	
			1268.9	0.7	
			1268.9	0.7	
			1202.8	0.4	
-4C, 7Hg	4/65	−4C	487.4	0.0	
			33.0	0.9	
			34.2	0.9	
			34.2	0.9	
			52.7	0.9	
			52.7	0.9	
			54.1	0.9	
-1C, OHgO, u	1/71	−1C	−62.0	0.0	
-1C, HgO, u	1/71	−1C	−4.0	0.0	
-1C, HHgH, u	1/71	−1C	339.3	0.0	
-2C, 2O, Hg	1/70	−2C	−62.0	0.0	
-6C, 6O, Hg	1/12	−6C	−1.7	0.4	
-6C, 6H, Hg	1/12	−6C	−2.7	0.5	

Table A.1: Summary of the DFT results obtained for various configurations of Hg adsorbed on graphene, in the presence of other species: water, oxygen and hydrogen. The V_{zz}, η and Hg-graphene distance (d) are obtained after ionic relaxation of the structure using VASP.

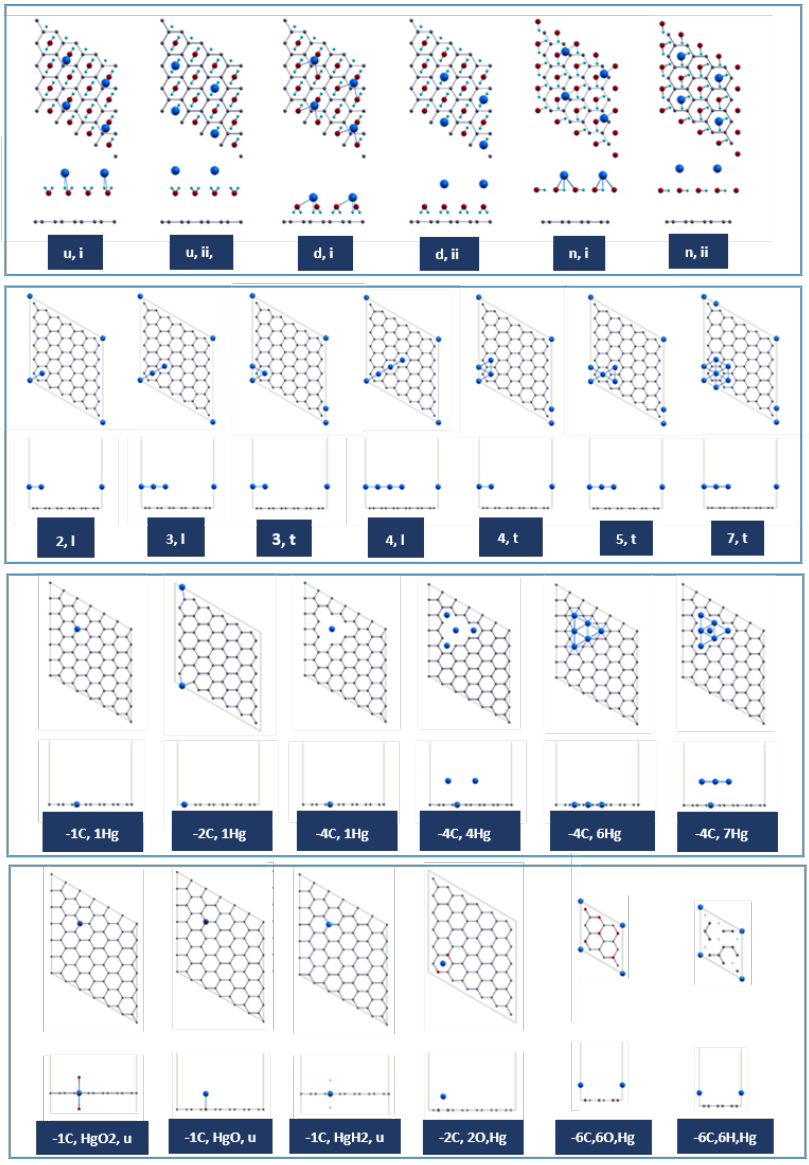

Figure A.1: View from the top and the side of different configurations investigated of water and Hg on top of graphene, Hg in a cluster configurations on pristine graphene and on defective graphene.

Bibliography

[1] M. Dresselhaus, G. Dresselhaus, and P. Eklund, *Science of Fullerenes and Carbon Nanotubes*. Academic Press, 1996.

[2] M. S. Dresselhaus, "Future Directions in Carbon Science," *Annual Review of Materials Science*, vol. 27, pp. 1–34, 1997.

[3] N. Nichols and J. Emsley, "Book Review: Nature's building blocks: an A-Z guide to the elements," *Astronomy*, vol. 31, no. 2, pp. 87–88, 2003.

[4] H. W. Kroto, , J. R. Heath, S. C. Obrien, R. F. Curl, and R. E. Smalley, "C(60): Buckminsterfullerene," *Nature*, vol. 318, p. 162, Nov. 1985.

[5] A. Oberlin, M. Endo, and T. Koyama, "Filamentous growth of carbon through benzene decomposition," *Journal of Crystal Growth*, vol. 32, no. 3, pp. 335 – 349, 1976.

[6] H. P. Boehm, R. Setton, and E. Stumpp, "Nomenclature and terminology of graphite intercalation compounds," *Pure and Applied Chemistry*, vol. 66, p. 1893–1901, 1994.

[7] P. R. Wallace, "The Band Theory of Graphite," *Physical Review*, vol. 71, pp. 622–634, 1947.

[8] J. W. McClure, "Diamagnetism of Graphite," *Physical Review*, vol. 104, pp. 666–671, 1956.

[9] J. C. Slonczewski and P. R. Weiss, "Band Structure of Graphite," *Physical Review*, vol. 109, pp. 272–279, 1958.

[10] G. W. Semenoff, "Condensed-Matter Simulation of a Three-Dimensional Anomaly," *Physical Review Letters*, vol. 53, pp. 2449–2452, 1984.

[11] A. K. Geim and K. S. Novoselov, "The rise of graphene," *Nature Materials*, vol. 6, pp. 183–191, 2007.

[12] R. Peierls, "Quelques propriétés typiques des corps solides," *Annales de l'institut Henri Poincaré*, vol. 5, no. 3, pp. 177–222, 1935.

[13] L. D. Landau, "Zur Theorie der phasenumwandlungen II," *Physikalische Zeitschrift der Sowjetunion*, vol. 11, pp. 26–35, 1937.

[14] N. D. Mermin, "Crystalline Order in Two Dimensions," *Physical Review*, vol. 176, pp. 250–254, 1968.

[15] K. S. Novoselov, A. K. Geim, S. V. Morozov, D. Jiang, Y. Zhang, S. V. Dubonos, I. V. Grigorieva, and A. A. Firsov, "Electric field effect in atomically thin carbon films," *Science*, vol. 306, no. 5696, pp. 666–669, 2004.

[16] K. S. Novoselov, D. Jiang, F. Schedin, T. J. Booth, V. V. Khotkevich, S. V. Morozov, and A. K. Geim, "Two-dimensional atomic crystals," *Proceedings of the National Academy of Science*, vol. 102, pp. 10451–10453, 2005.

[17] A. H. Castro Neto, "Drawing Conclusions from Graphene," in *APS New England Section Fall Meeting Abstracts*, p. A1.002, 2007.

[18] K. S. Novoselov, A. K. Geim, S. V. Morozov, D. Jiang, M. I. Katsnelson, I. V. Grigorieva, S. V. Dubonos, and A. A. Firsov, "Two-dimensional gas of massless Dirac fermions in graphene," *Nature*, vol. 438, pp. 197–200, 2005.

[19] A. K. Geim, "Graphene: Status and Prospects," *Science*, vol. 324, p. 1530, 2009.

[20] A. K. Geim, "Nobel lecture: Random walk to graphene," *Reviews of Modern Physics*, vol. 83, pp. 851–862, 2011.

[21] K. S. Novoselov, "Nobel Lecture: Graphene: Materials in the Flatland," *Reviews of Modern Physics*, vol. 83, pp. 837–849, 2011.

[22] K. S. Novoselov, V. I. FalKo, L. Colombo, P. R. Gellert, M. G. Schwab, and K. Kim, "A roadmap for graphene," *Nature*, vol. 490, pp. 192–200, 2012.

[23] S. Mizushima, Y. Fujibayashi, and K. Shiiki, "Electric Resistivity and Hall Coefficient of Very Thin Graphite Crystals," *Journal of the Physical Society of Japan*, vol. 30, p. 299, 1971.

[24] Y. Fujibayashi and S. Mizushima, "The residual resistivity of thin graphite crystals," *Journal of the Physical Society of Japan*, vol. 34, no. 1, pp. 281–281, 1973.

[25] Y. Ohashi, T. Koizumi, T. Yoshikawa, T. Hironaka, and K. Shiiki, "Size effect inthe in-plane electrical resistivity of very thin graphite crystals," *TANSO*, vol. 1997, no. 180, pp. 235–238, 1997.

[26] X. Lu, H. Huang, N. Nemchuk, and R. S. Ruoff, "Patterning of highly oriented pyrolytic graphite by oxygen plasma etching," *Applied Physics Letters*, vol. 75, no. 2, pp. 193–195, 1999.

[27] J. Warner, F. Schaffel, M. Rummeli, and A. Bachmatiuk, *Graphene: Fundamentals and Emergent Applications*. Elsevier, 2013.

[28] A. H. Castro Neto, F. Guinea, N. M. R. Peres, K. S. Novoselov, and A. K. Geim, "The electronic properties of graphene," *Reviews of Modern Physics*, vol. 81, pp. 109–162, Jan. 2009.

[29] U. Bangert, M. H. Gass, A. L. Bleloch, R. R. Nair, and A. K. Geim, "Manifestation of ripples in free-standing graphene in lattice images obtained in an aberration-corrected scanning transmission electron microscope," *Physica Status Solidi (a)*, vol. 206, no. 6.

[30] W. Bao, F. Miao, Z. Chen, H. Zhang, W. Jang, C. Dames, and C. N. Lau, "Controlled ripple texturing of suspended graphene and ultrathin graphite membranes," *Nature Nanotechnology*, vol. 4, pp. 562–566, 2009.

[31] V. Geringer, M. Liebmann, T. Echtermeyer, S. Runte, M. Schmidt, R. Rückamp, M. C. Lemme, and M. Morgenstern, "Intrinsic and extrinsic corrugation of monolayer graphene deposited on sio_2," *Physical Review Letters*, vol. 102, p. 076102, 2009.

[32] Z. Liu, K. Suenaga, P. J. F. Harris, and S. Iijima, "Open and closed edges of graphene layers," *Physical Review Letters*, vol. 102, p. 015501, 2009.

[33] M. I. Katsnelson and A. K. Geim, "Electron scattering on microscopic corrugations in graphene," *Philosophical Transactions of the Royal Society of London Series A*, vol. 366, pp. 195–204, 2008.

[34] P. M. Chaikin and T. C. Lubensky, *Principles of Condensed Matter Physics*. Cambridge University Press.

[35] D. R. Nelson, *Statistical Mechanics of Membranes and Surfaced: 2nd Edition*. World Scientific Publishing Co, 2004.

[36] A. Fasolino, J. H. Los, and M. I. Katsnelson, "Intrinsic ripples in graphene," *Nature Materials*, vol. 6, pp. 858–861, 2007.

[37] C. Lee, X. Wei, J. W. Kysar, and J. Hone, "Measurement of the Elastic Properties and Intrinsic Strength of Monolayer Graphene," *Science*, vol. 321, p. 385, 2008.

[38] A. S. Mayorov, R. V. Gorbachev, S. V. Morozov, L. Britnell, R. Jalil, L. A. Ponomarenko, P. Blake, K. S. Novoselov, K. Watanabe, T. Taniguchi, and A. K. Geim, "Micrometer-scale ballistic transport in encapsulated graphene at room temperature," *Nano Letters*, vol. 11, no. 6, pp. 2396–2399, 2011.

[39] R. R. Nair, P. Blake, A. N. Grigorenko, K. S. Novoselov, T. J. Booth, T. Stauber, N. M. R. Peres, and A. K. Geim, "Fine structure constant defines visual transparency of graphene," *Science*, vol. 320, no. 5881, pp. 1308–1308, 2008.

[40] M. I. Katsnelson, "Graphene: carbon in two dimensions," *Materials Today*, vol. 10, no. 1, pp. 20 – 27, 2007.

[41] L. E. F. Foa Torres, S. Roche, and J.-C. Charlier, *Introduction to Graphene-Based Nanomaterials*. 2014.

[42] N. M. R. Peres, F. Guinea, and A. H. Castro Neto, "Electronic properties of disordered two-dimensional carbon," *Physical Review B*, vol. 73, p. 125411, 2006.

[43] S. Das Sarma, S. Adam, E. H. Hwang, and E. Rossi, "Electronic transport in two-dimensional graphene," *Reviews of Modern Physics*, vol. 83, pp. 407–470, 2011.

[44] A. H. C. Neto and K. Novoselov, "New directions in science and technology: two-dimensional crystals," *Reports on Progress in Physics*, vol. 74, no. 8, p. 082501, 2011.

[45] Y. Zhang, Y.-W. Tan, H. L. Stormer, and P. Kim, "Experimental observation of the quantum Hall effect and Berry's phase in graphene," *Nature*, vol. 438, pp. 201–204, 2005.

[46] V. P. Gusynin and S. G. Sharapov, "Unconventional integer quantum hall effect in graphene," *Physical Review Letters*, vol. 95, p. 146801, 2005.

[47] N. M. R. Peres, F. Guinea, and A. H. Castro Neto, "Electronic properties of two-dimensional carbon," *Annals of Physics*, vol. 321, pp. 1559–1567, 2006.

[48] M. I. Katsnelson, K. S. Novoselov, and A. K. Geim, "Chiral tunnelling and the Klein paradox in graphene," *Nature Physics*, vol. 2, pp. 620–625, 2006.

[49] R. V. Gorbachev, A. S. Mayorov, A. K. Savchenko, D. W. Horsell, and F. Guinea, "Conductance of p-n-p graphene structures with "air-bridge" top gates," *Nano Letters*, vol. 8, no. 7, pp. 1995–1999, 2008.

[50] V. M. Pereira, F. Guinea, J. M. B. Lopes dos Santos, N. M. R. Peres, and A. H. Castro Neto, "Disorder induced localized states in graphene," *Physical Review Letters*, vol. 96, p. 036801, 2006.

[51] P. Ruffieux, M. Melle-Franco, O. Gröning, M. Bielmann, F. Zerbetto, and P. Gröning, "Charge-density oscillation on graphite induced by the interference of electron waves," *Physical Review B*, vol. 71, p. 153403, 2005.

[52] O. V. Yazyev and L. Helm, "Defect-induced magnetism in graphene," *Physical Review B*, vol. 75, p. 125408, 2007.

[53] P. O. Lehtinen, A. S. Foster, Y. Ma, A. V. Krasheninnikov, and R. M. Nieminen, "Irradiation-induced magnetism in graphite: A density functional study," *Physical Review Letters*, vol. 93, p. 187202, 2004.

[54] Y. Zhang, S. Talapatra, S. Kar, R. Vajtai, S. K. Nayak, and P. M. Ajayan, "First-principles study of defect-induced magnetism in carbon," *Physical Review Letters*, vol. 99, p. 107201, 2007.

[55] H. Amara, S. Latil, V. Meunier, P. Lambin, and J.-C. Charlier, "Scanning tunneling microscopy fingerprints of point defects in graphene: A theoretical prediction," *Physical Review B*, vol. 76, p. 115423, 2007.

[56] S. Okada and A. Oshiyama, "Magnetic ordering in hexagonally bonded sheets with first-row elements," *Physical Review Letters*, vol. 87, p. 146803, 2001.

[57] D. W. Boukhvalov, M. I. Katsnelson, and A. I. Lichtenstein, "Hydrogen on graphene: Electronic structure, total energy, structural distortions and magnetism from first-principles calculations," *Physical Review B*, vol. 77, p. 035427, 2008.

[58] P. O. Lehtinen, A. S. Foster, A. Ayuela, A. Krasheninnikov, K. Nordlund, and R. M. Nieminen, "Magnetic properties and diffusion of adatoms on a graphene sheet," *Physical Review Letters*, vol. 91, p. 017202, 2003.

[59] Y. Ma, A. S. Foster, A. V. Krasheninnikov, and R. M. Nieminen, "Nitrogen in graphite and carbon nanotubes: Magnetism and mobility," *Physical Review B*, vol. 72, p. 205416, 2005.

[60] D. C. Sorescu, K. D. Jordan, and P. Avouris, "Theoretical study of oxygen adsorption on graphite and the (8,0) single-walled carbon nanotube," *The Journal of Physical Chemistry B*, vol. 105, no. 45, pp. 11227–11232, 2001.

[61] O. V. Yazyev, "Magnetism in disordered graphene and irradiated graphite," *Physical Review Letters*, vol. 101, p. 037203, 2008.

[62] J. Fernández-Rossier and J. J. Palacios, "Magnetism in graphene nanoislands," *Physical Review Letters*, vol. 99, p. 177204, 2007.

[63] H. Lee, Y.-W. Son, N. Park, S. Han, and J. Yu, "Magnetic ordering at the edges of graphitic fragments: Magnetic tail interactions between the edge-localized states," *Physical Review B*, vol. 72, p. 174431, 2005.

[64] L. Pisani, J. A. Chan, B. Montanari, and N. M. Harrison, "Electronic structure and magnetic properties of graphitic ribbons," *Physical Review B*, vol. 75, p. 064418, 2007.

[65] Y.-W. Son, M. L. Cohen, and S. G. Louie, "Half-metallic graphene nanoribbons," *Nature*, vol. 444, pp. 347–349, 2006.

[66] W. L. Wang, O. V. Yazyev, S. Meng, and E. Kaxiras, "Topological frustration in graphene nanoflakes: Magnetic order and spin logic devices," *Physical Review Letters*, vol. 102, p. 157201, 2009.

[67] N. M. R. Peres, "Graphene, new physics in two dimensions," *Europhysics News*, vol. 40, pp. 17–20, May 2009.

[68] L. A. Ponomarenko, F. Schedin, M. I. Katsnelson, R. Yang, E. W. Hill, K. S. Novoselov, and A. K. Geim, "Chaotic Dirac Billiard in Graphene Quantum Dots," *Science*, vol. 320, p. 356, 2008.

[69] K. A. Ritter and J. W. Lyding, "The influence of edge structure on the electronic properties of graphene quantum dots and nanoribbons," *Nature Materials*, vol. 8, pp. 235–242, 2009.

[70] H. Şahin, R. T. Senger, and S. Ciraci, "Spintronic properties of zigzag-edged triangular graphene flakes," *Journal of Applied Physics*, vol. 108, no. 7, pp. 074301–074301–5, 2010.

[71] S. Yuanyuan, Z. Yongping, P. Hongzhe, C. Jie, Z. Weili, F. Lin, Z. Kaiyu, T. Nujiang, and D. Youwei, "Magnetism of graphene quantum dots," *Quantum Materials 2*, pp. –, 2017.

[72] T. Espinosa-Ortega, I. A. Luk'yanchuk, and Y. G. Rubo, "Magnetic properties of graphene quantum dots," *Physical Review B*, vol. 87, no. 20, p. 205434, 2013.

[73] O. V. Yazyev, "Emergence of magnetism in graphene materials and nanostructures," *Reports on Progress in Physics*, vol. 73, no. 5, p. 056501, 2010.

[74] R. R. Nair, M. Sepioni, I.-L. Tsai, O. Lehtinen, J. Keinonen, A. V. Krasheninnikov, T. Thomson, A. K. Geim, and I. V. Grigorieva, "Spin-half paramagnetism in graphene induced by point defects," *Nature Physics*, vol. 8, pp. 199–202, 2012.

[75] Z. Sun, D. K. James, and J. M. Tour, "Graphene chemistry: Synthesis and manipulation," *The Journal of Physical Chemistry Letters*, vol. 2, no. 19, pp. 2425–2432, 2011.

[76] S. Niyogi, M. A. Hamon, H. Hu, B. Zhao, P. Bhowmik, R. Sen, M. E. Itkis, and R. C. Haddon, "Chemistry of single-walled carbon nanotubes," *Accounts of Chemical Research*, vol. 35, no. 12, pp. 1105–1113, 2002.

[77] S. Chen, L. Brown, M. Levendorf, W. Cai, S.-Y. Ju, J. Edgeworth, X. Li, C. W. Magnuson, A. Velamakanni, R. D. Piner, J. Kang, J. Park, and R. S. Ruoff, "Oxidation resistance of graphene-coated cu and cu/ni alloy," *ACS Nano*, vol. 5, no. 2, pp. 1321–1327, 2011.

[78] A. Kaplan, Z. Yuan, J. D. Benck, A. Govind Rajan, X. S. Chu, Q. H. Wang, and M. S. Strano, "Current and future directions in electron transfer chemistry of graphene," *Chemical Society Reviews*, vol. 46, pp. 4530–4571, 2017.

[79] D. C. Elias, R. R. Nair, T. M. G. Mohiuddin, S. V. Morozov, P. Blake, M. P. Halsall, A. C. Ferrari, D. W. Boukhvalov, M. I. Katsnelson, A. K. Geim, and K. S. Novoselov, "Control of Graphenersquos Properties by Reversible Hydrogenation: Evidence for Graphane," *Science*, vol. 323, p. 610, 2009.

[80] S. Cheng, K. Zou, F. Okino, H. R. Gutierrez, A. Gupta, N. Shen, P. C. Eklund, J. O. Sofo, and J. Zhu, "Reversible fluorination of graphene: Evidence of a two-dimensional wide bandgap semiconductor," *Physical Review B*, vol. 81, p. 205435, 2010.

[81] R. R. Nair, W. Ren, R. Jalil, I. Riaz, V. G. Kravets, L. Britnell, P. Blake, F. Schedin, A. S. Mayorov, S. Yuan, M. I. Katsnelson, H.-M. Cheng, W. Strupinski, L. G. Bulusheva, A. V. Okotrub, I. V. Grigorieva, A. N. Grigorenko, K. S. Novoselov, and A. K. Geim, "Fluorographene: A two-dimensional counterpart of teflon," *Small*, vol. 6, no. 24, pp. 2877–2884, 2010.

[82] A. Hirsch, J. M. Englert, and F. Hauke, "Wet chemical functionalization of graphene," *Accounts of Chemical Research*, vol. 46, no. 1, pp. 87–96, 2013.

[83] M. Z. Hossain, M. A. Walsh, and M. C. Hersam, "Scanning tunneling microscopy, spectroscopy, and nanolithography of epitaxial graphene chemically modified with aryl moieties," *Journal of the American Chemical Society*, vol. 132, no. 43, pp. 15399–15403, 2010.

[84] Q. H. Wang, C.-J. Shih, G. L. C. Paulus, and M. S. Strano, "Evolution of physical and electronic structures of bilayer graphene upon chemical functionalization," *Journal of the American Chemical Society*, vol. 135, no. 50, pp. 18866–18875, 2013.

[85] J. M. Englert, C. Dotzer, G. Yang, M. Schmid, C. Papp, J. M. Gottfried, H.-P. Steinrück, E. Spiecker, F. Hauke, and A. Hirsch, "Covalent bulk functionalization of graphene," *Nature Chemistry*, vol. 3, pp. 279–286, 2011.

[86] B. D. Ossonon and D. Bélanger, "Functionalization of graphene sheets by the diazonium chemistry during electrochemical exfoliation of graphite," *Carbon*, vol. 111, pp. 83 – 93, 2017.

[87] S. Navalon, A. Dhakshinamoorthy, M. Alvaro, M. Antonietti, and H. Garcia, "Active sites on graphene-based materials as metal-free catalysts," *Chemical Society Reviews*, vol. 46, pp. 4501–4529, 2017.

[88] D. S. Su, S. Perathoner, and G. Centi, "Nanocarbons for the development of advanced catalysts," *Chemical Reviews*, vol. 113, no. 8, pp. 5782–5816, 2013.

[89] J.-K. Jeon, H. Kim, Y.-K. Park, C. H. Peden, and D. H. Kim, "Regeneration of field-spent activated carbon catalysts for low-temperature selective catalytic reduction of nox with nh3," *Chemical Engineering Journal*, vol. 174, no. 1, pp. 242 – 248, 2011.

[90] C. Coulson and R. McWeeny, *Coulson's Valence*. Oxford Chemistry Series, 1979.

[91] R. Ansari, B. Motevalli, A. Montazeri, and S. Ajori, "Fracture analysis of monolayer graphene sheets with double vacancy defects via md simulation," *Solid State Communications*, vol. 151, no. 17, pp. 1141 – 1146, 2011.

[92] F. Liu, P. Ming, and J. Li, "Ab initio," *Physical Review B*, vol. 76, p. 064120, 2007.

[93] F. Scarpa, S. Adhikari, and A. Srikantha Phani, "Effective elastic mechanical properties of single layer graphene sheets," *Nanotechnology*, vol. 20, no. 6, p. 065709, 2009.

[94] S. Ogata and Y. Shibutani, "Ideal tensile strength and band gap of single-walled carbon nanotubes," *Physical Review B*, vol. 68, p. 165409, 2003.

[95] R. G. Jian, *Graphene Simulations*. InTech, 2011.

[96] H. Zhao, K. Min, and N. R. Aluru, "Size and chirality dependent elastic properties of graphene nanoribbons under uniaxial tension," *Nano Letters*, vol. 9, no. 8, pp. 3012–3015, 2009.

[97] F. Hao, D. Fang, and Z. Xu, "Mechanical and thermal transport properties of graphene with defects," *Applied Physics Letters*, vol. 99, no. 4, p. 041901, 2011.

[98] K. M. Shahil and A. A. Balandin, "Thermal properties of graphene and multilayer graphene: Applications in thermal interface materials," *Solid State Communications*, vol. 152, no. 15, pp. 1331 – 1340, 2012. Exploring Graphene, Recent Research Advances.

[99] A. A. Balandin, "Thermal properties of graphene and nanostructured carbon materials," *Nature Materials*, vol. 10, pp. 569–581, 2011.

[100] A. C. Ferrari, J. C. Meyer, V. Scardaci, C. Casiraghi, M. Lazzeri, F. Mauri, S. Piscanec, D. Jiang, K. S. Novoselov, S. Roth, and A. K. Geim, "Raman spectrum of graphene and graphene layers," *Physical Review Letters*, vol. 97, p. 187401, 2006.

[101] I. Calizo, A. A. Balandin, W. Bao, F. Miao, and C. N. Lau, "Temperature dependence of the raman spectra of graphene and graphene multilayers," *Nano Letters*, vol. 7, no. 9, pp. 2645–2649, 2007.

[102] A. A. Balandin, S. Ghosh, W. Bao, I. Calizo, D. Teweldebrhan, F. Miao, and C. N. Lau, "Superior thermal conductivity of single-layer graphene," *Nano Letters*, vol. 8, no. 3, pp. 902–907, 2008.

[103] D. L. Nika, E. P. Pokatilov, A. S. Askerov, and A. A. Balandin, "Phonon thermal conduction in graphene: Role of umklapp and edge roughness scattering," *Physical Review B*, vol. 79, p. 155413, 2009.

[104] S. Ghosh, W. Bao, D. L. Nika, S. Subrina, E. P. Pokatilov, C. N. Lau, and A. A. Balandin, "Dimensional crossover of thermal transport in few-layer graphene," *Nature Materials*, vol. 9, pp. 555–558, 2010.

[105] S. Ghosh, I. Calizo, D. Teweldebrhan, E. P. Pokatilov, D. L. Nika, A. A. Balandin, W. Bao, F. Miao, and C. N. Lau, "Extremely high thermal conductivity of graphene: Prospects for thermal management

applications in nanoelectronic circuits," *Applied Physics Letters*, vol. 92, no. 15, p. 151911, 2008.

[106] S. Ghosh, D. L. Nika, E. P. Pokatilov, and A. A. Balandin, "Heat conduction in graphene: experimental study and theoretical interpretation," *New Journal of Physics*, vol. 11, no. 9, p. 095012, 2009.

[107] P. Blake, P. D. Brimicombe, R. R. Nair, T. J. Booth, D. Jiang, F. Schedin, L. A. Ponomarenko, S. V. Morozov, H. F. Gleeson, E. W. Hill, A. K. Geim, and K. S. Novoselov, "Graphene-based liquid crystal device," *Nano Letters*, vol. 8, no. 6, pp. 1704–1708, 2008.

[108] Y. Hernandez, V. Nicolosi, M. Lotya, F. M. Blighe, Z. Sun, S. de, I. T. McGovern, B. Holland, M. Byrne, Y. K. Gun'ko, J. J. Boland, P. Niraj, G. Duesberg, S. Krishnamurthy, R. Goodhue, J. Hutchison, V. Scardaci, A. C. Ferrari, and J. N. Coleman, "High-yield production of graphene by liquid-phase exfoliation of graphite," *Nature Nanotechnology*, vol. 3, pp. 563–568, 2008.

[109] I. Forbeaux, J.-M. Themlin, and J.-M. Debever, "Heteroepitaxial graphite on $6h-$SiC(0001) : interface formation through conduction-band electronic structure," *Physical Review B*, vol. 58, pp. 16396–16406, 1998.

[110] C. Berger, Z. Song, T. Li, X. Li, A. Y. Ogbazghi, R. Feng, Z. Dai, A. N. Marchenkov, E. H. Conrad, P. N. First, and W. A. de Heer, "Ultrathin epitaxial graphite:? 2d electron gas properties and a route toward graphene-based nanoelectronics," *The Journal of Physical Chemistry B*, vol. 108, no. 52, pp. 19912–19916, 2004.

[111] T. Ohta, A. Bostwick, T. Seyller, K. Horn, and E. Rotenberg, "Controlling the Electronic Structure of Bilayer Graphene," *Science*, vol. 313, pp. 951–954, Aug. 2006.

[112] C. Virojanadara, M. Syväjarvi, R. Yakimova, L. I. Johansson, A. A. Zakharov, and T. Balasubramanian, "Homogeneous large-area graphene layer growth on $6h$-sic(0001)," *Physical Review B*, vol. 78, p. 245403, 2008.

[113] J. Hackley, D. Ali, J. DiPasquale, J. D. Demaree, and C. J. K. Richardson, "Graphitic carbon growth on Si(111) using solid source molecular beam epitaxy," *Applied Physics Letters*, vol. 95, no. 13, p. 133114, 2009.

[114] S. Dhar, A. R. Barman, G. X. Ni, X. Wang, X. F. Xu, Y. Zheng, S. Tripathy, R. Ariando, A., K. P. Loh, M. Rubhausen, A. H. C. Neto, B. Åńzyilmaz, and T. Venkatesan, "A new route to graphene layers by selective laser ablation," *AIP Advances*, vol. 1, no. 2, p. 022109, 2011.

[115] R. S. Edwards and K. S. Coleman, "Graphene film growth on polycrystalline metals," *Accounts of Chemical Research*, vol. 46, no. 1, pp. 23–30, 2013.

[116] X. Li, W. Cai, J. An, S. Kim, J. Nah, D. Yang, R. Piner, A. Velamakanni, I. Jung, E. Tutuc, S. K. Banerjee, L. Colombo, and R. S. Ruoff, "Large-Area Synthesis of High-Quality and Uniform Graphene Films on Copper Foils," *Science*, vol. 324, p. 1312, 2009.

[117] S. Bae, H. Kim, Y. Lee, X. Xu, J.-S. Park, Y. Zheng, J. Balakrishnan, T. Lei, H. Ri Kim, Y. I. Song, Y.-J. Kim, K. S. Kim, B. Özyilmaz, J.-H. Ahn, B. H. Hong, and S. Iijima, "Roll-to-roll production of 30-inch graphene films for transparent electrodes," *Nature Nanotechnology*, vol. 5, pp. 574–578, 2010.

[118] G. D. Kwon, E. Moyen, Y. J. Lee, Y. W. Kim, S. H. Baik, and D. Pribat *Materials Research Express*, vol. 4, no. 1, p. 015604, 2017.

[119] Y. Kim, E. Moyen, H. Yi, J. Avila, C. Chen, M. C. Asensio, Y. H. Lee, and D. Pribat, "Synthesis of high quality graphene on capped cu thin films obtained by high temperature secondary grain growth on c -plane sapphire substrates," *2D Materials*, vol. 5, no. 3, p. 035008, 2018.

[120] H. Zhao and N. R. Aluru, "Temperature and strain-rate dependent fracture strength of graphene," *Journal of Applied Physics*, vol. 108, no. 6, pp. 064321–064321–5, 2010.

[121] A. Bagri, S.-P. Kim, R. S. Ruoff, and V. B. Shenoy, "Thermal transport across twin grain boundaries in polycrystalline graphene from nonequilibrium molecular dynamics simulations," *Nano Letters*, vol. 11, no. 9, pp. 3917–3921, 2011.

[122] L. Kong, A. Enders, T. S. Rahman, and P. A. Dowben, "Molecular adsorption on graphene," *Journal of Physics Condensed Matter*, vol. 26, p. 443001, 2014.

[123] J.-H. Chen, C. Jang, S. Adam, M. S. Fuhrer, E. D. Williams, and M. Ishigami, "Charged-impurity scattering in graphene," *Nature Physics*, vol. 4, pp. 377–381, 2008.

[124] R. S. Shishir and D. K. Ferry, "FAST TRACK COMMUNICATION: Intrinsic mobility in graphene," *Journal of Physics Condensed Matter*, vol. 21, no. 23, p. 232204, 2009.

[125] N. R. Wilson, P. A. Pandey, R. Beanland, R. J. Young, I. A. Kinloch, L. Gong, Z. Liu, K. Suenaga, J. P. Rourke, S. J. York, and J. Sloan,

"Graphene oxide: Structural analysis and application as a highly transparent support for electron microscopy," *ACS Nano*, vol. 3, no. 9, pp. 2547–2556, 2009.

[126] R. S. Pantelic, J. C. Meyer, U. Kaiser, W. Baumeister, and J. M. Plitzko, "Graphene oxide: A substrate for optimizing preparations of frozen-hydrated samples," *Journal of Structural Biology*, vol. 170, no. 1, pp. 152 – 156, 2010.

[127] J. S. Bunch, S. S. Verbridge, J. S. Alden, A. M. van der Zande, J. M. Parpia, H. G. Craighead, and P. L. McEuen, "Impermeable atomic membranes from graphene sheets," *Nano Letters*, vol. 8, no. 8, pp. 2458–2462, 2008.

[128] K. S. Kim, Y. Zhao, H. Jang, S. Y. Lee, J. M. Kim, K. S. Kim, J.-H. Ahn, P. Kim, J.-Y. Choi, and B. H. Hong, "Large-scale pattern growth of graphene films for stretchable transparent electrodes," *Nature*, vol. 457, pp. 706–710, 2009.

[129] X. Wang, L. Zhi, and K. Müllen, "Transparent, conductive graphene electrodes for dye-sensitized solar cells," *Nano Letters*, vol. 8, no. 1, pp. 323–327, 2008.

[130] R.-J. Shiue, Y. Gao, Y. Wang, C. Peng, A. D. Robertson, D. K. Efetov, S. Assefa, F. H. L. Koppens, J. Hone, and D. Englund, "High-responsivity graphene–boron nitride photodetector and autocorrelator in a silicon photonic integrated circuit," *Nano Letters*, vol. 15, no. 11, pp. 7288–7293, 2015.

[131] F. Withers, O. Del Pozo-Zamudio, A. Mishchenko, A. P. Rooney, A. Gholinia, K. Watanabe, T. Taniguchi, S. J. Haigh, A. K. Geim, A. I. Tartakovskii, and K. S. Novoselov, "Light-emitting diodes by band-structure engineering in van der Waals heterostructures," *Nature Materials*, vol. 14, pp. 301–306, 2015.

[132] P. Solis-Fernandez, M. Bissett, and H. Ago, "Synthesis, structure and applications of graphene-based 2d heterostructures," *Chemical Society Reviews*, vol. 46, pp. 4572–4613, 2017.

[133] F. Xia, T. Mueller, Y.-M. Lin, A. Valdes-Garcia, and P. Avouris, "Ultrafast graphene photodetector," *Nature Nanotechnology*, vol. 4, pp. 839–843, 2009.

[134] Y. Zhang, T.-T. Tang, C. Girit, Z. Hao, M. C. Martin, A. Zettl, M. F. Crommie, Y. R. Shen, and F. Wang, "Direct observation of a widely tunable bandgap in bilayer graphene," *Nature*, vol. 459, pp. 820–823, 2009.

[135] K. Roy, M. Padmanabhan, S. Goswami, T. P. Sai, G. Ramalingam, S. Raghavan, and A. Ghosh, "Graphene-MoS_2 hybrid structures for multifunctional photoresponsive memory devices," *Nature Nanotechnology*, vol. 8, pp. 826–830, 2013.

[136] S. Larentis, J. R. Tolsma, B. Fallahazad, D. C. Dillen, K. Kim, A. H. MacDonald, and E. Tutuc, "Band offset and negative compressibility in graphene-mos2 heterostructures," *Nano Letters*, vol. 14, no. 4, pp. 2039–2045, 2014.

[137] L. Britnell, R. V. Gorbachev, R. Jalil, B. D. Belle, F. Schedin, A. Mishchenko, T. Georgiou, M. I. Katsnelson, L. Eaves, S. V. Morozov, N. M. R. Peres, J. Leist, A. K. Geim, K. S. Novoselov, and L. A. Ponomarenko, "Field-effect tunneling transistor based on vertical graphene heterostructures," *Science*, vol. 335, no. 6071, pp. 947–950, 2012.

[138] F. Schedin, A. K. Geim, S. V. Morozov, E. W. Hill, P. Blake, M. I. Katsnelson, and K. S. Novoselov, "Detection of individual gas molecules adsorbed on graphene," *Nature Materials*, vol. 6, pp. 652–655, 2007.

[139] Q. A. Vu, Y. S. Shin, Y. R. Kim, V. L. Nguyen, W. T. Kang, H. Kim, D. H. Luong, I. M. Lee, K. Lee, D.-S. Ko, J. Heo, S. Park, Y. H. Lee, and W. J. Yu, "Two-terminal floating-gate memory with van der Waals heterostructures for ultrahigh on/off ratio," *Nature Communications*, vol. 7, p. 12725, 2016.

[140] G. Reina, J. M. Gonzalez-Dominguez, A. Criado, E. Vazquez, A. Bianco, and M. Prato, "Promises, facts and challenges for graphene in biomedical applications," *Chemical Society Reviews*, vol. 46, pp. 4400–4416, 2017.

[141] C. Cheng, S. Li, A. Thomas, N. A. Kotov, and R. Haag, "Functional graphene nanomaterials based architectures: Biointeractions, fabrications, and emerging biological applications," *Chemical Reviews*, vol. 117, no. 3, pp. 1826–1914, 2017. PMID: 28075573.

[142] P. Kang, M. C. Wang, and S. Nam, "Bioelectronics with two-dimensional materials," *Microelectronic Engineering*, vol. 161, pp. 18 – 35, 2016.

[143] S. Merino, C. Martín, K. Kostarelos, M. Prato, and E. Vázquez, "Nanocomposite hydrogels: 3d polymer–nanoparticle synergies for on-demand drug delivery," *ACS Nano*, vol. 9, no. 5, pp. 4686–4697, 2015.

[144] F. Perreault, A. Fonseca de Faria, and M. Elimelech, "Environmental applications of graphene-based nanomaterials," *Chemical Society Reviews*, vol. 44, pp. 5861–5896, 2015.

[145] M. N. Chong, B. Jin, C. W. Chow, and C. Saint, "Recent developments in photocatalytic water treatment technology: A review," *Water Research*, vol. 44, no. 10, pp. 2997 – 3027, 2010.

[146] D. Ravelli, D. Dondi, M. Fagnoni, and A. Albini, "Photocatalysis. a multi-faceted concept for green chemistry," *Chemical Society Reviews*, vol. 38, pp. 1999–2011, 2009.

[147] V. Berry, "Impermeability of graphene and its applications," *Carbon*, vol. 62, pp. 1 – 10, 2013.

[148] F. Guo, G. Silverberg, S. Bowers, S.-P. Kim, D. Datta, V. Shenoy, and R. H. Hurt, "Graphene-based environmental barriers," *Environmental Science & Technology*, vol. 46, no. 14, pp. 7717–7724, 2012.

[149] R. Roldan, L. Chirolli, E. Prada, J. A. Silva-Guillen, P. San-Jose, and F. Guinea, "Theory of 2d crystals: graphene and beyond," *Chemical Society Reviews*, vol. 46, pp. 4387–4399, 2017.

[150] J. Sone, T. Yamagami, Y. Aoki, K. Nakatsuji, and H. Hirayama, "Epitaxial growth of silicene on ultra-thin ag(111) films," *New Journal of Physics*, vol. 16, no. 9, p. 095004, 2014.

[151] P. Ares, F. Aguilar-Galindo, D. Rodríguez-San-Miguel, D. A. Aldave, S. Díaz-Tendero, M. Alcamí, F. Martín, J. Gómez-Herrero, and F. Zamora, "Mechanical Isolation of Highly Stable Antimonene under Ambient Conditions," *ArXiv e-prints*, 2016.

[152] A. Castellanos-Gomez, "Black phosphorus: Narrow gap, wide applications," *The Journal of Physical Chemistry Letters*, vol. 6, no. 21, pp. 4280–4291, 2015.

[153] J. N. Coleman, M. Lotya, A. O'Neill, S. D. Bergin, P. J. King, U. Khan, K. Young, A. Gaucher, S. De, R. J. Smith, I. V. Shvets, S. K. Arora, G. Stanton, H.-Y. Kim, K. Lee, G. T. Kim, G. S. Duesberg, T. Hallam, J. J. Boland, J. J. Wang, J. F. Donegan, J. C. Grunlan, G. Moriarty, A. Shmeliov, R. J. Nicholls, J. M. Perkins, E. M. Grieveson, K. Theuwissen, D. W. McComb, P. D. Nellist, and V. Nicolosi, "Two-Dimensional Nanosheets Produced by Liquid Exfoliation of Layered Materials," *Science*, vol. 331, p. 568, Feb. 2011.

[154] H. S. S. Ramakrishna Matte, A. Gomathi, A. K. Manna, D. J. Late, R. Datta, S. K. Pati, and C. N. R. Rao, "Mos2 and ws2 analogues of graphene," *Angewandte Chemie International Edition*, vol. 49, no. 24, pp. 4059–4062, 2010.

[155] R. Mas-Ballesté, C. Gómez-Navarro, J. Gómez-Herrero, and F. Zamora, "2D materials: to graphene and beyond," *Nanoscale*, vol. 3, pp. 20–30, 2011.

[156] J. O. Island, M. Buscema, M. Barawi, J. M. Clamagirand, J. R. Ares, C. Sánchez, I. J. Ferrer, G. A. Steele, H. S. J. van der Zant, and A. Castellanos-Gomez, "Ultrahigh photoresponse of few-layer tis3 nanoribbon transistors," *Advanced Optical Materials*, vol. 2, no. 7, pp. 641–645, 2014.

[157] M. Yankowitz, K. Watanabe, T. Taniguchi, P. San-Jose, and B. J. Leroy, "Pressure-induced commensurate stacking of graphene on boron nitride," *Nature Communications*, vol. 7, p. 13168, Oct. 2016.

[158] A. K. Geim and I. V. Grigorieva, "Van der Waals heterostructures," *ArXiv e-prints*, 2013.

[159] J. D. Caldwell, A. V. Kretinin, Y. Chen, V. Giannini, M. M. Fogler, Y. Francescato, C. T. Ellis, J. G. Tischler, C. R. Woods, A. J. Giles, M. Hong, K. Watanabe, T. Taniguchi, S. A. Maier, and K. S. Novoselov, "Sub-diffractional volume-confined polaritons in the natural hyperbolic material hexagonal boron nitride," *Nature Communications*, vol. 5, p. 5221, 2014.

[160] J.-H. Chen, L. Li, W. G. Cullen, E. D. Williams, and M. S. Fuhrer, "Tunable Kondo effect in graphene with defects," *Nature Physics*, vol. 7, pp. 535–538, 2011.

[161] S. Tongay, K. Berke, M. Lemaitre, Z. Nasrollahi, D. B. Tanner, A. F. Hebard, and B. R. Appleton, "Stable hole doping of graphene for low electrical resistance and high optical transparency," *Nanotechnology*, vol. 22, p. 425701, 2011.

[162] S. Casolo, O. M. Lovvik, R. Martinazzo, and G. F. Tantardini, "Understanding adsorption of hydrogen atoms on graphene," *Journal of Chemical Physics*, vol. 130, no. 5, pp. 054704–054704, 2009.

[163] C. Cab, R. Medina-Esquiel, C. Acosta, J. Mendez-Gamboa, F. Penunuri, and A. Tapia, "Influence of Electric Field in the Adsorption of Atomic Hydrogen on Graphene," *Advances in Condensed Matter Physics*, vol. 9, p. 847804, 2015.

[164] M. Moaied, J. A. Moreno, M. J. Caturla, F. Ynduráin, and J. J. Palacios, "Theoretical study of the dynamics of atomic hydrogen adsorbed on graphene multilayers," *Physical Review B*, vol. 91, p. 155419, 2015.

[165] C. Ataca, E. Aktürk, H. Şahin, and S. Ciraci, "Adsorption of carbon adatoms to graphene and its nanoribbons," *Journal of Applied Physics*, vol. 109, no. 1, p. 013704, 2011.

[166] H. S. S. Ramakrishna Matte, K. S. Subrahmanyam, K. Venkata Rao, S. J. George, and C. N. R. Rao, "Quenching of fluorescence of aromatic molecules by graphene due to electron transfer," *Chemical Physics Letters*, vol. 506, pp. 260–264, 2011.

[167] A. K. Manna and S. K. Pati, "Tuning the electronic structure of graphene by molecular charge transfer: A computational study," *Chemistry – An Asian Journal*, vol. 4, no. 6, pp. 855–860, 2009.

[168] I. Shtepliuk, N. M. Caffrey, T. Iakimov, V. Khranovskyy, I. A. Abrikosov, and R. Yakimova, "On the interaction of toxic Heavy Metals (Cd, Hg, Pb) with graphene quantum dots and infinite graphene," *Scientific Reports*, vol. 7, p. 3934, 2017.

[169] O. Leenaerts, B. Partoens, and F. M. Peeters, "Adsorption of h_2O, Nh_3, co, No_2, and no on graphene: A first-principles study," *Physical Review B*, vol. 77, p. 125416, 2008.

[170] R. Zangi and A. E. Mark, "Monolayer ice," *Physical Review Letters*, vol. 91, p. 025502, 2003.

[171] S. Han, M. Y. Choi, P. Kumar, and H. E. Stanley, "Phase transitions in confined water nanofilms," *Nature Physics*, vol. 6, pp. 685–689, 2010.

[172] G. Algara-Siller, O. Lehtinen, F. C. Wang, R. R. Nair, U. Kaiser, H. A. Wu, A. K. Geim, and I. V. Grigorieva, "Square ice in graphene nanocapillaries," *Nature*, vol. 519, pp. 443–445, 2015.

[173] Y. Zhu, F. Wang, J. Bai, X. C. Zeng, and H. Wu, "AB-stacked square-like bilayer ice in graphene nanocapillaries," *Physical Chemistry Chemical Physics*, vol. 18, pp. 22039–22046, 2016.

[174] T. O. Wehling, A. I. Lichtenstein, and M. I. Katsnelson, "First-principles studies of water adsorption on graphene: The role of the substrate," *Applied Physics Letters*, vol. 93, no. 20, p. 202110, 2008.

[175] X. An, T. Simmons, R. Shah, C. Wolfe, K. M. Lewis, M. Washington, S. K. Nayak, S. Talapatra, and S. Kar, "Stable aqueous dispersions of noncovalently functionalized graphene from graphite and their multifunctional high-performance applications," *Nano Letters*, vol. 10, no. 11, pp. 4295–4301, 2010.

[176] C.-H. Lu, H.-H. Yang, C.-L. Zhu, X. Chen, and G.-N. Chen, "A graphene platform for sensing biomolecules," *Angewandte Chemie*, vol. 121, no. 26, pp. 4879–4881, 2009.

[177] D. Soriano, F. Muñoz Rojas, J. Fernández-Rossier, and J. J. Palacios, "Hydrogenated graphene nanoribbons for spintronics," *Physical Review B*, vol. 81, p. 165409, 2010.

[178] F. Yndurain, "Effect of hole doping on the magnetism of point defects in graphene: A theoretical study," *Physical Review B*, vol. 90, p. 245420, 2014.

[179] H. González-Herrero, J. M. Gómez-Rodríguez, P. Mallet, M. Moaied, J. J. Palacios, C. Salgado, M. M. Ugeda, J.-Y. Veuillen, F. Yndurain, and I. Brihuega, "Atomic-scale control of graphene magnetism by using hydrogen atoms," *Science*, vol. 352, pp. 437–441, 2016.

[180] A. Ranjbar, M. S. Bahramy, M. Khazaei, H. Mizuseki, and Y. Kawazoe, "First-principles study of structural stability, magnetism, and hyperfine coupling in hydrogen clusters adsorbed on graphene," *Physical Review B*, vol. 82, p. 165446, 2010.

[181] D. Pesin and A. H. MacDonald, "Spintronics and pseudospintronics in graphene and topological insulators," *Nature Materials*, vol. 11, pp. 409–416, 2012.

[182] H. Sevinçli, M. Topsakal, E. Durgun, and S. Ciraci, "Electronic and magnetic properties of 3*d* transition-metal atom adsorbed graphene and graphene nanoribbons," *Physical Review B*, vol. 77, p. 195434, 2008.

[183] D. Jacob and G. Kotliar, "Orbital selective and tunable kondo effect of magnetic adatoms on graphene: Correlated electronic structure calculations," *Physical Review B*, vol. 82, p. 085423, 2010.

[184] M. Vojta, L. Fritz, and R. Bulla, "Gate-controlled kondo screening in graphene: Quantum criticality and electron-hole asymmetry," *Europhysics Letters*, vol. 90, no. 2, p. 27006, 2010.

[185] K. T. Chan, H. Lee, and M. L. Cohen, "Gated adatoms on graphene studied with first-principles calculations," *Physical Review B*, vol. 83, p. 035405, 2011.

[186] M. Sargolzaei and F. Gudarzi, "Magnetic properties of single 3d transition metals adsorbed on graphene and benzene: A density functional theory study," *Journal of Applied Physics*, vol. 110, no. 6, p. 064303, 2011.

[187] J. Ding, Z. Qiao, W. Feng, Y. Yao, and Q. Niu, "Engineering quantum anomalous/valley hall states in graphene via metal-atom adsorption: An ab-initio study," *Physical Review B*, vol. 84, p. 195444, 2011.

[188] T. O. Wehling, A. I. Lichtenstein, and M. I. Katsnelson, "Transition-metal adatoms on graphene: Influence of local coulomb interactions on chemical bonding and magnetic moments," *Physical Review B*, vol. 84, p. 235110, 2011.

[189] A. N. Rudenko, F. J. Keil, M. I. Katsnelson, and A. I. Lichtenstein, "Adsorption of cobalt on graphene: Electron correlation effects from a quantum chemical perspective," *Physical Review B*, vol. 86, p. 075422, 2012.

[190] R. Thapa, D. Sen, M. K. Mitra, and K. K. Chattopadhyay, "Palladium atoms and its dimers adsorbed on graphene: First-principles study," *Physica B Condensed Matter*, vol. 406, pp. 368–373, 2011.

[191] M. K. Srivastava, Y. Wang, A. F. Kemper, and H.-P. Cheng, "Density functional study of gold and iron clusters on perfect and defected graphene," *Physical Review B*, vol. 85, p. 165444, 2012.

[192] J. Hu, J. Alicea, R. Wu, and M. Franz, "Giant topological insulator gap in graphene with 5*d* adatoms," *Physical Review Letters*, vol. 109, p. 266801, 2012.

[193] D. Ma, Z. Li, and Z. Yang, "Strong spin–orbit splitting in graphene with adsorbed au atoms," *Carbon*, vol. 50, no. 1, pp. 297 – 305, 2012.

[194] O. Leenaerts, B. Partoens, and F. M. Peeters, "Water on graphene: Hydrophobicity and dipole moment using density functional theory," *Physical Review B*, vol. 79, p. 235440, 2009.

[195] F. Yavari, C. Kritzinger, C. Gaire, L. Song, H. Gulapalli, T. Borca-Tasciuc, P. M. Ajayan, and N. Koratkar, "Tunable bandgap in graphene by the controlled adsorption of water molecules," *Small*, vol. 6, no. 22, pp. 2535–2538, 2010.

[196] A. AlZahrani, "First-principles study on the structural and electronic properties of graphene upon benzene and naphthalene adsorption," *Applied Surface Science*, vol. 257, no. 3, pp. 807 – 810, 2010.

[197] J. Berashevich and T. Chakraborty, "Tunable band gap and magnetic ordering by adsorption of molecules on graphene," *Physical Review B*, vol. 80, p. 033404, 2009.

[198] A. Bachmatiuk, J. Zhao, S. Gorantla, I. Gonzalez Martinez, J. Wiedermann, C. Lee, J. Eckert, and M. Hermann Rummeli, "Low voltage transmission electron microscopy of graphene," vol. 11, 2014.

[199] F. Schäffel, M. Wilson, and J. H. Warner, "Motion of light adatoms and molecules on the surface of few-layer graphene," *ACS Nano*, vol. 5, no. 12, pp. 9428–9441, 2011.

[200] C. Gong, A. W. Robertson, K. He, C. Ford, A. A. R. Watt, and J. H. Warner, "Interactions of pb and te atoms with graphene," *Dalton Trans.*, vol. 43, pp. 7442–7448, 2014.

[201] R. J. Kashtiban, M. A. Dyson, R. R. Nair, R. Zan, S. L. Wong, Q. Ramasse, A. K. Geim, U. Bangert, and J. Sloan, "Atomically resolved imaging of highly ordered alternating fluorinated graphene," *Nature Communications*, vol. 5, p. 4902, 2014.

[202] T. P. Hardcastle, C. R. Seabourne, R. Zan, R. M. D. Brydson, U. Bangert, Q. M. Ramasse, K. S. Novoselov, and A. J. Scott, "Mobile metal adatoms on single layer, bilayer, and trilayer graphene: An ab initio dft study with van der waals corrections correlated with electron microscopy data," *Physical Review B*, vol. 87, p. 195430, 2013.

[203] Q. M. Ramasse, C. R. Seabourne, D.-M. Kepaptsoglou, R. Zan, U. Bangert, and A. J. Scott, "Probing the bonding and electronic structure of single atom dopants in graphene with electron energy loss spectroscopy," *Nano Letters*, vol. 13, no. 10, pp. 4989–4995, 2013.

[204] R. Zan, U. Bangert, Q. Ramasse, and K. S Novoselov, "Evolution of gold nanostructures on graphene," vol. 7, pp. 2868–72, 2011.

[205] M. Gyamfi, T. Eelbo, M. Waśniowska, and R. Wiesendanger, "Fe adatoms on graphene/Ru(0001): Adsorption site and local electronic properties," *Physical Review B*, vol. 84, no. 11, p. 113403, 2011.

[206] V. W. Brar, R. Decker, H.-M. Solowan, Y. Wang, L. Maserati, K. T. Chan, H. Lee, Ç. O. Girit, A. Zettl, S. G. Louie, M. L. Cohen, and M. F. Crommie, "Gate-controlled ionization and screening of cobalt adatoms on a graphene surface," *Nature Physics*, vol. 7, pp. 43–47, 2011.

[207] L. Li, Y.-Y. Ni, Y. Zhong, T.-F. Fang, and H.-G. Luo, "The kondo effect of an adatom in graphene and its scanning tunneling spectroscopy," *New Journal of Physics*, vol. 15, no. 5, p. 053018, 2013.

[208] L. Jisook, S. Sangdeok, K. Bongsoo, and S. H. Suk, "Surface-enhanced raman scattering of single- and few-layer graphene by the deposition

of gold nanoparticles," *Chemistry - A European Journal*, vol. 17, no. 8, pp. 2381–2387, 2011.

[209] F. Schedin, E. Lidorikis, A. Lombardo, V. G. Kravets, A. K. Geim, A. N. Grigorenko, K. S. Novoselov, and A. C. Ferrari, "Surface-enhanced raman spectroscopy of graphene," *ACS Nano*, vol. 4, no. 10, pp. 5617–5626, 2010.

[210] Z. Jin, J. Yao, C. Kittrell, and J. M. Tour, "Large-scale growth and characterizations of nitrogen-doped monolayer graphene sheets," *ACS Nano*, vol. 5, no. 5, pp. 4112–4117, 2011.

[211] L. Zhao, R. He, K. T. Rim, T. Schiros, K. S. Kim, H. Zhou, C. Gutiérrez, S. P. Chockalingam, C. J. Arguello, L. Pálová, D. Nordlund, M. S. Hybertsen, D. R. Reichman, T. F. Heinz, P. Kim, A. Pinczuk, G. W. Flynn, and A. N. Pasupathy, "Visualizing Individual Nitrogen Dopants in Monolayer Graphene," *Science*, vol. 333, p. 999, 2011.

[212] R. Dreizler and E. Gross, *Density Functional Theory*. Springer-Verlag, 1990.

[213] P. Jungwirth, "Density functional theory. a practical introduction. von david sholl und janice a. steckel.," *Angewandte Chemie*, vol. 122, no. 3, pp. 493–493, 2010.

[214] S. Cottenier, "Density Functional Theory and the Family of (L)APW-methods: a step-by-step introduction," *ISBN*, 2004.

[215] J. Hafner, "Ab initio density-functional calculations in materials science: from quasicrystals over microporous catalysts to spintronics," *Journal of Physics Condensed Matter*, vol. 22, p. 384205, 2010.

[216] R. G. Parr, S. R. Gadre, and L. J. Bartolotti, "Local density functional theory of atoms and molecules," *Proceedings of the National Academy of Science*, vol. 76, pp. 2522–2526, 1979.

[217] R. O. Jones, "Density functional theory: Its origins, rise to prominence, and future," *Reviews of Modern Physics*, vol. 87, pp. 897–923, 2015.

[218] K. Lejaeghere, G. Bihlmayer, T. Björkman, P. Blaha, S. Blügel, V. Blum, D. Caliste, I. E. Castelli, S. J. Clark, A. Dal Corso, S. de Gironcoli, T. Deutsch, J. K. Dewhurst, I. Di Marco, C. Draxl, M. Dułak, O. Eriksson, J. A. Flores-Livas, K. F. Garrity, L. Genovese, P. Giannozzi, M. Giantomassi, S. Goedecker, X. Gonze, O. Grånäs, E. K. U. Gross, A. Gulans, F. Gygi, D. R. Hamann, P. J. Hasnip, N. A. W. Holzwarth, D. Iuşan, D. B. Jochym, F. Jollet, D. Jones, G. Kresse, K. Koepernik, E. Küçükbenli, Y. O. Kvashnin, I. L. M. Locht, S. Lubeck, M. Marsman,

N. Marzari, U. Nitzsche, L. Nordström, T. Ozaki, L. Paulatto, C. J. Pickard, W. Poelmans, M. I. J. Probert, K. Refson, M. Richter, G.-M. Rignanese, S. Saha, M. Scheffler, M. Schlipf, K. Schwarz, S. Sharma, F. Tavazza, P. Thunström, A. Tkatchenko, M. Torrent, D. Vanderbilt, M. J. van Setten, V. Van Speybroeck, J. M. Wills, J. R. Yates, G.-X. Zhang, and S. Cottenier, "Reproducibility in density functional theory calculations of solids," *Science*, vol. 351, no. 6280, 2016.

[219] L. H. Thomas, "The calculation of atomic fields," *Proceedings of the Cambridge Philosophical Society*, vol. 23, p. 542, 1927.

[220] E. Fermi, "Un Metodo Statistico per la determinazione di Alcune priorieta dell' atome," *Rend. Accad. Naz. Lincei*, vol. 6, p. 602, 1927.

[221] S. B. Trickey, "Introduction," in *Density Functional Theory of Many-Fermion Systems* (P.-O. Löwdin, ed.), vol. 21 of *Advances in Quantum Chemistry*, pp. 1 – 5, Academic Press, 1990.

[222] J. J. Sakurai, *Modern quantum mechanics*. Reading, MA: Addison Wesley, c1985, edited by Tuan, San Fu, 1985.

[223] P. A. M. Dirac, *The principles of quantum mechanics*. The International Series of Monographs on Physics, Oxford: Clarendon Press, 1947.

[224] Goncalves, "Calculations of electronic structure and hyperfine parameters in oxides," Master's thesis, Universidade de Aveiro.

[225] P. A. M. Dirac, "Note on Exchange Phenomena in the Thomas Atom," *Proceedings of the Cambridge Philosophical Society*, vol. 26, p. 376, 1930.

[226] P. Hohenberg and W. Kohn, "Inhomogeneous Electron Gas," *Physical Review*, vol. 136, pp. 864–871, 1964.

[227] W. Kohn and L. J. Sham, "Self-Consistent Equations Including Exchange and Correlation Effects," *Physical Review*, vol. 140, pp. 1133–1138, 1965.

[228] J. Singh and L. Nordstrom, *Planewaves, Pseudopotentials, and the LAPW Method*. 2006.

[229] J. P. Perdew, K. Burke, and M. Ernzerhof, "Generalized gradient approximation made simple," *Physical Review Letters*, vol. 77, pp. 3865–3868, 1996.

[230] J. P. Perdew, S. Kurth, A. c. v. Zupan, and P. Blaha, "Accurate density functional with correct formal properties: A step beyond the generalized gradient approximation," *Physical Review Letters*, vol. 82, pp. 2544–2547, 1999.

[231] J. Tao, J. P. Perdew, V. N. Staroverov, and G. E. Scuseria, "Climbing the density functional ladder: Nonempirical meta–generalized gradient approximation designed for molecules and solids," *Physical Review Letters*, vol. 91, p. 146401, 2003.

[232] J. D. v. d. J. D. Waals

[233] K. Ray, *Van Der Waals Corrected Density Functional Theory Calculations on Zeolitic Imidazolate Frameworks*. 2013.

[234] S. Grimme, "Accurate description of van der waals complexes by density functional theory including empirical corrections," *Journal of Computational Chemistry*, vol. 25, no. 12, pp. 1463–1473, 2004.

[235] S. Grimme, "Semiempirical gga-type density functional constructed with a long-range dispersion correction," *Journal of Computational Chemistry*, vol. 27, no. 15, pp. 1787–1799, 2006.

[236] S. Grimme, J. Antony, S. Ehrlich, and H. Krieg, "A consistent and accurate ab initio parametrization of density functional dispersion correction (dft-d) for the 94 elements h-pu," *The Journal of Chemical Physics*, vol. 132, no. 15, p. 154104, 2010.

[237] C. Adamo and V. Barone, "Toward reliable density functional methods without adjustable parameters: The pbe0 model," *The Journal of Chemical Physics*, vol. 110, no. 13, pp. 6158–6170, 1999.

[238] K. E. Riley, M. Pitoňák, P. Jurečka, and P. Hobza, "Stabilization and structure calculations for noncovalent interactions in extended molecular systems based on wave function and density functional theories," *Chemical Reviews*, vol. 110, no. 9, pp. 5023–5063, 2010.

[239] A. Tkatchenko, L. Romaner, O. T. Hofmann, E. Zojer, C. Ambrosch-Draxl, and M. Scheffler, "Van der waals interactions between organic adsorbates and at organic/inorganic interfaces," *MRS Bulletin*, vol. 35, no. 6, p. 435–442, 2010.

[240] P. L. Silvestrelli, "van der waals interactions in density functional theory using wannier functions," *The Journal of Physical Chemistry A*, vol. 113, no. 17, pp. 5224–5234, 2009.

[241] P. L. Silvestrelli, "Improvement in hydrogen bond description using van der waals-corrected dft: The case of small water clusters," *Chemical Physics Letters*, vol. 475, no. 4, pp. 285 – 288, 2009.

[242] A. Ambrosetti and P. L. Silvestrelli, "Adsorption of rare-gas atoms and water on graphite and graphene by van der waals-corrected density functional theory," *The Journal of Physical Chemistry C*, vol. 115, no. 9, pp. 3695–3702, 2011.

[243] P. L. Silvestrelli, A. Ambrosetti, S. Grubisiĉ, and F. Ancilotto, "Adsorption of rare-gas atoms on cu(111) and pb(111) surfaces by van der waals corrected density functional theory," *Physical Review B*, vol. 85, p. 165405, 2012.

[244] A. Tkatchenko and M. Scheffler, "Accurate molecular van der waals interactions from ground-state electron density and free-atom reference data," *Physical Review Letters*, vol. 102, p. 073005, 2009.

[245] F. L. Hirshfeld, "Bonded-atom fragments for describing molecular charge densities," *Theoretica chimica acta*, vol. 44, no. 2, pp. 129–138, 1977.

[246] A. Tkatchenko, R. A. DiStasio, R. Car, and M. Scheffler, "Accurate and efficient method for many-body van der waals interactions," *Physical Review Letters*, vol. 108, p. 236402, 2012.

[247] V. G. Ruiz, W. Liu, E. Zojer, M. Scheffler, and A. Tkatchenko, "Density-functional theory with screened van der waals interactions for the modeling of hybrid inorganic-organic systems," *Physical Review Letters*, vol. 108, p. 146103, 2012.

[248] J. C. Phillips, "Energy-band interpolation scheme based on a pseudopotential," *Physical Review*, vol. 112, pp. 685–695, 1958.

[249] S. Kurth, J. P. Perdew, and P. Blaha, "Molecular and solid-state tests of density functional approximations: Lsd, ggas, and meta-ggas," *International Journal of Quantum Chemistry*, vol. 75, no. 4-5, pp. 889–909, 1999.

[250] V. N. Staroverov, G. E. Scuseria, J. Tao, and J. P. Perdew, "Tests of a ladder of density functionals for bulk solids and surfaces," *Physical Review B*, vol. 69, p. 075102, 2004.

[251] P. Haas, F. Tran, and P. Blaha, "Calculation of the lattice constant of solids with semilocal functionals," *Physical Review B*, vol. 79, p. 085104, 2009.

[252] G. I. Csonka, J. P. Perdew, A. Ruzsinszky, P. H. T. Philipsen, S. Lebègue, J. Paier, O. A. Vydrov, and J. G. Ángyán, "Assessing the performance of recent density functionals for bulk solids," *Physical Review B*, vol. 79, p. 155107, 2009.

[253] P. Pernot, B. Civalleri, D. Presti, and A. Savin, "Prediction Uncertainty of Density Functional Approximations for Properties of Crystals with Cubic Symmetry," *Journal of Physical Chemistry A*, vol. 119, pp. 5288–5304, 2015.

[254] L. A. Curtiss, K. Raghavachari, P. C. Redfern, and J. A. Pople, "Assessment of gaussian-2 and density functional theories for the computation of enthalpies of formation," *The Journal of Chemical Physics*, vol. 106, no. 3, pp. 1063–1079, 1997.

[255] J. Paier, R. Hirschl, M. Marsman, and G. Kresse, "The perdew–burke–ernzerhof exchange-correlation functional applied to the g2-1 test set using a plane-wave basis set," *The Journal of Chemical Physics*, vol. 122, no. 23, p. 234102, 2005.

[256] L. Goerigk and S. Grimme, "A thorough benchmark of density functional methods for general main group thermochemistry, kinetics, and noncovalent interactions," *Physical Chemistry Chemical Physics*, vol. 13, pp. 6670–6688, 2011.

[257] "WIEN2k web page." `http://susi.theochem.tuwien.ac.at/`. Accessed: 2018-02-17.

[258] "VASP web page." `https://www.vasp.at/`. Accessed: 2018-02-17.

[259] A. Lopes, *Local probe studies on lattice distortions and electronic correlations in manganites*. PhD thesis, Universidade de Aveiro, 2006.

[260] G. Schatz and A. Weidinger, *Nuclear Condensed Matter Physics*. John Wiley and Sons, England, 1996.

[261] J. D. Jackson, *Classical electrodynamics*. 1975.

[262] R. P. Feynman, *Feynman lectures on physics. Volume 2: Mainly electromagnetism and matter*. 1964.

[263] C. Cohen-Tannoudji,, B. Diu, and F. Laloe, *Quantum Mechanics*. 1977.

[264] P. Lehmann and J. Miller, "Interaction quadrupolaire dans cd-111," *Comptes Rendus Hebdomadaires des Seances de L Academie des Sciences*, vol. 240, pp. 298–299, 1955.

[265] J. N. Gonçalves, A. Stroppa, J. G. Correia, T. Butz, S. Picozzi, A. S. Fenta, and V. S. Amaral, "Ab initio study of the relation between electric polarization and electric field gradients in ferroelectrics," *Physical Review B*, vol. 86, p. 035145, 2012.

[266] E. L. Brady and M. Deutsch, "Angular Correlation of Successive Gamma-Rays," *Physical Review*, vol. 78, pp. 558–566, 1950.

[267] T. Butz, "Analytic perturbation functions for static interactions in perturbed angular correlations of γ-rays," *Hyperfine Interactions*, vol. 73, no. 3, pp. 387–388, 1992.

[268] C. Scherer, "Gamma-gamma angular correlations: A model for statistical perturbation with any correlation time," *Nuclear Physics A*, vol. 157, no. 1, pp. 81 – 92, 1970.

[269] A. Abragam and R. V. Pound, "Influence of Electric and Magnetic Fields on Angular Correlations," *Physical Review*, vol. 92, pp. 943–962, 1953.

[270] M. Morita and R. Morita, "Beta-Gamma Angular Correlations and Beta-Ray Angular Distributions," *Progress of Theoretical Physics Supplement*, vol. 37, pp. 458–472, 1966.

[271] H. Frauenfelder and R. Steffen, "Alpha-, beta-, and gamma-ray spectroscopy," *vol*, vol. 2, 1965.

[272] A. J. A. J. Ferguson, *Angular correlation methods in gamma-ray spectroscopy*. Amsterdam : North-Holland Pub. Co, 1965.

[273] A. R. Arends, C. Hohenemser, F. Pleiter, H. de Waard, L. Chow, and R. M. Suter, "Data reduction methodology for perturbed angular correlation experiments," *Hyperfine Interactions*, vol. 8, pp. 191–213, 1980.

[274] J. G. Correia, *Aplicacoes da tecnica de correlacoes angulares perturbadas e-gamma no ISOLDE-CERN,*. PhD thesis, Universidade de Lisboa, 1993.

[275] "ISOLDE." `http://isolde.web.cern.ch/`. Accessed: 2018-02-17.

[276] U. Köster, "Intense radioactive-ion beams produced with the isol method," *The European Physical Journal A*, vol. 15, no. 1, pp. 255–263, 2002.

[277] E. Kugler, "The isolde facility," *Hyperfine Interactions*, vol. 129, no. 1, pp. 23–42, 2000.

[278] M. Borge, "Highlights of the isolde facility and the hie-isolde project," *Nuclear Instruments and Methods in Physics Research Section B: Beam Interactions with Materials and Atoms*, vol. 376, pp. 408 – 412, 2016.

[279] A. Gottberg, "Target materials for exotic isol beams," *Nuclear Instruments and Methods in Physics Research Section B: Beam Interactions with Materials and Atoms*, vol. 376, pp. 8 – 15, 2016. Proceedings of the XVIIth International Conference on Electromagnetic Isotope Separators

and Related Topics (EMIS2015), Grand Rapids, MI, U.S.A., 11-15 May 2015.

[280] V. Mishin, V. Fedoseyev, H.-J. Kluge, V. Letokhov, H. Ravn, F. Scheerer, Y. Shirakabe, S. Sundell, and O. Tengblad, "Chemically selective laser ion-source for the cern-isolde on-line mass separator facility," *Nuclear Instruments and Methods in Physics Research Section B: Beam Interactions with Materials and Atoms*, vol. 73, no. 4, pp. 550 – 560, 1993.

[281] J. P. Biersack and J. F. Ziegler, "The stopping and range of ions in solids," in *Ion Implantation Techniques* (H. Ryssel and H. Glawischnig, eds.), (Berlin, Heidelberg), pp. 122–156, Springer Berlin Heidelberg, 1982.

[282] M. Jäger, K. Iwig, and T. Butz, "A user-friendly fully digital TDPAC-spectrometer," *Hyperfine Interactions*, vol. 198, pp. 167–172, 2010.

[283] M. Jäger, K. Iwig, and T. Butz, "A compact digital time differential perturbed angular correlation-spectrometer using field programmable gate arrays and various timestamp algorithms," *Review of Scientific Instruments*, vol. 82, no. 6, p. 065105, 2011.

[284] M. Jäger and T. Butz, "FPGA implementation of digital constant fraction algorithm with fractional delay for optimal time resolution," *Nuclear Instruments and Methods in Physics Research A*, vol. 674, pp. 24–27, 2012.

[285] K. Potzger, T. E. Mølholt, A. S. Fenta, and L. M. C. Pereira, "Surface science using radioactive ions at isolde: from metal surfaces to two-dimensional materials," *Journal of Physics G: Nuclear and Particle Physics*, vol. 44, no. 6, p. 064001, 2017.

[286] X. Mi, V. Meunier, N. Koratkar, and Y. Shi, "Facet-insensitive graphene growth on copper," *Physical Review B*, vol. 85, no. 15, p. 155436, 2012.

[287] O. Frank, J. Vejpravova, V. Holy, L. Kavan, and M. Kalbac, "Interaction between graphene and copper substrate: The role of lattice orientation," *ArXiv e prints*, 2014.

[288] P. Vingerhoets, K. T. Flanagan, M. Avgoulea, J. Billowes, M. L. Bissell, K. Blaum, B. A. Brown, B. Cheal, M. de Rydt, D. H. Forest, C. Geppert, M. Honma, M. Kowalska, J. Krämer, A. Krieger, E. Mané, R. Neugart, G. Neyens, W. Nörtershäuser, T. Otsuka, M. Schug, H. H. Stroke, G. Tungate, and D. T. Yordanov, "Nuclear spins, magnetic moments, and quadrupole moments of Cu isotopes from N=28 to N=46: Probes for core polarization effects," *Physical Review C*, vol. 82, no. 6, p. 064311, 2010.

[289] M. Stachura, A. Gottberg, K. Johnston, M. Bissell, R. Garcia Ruiz, J. Martins Correia, A. R. Granadeiro Costa, M. Dehn, M. Deicher, A. S. Fenta, L. Hemmingsen, T. E. Molholt, M. Munch, G. Neyens, S. Pallada, M. R. Silva, and D. Zakoucky, "Versatile Ion-polarized Techniques Online (VITO) experiment at ISOLDE-CERN," *Nuclear Instruments and Methods in Physics Research Section B*, vol. 376, pp. 369 – 373, 2016.

[290] J. Rafiee, X. Mi, H. Gullapalli, A. V. Thomas, F. Yavari, Y. Shi, P. M. Ajayan, and N. A. Koratkar, "Wetting transparency of graphene," *Nature Materials*, vol. 11, pp. 217–222, 2012.

[291] S. P. Koenig, N. G. Boddeti, M. L. Dunn, and J. S. Bunch, "Ultrastrong adhesion of graphene membranes," *Nature Nanotechnology*, vol. 6, pp. 543–546, 2011.

[292] J. Shim, C. H. Lui, T. Y. Ko, Y.-J. Yu, P. Kim, T. F. Heinz, and S. Ryu, "Water-gated charge doping of graphene induced by mica substrates," *Nano Letters*, vol. 12, no. 2, pp. 648–654, 2012.

[293] L. A. Ponomarenko, R. Yang, T. M. Mohiuddin, M. I. Katsnelson, K. S. Novoselov, S. V. Morozov, A. A. Zhukov, F. Schedin, E. W. Hill, and A. K. Geim, "Effect of a high-κ environment on charge carrier mobility in graphene," *Physical Review Letters*, vol. 102, p. 206603, 2009.

Publications

J. N. Gonçalves, A. Stroppa, J. G. Correia, T. Butz, S. Picozzi, **A. S. Fenta**, and V. S. Amaral, *Ab-initio study of the relation between electric polarization and electric field gradients in ferroelectrics*, Physical Review B, 86, 035145 (2012).

J. N. Gonçalves, V. S. Amaral, J. G. Correia, A. Stroppa, **A. S. Fenta**, A. Baghizadeh, S. Picozzi, *Local probing of multiferroics: First-principles study of hyperfine parameters in YMnO3 and YMn2O5*, EPJ, 75, 09002 (2014).

Stachura M., Gottberg A., Johnston K., Bissell, M., Garcia Ruiz R., Martins Correia J., Granadeiro Costa A. R., Dehn M., Deicher M., **Fenta A. S.**, Hemmingsen L., Molholt T. E., Munch, M., Neyens G., Pallada S., Silva M. R. and Zakoucky D., *Versatile Ion-polarized Techniques On-line (VITO) experiment at ISOLDE-CERN*, NIM in Physics, Research Section B, 376 (2016).

A. S. Fenta et al., *The 68mCu/68Cu isotope as a new probe for hyperfine studies: the nuclear moments*, European Physics Letters,115, 62002 (2016) - **selected for the EPL Highlights 2016**.

K. Potzger, T. E. Molholt, **A. S. Fenta**, L. M. C. Pereira, *Surface science using radioactive ions at ISOLDE: from metal surfaces to 2-dimensional materials*, Journal of Physics G, 101697 (2017).

Karl Johnston, Juliana Schell, J. G. Correia, M. Deicher, H. P. Gunnlaugsson, **A. S. Fenta**, E. David-Bosne, A. R. G. Costa, Doru C. Lupascu, *The solid-state physics programme at ISOLDE: recent developments and perspectives*, Journal of Physics G, 101811.R1 (2017).

C. O. Amorim, J. N. Goncalves, D. S. Tavares, **A. S. Fenta**, C. B. Lopes, E. Pereira, T. Trindade, J. G. Correia, and V. S. Amaral, *Ultra-Sensitive Quantification of Hg2+ sorption by Functionalized Nanoparticles using Radioactive Trackers Spectroscopy*, Microchemical Journal, 138, 418–423 (2018).